

**PHYSICAL ADSORPTION OF CARBON DIOXIDE CAPTURE BY NOVEL
MATERIALS**

BY

NAEF A. A. QASEM

A Dissertation Presented to the
DEANSHIP OF GRADUATE STUDIES

KING FAHD UNIVERSITY OF PETROLEUM & MINERALS

DHAHRAN, SAUDI ARABIA

In Partial Fulfillment of the
Requirements for the Degree of

DOCTOR OF PHILOSOPHY

In

MECHANICAL ENGINEERING

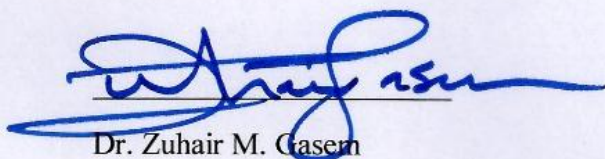
MAY 2017

KING FAHD UNIVERSITY OF PETROLEUM & MINERALS

DHAHRAN- 31261, SAUDI ARABIA

DEANSHIP OF GRADUATE STUDIES

This thesis, written by **NAEF ABDULJALIL ABDULRAHMAN QASEM** under the direction his thesis advisor and approved by his thesis committee, has been presented and accepted by the Dean of Graduate Studies, in partial fulfillment of the requirements for the degree of **DOCTOR OF PHILOSOPHY IN MECHANICAL ENGINEERING**.



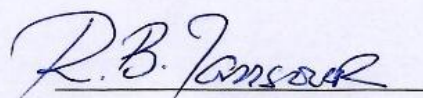
Dr. Zuhair M. Gasem
Department Chairman



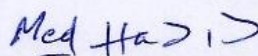
Dr. Salam A. Zummo
Dean of Graduate Studies



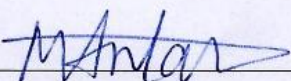
24 / 7 / 2017
Date



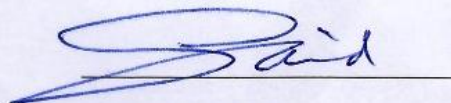
Dr. Rached Ben-Mansour
(Advisor)



Dr. Mohamed A. Habib
(Co-advisor)



Dr. Mohammed A. Antar
(Member)



Dr. Syed A. M. Said
(Member)



Dr. Saidur Rahman
(Member)

© Naef Abduljalil Abdulrahman Qasem

2017

*Dedicated to my beloved parents, siblings, wife, daughters
(Adhkar & Zahra) and son (Abdullah).*

ACKNOWLEDGMENTS

Thanks and all praise be to Allah (azzawagal) who created me, blessed me with health and who grant me success.

I would like to state my deep appreciation and gratitude to my dissertation advisor Dr. Rached Ben-Mansour who has always been providing kindest support, continual encouragement and supervision. I also would like to acknowledge my co-advisor Dr. Mohamed A. Habib and committee members: Dr. Syed A. M. Said, Dr. Mohammed A. Antar and Dr. Saidur Rahman for their valuable advices and guidance.

I also acknowledge King Fahd University of Petroleum and Minerals (KFUPM) and Mechanical Engineering Department (ME) as well as the all faculties who taught and helped me. I wish also to acknowledge the support received from King Abdulaziz City for Science and Technology (KACST) Carbon Capture and Sequestration Technology Innovation Center (CCSTIC #32-753) at King Fahd University of Petroleum and Minerals (KFUPM) for funding this work.

The support received from Taiz University, Taiz, Yemen to achieve my PhD is highly acknowledged.

Many thanks to my colleagues/friends who cooperated with me during my PhD including Dr. Bassem Al-Maythalony, Dr. Najam Ul Qader, Dr. Mehaboob Basha, Bamidele Olufemi, Mahmoud Abdelnabi, Ahmed Abulyamen, Binash Imtiyaz, Kyle E. Cordova and so on.

Finally, I acknowledge Kingdom of Saudi Arabia for providing me MS, and PhD scholarship and for all other facilitations.

TABLE OF CONTENTS

ACKNOWLEDGMENTS	V
TABLE OF CONTENTS	VI
LIST OF TABLES.....	IX
LIST OF FIGURES.....	XI
LIST OF ABBREVIATIONS	XVII
ABSTRACT	XXI
ملخص الرسالة.....	XXII
CHAPTER 1 INTRODUCTION.....	1
1.1 Introductory Background	1
1.2 Carbon Capture Technologies	4
1.3 Research Objectives.....	7
1.4 Dissertation Outline.....	9
CHAPTER 2 LITERATURE REVIEW.....	10
2.1 Background.....	10
2.2 Post-Combustion Carbon capture Technologies.....	12
2.2.1 Adsorption	15
2.2.2 Adsorption Process Types.....	19
2.3 Thermodynamic Analysis of Physical-Adsorption Carbon Capture	20
2.4 Carbon Capture Adsorption Materials.....	23
2.4.1 Porous Materials	27
2.4.2 Carbon Based Adsorbents.....	29

2.4.3	Solid Adsorbents.....	30
2.4.4	Carbon Nanotubes (CNTs).....	30
2.4.5	Metal Organic Frameworks (MOFs).....	32
2.4.6	Comparison of Different CO ₂ Adsorbents	37
2.5	Experimental Studies on Adsorption Carbon Capture	41
2.5.1	Experimental Adsorption Using MOFs.....	42
2.5.2	Experimental Adsorption Using Zeolites.....	48
2.5.3	Experimental Adsorption Using Carbon Based Adsorbents	54
2.5.4	Experimental Adsorption Using Other Adsorbents	57
2.6	Numerical studies and Mathematical Approaches for Fixed Bed Column Adsorption	61
2.6.1	Mathematical Models.....	65
CHAPTER 3 RESEARCH METHODOLOGY		84
3.1	Experimental Methods.....	84
3.1.1	Synthesis/Preparation of the Adsorbents.....	84
3.1.2	X-ray Powder Diffraction Analysis	88
3.1.3	Gas Sorption Measurements.....	89
3.1.4	Binary gas (CO ₂ +N ₂) and Ternary Gas (CO ₂ +N ₂ +H ₂ O) Breakthrough Experiments.....	89
3.1.5	Thermal Properties of Adsorbents	92
3.1.6	CO ₂ Adsorption Cycling by TSA, and PSA (VSA)	93
3.2	Numerical Modeling Methods.....	94
3.2.1	Mass Conservation Equation.....	94
3.2.2	Momentum Conservation Equation	95
3.2.3	Energy Conservation Equation	96
3.2.4	Adsorption Isotherm and Kinetics Models.....	97
3.2.5	General Boundary Condition.....	101
3.2.6	Materials Properties	103
3.2.7	VPSA/TSA and Adsorption Storage Performances.....	106
3.2.8	Breakthrough Case Studies	108
3.2.9	Pressure and Temperature Swing Adsorption Cases.....	116
3.2.10	Carbon dioxide Adsorptive Storage Cases	124
CHAPTER 4 EXPERIMENTAL RESEARCH RESULTS AND DISCUSSION.....		129
4.1	Carbon Nanotubes/Zeolite 13X Composites.....	129
4.1.1	Powder X-Ray Diffraction Analysis.....	131
4.1.2	Adsorption Equilibrium Isotherms of Carbon Dioxide and Nitrogen	132
4.1.3	Experimental Adsorption Breakthrough of Test MWCNT/13X.....	136
4.2	Carbon Nanotubes/Mg-MOF-74 and Carbon Nanotubes/MIL-100(Fe) Composites.....	142
4.2.1	Powder X-ray Diffraction (PXRD) Analysis.....	142
4.2.2	Adsorption Equilibrium Isotherms of Carbon Dioxide and Nitrogen	143

4.2.3	Experimental Adsorption Breakthrough Test for MWCNT/Mg-MOF-74 and MWCNT/MIL-100(Fe) Composites	151
4.3	Carbon Nanotubes/MIL-101(Cr) Composites.....	157
4.3.1	Powder X-ray Diffraction (PXRD) Analysis.....	157
4.3.2	Adsorption Equilibrium Isotherms of Carbon Dioxide and Nitrogen	158
4.3.3	Experimental Adsorption Breakthrough Test for MIL-101(Cr) and MWCNT/MIL-101(Cr) Composites.....	164
4.3.4	Comparison amongst Investigated Adsorbents and Literature	167
4.4	CO₂ Adsorption Cycling for Selective Composites.....	168
CHAPTER 5 SIMULATION MODELING RESULTS AND DISCUSSION		178
5.1	Adsorption Breakthrough for Dry and Humid CO₂/N₂.....	178
5.1.1	Mesh Independence.....	178
5.1.2	Model Validation	179
5.1.3	Parametric Study of Adsorption Breakthrough of Dry and Humid CO ₂ /N ₂	184
5.2	Vacuum/Pressure Swing Adsorption.....	196
5.2.1	PSA Validation	197
5.2.2	Comparison between VPSA of 2D and 3D Simulations.....	198
5.2.3	VPSA Cases.....	203
5.3	Temperature Swing Adsorption	208
5.3.1	Comparison between TSA 2D and 3D Simulations	208
5.3.2	TSA Cases	212
5.4	Carbon Dioxide Adsorptive Storage	221
5.4.1	CO ₂ Adsorptive Storage Using MOF-5.....	224
5.4.2	CO ₂ Adsorptive Storage Using MOF-177.....	227
CHAPTER 6 CONCLUSIONS AND RECOMMENDATIONS.....		231
6.1	Conclusions.....	231
6.2	Recommendations	237
REFERENCES		238
VITAE.....		255

LIST OF TABLES

Table 2.1	Adsorbent materials utilized for CO ₂ capture.....	38
Table 2.2	Comparison of different adsorbents.	40
Table 2.3	Valve sequencing for different steps in PSA cycle.	49
Table 2.4	Carbon Capture by Zeolites.	53
Table 2.5	Comparison among different regeneration processes in terms of CO ₂ purity and recovery [161].	58
Table 2.6	Detailed review of adsorption numerical models including mass isotherm type and mass transfer models.	75
Table 3.1	Polynomial constants for gas components thermal properties.....	104
Table 3.2	Bed, adsorption , and thermal properties of AC bed [165].	109
Table 3.3	Equilibrium isotherm parameters for AC [165].	110
Table 3.4	Bed, adsorption , and thermal properties of Mg-MOF-74 bed.	110
Table 3.5	Equilibrium isotherm parameters for Mg-MOF-74.	111
Table 3.6	Bed, adsorption , and thermal properties of 13X bed.....	112
Table 3.7	Equilibrium isotherm parameters for 13X.	113
Table 3.8	Case studies of effect of water on the CO ₂ separation.	114
Table 3.9	LDFadsorption time constnt of AC and 13X.	114
Table 3.10	Equilibrium isotherm parameters for Mg-MOF-74 [26].	115
Table 3.11	LDF adsorption properties of Mg-MOF-74 at different temperatures.	116
Table 3.12	Properties of the bed column and adsorbent (13X) used in the experimental work [151] and the current simulation.	118
Table 3.13	VPSA study cases.....	120
Table 3.14	TSA study cases.	123
Table 3.15	Tank, AC, and H ₂ properties used in the numerical modeling at the same conditions of the experimental work [212].	124
Table 3.16	Inlet mass flux of PSA validation [212].	125
Table 3.17	Dubnin-Astackov parameters for H ₂ isotherms of AC.....	126
Table 3.18	Thermal and adsorptive propertirs of MOF-5/CO ₂	126
Table 3.19	Thermal and adsorptive properties of MOF-177/CO ₂	128
Table 4.1	Pores characterization of the 13X incorporated with MWCNT.	134
Table 4.2	Pores characterization of the MWCNT/Mg-MOF-74 and MWCNT/MIL-100(Fe) composites for N ₂ at 77 K.	145
Table 4.3	Pores characterization of the MWCNT/MIL-101(Cr) composites for N ₂ at 77 K.	160
Table 4.4	Dynamic CO ₂ adsorption capacity of adsorbents.	168
Table 4.5	CO ₂ adsorption/desorption cycling comparison between 13X and XC3. .	173
Table 4.6	CO ₂ adsorption/desorption cycling comparison between Mg-MOF-74 and MFC4.....	177

Table 5.1	Comparison of CO ₂ separation performances amongst different processes.....	221
-----------	--	-----

LIST OF FIGURES

Figure 1.1	Sources and effect of emitted greenhouse gases.....	3
Figure 1.2	Post combustion capture [8].	4
Figure 1.3	Pre-combustion capture [8].	5
Figure 1.4	Oxy-fuel combustion capture [8].	6
Figure 1.5	Schematic view of CC for different combustion processes [4].	7
Figure 2.1	Combustion carbon capture processes.	13
Figure 2.2	Schematics of absorption carbon capture process using amine.	14
Figure 2.3	Schematics of membrane carbon capture process.	14
Figure 2.4	Schematics of cryogenic carbon capture process.	15
Figure 2.5	Schematics of adsorption carbon capture process in a cylindrical bed (a) and typical breakthrough curve (b).	17
Figure 2.6	Schematics design of two-column PSA unit.	49
Figure 3.1	Small samples of CNT/13X compounds.	85
Figure 3.2	Schematic diagram of carbon dioxide adsorption capture breakthrough setup.	92
Figure 3.3	Types of macroporous diffusion [206].	101
Figure 3.4	Adsorbent beds used for CO ₂ separation.	109
Figure 3.5	Boundary conditions for the 4 steps of the 1st cycle of PSA according to the experimental work [151]	119
Figure 3.6	Boundary conditions for five steps of VPSA.	121
Figure 3.7	Operating pressure of the case 2 during the first three cycles.	121
Figure 3.8	Boundary conditions for four steps of TSA.	123
Figure 3.9	Scheme of adsorptive tank.	124
Figure 3.10	Inlet pressure for MOF-5/CO ₂ adsorption storage.	127
Figure 4.1	Optical microscopic photos of MWCNT/13X compounds.	130
Figure 4.2	Particle size distribution of MWCNT/13X compounds.	130
Figure 4.3	Powder X-ray diffraction (PXRD) data of MWCNT/13X compounds and pure materials (13X and MWCNT).	131
Figure 4.4	N ₂ adsorption isotherms of MWCNT/13X compounds at 77K.	132
Figure 4.5	CO ₂ adsorption isotherms of MWCNT/13X compounds at 273K.	133
Figure 4.6	N ₂ adsorption isotherms of CNT/13X compounds at 298 K.	135
Figure 4.7	CO ₂ adsorption isotherms of CNT/13X compounds at 298 K.	135
Figure 4.8	CO ₂ heat of adsorption (ΔH) for CNT/13X compounds.	136
Figure 4.9	CO ₂ /N ₂ breakthrough curves of MWCNT/13X compounds at 297 K with variable packing density, noticeable pressure drop and non- sufficient degasification process.	138
Figure 4.10	CO ₂ breakthrough curves of MWCNT/13X compounds at 297K and 101.3kPa for the same amounts of adsorbents.	139

Figure 4.11	The average particle size (d_p) and diffusion time constant (D/rc^2) for 13X, XC2, XC3 and XC5.....	141
Figure 4.12	Carbon dioxide adsorption capacity (cubic bars) and separation breakpoint (cylindrical bars) improvements (percent) for MWCNT/13X compounds at 297 K and 1.013 bars.	141
Figure 4.13	PXRD patterns for (a) MWCNT/Mg-MOF-74 and (b) MIL-100(Fe).	143
Figure 4.14	CO ₂ adsorption isotherms of MWCNT/Mg-MOF-74 composites at: (a) 273 K, (b) 298 K, and (c) 313 K.....	147
Figure 4.15	CO ₂ adsorption isotherms of MWCNT/MIL-100(Fe) composites at: (a) 273 K, (b) 298 K, and (c) 313 K.....	148
Figure 4.16	N ₂ adsorption isotherms at 298 K for (a) MWCNT/Mg-MOF-74 and (b) MWCNT/MIL-100(Fe) composites.	149
Figure 4.17	CO ₂ heat of adsorption (Q_{st}) (a) MWCNT/Mg-MOF-74 and (b) MWCNT/MIL-100(Fe) composites.	151
Figure 4.18	Breakthrough curves for (a) MWCNT/Mg-MOF-74 composites for CO ₂ /N ₂ (0.2/0.8 v/v) and (b) MWCNT/MIL-100(Fe) composites for CO ₂ /N ₂ (0.15/0.85 v/v), measured at 297 K and 101.3 kPa.	153
Figure 4.19	Carbon dioxide adsorption capacity (cubic bars) and breakpoint (cylindrical bars) improvements (percent) for (a) MWCNT/Mg-MOF-74, and (b) MWCNT/MIL-100(Fe) composites measured at 297 K.	156
Figure 4.20	PXRD patterns for MIL-101(Cr) and MWCNT/MIL-101(Cr) composites.	158
Figure 4.21	CO ₂ adsorption isotherms of MWCNT/MIL-101(Cr) composites at 273K.....	161
Figure 4.22	CO ₂ adsorption isotherms of MWCNT/MIL-101(Cr) composites at 298 K.....	161
Figure 4.23	CO ₂ adsorption isotherms of MWCNT/MIL-101(Cr) composites at 313 K.....	162
Figure 4.24	N ₂ adsorption isotherms of MWCNT/MIL-101(Cr) composites at 298 K.....	162
Figure 4.25	CO ₂ heat of adsorption (Q_{st}) for MWCNT/MIL-101(Cr) composites.	163
Figure 4.26	CO ₂ /N ₂ breakthrough curves at 297 K and 101.3 kPa as concentration ratios of MWCNT/MIL-101(Cr) composites. The adsorbent masses are 0.475, 0.33, 0.32, 0.41, and 0.477 g for MIL-101(Cr), 2 wt% MWCNT/MIL-101(Cr), 4 wt% MWCNT/MIL-101(Cr), 6 wt% MWCNT/MIL-10.	165
Figure 4.27	Carbon dioxide adsorption capacity (cubic bars) and breakpoint (cylindrical bars) improvements (percent) for MWCNT/MIL-101(Cr)	

	composites over pristine MIL-101(Cr) measured at 297 K and 1.013 bar (gas mixture pressure).	167
Figure 4.28	CO ₂ adsorption/desorption cycles of 13X.	170
Figure 4.29	CO ₂ adsorption/desorption cycles of XC3 (0.5 wt% CNT/13X).....	172
Figure 4.30	CO ₂ adsorption/desorption cycles of Mg-MOF-74.	174
Figure 4.31	CO ₂ adsorption/desorption cycling of MFC4 (0.75 wt.% CNT/Mg-MOF-74).....	176
Figure 5.1	Mesh independency as a comparison of concentration ratio profiles for 1120, 1320, 1690, and 1980 cells.	179
Figure 5.2	Breakthrough concentration ratio curves of CO ₂ separation at the bed outlet during the adsorption process using AC as a comparison of the modeled concentration ratio with the experimental values at 301 K.	180
Figure 5.3	Breakthrough concentration ratio curves of CO ₂ separation at the bed outlet during the adsorption process using Mg-MOF-74 as a comparison of the 1D, 2D, and 3D modeled concentration ratio with the present experimental values at 301 K and 101.3 kPa.	181
Figure 5.4	2D and 3D temperature contours of bed using Mg-MOF-74 at 101.3 kPa.	182
Figure 5.5	2D and 3D CO ₂ mass fraction during CO ₂ /N ₂ separation process using Mg-MOF-74 at 297 K, 101.3 kPa.....	183
Figure 5.6	2D and 3D CO ₂ adsorbed amounts during CO ₂ /N ₂ separation process using Mg-MOF-74 at 297 K, 101.3 kPa.	183
Figure 5.7	CO ₂ /N ₂ /H ₂ O breakthrough curves of concentration ratio using 13X at 92% RH, 297 K and 101.3 kPa. Symbols are experimental results and lines are numerical ones.....	184
Figure 5.8	Dry and humid CO ₂ /N ₂ adsorption breakthrough curves of concentration ratio for AC at 86% RH, 300 K, and 101.3 kPa.	185
Figure 5.9	Temperature profiles at the bed outlet during dry and humid CO ₂ /N ₂ separation process for AC at 86% RH, 300 K, and 101.3 kPa.	186
Figure 5.10	CO ₂ /N ₂ adsorbed amounts during the dry and humid CO ₂ separation process for AC at 86% RH, 300 K, and 101.3 kPa.....	187
Figure 5.11	Dry and humid CO ₂ /N ₂ adsorption breakthrough curves of concentration ratio for 13X at 86% RH, 300 K, and 101.3 kPa.	188
Figure 5.12	Temperature profiles at the bed outlet during dry and humid CO ₂ /N ₂ separation process for 13X at 86% RH, 300 K, and 101.3 kPa.....	188
Figure 5.13	CO ₂ /N ₂ /H ₂ O adsorbed amounts during the dry and humid CO ₂ separation process for 13X at 86% RH, 300 K, and 101.3 kPa.....	189
Figure 5.14	Dry and humid CO ₂ /N ₂ adsorption breakthrough curves of concentration ratio for Mg-MOF-74 at 86% RH, 300 K, and 101.3 kPa..	190

Figure 5.15	Temperature profiles at the bed outlet during dry and humid CO ₂ /N ₂ separation process for Mg-MOF-74 at 86% RH, 300 K, and 101.3 kPa. .191	191
Figure 5.16	CO ₂ /N ₂ /H ₂ O adsorbed amounts during the dry and humid CO ₂ separation process for Mg-MOF-74 at 86% RH, 300 K, and 101.3 kPa. .192	192
Figure 5.17	Dry and humid CO ₂ /N ₂ adsorption breakthrough curves of concentration ratio for Mg-MOF-74 at different RH, 323 K, and 101.3 kPa. 193	193
Figure 5.18	Temperature profiles at the bed outlet during dry and humid CO ₂ /N ₂ separation process for Mg-MOF-74 at different RH, 323 K, and 101.3 kPa. 194	194
Figure 5.19	CO ₂ /N ₂ /H ₂ O adsorbed amounts during the dry and humid CO ₂ separation process for Mg-MOF-74 at different RHs, 323 K, and 101.3 kPa. 194	194
Figure 5.20	Humid CO ₂ /N ₂ adsorption breakthrough curves of concentration ratio for Mg-MOF-74 at 9.1% RH, 373 K, and 101.3 kPa..... 195	195
Figure 5.21	Temperature profile at the bed outlet for humid CO ₂ /N ₂ mixture during separation process using Mg-MOF-74 at 9.1% RH, 373 K, and 101.3 kPa. 196	196
Figure 5.22	CO ₂ /N ₂ /H ₂ O adsorbed amounts during the humid CO ₂ separation process for Mg-MOF-74 at 9.1% RH, 373 K, and 101.3 kPa. 196	196
Figure 5.23	Variation of the bed pressure (Pa) with the 1 st cycle time of the experimental work [151] and the present simulation..... 197	197
Figure 5.24	A comparison of the CO ₂ molar flow rate history between the experimental work, the 1D simulation [151] and the present 1D, 2D (laminar and turbulent) and 3D simulations during a full PSA 1 st cycle. .198	198
Figure 5.25	A comparison of molar flowrate between 2D and 3D VPSA during 3 cycles..... 200	200
Figure 5.26	A comparison of CO ₂ adsorbed amounts between 2D and 3D VPSA during 3 cycles..... 200	200
Figure 5.27	A comparison of temperature contours of the bed between 2D and 3D VPSA during a steady state cycle. 201	201
Figure 5.28	A comparison of CO ₂ molar fraction between 2D and 3D VPSA during a steady state cycle. 202	202
Figure 5.29	A comparison of CO ₂ adsorbed amounts between 2D and 3D VPSA during a steady state cycle. 202	202
Figure 5.30	Pressure history of 11 VPSA cycles (Pressurization=20s, feed=250s, rinse=40s, blowdown=100s, and purge=40s). 203	203
Figure 5.31	CO ₂ /N ₂ molar flow rate of 11 VPSA cycles (Pressurization=20s, feed=250s, rinse=40s, blowdown=100s, and purge=40s). 204	204

Figure 5.32	CO ₂ uptake of 11 VPSA cycles (Pressurization=20s, feed=250s, rinse=40s, blowdown=100s, and purge=40s).....	205
Figure 5.33	Effect of blowdown time on CO ₂ purity, recovery and productivity of VPSA (Pressurization=20s, feed=250s, rinse=40s, and purge=100s).....	206
Figure 5.34	Effect of purge time on CO ₂ purity, recovery and productivity of VPSA (Pressurization=20s, feed=250s, rinse=40s, and blowdown=150s).....	207
Figure 5.35	Effect of blowdown and purge times on VPSA power consumption (Pressurization=20s, feed=250s, rinse=40s).....	207
Figure 5.36	A comparison of molar flowrate between 2D and 3D TSA during 2 cycles.....	209
Figure 5.37	A comparison of CO ₂ uptake between 2D and 3D TSA during 2 cycles.....	210
Figure 5.38	A comparison of temperature contours of the bed between 2D and 3D TSA during a steady state cycle.....	210
Figure 5.39	A comparison of CO ₂ mass fraction between 2D and 3D TSA during a steady state cycle.....	211
Figure 5.40	A comparison of CO ₂ uptake contours between 2D and 3D TSA during a steady state cycle.....	211
Figure 5.41	Temperature profile at the middle of the bed for 11 TSA cycles (feed=250s, rinse=40s, heating=200s, and cooling=400s).....	213
Figure 5.42	CO ₂ /N ₂ molar flowrate of 11 TSA cycles (feed=250s, rinse=40s, heating=200s, and cooling=400s).....	213
Figure 5.43	CO ₂ uptake of 11 TSA cycles (feed=250s, rinse=40s, heating=200s, and cooling=400s).....	214
Figure 5.44	Effect of heating time on CO ₂ purity, recovery and productivity of TSA (feed=250s, rinse=40s, and cooling=300s).....	215
Figure 5.45	Effect of cooling time on CO ₂ purity, recovery and productivity of TSA (feed=250s, rinse=40s, and heating=200s).....	216
Figure 5.46	Effect of Heating time on TSA regeneration energy (feed=250s, rinse=40s, and cooling=300s).....	216
Figure 5.47	Effect of cooling time on TSA regeneration energy (feed=250s, rinse=40s, and heating=200s).....	217
Figure 5.48	Effect of heating time on TSA power consumption (feed=250s, rinse=40s, and cooling=300s).....	218
Figure 5.49	Effect of cooling time on TSA power consumption (feed=250s, rinse=40s, and heating=200s).....	218
Figure 5.50	Effect of wall thickness to internal diameter of the bed on CO ₂ purity, recovery and productivity for TSA (feed=250s, rinse=40s, and heating=200s).....	219

Figure 5.51	Effect of wall thickness to internal diameter of the bed on TSA power consumption (feed=250s, rinse=40s, and heating=200s).....	220
Figure 5.52	A comparison of storage pressure between experimental work [212] and present 2D and 3D simulation for H ₂ adsorptive storage.	222
Figure 5.53	A comparison of temperature history of the bed (at z=0.27875 m, x=0m, y=0m) between experimental work [212] and present 2D and 3D simulation for H ₂ adsorptive storage.	222
Figure 5.54	2D and 3D temperature contours of H ₂ adsorptive storage tank for AC. .	223
Figure 5.55	2D and 3D H ₂ uptake of the AC adsorptive storage tank.	224
Figure 5.56	Temperature profiles of CO ₂ adsorptive tank at the tank center for different storage pressures for MOF-5.....	226
Figure 5.57	CO ₂ uptake of different storage pressures for MOF-5.....	226
Figure 5.58	Adsorbed CO ₂ amounts per MOF-5 amounts ratio for different storage pressures.	227
Figure 5.59	CO ₂ storage energy consumption for different storage pressures for MOF-5.....	227
Figure 5.60	Temperature profiles of CO ₂ adsorptive tank at the tank center for different storage pressures for MOF-177.....	229
Figure 5.61	CO ₂ uptake for different storage pressures for MOF-177.....	229
Figure 5.62	CO ₂ adsorptive amounts per MOF-177 amounts for different storage pressures.	230
Figure 5.63	CO ₂ storage energy consumption for different storage pressures for MOF-177.....	230

LIST OF ABBREVIATIONS

Nomenclature

A_o	pre-exponential constant, $m^2 s^{-1}$
C	Concentration, mol/m^3
C_p	specific heat capacity, $J kg^{-1} K^{-1}$
D, d	diameter, size, m
D_{disp}	mass dispersion coefficient, $m^2 s^{-1}$
E_g	total gas energy, $J m^3$
E_s	total adsorbent energy, $J m^{-3}$
F	molar flow rate, $mol s^{-1}$
h	sensible enthalpy, $J kg^{-1}$
h_{ext}	external heat transfer coefficient, $W m^{-2} K^{-1}$
h_{int}	internal heat transfer coefficient, $W m^2 K^{-1}$
ΔH	heat of adsorption, $J mol^{-1}$
\vec{g}	gravity acceleration vector, $m s^{-2}$
\vec{j}	diffusion flux, $kg m^{-2} s^{-1}$
K_o	Total adsorption constants, Pa^{-1}
K_{eq}	isotherm adsorption constant, Pa^{-1}
k	thermal conductivity, $W m^{-1} K^{-1}$
k_L	LDF adsorption time constant, s^{-1}
M	molecular weight, $kg mol^{-1}$
n	isotherms adsorption constant
q	adsorption uptake, $mmol g^{-1}$

q^*	equilibrium adsorption uptake, mmol g^{-1}
q_m	adsorption uptake limit, mmol g^{-1}
Q_F	feed volumetric flow rate at standard conditions, $\text{m}^3 \text{s}^{-1}$
P	pressure, Pa
R	universal gas constant, $\text{J mol}^{-1} \text{K}^{-1}$
r	radius, m
Re	Reynolds number
t	time, s
T	temperature, K
t_{ss}	stoichiometric time, s
$\bar{\tau}$	stress sensor, N m^{-2}
x	mole fraction
y	mass fraction
\vec{v}	velocity vector, m s^{-1}

Greek letters

α	enthalpic factor, J mol^{-1}
β	intropic factors, $\text{J mol}^{-1} \text{K}^{-1}$
γ	specific heat capacity of gas mixture
ρ	mixture gas density, kg m^{-3}
ε	bed porosity
ϵ	thermal emissivity
μ	dynamic viscosity, Pa s^{-1}
Ω_{ij}	diffusion collision integral of two species
σ_{ij}	collection diameter of two species, \AA

σ Steffen Boltzmann coefficient, $\text{W m}^{-2} \text{K}^{-4}$
 τ tortuosity
 η vacuum/compressor efficiency

Subscript

CO_2, N_2 Carbon dioxide, nitrogen gas

ac actual conditions

cycle whole cycle time

eff effective

p particle

pore adsorbent pore

i gas species index

g gas

s standard conditions

0 inlet, saturation

w wall

Abbreviations

13X zeolite 13X

XC1 0.1 wt. % CNT/13X

XC2 0.25 wt. % CNT/13X

XC3 0.5 wt. % CNT/13X

XC4 0.75 wt. % CNT/13X

XC5 1.5 wt. % CNT/13X

MFC1 0.1 wt. % CNT/Mg-MOF-74

MFC2 0.25 wt. % CNT/Mg-MOF-74
MFC3 0.5 wt. % CNT/Mg-MOF-74
MFC4 0.75 wt. % CNT/Mg-MOF-74
MFC5 1 wt. % CNT/Mg-MOF-74
MFC5 1.5 wt. % CNT/Mg-MOF-74
MMC1 0.1 wt. % CNT/MIL-100(Fe)
MMC2 0.25 wt. % CNT/MIL-100(Fe)
MMC3 0.5 wt. % CNT/MIL-100(Fe)
CNT carbon nanotubes

ABSTRACT

Full Name : Naef Abduljalil Abdulrahman Qasem
Thesis Title : Physical Adsorption of Carbon Dioxide Capture by Novel Materials
Major Field : Mechanical Engineering
Date of Degree : May 2017

Carbon capture by physical adsorption can strongly participate in the reduction of the climate change. Metal-organic frameworks (MOFs) are one class of porous materials with specific surface areas measured to be much higher than conventional porous materials like silica gels, activated carbons, and zeolites. Accordingly, a certain class of MOFs has recently been developed with the primary objective of CO₂ capture from flue gases with minimum energy penalties. Mg-MOF-74 is a distinct adsorbent owing to its distinguished CO₂ uptake and selectivity under low-pressure applications while MIL-101(Cr) and MIL-100(Fe) have extraordinary thermal and hydro stability. In this research, we report the experimental data for enhancing CO₂ uptake of zeolite 13X, Mg-MOF-74, MIL-100(Fe) and MIL-101(Cr) incorporated with multi-walled carbon nanotubes. This was done to improve the thermal diffusion properties of the base adsorbents in order to enhance their adsorption capacities. The new composites have been characterized for degree of crystallinity, CO₂ and N₂ equilibrium adsorption capacity and actual dynamic breakthrough separation at 297 K and 101.325 kPa.

In numerical side, 2D and 3D models have successfully been developed to carry out adsorption breakthrough, vacuum pressure swing adsorption (VPSA), temperature swing adsorption (TSA) and CO₂ adsorptive storage.

The experimental powder X-ray diffraction patterns of the adsorbent composites did not show any extraneous peaks or noticeable peak shifts indicating that the crystal lattices of 13X, Mg-MOF-74, MIL-100(Fe), and MIL-101(Cr) were unaffected by the incorporation of multi-walled carbon nanotubes up to 8 wt%. In comparison to the pristine adsorbents, the composites of 0.5 wt% MWCNT/13X, 1.5 wt% MWCNT/Mg-MOF-74, 0.1 wt% MWCNT/MIL-100(Fe), and 2 wt% MWCNT/MIL-101(Cr) exhibited optimal CO₂ breakthrough uptake enhancements by about 21.2%, 7.4%, 12.0%, and 37.7%, respectively. The optimal adsorption breakpoint improvements were about 25.3%, 8.0%, 9.2%, and 32.1% for 0.5 wt% MWCNT/13X, 1.5 wt% MWCNT/Mg-MOF-74, 0.1 wt% MWCNT/MIL-100(Fe), and 2 wt% MWCNT/MIL-101(Cr), respectively. Carbon dioxide adsorption/desorption cycles showed that heating (> 120 °C for MOFs and >150 °C for 13X) and/or vacuum (< 2 Pa) could satisfactorily regenerate the adsorbent materials.

The results obtained from numerical modeling exhibited significant reduction in CO₂ uptake with the presence of water vapor (> 5 vol%) using Mg-MOF-74. The optimal VPSA key performance indices were about 98.3% of CO₂ purity, 95.7% of CO₂ recovery, 0.73 kg-CO₂/hr.kg-MOF of CO₂ productivity, and 63.9 kWh/tonne-CO₂ of process power consumption. On the other hand, the TSA optimal key performance indices were about 96.2% of CO₂ purity, 93.7% of CO₂ recovery, 0.28 kg-CO₂/hr.kg-MOF of CO₂ productivity, and 663.8 kWh/tonne-CO₂ of power consumption. MOF-5 is found to be the best choice for CO₂ storage applications at pressure less than 5 bar, while MOF-177 is superior for the same purpose at higher pressures (≥ 10 bar).

ملخص الرسالة

الاسم الكامل: نائف عبدالجليل عبدالرحمن قاسم

عنوان الرسالة: الإمتزاز الفيزيائي لإحتجاز ثاني أكسيد الكربون باستخدام ممتزات حديثة

التخصص: هندسة ميكانيكية

تاريخ الدرجة العلمية: مايو 2017 م

إحتجاز ثاني أكسيد الكربون المنبعث من العوادم بواسطة الإمتزاز الفيزيائي يستطيع أن يخفف من التغير المناخي. الممتزات المعدنية-العضوية والتي تسمى MOFs هي مواد مسامية ذات أسطح كبيرة تتجاوز المواد المسامية التقليدية كالكاربون المنشط والزيولايت والسيليكا جل. لهذا يوجد نوعية من هذه MOFs تم تطويرها في السنوات الأخيرة لغرض إمتصاص ثاني أكسيد الكربون من غاز المداخن و بتكلفة تشغيلية قليلة. أحد أنواع MOFs والمسمى Mg-MOF - 74 يحمل خصائص فريدة في إمتصاص وفصل ثاني أكسيد الكربون تحت الضغوط المنخفضة وهناك نوعان من MOFs تسمى MIL-100(Fe) و MIL-101(Cr) تمتاز باستقرارية حرارية ومائية كبيرة. لقد دوننا في هذا البحث تحسين سعة الممتزات المذكورة سابقا بالإضافة للزيولايت وذلك بخلطها و اشراكها مع الكربون نانوتيوب متعدد الأسطح وذلك عن طريق تحسين الانتقال الحراري خلال الممتزات. خضعت المواد لتوصيفات متعلقة بالتركيب البلوري و سعة المواد الأيزوثرمية لغازي ثاني أكسيد الكربون والنيتروجين وفصل البريكثرو عند حرارة وضغط الغرفة. أيضاً قمنا بتطوير محاكاة عددية ثنائية وثلاثية الأبعاد لدراسة فصل ثاني أكسيد الكربون بواسطة البريكثرو و الإمتزاز التآرجي بالإضافة الى تخزين ثاني أكسيد الكربون.

أشارت النتائج المستخلصة من نماذج حيود الأشعة السينية لمسحوق الممتزات المركبة أن إضافة الكربون نانوتيوب إلى الممتزات حتى 8 بالمائة من الوزن لا يؤثر على التركيب البلوري للممتزات الأصلية. أثبتت نتائج التجارب أيضاً أن الممتزات المركبة ذات الخلائط 0.5 wt% MWCNT/13X و 1.5 wt% MWCNT/Mg-MOF-74 و 0.1 wt% MWCNT/MIL-100(Fe) و 2 wt% MWCNT/MIL-101(Cr) تمتلك أعلى سعة إمتصاص لغاز ثاني أكسيد الكربون بتحسينات تصل إلى 21.2% و 7.4% و 12.0% و 37.7% و تمتلك تحسينات في نقاط

الفصل تصل إلى 25.3% و 8.0% و 9.2% و 32.1% على التوالي مقارنة بالمتزاز الأساسية. عملية إمتزاز وتفرغ ثاني أكسيد الكربون من المواد بشكل دورات متكررة يمكن أن يتحقق بواسطة الإمتزاز التآرجي عن طريق التفرغ الضغطي او الحرارة او كليهما.

النتائج المستخلصة من تأثير الرطوبة على كمية ثاني أكسيد الكربون المخزن أشارت إلى أن نسبة بخار الماء إذا تجاوزت 5% فهذا يقلل من قدرة الممتزاز على إمتزاز ثاني أكسيد الكربون بشكل كبير. الدراسة الخاصة بتأثير الإمتزاز التآرجي بواسطة التفرغ والضغط أثبتت كفاءة وصلت إلى 98.3% لنقاوة ثاني أكسيد الكربون و 95.7% لإسترجاع ثاني أكسيد الكربون و 0.73 كجم من غاز ثاني أكسيد الكربون لكل جرام من الممتز بالساعة للإنتاجية و 63.9 كيلوات ساعة لكل طن من ثاني أكسيد الكربون المنتج للطاقة المستهلكة. كما أن الدراسة الخاصة بتأثير الإمتزاز التآرجي بواسطة الحرارة أثبتت كفاءة وصلت إلى 96.2% لنقاوة ثاني أكسيد الكربون و 93.7% لإسترجاع ثاني أكسيد الكربون و 0.28 كجم من غاز ثاني أكسيد الكربون لكل جرام من الممتز بالساعة للإنتاجية و 663.8 كيلوات ساعة لكل طن من ثاني أكسيد الكربون المنتج للطاقة المستهلكة. أثبت MOF-5 أنه خيار جيد لتخزين ثاني أكسيد الكربون في ضغوط أقل من 5 بار لكن MOF-177 لديها كفاءة عالية لتخزين ثاني أكسيد الكربون بالضغوط العالية أكبر من عشرة بار.

CHAPTER 1

INTRODUCTION

1.1 Introductory Background

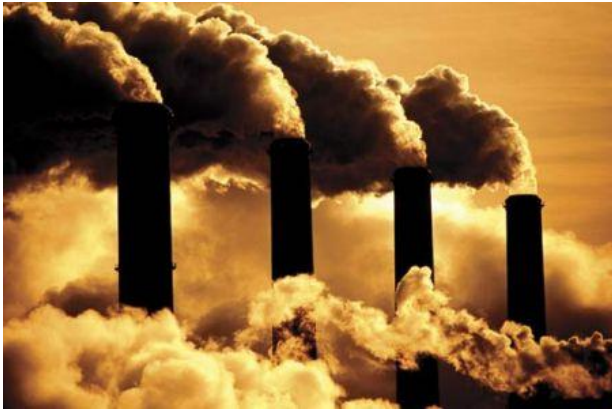
Global warming, caused by greenhouse effect, endangers the human's life. The greenhouse gases including those emitted from combustion and industrial processes such as carbon dioxide, nitrogen oxide, methane and water vapor leads significantly to shore floods, atmospheric heat waves, land droughts, and destruction of cold-marine life and whole ecosystems as well as the economic loss because of the changing in climate is expected to be 5–20% of the world's gross domestic product [1]. The increase of the world temperature was about 0.74% in last 100 years and is expected to reach 6.4% at the end of this century [1]. This increase in temperature due to global warming/greenhouse effect leads to gross discomfort for inhabitants of the earth. In addition, hundreds billions of sea and glaciers ice have being melt causing at least 0.2 mm rising in global sea level [2]. Figure 1.1 shows some aspects of the drastic effects can be made by CO₂ and other greenhouse emitted gases from the industry (Figure 1.1-a) and automobiles (Figure 1.1-b) to the atmosphere as the negative impacts on the land (Figure 1.1-c) and on the ocean ice glacier (Figure 1.1-d).

The most predominant of the greenhouse gases is carbon dioxide (CO₂) [3]. Therefore, in May 2013, the majority of the world environmental organizations have declared that a critical level of carbon dioxide concentration of 400 ppm was reached. This awareness event had forced all countries, including those who were reluctant to take serious action

about carbon emissions, to take unprecedented measures to reduce carbon dioxide emissions. Fossil fuel is the prevailing source of the global primary energy demand, and has been lasting to the next several decades. As, the carbon dioxide (CO₂) is really considered as one of the main promoters for climate change, carbon capture (CC) is essential solution to enable the use of fossil fuels while reducing the emissions of CO₂ into the atmosphere, and thereby mitigating global climate change. Research is the only way to address technical challenges of carbon capture such as improved efficiency and reduced cost of CO₂ capture [4]. Among the main sources of CO₂ emissions, the road transport field accounts for about 25% of CO₂ emissions, while energy electricity generation involves 26% of the total emissions. Therefore, CO₂ emissions from fixed and mobile sources should be drastically reduced in the forthcoming decades. Reducing CO₂ emissions from fixed and mobile sources are equally important though the mobile sources may pose more difficult challenges to be addressed. Global pursuit of sustainable and healthy environment has been the interest subject in the last years.

In order to continue use the fossil energy sources for comfortable and lasting human living, enhancing the power plants energy efficiency is a major to minimize the emissions of greenhouse gases [4]. Furthermore, minimization of the greenhouse gases emitted from fossil fuel combustion processes can be achieved through [5, 6]: (a) lowering burning of fossil fuels (b) enhancing efficiency of fossil fuel power plant (c) carbon capture and sequestration (CCS) (d) improving partial pressure for CO₂ at exhaust. The first solution might be difficult to achieve due to it entails reduction in electricity production and then to keep the same electricity production, a replacement source of energy could be used instead

of fossil fuels. The second solution suggested may have insufficient effect comparing to the aim at reducing emitted CO₂ to near-zero. Therefore, Herzog et. al [6] suggested the third (CCS) to be an appropriate matchless method which could permit continuous use fossil fuels as source of energy associating with reduction of carbon capture emissions. The fourth solution has just been suggested for the third solution in order to obtain better electrical energy efficiency [7]. The storage CO₂ from CCS processes can be beneficially utilized to improve oil and gas production.



(a) Flue gas emitted from industry.



(b) Flue gas emitted from automobiles.



(c) Effect of the global warming on the land.



(d) Effect of the global warming on ice glacier melting.

Figure 1.1 Sources and effect of emitted greenhouse gases.

1.2 Carbon Capture Technologies

There are three basic types of capturing CO₂ processes regarding to the function of CO₂ separation.

Post-combustion capture

Through this process, the capture system is after the combustion process (Figure 1.2) in which CO₂ is captured from a flue gas at low molar fraction (10-20 %) and 1 bar as operational pressure. The separation process usually removes CO₂ from a mixture of mainly nitrogen with/without water vapor. The post-combustion capture would be appropriate for power plants and also applicable for automobile exhausts.

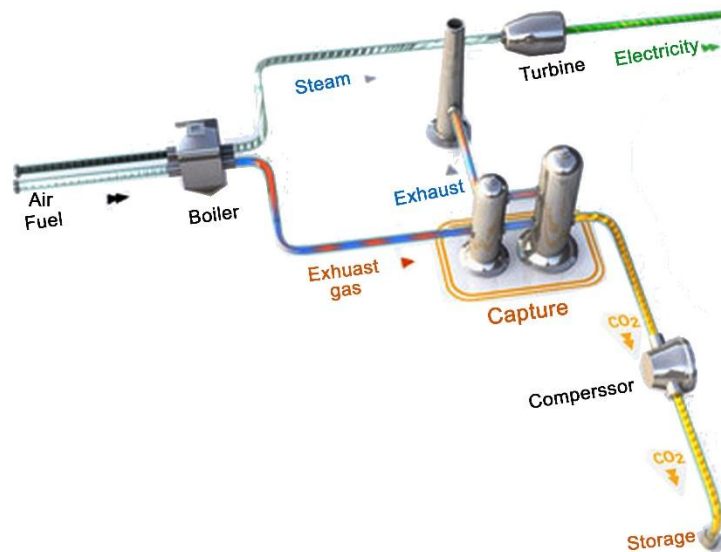


Figure 1.2 Post combustion capture [8].

Pre-combustion capture

Carbon dioxide is captured prior to the combustion process and after the gasification unit, Figure 1.3. The CO₂ is separated from a mixture involving H₂ gas at a significant molar fraction (15-40 % by volume) and high operational pressure (15-40 bar). This technology would be applicable for modern plant that depends on hydrogen as the energy source. The advantage of this method over the post combustion is that it is cheaper [6]. However, the post-combustion capture cannot stop the operation of the combustion process if there is any maintenance or break down issues of capture system, unlike the pre-combustion capture system.

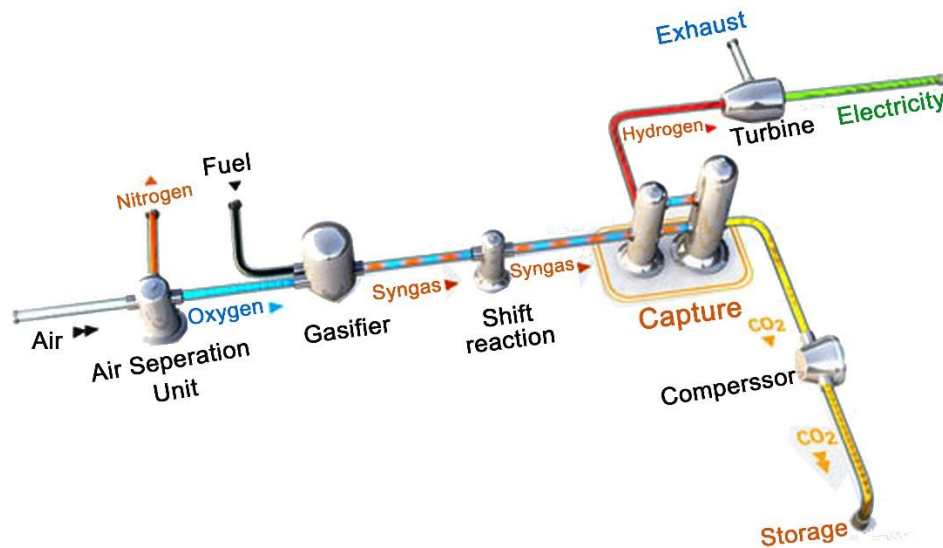


Figure 1.3 Pre-combustion capture [8].

Oxy-combustion capture

For burning the fuel by pure oxygen ($\geq 95\%$) instead of air, oxy-fuel burning takes place after excluding N₂ from air. The capture process is to separate CO₂ from other gases mainly

water vapor as the constituent of the exhaust gas. The application of oxy-fuel capture is for the power plants that built or modified to burning by Oxygen.

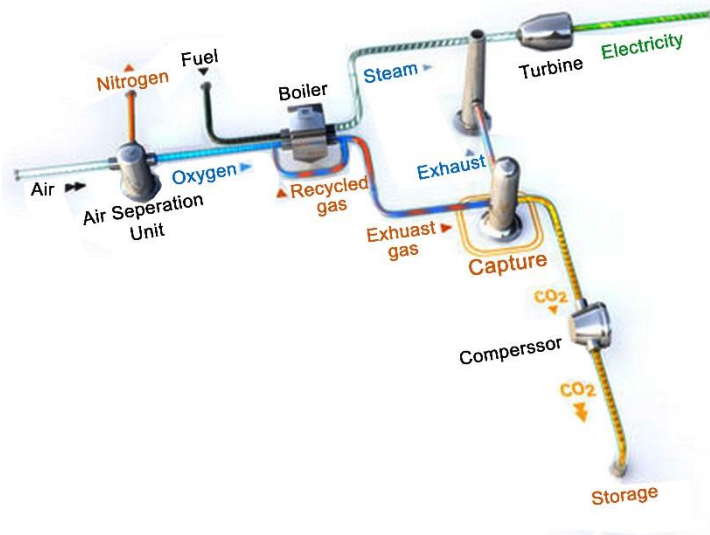


Figure 1.4 Oxy-fuel combustion capture [8].

Figure 1.5 combines all these separation methods to represent all available techniques used for carbon dioxide separation.

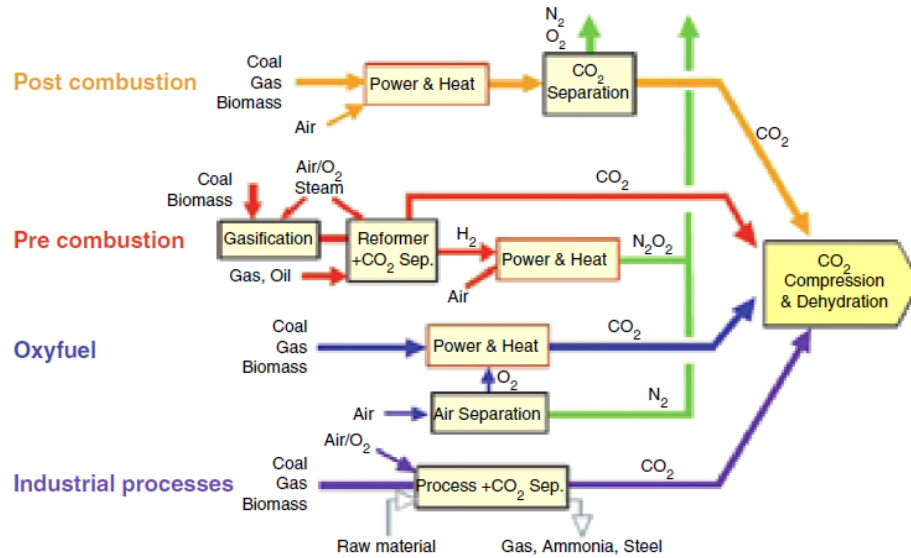


Figure 1.5 Schematic view of CC for different combustion processes [4].

1.3 Research Objectives

The majority of related research aimed at presenting the adsorption-carbon dioxide capture by using activated carbons and zeolites. A new class of synthesized materials named Metal Organic Frameworks (MOFs) has shown much higher CO₂ adsorption capacity and better selectivity. Few works have focused on cyclic adsorption of these materials using relatively large quantities. Furthermore, no investigations have been focused on improving the adsorption capacity of CO₂ by enhancing the thermal properties of MOFs such as the heat capacity and thermal conductivity. On the modeling side of the adsorption process, the published models are all one-dimensional transient ones. This treatment is satisfactory for breakthrough and PSA setups but not adequate for other application such as storage in complex-geometry containers.

Consequently, the overall aim of this study is to test and evaluate the adsorption based systems for CO₂ separation from exhaust sources and to improve the adsorbent material characteristics *via* enhancing the thermal properties of such materials.

The specific objectives are to address the main objective are:

1. Determine the adsorption properties of adsorbent materials especially MOFs including Mg-MOF-74 by obtaining their isotherm curves for N₂ at 77 K and for CO₂ at 300 K. Additional material characterization will be also performed.
2. Design and construct a fixed bed column for N₂/CO₂ breakthrough separation to investigate the adsorption separation capability and to show the transient separation behavior of different adsorbent materials.
3. Explore the enhancement of the heat capacity and the thermal conductivity of MOF adsorbents including Mg-MOF-74 in pursuit of improving their adsorption separation capability.
4. Test the effect of regeneration processes using Pressure Swing Adsorption as well as Temperature Swing.
5. Develop multi-dimensional transient models for adsorption separation and storage of carbon dioxide and use the model to simulate realistic adsorption processes.
6. Carry out parametric simulations to investigate the effect of different materials and different operating parameters on the separation and storage of CO₂.

1.4 Dissertation Outline

In order to achieve the objectives stated above, the approach consists of six chapters; namely: (1) introduction (2) literature review, (3) research methods, (4) experimental results and discussion, (5) modeling results and discussion, and (6) conclusion.

Chapter 1 introduces the background of the research and the available solutions. It presents the well-known problem of CO₂ emissions, suggested solution of carbon capture, and the different available technologies of carbon dioxide capture.

Chapter 2 reviews the previous search work related to physical adsorption carbon dioxide capture. It includes a lot of previous research related to CO₂ adsorption materials, experimental and experimental investigations and findings.

Chapter 3 describes the all methods adopted to carry out experimental and numerical modeling of carbon capture and storage. In this chapter, the experimental methods includes MOFs synthesis, XRD, adsorption isotherms, and adsorption breakthrough characteristics. Moreover, the modeling part exposes a numerical models used for CO₂/N₂ and CO₂/N₂/H₂O breakthrough, PSA, TSA, and CO₂ adsorptive storage.

Chapter 4 shows the experimental results including adsorption characterizations and transient breakthrough of incorporated MOFs with CO₂. Deep discussion related to experimental findings are provided as well.

Chapter 5 shows the numerical modeling validation and investigation results. Dry and humid adsorption breakthroughs, PSA, TSA, CO₂ storage are reported and discussed in this chapter.

Chapter 6 concludes the main results and findings, and suggesting the future work.

CHAPTER 2

LITERATURE REVIEW

The on-going research in the field of Carbon Capture and Storage (CCS) is gaining momentum every day. A vast majority of researchers have already investigated CO₂ separation and storage, using both experimental and simulation methods, with the primary objective of developing novel adsorption materials or adsorbents for this purpose [9]. The foremost advantage of using adsorption as a means of CO₂ separation is the ease of regeneration of the adsorbent material by applying heat and/or decreasing the operating pressure [10]. In this section, materials used for adsorption, related experimental and numerical work are worthy reviewed.

2.1 Background

Recently, research in the Carbon Capture and Storage (CCS) has been fast growing. A wide diverse of CCS technologies have been researching and developing by the day [11]. Although, some technologies have been developed, most studied technology require further improvements to improve their efficiency and to reduce the operation cost. The major challenges for CO₂ capture methods are stated briefly as follows. In oxy-fuel combustion capture we are faced with (a) high energy consumption for supply of pure oxygen and (b) the lack of full readiness for this technology with very little experience on a commercial scale. In pre-combustion capture, the challenges include (a) high cost (b) insufficient technical know-how for good operability (c) absence of single concise process for overall operational performance; and (d) lack of development work for industrial

application. For post-combustion capture case, the difficulties include: (a) additional energy requirement for compression of captured carbon dioxide, (b) need for treatment of high gas volumes, because CO₂ has low partial pressure and concentration in flue gas and (c) large energy requirement for regeneration of sorbent e.g. amine solution .

A wide variety of potential methods and materials for Carbon Capture and Sequestration (CCS) applications that could be employed in post-combustion processes are being suggested as substitutes for the traditional chemical absorption process. The suggested processes comprise: the use of membranes, physical absorbents, adsorption of the gases on solids with the use of Temperature Swing or Pressure Swing (PSA/TSA) processes, hydrate formation, cryogenic distillation, and the use of metal oxides for chemical-looping combustion, and adsorption. A popular technology of post-combustion carbon capture involves the absorption of carbon dioxide in amine solution. This method has been in use on industrial scale for quite a long time. At the same time, varieties of some other of materials are available for other similar technologies (e.g. adsorption), some of which are old while some are newly developed .

Post-Combustion Carbon Capture is advantageous because of the following reasons:

- a. It is easier to integrate into existing plant without needing to substantially change the configuration/combustion technology of the plant
- b. It is more suitable for gas plants than the Oxy-Combustion or the Pre-Combustion plants.
- c. It is flexible as its maintenance does not stop the operation of the power plant and it can be regulated or controlled.

The post-combustion CO₂ capture technology is widely deployed in chemical processing. However, the application of this technology to CC specific applications needs further investigation especially in the area of optimizing CO₂ capture systems for fixed and mobile sources. The priority activities in this task are: 1) development of better materials for post-combustion CO₂ capture; 2) identifying optimal capture process designs and ways of integrating the capture systems with emitting sources to reduce energy loss and environmental impact; 3) identifying advantages and limitations of precipitating systems (e.g., carbonates) and 4) carrying out a detailed assessment of the environmental impact of various CO₂ capture technologies.

This research is to focus on post-combustion capture system especially and particularly on the physical adsorption capture of carbon dioxide, so that the next literature review is to selectively emphasize for such systems.

2.2 Post-Combustion Carbon capture Technologies

A few Post-Combustion separation technologies have been reported, some of which are; (i) absorption CO₂ separation [12] (ii) membrane CO₂ separation [13, 14] (iii) cryogenic CO₂ separation [15] (iv) Micro algal bio-fixation (v) Condensed Centrifugal Separation [16] and (vi) adsorption. Figure 2.1 and the following paragraphs briefly describe these methods [4].

Absorption of carbon dioxide (Figure 2.2) is a process whereby Carbon dioxide is taken in or embedded (absorbed) from flue gas into an absorbent solution (e.g. amine) by chemical action, leaving the remaining gas stream to pass through the absorption column freely [17]. In order to use the absorbent again for CO₂ absorption, the dilute absorbent is

re-concentrated (regenerated). CO₂ absorption using amine based solvents presents a great deal of disadvantages, some of which are: (i) high heat/power requirement for solvent regeneration, (ii) need for corrosion control measures and (iii) the sensitivity of the solvents to losses in chemical purity/quality due to infiltrations from other by-products (e.g. SO_x, NO_x etc.) in the flue gas streams, which leads to reduction in efficiencies and increment in costs of power supply [18].

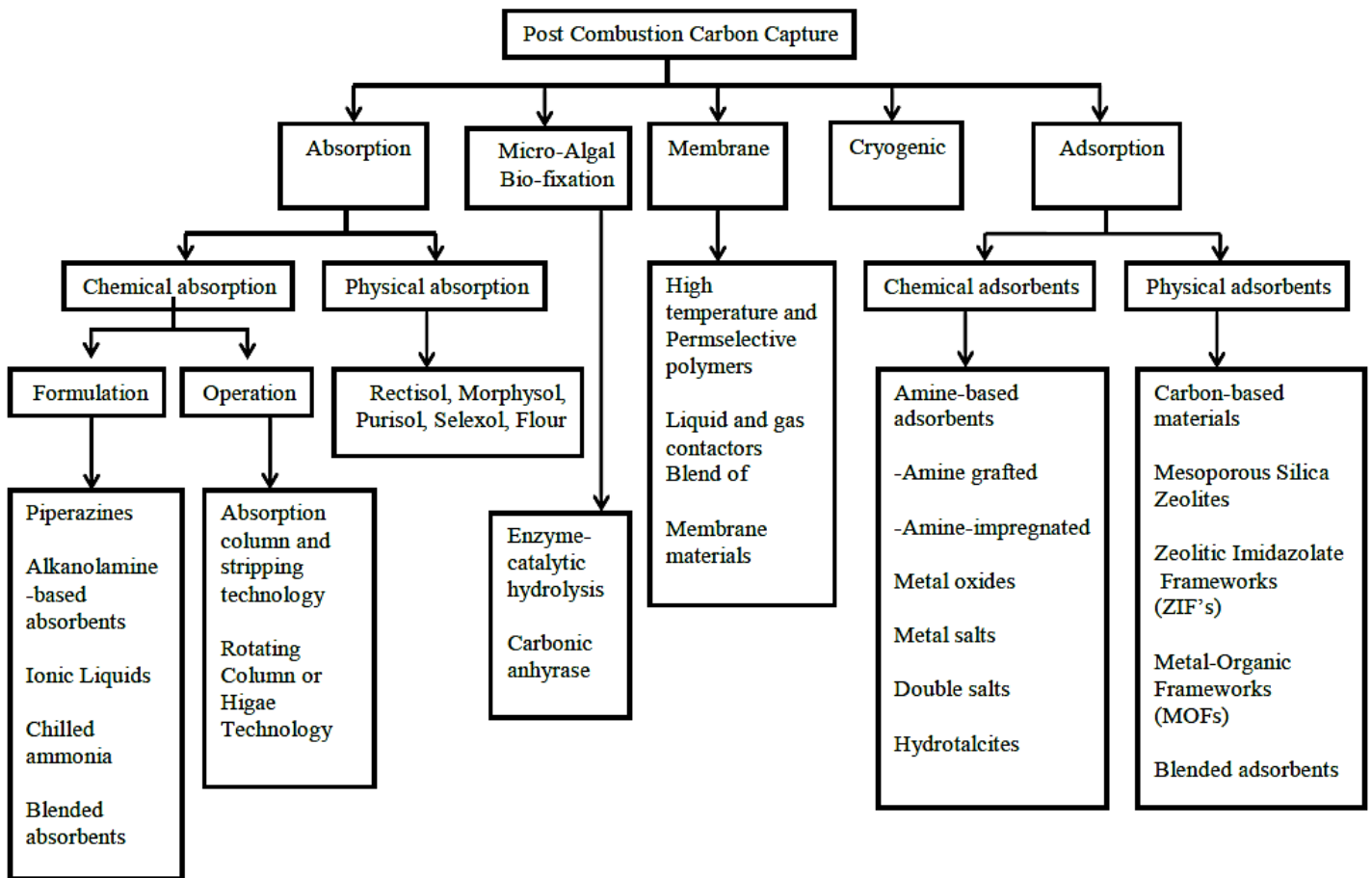


Figure 2.1 Combustion carbon capture processes.

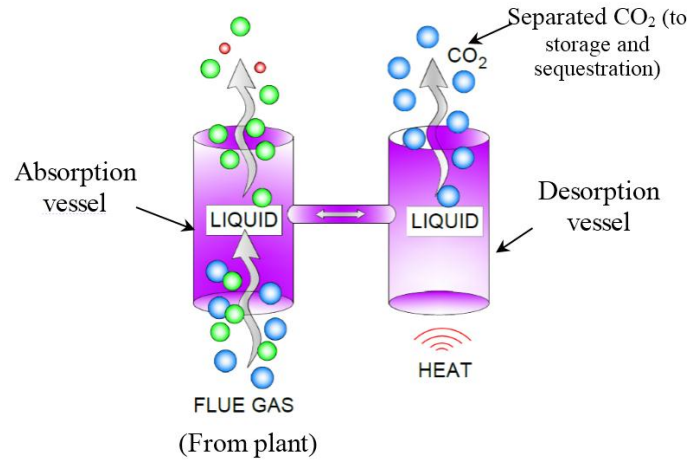


Figure 2.2 Schematics of absorption carbon capture process using amine.

Membrane separation of carbon dioxide (Figure 2.3) involves the use of polymer/ceramic made membranes to sieve out the CO_2 gas from the flue gas under pressure gradient. The membranes are made from polymer or ceramic materials and their configurations are specially designed for CO_2 selectivity. Challenges are still being faced in the application of this technique on a large scale, and in the design of membranes that would operate efficiently for the desired purpose at relatively high temperatures.

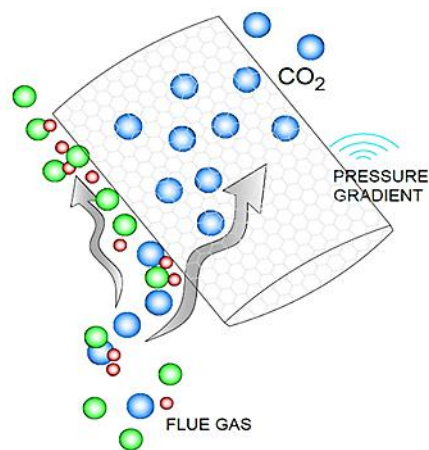


Figure 2.3 Schematics of membrane carbon capture process.

Cryogenic CO₂ separation technique, Figure 2.4, applies the principle of liquid state temperature and pressure difference in constituent gases of flue gas. In this technique, CO₂ is cooled and condensed, thereby removed from stream of flue gases [15].

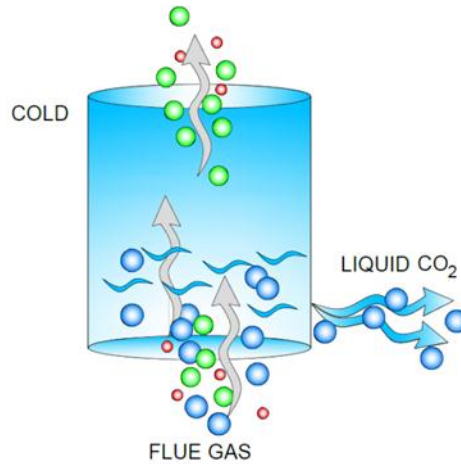


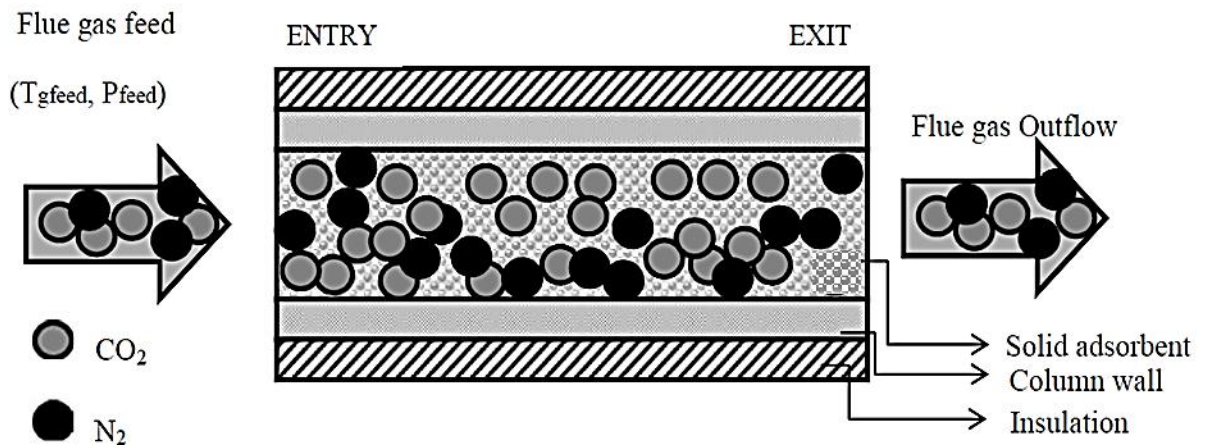
Figure 2.4 Schematics of cryogenic carbon capture process.

Micro-Algae bio fixation is a potential technique for removal of CO₂ from flue gases. This technique entails the use of photosynthetic organisms (microalgae) for anthropogenic CO₂ capture in CCS. Aquatic microalgae have been suggested to be of greater potential because they have higher carbon fixation rates than land plants. Micro-algal culturing is quite expensive but the process produces other compounds of high value that can be used for revenue generation. Micro-algal photosynthesis also causes precipitation of calcium carbonate which serves as Carbon long lasting sink [19].

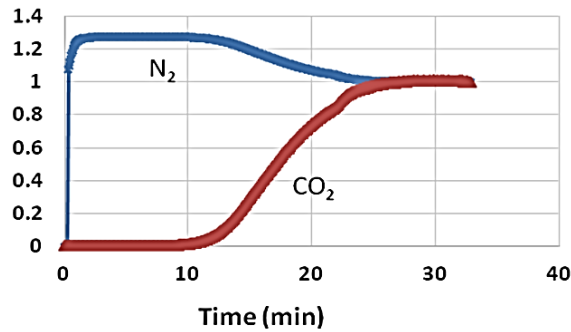
2.2.1 Adsorption

Adsorptive separation, Figure 2.5, is a mixture separating process in which the inherent separation mainly relies on the principle of differences in adsorption/desorption properties of the mixture constituent [20]. The word adsorption is defined as the adhesion of ions,

atoms or molecules from a liquid, gas or dissolved solid into a material surface. The adhered material ions, atoms or molecules form film on the surface of another materials is called *adsorbate* while the other material on which they are attracted is called the *adsorbent*. Adsorption is different from absorption because in absorption, the fluid (adsorbate) is dissolved by a solid or liquid (absorbent). Adsorption occurs on the surface while absorption entails the whole material volume. Sorption is related to the two processes while desorption is the counter reaction or reverse process of adsorption. In adsorption, superficial atoms of the adsorbents are not completely encompassed by the remaining adsorbent atoms. Adsorption results in surface energy due to the filling of these bonding requirements of the adsorbent by the adsorbate atoms. The particular type of bonding involved is a function of the involved species. Adsorption may take place physically; this will involve weak van der Waals forces (physi-sorption). It may take place chemically, which will involve covalent bonding (chemi-sorption) and it may occur due to electrostatic attraction.



a) Adsorption bed.



b) Typical experimental breakthrough curve.

Figure 2.5 Schematics of adsorption carbon capture process in a cylindrical bed (a) and typical breakthrough curve (b).

Adsorption has a major advantage with regard to the ease of adsorbent regeneration by thermal or pressure modulation [10], reducing the energy of Post-Combustion Carbon Capture. Songolzadeh et. al [10] in their review of adsorbents defined adsorption to be; a physical process that involves attachment of fluid to solid surface. Important factors in adsorption include; (a) ease of regeneration to adsorb CO₂ again, (b) adsorbent durability, (c) selectivity of adsorbent for CO₂, (iv) adsorption capacity and, (v) stability of adsorbent after several adsorption/desorption cycle [10].

Several challenges are being faced by scientists and engineers alike with respect to commercialization of these materials. This is so because the researched materials require further work to improve their performance and stability. Suitable materials for carbon capture must account for size of gas molecules and electronic behavior of such molecules. There is no much difference in the kinematic diameters of gas molecules; this makes it difficult to base CO₂ separation solely on gas molecule size (CH₄:3.76Å°, CO₂:3.30Å°, N₂ 3.64Å°) [11]. However, electronic properties like quadru-polar moment and polarization

have been of great help, as bases of separation as they are significantly different for each gas.

CO₂ Capture Using Chemical Sorbents

In order to overcome these challenges, a lot of research has been carried out on advanced materials. However, despite the extent of investigations, it has been difficult to find a single technology that is able to meet the requirements set by the Department of Energy (DOE) and National Energy Technology Laboratory (NETL): i.e. below 35% increment in cost of electricity for 90% CO₂ capture [11]. Most chemical adsorption and absorption processes, in carbon capture/separation procedures involve the interaction between chemicals which lead to the formation of molecular structures that are CO₂-based, after which regeneration of the captured CO₂ is done through sufficient increase in temperature by heating. This procedure (i.e. regeneration) consumes most of the power requirement in CCS. Hence, there is a need to develop efficient materials and processes for CO₂ capture that can greatly decrease operation cost through reduction in regeneration cost.

CO₂ Capture Using Physical Sorbents

CO₂ capture using physical sorbents and inorganic porous materials (e.g. carbonaceous materials and zeolites respectively) consumes lesser energy when compared with CCS with chemical sorbents. This is because no new bond is formed between the sorbate and sorbent, therefore much lesser energy is required for CO₂ regeneration. Nevertheless, some well-known materials (e.g. activated carbon), have the disadvantage of poor CO₂/N₂ selectivity. If the challenges of selectivity in physical sorbents and membranes are successfully overcome, their use for CO₂ capture could be a good potential for energy saving by the

dominant amine-based absorption systems. Zeolites show much higher selectivity, but, they also have a disadvantage of lower CO₂ loading and their efficiency is reduced in the presence of water [11]. Furthermore, molecular sieve membranes have great potentials, however, traditional molecular sieves (e.g. zeolites) have restricted use in CO₂/N₂ separation because of similar kinetic diameters of N₂ (3.64Å) and CO₂ (3.3Å). In all, development of advanced physical adsorbents with high CO₂ capacity and selectivity is crucial. Good stability, CO₂ affinity, scalability and additional required energy are major concerns in carbon capture research. This is crucial to the research and development of potential carbon capture materials that will challenge the available technologies that have been discussed above. More attention should be paid to better understanding molecular level gas-sorbent synergy.

2.2.2 Adsorption Process Types

It has been reported that the incurred cost in CO₂ capture and its associated procedures, with the use of liquid solvent absorption, can be cut down by a great deal if adsorption separation technique is used [21]. Numerous technological successes have been reported recently in the research of adsorption carbon capture processes. Out of the researched technologies for adsorption carbon capture, two potential technologies have been considered feasible for industrial scale CCS:

(a) Pressure/Vacuum Swing Adsorption (PSA/VSA) [22, 23]

Carbon capture capacity in a PSA system is affected by two main factors: Adsorption selectivity and carbon dioxide working capacity [24]. In PSA, adsorption step is done at

elevated pressure than atmospheric pressure while in VSA adsorption is performed at atmospheric pressure or lower.

(b) Temperature Swing Adsorption (TSA) [25, 26]

In temperature swing system, the adsorption bed heating is done using a feed of hot gas or steam. Following the regeneration step is the cooling of the adsorption bed by a feed of cold gas stream before the next adsorption step.

Of these two processes, it has been demonstrated that PSA is a better option [25] because of (i) simplicity in application with wide range of temperature and pressure application, (ii) low energy demand and (iii) lower investment cost.

In adsorption carbon capture process, material selection precedes process design. Before an adsorption process is designed, selection of suitable adsorbent, with desired properties for the required purpose must be done. In doing this, properties such as: adsorbent selectivity, adsorption capacity, ease of and energy required in desorption are of great importance. In view of this, a lot of research has been carried on broad species of materials such as: synthetic zeolite, metal oxides, silica's, carbon molecular sieves, and activated carbon.

2.3 Thermodynamic Analysis of Physical-Adsorption Carbon Capture

The availability and irreversibility of adsorption processes of post-combustion CO₂ capture unit associated with a natural gas combined cycle power plant were investigated by Amrollahi et. al [27]. The results showed that the second efficiency of the absorption CO₂ capture unit was as low as 21.2% while the CO₂ compression unit had 67% of exergy

efficiency. The overall exergy efficiency of carbon dioxide capture and compression unit was about 31.6%. The general impression was that the exergy losses from CO₂ capture and compression units were very smaller than those lost in gas turbine, HRSG and steam turbine. The entropy generation analysis of the new Endex calcium looping method that is driven by the heat of carbonation and pressure-swing was studied by Ball [28]. For CO₂ capture processes optimizing, the research utilized two methods; first method was minimizing the total specific entropy generation and the other was maximizing the CO₂ capture efficiency. The paper claimed some important remarks regarding to CO₂ capture such as; the optimization of entropy generation caused dropping of CO₂ capture efficiency, operative pressure and temperature were only a part contributors of entropy generation, reducing irreversibility of one process could increase it in another, and the regeneration (desorption) was a significant entropy generator. Lara et. al [29] discussed the irreversibility of the components of post combustion and oxy-fuel combustion CO₂ capture, and power plants systems. Calbry-Muzyka and Edwards [30] derived equation to estimate the exergy of an adsorbed phase for applying on adsorption processes. The calculations were performed for evaluating the exergy of adsorbed air, N₂, CO₂ and flue gas by Zeolite 13X. The results confirmed that, for air and CO₂, the exergy depended mainly on the pressure and temperature values (the exergy values dropped suddenly by increase the pressure and decrease the temperature to a certain point (0 kJ/mol-air and 1 kJ/mol-N₂) and then the values increased steadily by increase pressure and decrease temperature). For adsorbed CO₂ and flue gas, the values of exergy were improved by decreasing the temperature values regardless of the pressure values. Furthermore, increasing the pressure up to about 1 bar lifted the exergy values in sharp trend and then the values remained

constant (for CO₂) or increased slowly (for flue gas). Thermodynamic analysis of post-combustion capture processes using amines was considered to minimize the cost of CO₂ avoiding [31]. The article relied on a macro-scale technico-economic analysis (MEA) to demonstrate that the reboiler energy consumption was the significant part required to minimize.

The availability of a post-combustion carbon capture plant was analysed by McGlashan and Marquis [32]. The analysis started by fixing the temperature of flue gas to equal that of sink of the plant to pursue the minimum work input; This stage showed the ideal work input is so low and approximately was equal to the amounts of work required for CO₂ separating and compressing. As changing the temperature of flue gas from sink temperature, there was a considerable quantity of available energy in the flue gas of a normal power station. That was because of existing of a large amount of sensible and latent heat in the flue gas. Mansouri and Mousavian [33] investigated coal fired power plant with post-combustion CO₂ capture system thermodynamically. The study indicated that about 9.1 % of the energy decreased due adding the capture system to the conventional coal fired power plant. Another remark discussed was that the most irreversibility was estimated from the plant boiler. The first law analysis also showed that the net power efficiency and the net electric efficiency decreased by 15% and 9.7%, respectively, due to increasing the power consumption by adding CO₂ separation system. The results confirmed that, for air and CO₂, the exergy depended mainly on the pressure and temperature values (the exergy values dropped suddenly by increase the pressure and decrease the temperature to a certain point (0 kJ/mol-air and 1 kJ/mol-N₂) and then the values increased steadily by increase pressure and decrease temperature). For adsorbed CO₂ and flue gas, the values of exergy

were improved by decreasing the temperature values regardless of the pressure values. Furthermore, increasing the pressure up to about 1 bar lifted the exergy values in sharp trend and then the values remained constant (for CO₂) or increased slowly (for flue gas). For oxy fuel system, the majority of the exergy destruction was coming from air separation unit. Calcium looping analysis exhibited a good efficiency obtained as a result of utilizing waste heats from the capture system. The results revealed that the HiCapt+™ process could minimize the cost by 15% and the DMX-1™ could reduce it more up to 25% compared with the reference MEA process. Iribarren et. al [34] investigated six coal-fired power plants with associated with carbon capture and sequestration thermodynamically and environmentally. They addressed that the post-combustion through membrane separation and pre-combustion CO₂ capture showed relatively low life-cycle environmental impacts as well as high exergetic efficiencies. Thermodynamic efficiency of the capture system and the life-cycle included the energy and cost of whole system for metal–organic frameworks were discussed by Sathre and Masanet [35]. The study suggested that the life-cycle energy was lower for MOFs than for MEA due to low regeneration energy.

2.4 Carbon Capture Adsorption Materials

Different classes of Carbon capture materials have been identified over the years e.g. Songolzadeh et. al [10] discussed two classes of CO₂ adsorbents: (i) physical and (ii) chemical adsorbents. Physical adsorbents have substantial benefits for energy efficiency in comparison with chemical and physical absorption routes. The adsorption involves either physisorption (van der Waals) or chemisorption (covalent bonding) interaction between the gas molecules and the surface of the material. An important factor in the case of

physical adsorbent is balancing a solid affinity for removing the undesired component from a gas mixture with the energy consumption required for their regeneration. Selectivity is another factor in addition to the adsorption capacity, which is relevant to the adsorptive gas separation. The following mechanisms are proposed for adsorptive separation: (a) the molecular sieving effect, based on size/shape exclusion of the components in the gas mixture; (b) the thermodynamic equilibrium effect, that depends on the surface-adsorbate interactions; (c) the kinetic effect, due to the diffusion rate differences in the gas mixture components [36].

Several physical adsorbents have been studied for CO₂ capture including metal oxides, hydrotalcite-like compounds, microporous and mesoporous materials (including activated carbon and carbon molecular sieves, zeolites, chemically modified mesoporous materials) [37-40]. Physical adsorbents (physisorbents) are barely disturbed during adsorption. Pore sizes are of great importance in physical adsorption. When pores are of size 2nm, they are termed micro-pores, pores of sizes between 2 to 50nm are termed meso-pores, and when pores are of size 50nm, they are termed macro-pores. Materials with micro pores have better adsorption selectivity for CO₂ over CH₄. Some examples of physical adsorbents include activated carbon, zeolite, hydrotalcites, carbon nanotubes (CNTs), coal etc. Activated carbon has high adsorption capacity for CO₂, high hydrophobicity, low cost, little regeneration energy requirement and is insensitive to moisture. Zeolite on the other hand has better selectivity for CO₂/N₂ than carbonaceous materials.

Some examples of metal oxides that have been studied for carbon capture include: calcium oxide (CaO), magnesium oxide (MgO) and lithium oxides (e.g. Li₂ZrO₃, Li₄SiO₄) [41, 42]. Some examples of metal salts are lithium silicate and lithium zirconate, both of which are

alkali metal compounds. Magnesium oxide and calcium oxide are examples of alkali earth metal compounds. Some other examples of chemical adsorbents are the hydrotalcites and double salts. During CO₂ adsorption, solid compounds react with CO₂ to form new compounds e.g. Metal Carbonates. These reactions can be reversed in regenerators to harvest CO₂ for storage. Metal oxides are promising capture materials with high adsorption capacities at above 300°C [43]. Lithium based oxides found recent attraction for their high CO₂ adsorption capacities [44]. Calcium oxide is of special interest to researchers because it is cheap and it has high adsorption capacity for CO₂ compared to lithium salts which are more expensive especially in production. Hydrotalcites are anionic and basic clays and their derivatives are also found suitable for CO₂ adsorbents at temperatures as high as 400°C [45]. Most naturally occurring and well-studied hydrotalcite is Mg-Al-CO₃. Hydrotalcites have the disadvantage of high loss in adsorption capacity after cycles of operation. During CO₂ adsorption, solid compounds react with CO₂ to form new compounds e.g. metal carbonates. Materials with at least one dimension less than 100nm (nanomaterials) have also been investigated [46]. These materials have improved stability and they maintain CO₂ capturing capacity for longer adsorption/desorption cycles. However, nanomaterials have disadvantage of high cost and complicated process of synthesis. Webb [47] stated that CO₂ capture efficiency, rate of absorption, required regeneration energy and volume of absorber are some of the major challenges of CO₂ absorption method. They reviewed adsorbents and some meso-porous solid adsorbents with polyamines embedded in them. They stated that some factors for adsorbent selection are rate of adsorbent, cost, and capacity of the adsorbent to adsorb CO₂ and thermal stability. They identified of the following types of adsorbents;

Chemical adsorbents e.g. amine based adsorbent. Amines were said to have low heat of regeneration due to low heat capacity of solid support. They are costly and they have low CO₂ adsorption capacity, therefore, they are difficult to commercialize. CO₂ adsorption properties of amines can be improved by preparation of support with high Amine loading, by increasing the nitrogen content in amines and by improving methods of Amine introduction. Two special cases are amine impregnated adsorbents and amine-grafted adsorbents. In amine impregnated adsorbents, increased polyethylenimine loading would lead to improved CO₂ adsorption capacity, reduced surface area for adsorption, pore size and volume. Therefore, it was suggested [48] that amine impregnated adsorbents do not have thermal stability in desorption. In amine-grafted adsorbents and in order to overcome the limitations of amine impregnated adsorbents it is suggested that CO₂ adsorption capacity for this group of materials can be improved through silylation. They can be grafted covalently to the intra-channel surface of meso-porous Silica. It is indicated that improvement of Amine loaded adsorbent could be improved by infusing amines into meso-porous support with the use of effective solvents. This was termed supercritical fluid approach. However, this group of materials has disadvantages of high toxicity, low diffusivity and high viscosity. These features can lead to lower adsorption capacity and high pressure drop. Due to large volume of flue gases are to be treated, and low partial pressure of CO₂ in flue gas, chemical adsorption would be more feasible for CO₂ capture than physical adsorption. However, it has the disadvantage of being an energy intensive process. It was indicated that that physical adsorption is good for CO₂ adsorption at high

pressure and low temperature. In this light, they might not be practically applicable for post combustion carbon capture.

Physical adsorbents. These include activated carbon with advantage of enormous availability, zeolites with advantage of highly crystalline structure, high surface area, ability to alter their composition structure and ratio. They also include meso-porous silica with advantage of high volume, surface area and tunable pore size, thermal and mechanical stability and Metal Organic Frameworks (MOFs) with advantages of very high surface area, adjustable pore spaces, pore surface properties, and exceptional adsorption capacity for CO₂. They however stated that activated carbon has disadvantage of application to only high pressure gases, at high temperature they have high sensitivity and low selectivity. They also stated that Zeolites have very low selectivity, zeolites are hydrophilic and their CO₂ adsorption capacity drops with the presence of moisture in gas. The authors further mentioned that the adsorption capacity of meso-porous silica is not sufficient most especially at atmospheric pressure. They stated that MOFs have the disadvantages of reduction in adsorption capacity on exposure to gas mixture and insufficient research on them, however, they are prospective materials. Generally, CO₂ capture by physical process requires less energy when compared to typical procedure using chemical sorbents. As mentioned earlier, this is because of the absence of newly formed chemical bonds between the sorbate and sorbent, which reduce the energy requirement for regeneration [11].

2.4.1 Porous Materials

Zeolites are the most commonly used physical adsorbents for commercial hydrogen production using pressure swing adsorption with most popular zeolites 13X [38, 49] They

are used at high pressures (above 2 bar) and their capacity is greatly reduced by the presence of moisture in the gas; resulting in very high regeneration temperatures [22, 50]. Experimental and computational studies of CO₂ removal from flue gas using naturally occurring zeolites and other synthetic zeolites 5A and 13X indicate that synthetic zeolites are most promising adsorbents for CO₂ capture from flue gas mixture [50, 51]. However, they experience weak adsorbent-adsorbate interactions which are not well-suited with a high CO₂/N₂ selectivity. The low SiO₂/ Al₂O₃ ratio and presence of cations in the zeolite structure can enhance the adsorption. The presence of cations leads to strong electrostatic interactions of the zeolites with CO₂ [50]. Although these adsorbents are satisfactory for pressure swing adsorption, significant energy is needed for their regeneration and that possibly leads to the disadvantages of these materials.

In the meantime, it is possible to modify these porous solid materials by impregnating active alkyl amines into their internal surfaces leading to an enhancement in their gas adsorption properties at low pressures. Several amine modified silica have been investigated [38, 52]. Carbamate species are formed through adsorption of CO₂ in the surface modified silica with primary amines. Removal of CO₂ can be performed at lower temperatures than those required for the regeneration of amine solvents [53, 54]. A significant enhancement in the CO₂ adsorption capacity is obtained through pressure swing adsorption using MCM-41 with impregnated polyethylenimine [55]. Amine immobilized support such as poly(methyl methacrylate) has exhibited increased adsorption capacities [56]. However, after impregnation, the materials suffer from a lack of stability over repeated cycles. To increase the stability of the materials in repeated cycles, alkylamines have been covalently tethered to the surface of the mesoporous support. For example,

polymerization of aziridine on the surface of mesoporous silica generates a hyperbranched material which shows reversible CO₂ binding and multi-cycle stability under simulated flue gas conditions using temperature swing adsorption [52]. The grafted monoamino, diamino, triamino ethoxysilanes SBA-15 have been used to study the effect of amine and the presence of moisture on CO₂ adsorption performance [57]. The capacity slightly decreased for primary amine, but increased for secondary and tertiary amines. Although amine grafting materials show significant improvement over non-grafted materials, it is very important that the amount of grafted amine be optimal for the particular CO₂ capture process. It is also important to study the influence of the quantity of grafting reagent added to the actual amount of amine that is covalently attached to the surface.

2.4.2 Carbon Based Adsorbents

Carbon based materials such as activated carbon, charcoal and coal have been reported for high pressure CO₂ capture applications [38, 58]. The key advantages of these materials are their low cost, their insensitivity to moisture and the possibility of their production/synthesis from numerous carbon based naturally existing or spent materials [59]. The activated carbon can be synthesized from different waste materials like seed, wood, charcoal and so on. One additional advantage of activated carbons over zeolites is that they are affected by water vapor. They also require a lower temperature for regeneration compared with zeolites [60] However, they have moderate selectivity for CO₂ separation from CO₂/N₂ mixture at ambient pressure [61]. The CO₂ capture using physical adsorbents including traditional materials like activated carbon based and zeolites low energy consumer compared to the metal oxides and others. This is because of no covalent forces between adsorbent/adsorbate. However, the selectivity of carbon based materials is

very low, whereas zeolites exhibit significantly higher selectivity while they suffer from lower CO₂ loading and their performance is reduced in the presence of moisture.

2.4.3 Solid Adsorbents

Organic calixarene compounds, for example non-porous self-assembled *p*-*tert*-butylcalix{4}arene organic solids have been considered for CO₂ capture [62, 63]. Their structure involves cone-shaped calixarene molecules and the molecules are stabilized by intramolecular hydrogen bonds and the presence of hydrophobic nanodimensional channels [62]. The material may be suitable for high pressure CO₂/H₂ syngas separations. Other potential solids reported for CO₂ capture are covalent organic frameworks (COFs) [64]. They are microporous materials similar to MOFs but with frameworks with light weight organic components instead of the metal connectors. For example, COF-102 (C₂₅H₂₄B₄O₈) is constructed with tetra(4-(dihydroxy)borylphenyl)methane unit and shows the highest CO₂ uptake in this class (27 mmol g⁻¹ at 55 bar and 298 K) [64]. Molecular simulation studies performed on these materials predict also their exceptional high uptake [65, 66].

2.4.4 Carbon Nanotubes (CNTs)

The adsorption of CO₂ on various carbonaceous materials such as activated carbon AC [67-71] and carbon nanotubes CNTs [72-76] attracted the attention many researchers in recent years. AC, derived from different sources of carbon materials, was the first carbon adsorbent agent used for CO₂ capture [77-80]. Currently, CNTs are being considered in this field due to their promising physical and chemical properties, high thermal and electrical conductivity, along with the possibility to modify their surfaces chemically by

adding a chemical function group, using fisher esterification method, yielding high adsorption storage capacity [81-89]. These CNTs have proven to have good potential as highly adsorbent materials for removing different kinds of inorganic and organic pollutants and microorganisms [90-96]. It is believed that a chemical modification of CNTs would also be expected to have a good potential for CO₂ capture from a flue gas. However, such studies are still very limited in the literature. Functionalized CNTs with amino-functional groups [97-100] have been considered. Su et. al [101] investigated the effect of functionalized CNTs with 3-aminopropyltriethoxysilane (APTES) at different adsorption temperatures. They found that by increasing the temperature of the system, the adsorption storage capacity decreased, while increasing the water content increased the adsorption capacity, which reflected the exothermic process of adsorption. Their experimental CO₂ adsorption capacity of ~2.59 mmol/g at 293 K for APTES-CNT is the evidence for the potential of CNTs as low-temperature adsorbents. Hsu et. al [73] combined vacuum and thermal adsorption system in order to trim down the regeneration time. They were able to sustain adsorption/regeneration of CNT-APTES for twenty cycles at 493 K while maintaining the CNTs' physiochemical properties and adsorption capacity. Dillon et. al [102] functionalized the surfaces of single-walled CNTs with polyethylene Imine (PEI) functional group and reached a maximum adsorption capacity of 2.1 mmol/g at 300 K. The reported good CO₂ capture capacities suggest that the amine-functionalized CNTs are promising CO₂ adsorbents, given that the adsorption mainly depends on physical effects, thus relatively low energy is required for the regeneration. Very few works are reported on the use of CNTs as membrane for CO₂ capture.

2.4.5 Metal Organic Frameworks (MOFs)

About two decades ago, a new class of materials was discovered; they are made of MOFs and are simply called MOFs [20]. They are organic-inorganic hybrid, porous, solid materials. Out of all known materials to date, MOFs have the highest adsorption surface area per gram. They have great potentials for CO₂ capture, flexible design-ability in terms of structure and function. This has made these materials highly used in research works of Carbon Capture and Sequestration. MOFs has emerged and first synthesized by Hoskins and Robson in 1989. MOFs, also known as coordination polymers [103] have been described as porous hybrid nano-cubes that harness bi-properties; they establish properties of organic and inorganic porous materials. The descriptive term MOF was first introduced by Yaghi and co-workers in 1995. MOFs are a class of porous crystalline materials constructed from metal-containing nodes that bonded or linked through organic ligands [11, 20]. The linked metal and organic ligands bridges and assembled to form 1D, 2D and 3D coordination network. , The metal containing unit which is referred as secondary building units (SBUs) linked with organic ligands using strong bonds [20]. MOFs have shown extraordinary porosity and can be used for wide application such as gas storage, gas separation and catalysis. One of the most advantages of MOFs shows its possibility of tuning the pore size from several angstroms to nanometres by controlling the length and functionality of the ligands. These properties are not achievable in the case of zeolites and porous carbon materials. The most prominent and distinctive property of MOFs are its large surface area. The surface area, pore size and framework topology can be tuned by using different organic building blocks and metal ions .

The metals ions can vary from transition metals to lanthanides and even some p-block metals to form wide range of network topologies. There are wide range of network topologies are known and they are constructed with different combination of metal ion and the ligands. The organic linkers and metal SBUs can be varied and that leads to variety of thousands of MOFs and that number increasing year and year [104]. The layered zinc terephthalate was the first proof of permanent porosity of MOF observed by measuring nitrogen and carbon dioxide isotherms [104]. Later the thrust was looking for ultrahigh porosity MOFs that can be achieved by using longer linkers which eventually increase the storage space and number of adsorption sites. The longer linkers were using the longer linkers that always prone to form the network to undergo interpenetration. The interpenetration can be avoided by targeting the topology which are not prone to interpenetrate [104]. Since the emergence of MOFs as potential material for carbon capture, a lot of research has been done on MOFs .

Since MOFs provide reversible carbon dioxide adsorption, they are excellent materials for the carbon capture. Carbon dioxide adsorption first reported using MOF-2 in 1998. The systematic carbon dioxide adsorption study of MOF-177 with an uptake of 1470 mg/g at 35 bar which exceeded that of any known porous material in similar conditions. Li et. al [105] worked on carbon capture using MOFs as adsorbent. CO₂ adsorption in MOFs depends on pore size or volume and nature of pore surface. MOFs have higher adsorption capacity than Zeolite and activated Carbon because they have more surface area and larger pore size in contrast to them. The volume and nature of pore to a great extent determine the shape of adsorption isotherms; due to interaction between molecules of CO₂ leading to large condensation. Typically, MOFs are synthesized in a hydro/solvothermal reaction

which involves combination of organic ligands and metal salts in dilute solution of polar solvents such as water, alcohol, alkyl formamides (such as DMF, DEF) or DMSO and heated at comparatively low temperatures usually below 50-300 °C. The solvent utilized in the synthesis itself act as a template and the solvent can provide the framework intact and accessible porosity. It is important to get high quality single crystals to characterize the MOF crystals. Although solvothermal technique used extensively other techniques also known for example slow evaporation of the solution precursors, layering or slow diffusion. Hydro/solvothermal techniques have advantage over other former techniques since they reduce the synthesis time. The ligand properties such as ligand length, bulkiness, bond angles, chirality etc. act as major factors to determine the frame work topology of the resultant compound [106]. The synthesis of MOF also depends on the concentration, solvent polarity, pH and temperature. A minor change in the former parameters can leads to poor quality crystals, lower yields or even the formation of new structures. To improve the crystal growth mixed solvent are often used which also provide to tune the polarity of the solution. Besides this standard method, some other methods have been described by researchers. These methods include: The mixture of non-miscible solvents [107], spray drying technic [108], an electrochemical approach [109, 110], and a high-throughput approach [111] and microwave irradiation. Micro wave irradiation enables access to increased range of temperatures, it can be used to reduce crystallization time and for controlling distribution of particle size and face morphology [112, 113]. Microwave irradiation however has a disadvantage of small crystal size formation, therefore difficult to get enough size crystal for single crystal X-ray diffraction .

Over time, several MOFs have been prepared by different group of researchers with the aim of arriving at a suitable formulation for efficient capture of CO₂. As at August 2012, a total of about 37,241 MOF structures were available in the Cambridge Structure Data base [114]. A typical example is MOF-177 [115] synthesized using Zn(NO₃)₂•6H₂O and of 4,4',4''-benzene-1,3,5-triyl-tri-benzoic acid (H₃BTB) were dissolved in 10mL of DEF inside a 20 mL vial. It was subjected to heat at temperature of 100 °C for 20 hours. The solution drained; the resulting clear crystals were washed in DMF and replaced with CHCl₃ three times in three days. Evacuated of the material was carried out at 125 °C for 6 hours prior to further analysis. For proper selection of appropriate building blocks for any desired application, a proper understanding of the influence of characteristics of the building blocks and resulting material on the adsorption behavior is important. Hydrothermal stability of MOFs could be estimated by exposing MOFs to steam at concentration and temperature more than anticipated in practical operating condition of flue gas. A throughput apparatus could be employed for the steaming. After which, sample materials are exposed to X-ray diffraction (XRD) examination to ascertain their structural stability [115].

MOFs could be rigid or flexible, depending on whether there is relative movement within their frameworks or not [11]. Several researches have been carried out on this topic: [116-119]. Usually, rigid MOFs; MOFs that do not display movement within frameworks show adsorption isotherms that are I-shaped. However, some MOFs have bi-porous structures that have channels and cages existing together within them. This makes them having stepwise adsorption isotherms [120] e.g. at low temperature, Ni^{II}₂Ni^{III}(_3-OH)(pba)₃(2,6-ndc)_{1.5} (MCF-19; pba = 4-(pyridin-4-yl)benzoate, 2,6-ndc = 2,6-naphthalenedicarboxylate). Flexible MOFs; MOFs that show flexible behaviour due to

movement within frameworks; display stepwise or hysteretic desorption for CO₂ and other gases [105]. Such MOFs are said to ‘breathe’ during adsorption/desorption e.g. M(OH)(bdc) (MIL-53) series, Sc₂(bdc)₃ etc. Gate phenomenon, movement within frameworks during adsorption/desorption, in MOFs has been given quite attention over the years; [121, 122]. Kitagawa et al. observed a phenomenon which was termed “gate” effect in some flexible MOFs. This was described as an abrupt rise in adsorption isotherm at relatively low pressure. This pressure was termed “gate” opening pressure. Saturation of the materials occurred at a different pressure. However, the isotherms for desorption, did not follow reverse trace of the adsorption isotherm, rather, it showed a sudden drop at another pressure (third pressure). Gate phenomenon also noticed in {Cu(4,4'-bipy)(H₂O)₂(BF₄)₂} (4,4'-bipy) (4,4'-bipy = 4,4'-bipyridine), when bared to water. Similarly, Rosseinsky et al. reported that Zn (Gly-Ala)₂; a peptide base MOF; exhibited “gate” behaviour at pressure of about 2bar .

Heat of adsorption is another property, for gas adsorption, can affect CO₂ uptake capacity of MOFs [11]. Heat of adsorption can be evaluated from adsorption isotherms of a CCS process for various temperatures. This property is an important factor in desorption. High value of heat of adsorption indicate that high energy is required for desorption process. Heat of adsorption also reduces with increase in loading. The capability to change the pores of MOFs is one of the important properties that distinguish them from other porous materials. Often, the length of organic linkers is the major determinant of the pores size in MOFs [123]. An analysis of the sorbate/framework interactions by Düren [103] showed that one dimensional pores with sharp edges are good for gas separation and gas storage at low pressure. However, this is less feasible at higher pressure because of the small volume

of these preferred energetic corner regions. This was illustrated with the investigation of the adsorption of pure methane and ethane in Zn MOFs of different pore morphologies (e.g. 3D cubic, 1D Rhombic, 1D triangular). It was shown that at lower pressure, as the pore volume is designed smaller, the selectivity becomes better while the adsorption rate per unit volume becomes higher. However, saturation is quicker due to smaller pore volume. However, at higher pressure, there is much lower uptake because of the small pore volumes. It was concluded that adsorption in MOFs with one dimensional pore is as a result of presence of sharp corners which brings about more framework atoms in the sharp corners.

Some of the ways by which CO₂ uptake of MOFs have to be improved include the following. 1) Capacity of MOFs at pressure can be improved by introduction of metal ions like Magnesium, Cobalt, Vanadium, Titanium etc. [115, 124]. 2) After-synthesis-exchange of extra framework cations inside anionic MOFs. 3) Introduction CNTs into MOFs, which could be ameliorated by addition of lithium and 4) Functionalizing the pores with alkyl amino group.

2.4.6 Comparison of Different CO₂ Adsorbents

The data of the different materials are summarized in Table 2.1. The table provides the different properties of CO₂ uptake, surface area, CO₂/N₂ selectivity and stability in humid conditions. The data are provided for materials of the different groups including carbon-based adsorbents, Zeolites and MOFs. The table indicates the dependence of the properties on the application pressure. It also indicates that some new materials are well stable in humid conditions. However, many materials require more development for consideration

for carbon capture of flue gases of the industrial applications. As well, the CO₂ uptake in some materials needs improvement.

Table 2.1 Adsorbent materials utilized for CO₂ capture.

Sorbent	Temp (°C)	Press ure (kPa)	CO ₂ molar fracti on (%)	Uptake CO ₂ (mol/kg)	Surface area (m ² /g) BET	Selectivity CO ₂ /N ₂	Stability in humid conditions	Reference
<u>Activated carbon based</u>								
NCLK3	25	120	-	3.5	-	30 (at 130 kPa, 323 K)	-	[125]
NCHA29	25	120	-	2.3	-	20 (at 130 kPa, 323 K)	-	[125]
NaSB31	25	4000	100	27	3024	-	-	[126]
KL31	25	4000	100	22	2540	-	-	[126]
KA21	25	4000	100	17.5	2156	-	-	[126]
NORIT R2030CO2	30	120	17	2.4	942	7	-	[127]
Carbon fiber composites	25	101.3	13	3.1	490.6	-	-	[128]
Olive stones	50	120	14	0.61	1113	18	hydrophobic and high stability	[129]
Almond shells	50	120	14	0.58	822	20	hydrophobic and high stability	[129]
No1KCl-a-600	25	120	50	2.03	1091	2.54 over CH ₄	-	[130]
No1KCl-b-1000	25	120	50	1.91	804	2.69 over CH ₄	-	[130]
No2OS-1000	25	120	50	1.83	1233	2.26 over CH ₄	-	[130]
Cu/Zn-16% AC	30	100	15	1.98	730.53	-	-	[130]
Cu/Zn-20% AC	30	100	15	2.26	599.41	-	-	[130]
Cu-20% AC	30	100	15	1.99	645.21	-	-	[131]
<u>Zeolite</u>								
Zeolite 13X	50	100	15	3	585.5	-	-	[132]
Zeolite 13X- APG	30	100	15.9	4.3	-	-	-	[133]
Zeolite A5	30	100	16	3	499	-	-	[133]

LEZ -13X	50	101.3	-	4.6	12.7	-	stable	[134]
LEZ -A5	50	101.3	-	5.2	16.8		stable	[134]
ZSM-5	25	120	25	0.7	-	4.6	-	[135]
Zeolite 13X	25	120	25	4.5	-	28	-	[135]
<u>MOFS</u>								
HKUST-1	30	1000	20	8.07	1326	-	stable	[136]
MIL-101(Cr)	30	1000	20	7.19	2549	-	stable	[136]
Zn₂(hfpbb)₂ (ted)	25	101.3	-	0.4545	-	40	-	[137]
CPM-5	0-25-40	105	15	3-2.3-1	-	14.2 (273 K)-16.1 (298 K)	stable for few weeks	[138]
MOF-177	40	100	15	0.65	4690	3	-	[26]
Mg₂-MOF-74	40	100	15	7.5	1800	63	-	[26]
IRMOF-1	25	3500	100	11.1	2833	-	-	[139]
IRMOF-3	25	3500	100	10.3	2160	-	-	[139]
IRMOF-6	25	3500	100	10.5	2516	-	-	[139]
IRMOF-11	25	3500	100	8.9	2096	-	-	[139]
HKUST-1	25	3500	100	7.3	1781	-	-	[139]
Zn-MOF-74	25	3500	100	7.1	816	-	-	[139]
MOF-505	25	3500	100	0.70	1547	-	-	[139]
Cu-TDPAT	25	100	10	0.59	1938	79	-	[140]
Na-rhoZMOF	25	100	20	6.2	-	440	-	[141]
Mg-rhoZMOF	25	100	20	8	-	680	-	[141]
Al-rhoZMOF	25	100	20	8	-	590	-	[141]
MIL-53(Al)	30	1000	100	5	-	5.5	-	[142]
MIL-100(Fe)	30	101.3	15	0.67	1894	4.6	stable	[143]
MIL-101(Cr)	30	101.3	15	1.05	3360	5.5	stable	[143]

Another table (Table 2.2) provides a comparison of the different materials group of zeolites, MOFs and activated carbon based materials. It is shown that MOFS have much

priority on other materials regarding the capacity but it is very expensive. As well MOFs in general are not stable in humid conditions. The three groups discussed in the table differ in terms of conductivity, thermal and chemical stability and possibility of tuning. The selectivity of CO₂/N₂ changes from low in zeolites to moderate in carbon-based adsorbents and becomes high in MOFs.

Table 2.2 Comparison of different adsorbents.

Specifications	Zeolites	Carbon-based adsorbents	MOFs
Major application	H ₂ production	High pressure CO ₂ adsorption flue gas	CO ₂ separation
CO₂ / N₂ selectivity	Low	Moderate selectivity for CO ₂ over N ₂	High
Energy for regeneration	Significant	Lower temperature for regeneration compared to zeolites. Better energy efficiency compared to metal oxides	Limited by low temperatures for generation, but still low economic efficiency
Capacity	Moderate	Lower than zeolites at low pressures and gets high at high pressures	High
Stability under moisture conditions	Reduced capacity	Do not suffer from breakthrough or decreased capacity under moist conditions	Mainly unstable: improvement under research
Cost	Low production cost	Reasonable cost	Expensive
Advantages	<ul style="list-style-type: none"> • Large micropores/mesopores • Medium CO₂ adsorption at ambient conditions 	<ul style="list-style-type: none"> • High conductivity • High thermal and chemical stabilities • Light weight with high surface areas as well as large pore volumes • Energy consumption is low 	<ul style="list-style-type: none"> • Possibility of tuning the pore size • Large surface area

Disadvantages	<ul style="list-style-type: none"> • Adsorb moisture, so CO₂ adsorption is poor with moisture existence • High energy consumption • Difficult readiness 	<ul style="list-style-type: none"> • Low adsorption and desorption temperatures • Low CO₂ uptake compared to some types of Zeolites and MOFs 	<ul style="list-style-type: none"> • Has low performance at partial pressure of CO₂ • Low economic efficiency • Synthesis is tedious and complicated • So sensitive to moisture • It is difficult to use at high temperatures due to destroying the MOF construction
----------------------	---	---	--

2.5 Experimental Studies on Adsorption Carbon Capture

Generally speaking, post-combustion carbon capture is a costly process due to process challenges including many parameters. These include design of capture CO₂ process and materials, structuring of carbon capture materials, dealing with impurities with CO₂ that can cause adverse effect on capture materials. They also include CO₂ storage and thermodynamics of power plants, integration of heat dissipation during carbon capture with heat dissipated in power plants, optimization of carbon capture materials with respect to ease of recycling, rate of carbon capture, CO₂ selectivity and capacity etc. [144]. Many types of MOFs and zeolites as adsorbents for carbon capture by adsorption in post combustion were studied in terms of CO₂/N₂ selectivity, adsorption capacity and breakthrough time [23]. Furthermore, many types of MOFs studied in literature for post combustion CO₂ capture were tabulated [145] regarding to CO₂ and N₂ uptake and selectivity for conditions closed to the ambient conditions which generally mimicked the post combustion exhaust conditions. This section presents the experimental studies that are

available for CO₂ adsorption. These are provided in two sub-sections including adsorption by MOFs and adsorption by zeolites and other materials.

2.5.1 Experimental Adsorption Using MOFs

A large number of literature investigations related to carbon capture is focused on methods and procedures for synthesis and testing of materials for post combustion capture. MOF type UiO-66 was synthesized and evaluated by Andersen et. al [82] as adsorbent for post combustion CO₂ capture using vacuum swing adsorption (VSA) process. The study focused on equilibrium isotherm, breakthrough curves, purity, and recovery of CO₂ (for 15% dry CO₂ and for 15% of CO₂ associated with 9% of water vapor; the remaining fraction was N₂). Single adsorber column of 1.1 cm diameter and 10.5 cm of length was used in experimental work. The gases were directed by solenoid valves while the mass flow controllers determined the need amounts of CO₂ and N₂ to mix and to purge into the adsorbent. Six steps represented the VSA cycle. These are feed pressurization, counter-current blow-down (adsorption), concurrent rinse with CO₂, counter-current evacuation (desorption), and counter-current evacuation with nitrogen purge (completing desorption). Equilibrium isotherms of CO₂ and N₂ were obtained at 303 K and 328 K for pressure increased up to 100 kPa. The results showed that the best CO₂ adsorbed amounts were obtained at high pressures and low temperatures. Breakthrough curves were evaluated for three different conditions of pressure (2 bar, 3 bar and 4 bar) and the obtained values showed the longer time was for the higher pressure which exhibited the better adsorption process. Increasing the times for adsorption and rinse processes (up to 61% and 13% of CO₂ breakthrough time for adsorption and rinse time, respectively) enhanced the recovery and purity of CO₂ up to 70% and 60%, respectively. The effect of water vapor was also

studied through 50 consecutive cycles; it showed that the CO₂ capacity of adsorbent is reduced 25% without any deterioration of MOF compared to dry cases.

Adsorption desorption regeneration

Adsorption, desorption and regeneration of CO₂ in two types of MOFs (HKUST-1 and MIL-101(Cr)) were experimentally investigated by Ye et. al [136]. The experimental set-up was built from one adsorbent bed connected to two cylinders; one had mixture of CO₂ (20% by volume) and N₂ and the other was filled by pure N₂ (for supporting desorption process). The concentrations of effluent gases from adsorbent bed were measured by a dual channel gas chromatograph fitted with a thermal conducted detector using H₂ as the carrier gas. The study started focusing on the CO₂ adsorption capacity of both HKUST-1 and MIL-101(Cr) at temperature varied between 30 and 200 °C and pressure up to 10 bar. The corresponding results showed that the maximum CO₂ adsorption capacities were 8.07 and 7.19 mmol/g for HKUST-1 and MIL-101(Cr), respectively, at 30 °C and 10 bar. This is attributed to the fact that the pore volume of HKUST-1 (0.58 cm³/g) is smaller than that in MIL-101(Cr) (1.3 cm³/g), even though, the surface area of MIL-101(Cr) (2549 m²/g) was over that of HKUST-1 (1326 m²/g). The comparison between both MOFs was done by TSA at 25 °C for adsorption and 100 °C for desorption (with purging N₂). It was noticed that HKUST-1 had a higher CO₂ adsorption capacity (1.82 mmol/g) than MIL-101(Cr) (1.17 mmol/g) at this condition. Furthermore, HKUST-1 was exploited to compare the sorption capacity for TSA and VSA processes. The CO₂ regeneration showed obviously that the TSA is better than VSA. The amount of CO₂ desorbed by VSA was about 1.05 mmol/g for 16 minutes while the desorption of CO₂ by TSA process was up to 1.85 mmol/g for 100 °C after 6 minutes only. These behaviours were interpreted by the MOFs containing

co-ordinately unsaturated metal sites (CUMs) that might not be efficient desorption by VSA. W. Xu et. al [137] synthesized two types of MOFs ($Zn_2(hfipbb)_2(ted)$ and $Co_2(hfipbb)_2(ted)$) and only investigated the CO_2 adsorption in one of them ($Zn_2(hfipbb)_2(ted)$). The study reported microporous MOFs synthesis, crystal structure analysis, porosity characterization and CO_2 adsorption selectivity and capacity as well. For 298 K and 1 atm condition, the equilibrium isotherms showed the maximum CO_2 adsorption was about 2% (by wt.) and the selectivity ranged between 208 and 40 for low vacuum pressure and up to 1 atm. These values of selectivity were claimed to be higher than zeolite materials and some MOFs as Cu-TPBTM, CuBTTri and PCN-61. It was observed that the adsorption heat was close to be constant (27 kJ/mol). The other results concerned with H_2 adsorption and pure CO_2 adsorption.

Adsorption and kinetic studies

Another MOF called CPM-5 was synthesized and undergone to CO_2 adsorption equilibrium and kinetic study by Sabouni [146]. Adsorption studies of carbon dioxide started by investigating the adsorption equilibriums of CO_2 and N_2 for pressure up to 105 kPa and for three different temperatures (0, 25 and 40 °C). BET instruments were used for measuring the adsorption equilibriums volumetrically and ASAP 2010 system equipped with software (Rate of Adsorption program) to measure CO_2 adsorption rates. The experiments commenced with degassed process at 423 K and vacuum pressure (10⁻⁶ kPa) previous to adsorption process. Unlike many of MOFs, CPM-5 showed stable structure under Lab conditions with relevant humidity of 62% for several weeks. Regarding to experimental isotherms at several conditions, CO_2 adsorption rate was about 3 mmol/g (13.2 wt. %), 2.3 mmol/g (10.1 wt. %) and 1 mmol/g (4.3 wt. %) at 105 kPa for 273 K, 298

K and 318 K, respectively. Moreover, the selectivity factor of CPM-5 was evaluated as 14.2 for 273 K and 16.1 for 298 K. CO₂ diffusivity in CPM-5 at 273K, 289K and 318 K for the same pressure (105 kPa) was estimated as 1.86×10^{-12} m²/s, 7.04×10^{-12} m²/s and 7.87×10^{-12} m²/s, respectively, while the maximum adsorption heat was about 36 kJ/mol. Comparison to other MOFs in the literature in terms of adsorption capacity performance, the CPM-5 showed a better CO₂ adsorption performance than some kinds of MOFs as MOF-5 and MOF-177 and in the same adsorption capacity performance of MIL-53(Al), UMCM-150 and Ni-STA-12. However, the adsorption capacity of CPM-5 is lower than functionalized and open metal sites MOFs such as HKUST-1, Mg-MOF-74 and NH₂MIL-53(Al).

Fourteen different types of MOFs were investigated for capturing CO₂ from the flue gas by Yazaydin et. al [147]. Seven types of MOFS were synthesized, characterized and measured regarding to the adsorption properties while the other 7 types were taken from the literature to study their CO₂ capture capability. Some experimental and simulation work was done for this purpose; the simulation study was performed by use Grand Canonical Monte Carlo (GCMC) at the ambient conditions (room temperature and 0.1 bar, the normal partial pressure of CO₂ in flue gas). The experimental work demonstrated that the best types could be used for CO₂ adsorption were Mg/ DOBDC (above 250 mg/g) followed by Ni/ DOBDC (180 mg/g) and CO/DOBDC (140 mg/g). On the other hand, the worst types were ZIF-8, IRMOF-3, IRMOF-1, UMCM-1 and MOF-177 (all of them less than 10 mg/g). Another point was the reversal effect of the metal-organic (M-O) bond length, it showed that the good captured CO₂ was for lower M-O bond length (Mg-O (1.069 Å) is better than Ni-O (2.003 Å)). The simulation study proved only some agreements

with experimental data in the cases of the best MOFs types for CO₂ pressure about 0.5 and 1 bar.

Temperature swing adsorption methods

Two types of MOFs (MOF-177 and Mg₂-dobdc (Mg/DOBDC)) were compared to capture CO₂ for post-combustion by using temperature swing adsorption method (TSA) [26]. Effect of temperature range between 20 °C and 200 °C on CO₂ caption was investigated at low pressure (0.15 bar for CO₂ in flue gas) to study the equilibrium isotherms of both MOFs as well as of zeolite NaX (well known in the literature). The results showed that Mg₂-dobdc exhibited the best capture performance: in term of amount of adsorbed CO₂, Mg₂-dobdc adsorbed 189 mg/g at 40 °C whereas Zeolite NaX and MOF-177 captured about 81 and 4.3 mg/g, respectively. Furthermore, the selectivity of Mg₂-dobdc is the highest (148.1 at 50°C, while 87.4 and unity for zeolite NaX and MOF-177, respectively). In addition, the working capacity by means of desorbing amount of CO₂ at higher temperatures indicated a superior amount for Mg₂-dobdc over the others. Thus, 0-176 mg/g could be desorbed by Mg₂-dobdc for temperature between 90 -120 °C and about 0-75 mg/g could be desorbed by zeolite NaX while MOF-177 did not express any positive values of desorbed CO₂ at the same range of temperature.

Performance in presence of water vapour

The most issue faces the use of MOFs as the adsorbents in separation processes is the decomposition under exposure to humid air. A few researches deal with this issue because the majority dealt with flue gas as a dry mixture gas only consists of CO₂ and N₂. Han et. al [148] studied the stability of seven types of MOFs (CdZrSr, Ni-Nic, La-Cu, Eu-Cu, Zn-

NDC, ZnPO₃ and Cu-HF) under exposure to moist air, liquid water, SO₂ and NO₂. They significantly emphasized on three types: Cu-HF, Zn-NDC and Ni-Nic as they had larger adsorption capacity and selectivity than the other four types. Exposing Cu-HF, Zn-NDC and Ni-Nic to liquid water and NO₂ during 5 days decreased the CO₂ adsorption capacity of Zn-NDC by about 30% due to partial decomposition of organic structure, whereas, Cu-HF and Ni-Nic did not suffer from decompositions. Oppositely, Cu-HF and Ni-Nic showed decreases in CO₂ adsorption capacity under exposing to humidity (3 days) and SO₂ (2 days) while Zn-NDC expressed some increasing in adsorption in the same exposed gases.

The best MOF type (Mg-MOF-74) also has some CO₂ adsorption deficiency with existing of moisture, unlike HKUST-1 type. The study investigated by [149] showed the decreasing of CO₂ adsorption at several conditions. For 1 bar and 298 K, the dry Mg-MOF-74 could adsorb about 8.4 mmol/g of CO₂ while with hydration 6.5% and 13% the CO₂ adsorbed amounts were 6.7 mmol/g and 5.4 mmol/g, respectively. Meanwhile, the CO₂/N₂ selectivity increased significantly due to drop in N₂ adsorption in hydrated gas. The interpretation of CO₂ decreases with existing humidity was the strong binding energy between CO₂ and co-ordinately unsaturated metal sites in MOF more than the binding energy between CO₂ and coordination water interacting. The reverse action (the binding energy between CO₂ and coordination water interacting is stronger) made the HKUST-1 adsorbing more CO₂ under increasing of hydration level. IRMOF-74-III as a MOF was covalently functionalized by anime [150] to study impact of humidity on the MOF construction and CO₂ adsorption capacity. The anime compounds added to IRMOF-74-III were -CH₃, -NH₂, -CH₂NHBoc, -CH₂NMeBoc, -CH₂NH₂, and -CH₂NHMe. IRMOF-74-III-CH₂NH₂ showed high adsorption capacity of CO₂ (3.2 mmol/g at 106 kPa and 298 K)

and was not affected by water vapor. Comparing dry and wet (RH=65%) cases of flue gas (16% CO₂, and the balance was N₂), the breakthrough curves were identical for both cases (dry and wet by using IRMOF-74-III-CH₂NH₂).

2.5.2 Experimental Adsorption Using Zeolites

Pressure swing adsorption process

Flue gas separation by zeolite 13X through pressure swing adsorption process (PSA) was investigated by experimental and mathematical model at two different temperatures (50, 100 °C) [151]. The experimental set-up relied on fixed bed filled with zeolite 13X which was undergone to four steps to represent separation process namely: pressurization, flue gas feed (15% CO₂, 85% N₂ by volume), blowdown (depressurization), purging. The gas chromatograph unit was used to measure the outlet concentrations of CO₂ and N₂ and mass flow controllers were used to control the flow amount of gases during working. Pressurization process was used to rise the pressure of the bed up to 1.3 bar with purging nitrogen, and then, the mixture of CO₂ and N₂ was fed to the bed at constant pressure (1.3 bar) to represent the adsorption process. After CO₂ saturation observed, the inlet gases were closed with depressurization the bed down to 0.1 bar for remove adsorbent amount of CO₂. For enhancing the desorption process, some amount of nitrogen was purging to the bed under low pressure (0.1 bar), this process called purging process. The experimental and theoretical equilibrium isotherms showed that zeolite 13X could adsorb 3 mmol/g of CO₂ at 1 bar and 50 °C and about 1 mmol/g of CO₂ for 100°C at the same pressure while the noticeable adsorbed amount of N₂ was less than 0.25 mmol/g for the same conditions. The results also showed good percentages of CO₂ recovery reached about 91.8% and 90% for

temperatures 50 and 100 °C (P=1.3 bar), respectively, while the CO₂ purity exhibited low percentages about 33.3% for 50 °C and about 36.8% for 100 °C. The decrease in purity of CO₂ can be solved by adding rinse process after adsorption by purging pure amount of CO₂ into the adsorbent to remove N₂ and replaced by CO₂. This process increases the cycle cost, but it is a solution when the pure CO₂ (above 90%) is needed. Figure 2.6 and Table 2.3 show a schematic of PSA and valve sequencing for different steps in the cycle respectively.

Table 2.3 Valve sequencing for different steps in PSA cycle.

M1	Feed	Blow down	Purge	Pressurization
	V1, V7	V3	V5, V3	V1
M2	Purge	Pressurization	Feed	Blow down
	V4, V6	V2	V2, V8	V4

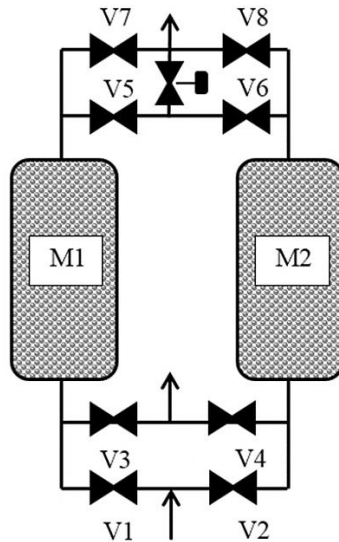


Figure 2.6 Schematics design of two-column PSA unit.

In the PSA set up (Figure 2.6), the first column (M1) is fed with flue gas at a pressure above atmospheric pressure, the packed bed selectively remove CO₂ from the gas stream leaving nitrogen rich effluent to flow out from valve 7(V7). After a set time e.g. breakthrough, the adsorbent packed in M1 is saturated hence, it no longer adsorbs CO₂. The feed is then directed to the second column (M2). In order to regenerate the saturated bed (M1), valve 3(V3) is opened to initiate pressure drop within the bed. The induced pressure causes desorption of the adsorbed CO₂ making the gas exiting V3 rich in CO₂. A purge step is then initiated to facilitate additional removal of CO₂ from the column. After purging, the bed pressure is restored by pressurizing with the less adsorbed gas. These are the four steps that make up a typical PSA cycle. At the end of a complete cycle additional cycles can be conducted to ensure further purity of the desorbed stream.

Vacuum swing adsorption

The problems associated with use vacuum swing adsorption were investigated by Chaffee et. al [152] by improving the cycle design with good temperature control. The adsorbent was zeolite 13X to capture CO₂ from flue gas (simulated by adding pure CO₂ to the air). This adsorbent material was insensitive to moisture. Furthermore according to the results, the CO₂ adsorption might be increased in the presence of H₂O; N-containing hybrid material adsorbed higher amount of CO₂ than N₂ (contained in feed flue gas). The study also claimed that the fully filled pores adsorbed by N-containing had lower CO₂ caption at low temperature (room temperature) while significant amount of CO₂ was adsorbed for higher temperature (as 70 °C), and the vice versa for partially filled pores (open pores) by N-containing. Generally, for open pores adsorbent, increasing the gas feed temperature decreased the amount of adsorbed CO₂ while increasing the feed pressure improved the

captured CO₂; the optimum vacuum pressure to minimize the power used for adsorption process was 0.04 bar.

Zeolite testing under humid conditions

Experimental investigation of CO₂ capture from wet (humid) flue gas was studied by Li et. al [153]. Zeolite X13 was used and the vacuum swing adsorption method was applied to study the impact of moist flue gas (PH=95%) on the adsorption and desorption processes at 30°C. The investigation demonstrated that the CO₂ recovery reduced by 22% with existence of H₂O. Furthermore, high concentration of H₂O appeared during vacuum process and about 27% of the condensed H₂O was accumulated in the vacuum pump itself. A comparative experimental study between two adsorbents (13X and A5 Zeolites) for CO₂ capture by indirect thermal swing adsorption (indirect heating/cooling by internal heat exchanger) was studied by Mérel et. al [154]. 90% of N₂ and 10% of CO₂ were modeled the flue gas to pursue CO₂ capturing. The Zeolite A5 showed the better performance than Zeolite 13X for capturing CO₂ such as the capture rate of CO₂, volumetric productivity and specific heat consumption were (+ 14.5%), (+22%) and (-19%), respectively, for Zeolite A5 over than 13X.

The experimental work for CO₂ capture from flue gas of coal fired power plant is studied by Wang et. al [155] using zeolite 13XAPG by vacuum pressure swing adsorption technique VPSA). The capture plant consisted of two units: dehumidification unit and CO₂ capture unit. The dehumidification unit consisted of two cylinders filled with 156 kg of alumina for removing water vapor and the contaminants amount of SO_x and NO_x via temperature swing process. The output gases of this unit were CO₂ (15.5-16.5% by volume)

and N₂ and less than 0.5% of relative humidity. The other unit formed of three column cylinders (adsorbers) occupied by 261 kg of zeolite 13XAPG for representing CO₂ capture unit by VPSA process. The cycle of the VPSA was quite complicated to consist of eight steps for each adsorber such as pressurization, feed, depressurization, rinse, provided pressure equalization, blowdown, purge, and received equalization. All processes were done automatically by programmable logic controller and software. The results showed the beds reached steady state after 100 operating cycles and the adsorption temperature raised to 323 K. The adsorption isotherms announced the maximum CO₂ adsorption was about 4.3 mmol/g comparing with 3 mmol/g with using A5 molecular sieve in their previous work at the same conditions (T=303 K, P=100 kPa). For inlet flow rate of flue gas about 32.9-45.9 Nm³/h, the CO₂ recovery and purity were about 85-95% and 37-82%, respectively, with power consumed for blower and vacuum pump about 1.79-2.14 MJ/kgCO₂ (two third of the consumed power was by vacuum pump). The maximum CO₂ productivity of the unit was 0.207 molCO₂/m³ adsorbent.

Zeolite 13X-APG was utilized [133] as the adsorbent for post combustion CO₂ capture by VTSA process. Experimental and simulation investigation focused mainly on the type of process such as TSA, VSA and VTSA that was more efficient in terms of CO₂ recovery and purity. The setup consisted substantially of one bed heated and cooled indirectly by oil passing around the adsorber. The studied flue gas had 15% of carbon dioxide by volume while the complement percentage was nitrogen. The maximum isotherm adsorption was about 4.3 mmol/g of CO₂ at 303 K and 100 kPa. The comparison of results among the three generation methods (TSA, VSA and VTSA) illustrated that the best CO₂ recovery and purity for VSA process were 78.6% and 78.4%, respectively, at P=3kPa for 5 minutes of

evacuation and 0.15 SLPM of N₂ purging while alone. TSA process without evacuation could achieve 78.1% of CO₂ recovery and 91.6% of CO₂ purity for 443 K of desorption. The cooling was at close to ambient conditions during 10 minutes to maximize adsorption capability. In the other hand, the combined processes in one process (VTSA) at 403 K of desorption temperature and 3 kPa of vacuum pressure could reach 98.2% and 94% of CO₂ recovery and purity, respectively. Furthermore, researchers conducted with the Zeolite 13X as adsorbent for CO₂ capture and the generation processes correspondingly are shown in Table 2.4 to show the ability of this material (Zeolite 13X) of adsorption CO₂ at several conditions.

Table 2.4 Carbon Capture by Zeolites.

Process	Cycle steps	CO ₂ % (by vol.)	Abs./des. pressure (kPa)	Abs./des. temperatu re (oC)	Recovery CO ₂ (%)	Purity CO ₂ (%)	Ref.
PSA	FP,FD,DP,PUR	15	130/10	50-100	91.8-90	33.3- 36.8	[151]
PSA	FP,FD, DP,PUR	8.3	303/101.3	25	50	78	[156]
VPSA	1st-stage: EQ,FP,FD,EQ,DP,PUR	10.5	6.67	30	80	99	[157]
(2-stages)	2st-stage: EQ,FP,FD,EQ,DP	15	13.34	30	78.8	99.7	
VSA	FP,FD,DP	11.2	118/3	30	78.5	69	[153]
VSA	FD,PR1,PR2,EQ,RIN, DP,EQ,PR3,PR4	8-15	130/5-6	40	60-70	90-95	[158]
VSA	FP,FD,EQ,RIN1,RIN2,DP, EQ	13	172/5.07	30	69	99.5	[159]
TSA		10	101	15/110	56	~100	[160]
VTSA	FP,FD,H,DP,PUR,C	15	101/3	30/90	98.5	94.4	[133]

FP, pressurization with feed; FD, feed; RIN, rinse; EQ, pressure equalization; DP, depressurization; PUR, purge; PR, re-pressurization; H, heating; C, cooling.

2.5.3 Experimental Adsorption Using Carbon Based Adsorbents

Activated carbon

González and Plaza [125, 129] prepared a cheap activated carbon from spent coffee grounds to study the potential of CO₂ capture by adsorption of flue gas mimicking the post combustion CO₂/N₂ percentages. Two types of activated carbon obtained from spent coffee ground were investigated in this study such as NCLK3 and NCHA29 at pressure between 0 and 120 kPa and temperature varied between 0, 25 and 50 °C by volumetric apparatus. The isothermal adsorption showed NCLK3 had about 3.5 mmol/g of CO₂ as a maximum adsorption at 120 kPa and 25 °C with average heat of adsorption about 27.19 kJ/mol while NCHA29 was less efficient with CO₂ adsorption with about 2.3 mmol/g at the same conditions and 36.42 kJ/mol of isosteric adsorption heat. The selectivity and adsorption working capacity also showed some advantages for NCLK3 over NCHA29 in which the authors claimed that NCLK3 was competitive with zeolite 13X.

The main properties of the adsorbent affecting CO₂ capture by adsorption was experimentally investigated by Marco-Lozar et. al [126] through comparing the adsorption performance of 17 types of activated carbon. The different pore size distribution and density of the adsorbent were found to play main roles of selection of adsorbent type at proper pressure. For pressure between 0.1 and 1.2 MPa and ambient temperature (post combustion case), it was observed that the adsorption capacity did not change much by increasing microspore volume and it was appropriate to consider the volume of the microspore less than 0.7 nm. However, in application that have higher operation pressure (>1.2 MPa: pre combustion and oxy combustion cases), the microspores volume should be

larger to adsorb more amount of carbon dioxide. Regarding to density, the adsorbent bed has a specific volume, so the less adsorbent density means a little amount of the solid material would occupy the size and that significantly reduces the overall amount of adsorbate material. Therefore, the larger density with high adsorption capacity was preferable. Plaza et. al [127] focused on the commercial activated carbon NORIT R2030CO₂ to study its CO₂ adsorption capability from flue gas (17% CO₂, 83% N₂ by volume) and comparing some regeneration methods. The set-up of experimental work consisted of one adsorbent bed receiving a mixture CO₂/N₂ from two cylinders, each for one gas controlled by mass flow controller and then mixing by a helical distributor. The bed was heating by a coil around it and the outlet of the bed was connected by pressure regular and then by dual channel chromatograph fitted with thermal conductive detector to calibrate and measure the output concentrations of effluent gases (CO₂ and N₂). The study addressed the comparison between TSA, VSA and VTSA for flow rate of 34 cm³/min and adsorption pressure of 130 kPa as well as the adsorption temperature was 303 K. The isotherms showed the maximum CO₂ adsorption was about 2.4 at 120 kPa and 303 K and the CO₂/N₂ selectivity was 7 at the same conditions. TSA announced the smallest values of the CO₂ recovery and productivity by about 40% and 0.8 mmol/g.hr, respectively, at the mentioned adsorption conditions (T=303 K, P=303 kPa) since N₂ purging for desorption process (at 373 K and 2.7 cm³/min). However, VSA adsorption performed under the vacuum (P=5 Pa) and temperature about 303 K produced about 1.7 mmol/g.hr of CO₂ with 87% of recovery. For enhancing the performance, VTSA was applied to produce about 1.9 mmol/g.hr and to increase the CO₂ productivity up to 97% under the vacuum conditions and increasing temperature to 323 K.

Carbon fibre composites

Carbon fibre composites also promised a better CO₂ capture compared to other types of activated carbon [128]. It was synthesized by consolidation as a one brick. There were some small tubes put inside the material for air and water heating and cooling during desorption and adsorption processes, respectively. Two large beds (2 m) were filled with adsorbent for investigation the CO₂ capture at ambient conditions (298 K and 1 bar) from flue gases which contained 13% CO₂, 5.5% O₂ and the remaining was N₂. The setup controls and monitors included flow mass meter, CO₂ analyzer, O₂ analyzer and volume meter. The study relied firstly on temperature swing adsorption method for adsorbent regeneration at T=383K and ambient pressure (1 bar) without purging any gas and then on vacuum swing adsorption for ambient temperature and 30 kPa of pressure. However, the results showed the two methods were not sufficient for efficient recovery CO₂ and then suggested vacuum temperature swing adsorption for efficient regeneration process.

The maximum adsorbed CO₂ showed by adsorption isotherms was 2.51-3.1 mmol/g at ambient condition which added some advances to activated carbon CO₂ capture research. Regarding to desorption techniques, TSA at 398 K and 1 bar had 100% of CO₂ concentration and the CO₂ recovery was less than 20% while VSA at 298 K and 30 kPa presented lower than 5% of CO₂ recovery with higher energy consumption by vacuum pump. On the other hand, utilizing two methods simultaneously (VTSA: T=398 K and P=75 kPa) enhanced the performance significantly. Besides VTSA, flushing some amount of pure CO₂ soon after adsorption process (for remove the amounts of adsorbed N₂ and O₂ from the bed) improving the CO₂ recovery up to 97% with 100% of the purity. Two cheap activated carbon adsorbents were made from olive stones and almond shells with single

step activation for investigating CO₂ adsorption separation of flue gas [125]. The study considered the equilibrium isotherms at different conditions (0, 25 and 50 373 K and 2.7 cm³/min of for pressure reached 120 kPa). For olives stone carbon, the maximum adsorption of CO₂ was about 3.2 mmol/g for 100 kPa and 25 oC while almond shell carbon showed about 2.5 mmol/g at the same conditions. Simulating the flue gas by 14% CO₂ and 86% N₂ and passing it through adsorbents, the obtained breakthrough curves determined that the breakthrough time of olive stone-based carbon had lower time than almond shell-based carbon (by 1 minute out of 8 minutes). But, the CO₂ adsorption capacity of olive stone-based carbon expressed a little higher value than that in the almond shell-based carbon (0.61mmol/g for olives type and 0.58 for almond shell one at 120 kPa and 50°C). The desorption process in this study was done by passing helium gas, because it only focused on adsorption process regardless the complete cycle methods.

2.5.4 Experimental Adsorption Using Other Adsorbents

Regeneration process techniques

The regeneration process (desorption) refers to the rejection of the adsorbed amount and the best measures for its performance that is CO₂ recovery and CO₂ purity. The performance of regeneration process techniques for purity and recovery of flue gas was summarized as shown in Table 2.5 [161]. It is clear from this table and as mentioned above [125, 127, 128, 161] that the best percentages of CO₂ recovery and purity above 90% were obtained by combined processes such as pressure temperature swing adsorption (PTSA) and vacuum temperature swing adsorption (VTSA). Also, the CO₂ recovery and purity reasonable percentages can be obtained from vacuum pressure swing adsorption process.

Table 2.5 Comparison among different regeneration processes in terms of CO₂ purity and recovery [161].

Process		CO ₂ recovery (%)
ESA	23.33	29.57
VPSA	99	53-70
PTSA	99	90
2-bed-2-step PSA	18	90
VPSA	99.5-99.8	34-69
PSA	99.5	69
PSA/VSA	58-63	70-75
VSA	90	90
PSA/VSA	58	87
PSA/VSA	82.7	17.4
3-bed VSA	90-95	60-70
TSA	95	81
ESA	89.7	79
PSA	16	89

A hybrid adsorbent consisted of monolithic activated carbon and zeolite was investigated for CO₂ capturing performance using electrical swing adsorption technique (ESA) [162]. The holes in consolidated activated carbon were filled by Zeolite 13X to occupy about 82 % of the volume of the bed. ESA was designed to desorb the adsorbed amount of CO₂ inside the adsorbent by electrothermal regeneration (Joule effect) with temperature reached about 460 °C. Furthermore, ESA was represented by two cases: first case was performed by four steps such as feeding, electrothermal desorption, purging with electrothermal desorption, and cooling while the other case study expanded the capture cycle to six steps such as feeding, rinsing, electrothermal desorption, purging with electrothermal desorption, purging and cooling. The flue gas in these cycles was about 8.1% (by vol.) of CO₂ and the balance is N₂. For the same cycle time of the two case studies, the results

showed the six steps cycle had higher CO₂ purity about 46.6% compared to 44.8% of four step cycle due to rinse process, whereas the CO₂ recovery had high percentage for four step cycle with 92.4% and the lower was 81.4% for the six steps cycle. However, the cost of both was considered high compared ESA to other process techniques with about 44.8 GJ/tonCO₂ and 33.3 GJ/tonCO₂ for four and six steps cycles, respectively. Moreover, the hybrid adsorbent addressed some drawbacks as enlarging the mass transfer zone due to non-homogeneously. Some increasing in adsorbed amount of dioxide carbon and elongating the breakthrough curve were due to existing of zeolite 13X itself with good percentage (82%).

The adsorption behavior of zeolite 13X to Methane, Nitrogen and Carbon Dioxide were investigated experimentally by Cavenati et. al [163]. Activation of Zeolite 13X samples was done with Helium, under vacuum through the night at temperature of 593K. The samples were heated at a rate of 2K/min while Isotherms were measured at 293, 308 and 323K at pressure range of 0-5MPa. All of the Isotherms were made completely reversible. A Magnetic Suspension Microbalance (Rubotherm) was employed to perform adsorption equilibrium of the pure gases. The authors' data fitted with the Toth and Multisite Langmuir Model. A strong CO₂ adsorption was recorded, which make them recommend Zeolite 13X as potential material for CO₂ sequestration from flue gas. Casas et. al [164] performed breakthrough experiment, describing pre-combustion CO₂ capture using MOFs (e.g. USO-2-Ni MOF) and UiO-67/MCM-41 hybrid adsorbents by Pressure Swing Adsorption (PSA). MOF UiO-67/MCM-41 hybrid was designed jointly with meso-porous silica, (i.e. MCM-41), of average sized particles: say 1 mm. MCM-41 has a very good adsorption capacity, stabilizing effect, and lower Henry's constant. These are favorable

characteristics for desorption at high pressure. Furthermore, the 1 mm particles qualify for use at industrial level, for feasible range of resulting pressure drop. On the other hand, formulation of $\text{USO}_2\text{-Ni}$ MOF particles is yet to be up scaled; therefore, only particles of size 0.2–0.5 mm were produced. Material and particle densities were characterized by Helium pycnometry and Hg-pycnometry respectively. The material heat capacity of the two materials was estimated with the use of a Differential Scanning Calorimeter (DSC). The authors [164] performed process scale up by first conducting a fixed bed experiment, during which the adsorbent was packed into column after which three grades of CO_2/H_2 mixtures were feed through them at temperature of 25 C and pressure range of 1–25 bar to determine the transfer parameters. In the breakthrough experiment, it was found that the feed flow rate had negligible impact on the mass adsorbed and heat transferred under the considered span of conditions.

Adsorbent packing processes

Formation of particle is very important; it has a huge effect on the adsorbent packing properties, hence, on the process performance by Casas et. al [164]. They concluded that existing research on formulated MOFs with average particles size greater than 1 mm (that permit scaling up) is adequate to enable their exploration for industrial scale usage. In addition, bed density and particles, are of great importance in process design. This is because they are responsible for the quantity of adsorbent materials that can be packed in enclosed column volume. In this light, the UiO-67/MCM-41 hybrid showed good packing properties, not withstanding, further research and improvement is required in their mechanical stability in order to make them useable on industrial scale. Dantas et. al [165] worked on fixed bed CO_2 adsorption from a gas mixture of 20% CO_2/N_2 . The adsorption

medium used was activated carbon. Helium was used for pre-treatment of the bed. Break through curves were obtained by varying temperatures, while Linear Driving Force approximation (LDF) was used for the mass balance, the momentum and energy balance were also accounted for in order to reproduce the break through curves. Investigation of changes in the surface of the activated carbon used due to CO₂ accumulation was carried out with Fourier Transform Infrared Spectroscopy (FTIR) and X-ray Photoelectron Spectroscopy (XPS) analysis. Gas mixture was subjected to different temperatures of 301K, 323K, 373K, and 423K at a total pressure of 1.02bar. The adsorption column was located inside a furnace for easy control of the process temperature, the column and furnace; which was the adsorption system; were therefore assumed adiabatic as they were isolated using a fiberglass layer and a non-convective refractory material. However, the breakthrough experiment was treated adiabatically. Siriwardane et. al [49] also observed similar behavior while using 13X zeolite for CO₂/N₂ gas mixture adsorption. Dantas et. al [132] suggested that resistances to internal mass transfer are negligible in the adsorption system. It was suggested that for turbulent system, mass spread is due to axial dispersion [151].

2.6 Numerical studies and Mathematical Approaches for Fixed Bed

Column Adsorption

In order to achieve a suitable and effective design of adsorption process, there is need for an appropriate model to describe the dynamics of the adsorption system [49, 132, 165]. Most of suggested models are mathematical models and more recently, Artificial Neural Network models (ANN) [166] amongst others. The computer simulation tool requires

experimental validation for the development of new system. Since experimental setups are quite costly and time consuming, a mixed design approach using a well validate simulation tool with reasonable experimental validation seems to give the best design results. The simulation tool is composed of a descriptive mathematical model to predict the adsorption system (fixed bed/column) behavior [167]. Such mathematical models are experimentally verified and make use of independent parameters to estimate the required dynamic properties of the adsorption system with no extra time and cost as compared to the experimental procedures. The models also enable break through curve estimation, temperature profile of constituent gases at different time and point within the adsorption column. Varieties of materials and their properties could be quickly and easily tested using the mathematical models. In addition, variations in compositions and temperatures within the adsorbent column, with respect to time and space, and their effect on the overall performance of the adsorbent system; can be modeled and simulated [168].

Mathematical models capable of predicting the dynamics of adsorption systems are made of coupled partial differential equations representing the flow field, mass and energy transfer within the field (mass, species, momentum and energy balances) [165]. The flow field is usually modeled as a fixed bed (with suitable boundary condition) in which adsorption takes place. A simultaneous solution is required for the system of PDE's, making the solution to the system involved and complex, hence the need for a simplified model with good assumptions for easier computation and optimization. The study of modeling and optimization of CO₂ adsorption on fixed bed has grown over the years and is still of important interest in the field of Carbon Capture and Sequestration (CCS). The dynamic behavior of an adsorption chamber system can be categorized based on the nature

of the relationship between the constituent gas species and the solid at equilibrium and the complexity of the mathematical needed for describing the adsorption mass transfer process [169]. The complexity of the mathematical model for describing adsorption process behavior depends on the level of concentration, the choice of rate equation and the choice of flow model [169].

The fixed bed mathematical models are used to temporarily forecast the performance of an adsorption system in terms of dynamic property variation of the gas and the adsorption bed during adsorption e.g. flow rate, temperature, concentration, etc. The description of the pattern of flow within the adsorption column is usually done using the plug flow model or axially dispersed plug flow model. Some assumptions are usually made but, they differ from one model to another. E.g. some models account for the effects of heat generation and heat transfer in the adsorbent bed, based reasons that it may affect the adsorption rates etc. Some of these assumptions include a) Ideal gas behavior, b) Negligible radial gradient of concentration (and temperature and pressure where applicable), c) Negligible heat transfer between gas and solid phase for non-isothermal operation i.e. instantaneous thermal equilibrium and d) Negligible pressure drop across bed. The assumption of negligible radial gradient has been made by a number of researchers [170, 171]. A lot of existing models are based on the effects of finite mass transfer rate with mathematical models closely representing real process. Most of the popular existing models use a linear driving force approximation for the description of mass transfer mechanism in CO₂ adsorption process. After several years of research it has been discovered that it is equally important to consider the effect of momentum balance and heat generation and heat transfer in the adsorbent bed. This is important because the concentration profile has a

dependence on temperature variations, may be eminent for high-concentration feeds, because the heat of adsorption in high concentration feed generates thermal waves which travel in axial and radial directions [172].

Adsorption equilibrium has been mostly represented with non-linear isotherms such as the Langmuir isotherm/hybrid Langmuir–Freundlich isotherm. Linear isotherms have been used but only few cases. The Langmuir model works on the assumption of ideal localized molecular interaction between adsorbate and adsorbent with no further interaction on other groups of identical sites. Adsorption system hardly adhere strictly to Langmuir model assumptions, most times, their equilibrium isotherms deviate from the Langmuir model form. This may be due to the variation in heat of adsorption which is required to be constant based on Langmuir. From this, it can be stated that: Since the heat of adsorption changes with concentration, at lower concentration, the Langmuir model can give an appropriate representation of the system, however, as the concentration of the gas to be tested increases, the accuracy of the model would drop [169]. Due to the limitations of the Langmuir model, several authors e.g. Freundlich have modified the model e.g. by introduction of power law expression (Langmuir-Freundlich equations), and a host of other authors. The gas phase material balance includes an axial dispersion term, convective term, fluid phase accumulation, and the source term due to adsorption of the gas molecules (adsorbate) on the solid surface (adsorbent). The equation accounts for: The variation in adsorbate velocity and concentration in fluid phase with distance along the bed, the average concentration of adsorbate components in the solid adsorbent particles, while the axial dispersion coefficient represents the effect of axial mixing and the contributing mechanisms. This equation is used to find the transportation of gas composition along the bed, with an assumption of

negligible radial variation in gas concentration and solid loading [132, 165]. Danckwert's boundary conditions are applied here [168, 173].

2.6.1 Mathematical Models

Mathematical modeling of CO₂ adsorption and separation depends mainly on the mixture from which CO₂ is to be separated. It also depends on the type of adsorption process and the adsorbent media. The following are examples of CO₂ separation from different mixtures such as CO₂/ CH₄, CO₂/ N₂, CO₂/ H₂, CO₂/ He, CO₂/ Air, CO₂/ CO and flue gas mixtures as well as pressure swing or vacuum swing adsorption.

CO₂ in a binary mixture (with CH₄, N₂, H₂ or He)

Kumar [174] obtained a mathematical model to describe adsorption separation of CO₂ from binary gas mixtures of Carbon dioxide (CO₂) and Nitrogen (N₂), Carbon dioxide (CO₂) and methane (CH₄), and carbon dioxide and Hydrogen. The model was made up of a system of coupled partial differential equations. The adsorption media (adsorbents) used was 5A zeolite and BPL carbon. The flow pattern was described using plug flow model, while the mass transfer pattern was described using local equilibrium model. The mathematical model was solved numerically using finite difference method after which adiabatic simulation was carried out. The following assumptions were made: Negligible radial variation in temperature, concentration, negligible pressure drop within bed, thermal equilibrium between the gas and solid particles, and non-isothermal heat effects. A Langmuir-Freundlich equilibrium isotherm was assumed. It was concluded that isothermal assumption was improper for the process design, but it could be useful for semi-quantitative forecast of adsorption column behavior.

Delgado [175, 176] described a mathematical model to describe the adsorption separation of CO₂ from binary gas mixtures (CO₂-N₂, CO₂-He and CO₂-CH₄) on sepiolite, silicate pellets and a resin. The flow pattern was described using axial dispersed plug flow model, while the mass transfer pattern was described using the LDF approximation model. The mass transfer coefficient was determined by fitting the experimental data (i.e. lumped). Ergun's equation was employed to describe the momentum balance of the system. The PDE's in the mathematical model were solved numerically using method of orthogonal collection on finite element using PDECOL software. The following assumptions were made: Negligible radial variation in temperature and concentration, negligible pressure drop within bed, thermal equilibrium between the gas and the solid particles, and non-isothermal heat effects. An Extended Langmuir equilibrium isotherm was assumed. The mathematical model gave a good description of the breakthrough experiment with lower CO₂ concentration. However, for the experiments with high concentration of CO₂ were predicted with higher percentage of error. It was suggested that, introduction of interaction factor into the model boosted the accuracy of the model based on the interaction between adsorbed molecules of CO₂. Shafeeyan et. al [168] reviewed different existing mathematical modeling methods of the fixed-bed adsorption of carbon dioxide. Shendalman and Mitchell [177] obtained a linear mathematical model using characteristic method while working on a mathematical model to describe Pressure Swing Adsorption separation of CO₂ from a binary gas mixture of Carbon dioxide and Helium (CO₂-He). Their adsorption medium (adsorbent) was Silica gel. The flow pattern was described using plug flow model, while the mass transfer pattern was described using local equilibrium model. The mathematical model was solved analytically, by assuming: Negligible radial

variation in concentration, negligible pressure drop, trace system and isothermal heat effects. A linear equilibrium isotherm was assumed. Their model had a limitation of neglecting the mass transfer resistance effect which made their results differ from experimental results. Cen and Yang [178] Obtained a mathematical model to describe Pressure Swing Adsorption separation of CO₂ and other gaseous products of coal gasification. Their adsorption medium (adsorbent) was activated carbon. The flow pattern was described using plug flow model while the mass transfer pattern was described using local equilibrium model and Linear Driving Force approximation model (LDF). An empirical relation was utilized to determine mass diffusivity of CO₂. The mathematical model was solved using the implicit finite difference method, by assuming: Negligible radial variation in temperature and concentration, thermal equilibrium between gas and solid phase, and non-isothermal heat effect. A Langmuir-Freundlich isotherm was assumed. Their model differs from experimental data. This was more pronounced in the CO₂ concentration. However, the LDF was closer to the experimental data. A mathematical model was developed by Raghavan et. al [179] to describe Pressure Swing Adsorption separation of CO₂ from a binary gas mixture of Carbon dioxide and Helium (CO₂-He). Their adsorption medium (adsorbent) was Silica gel. The flow pattern was described using axial dispersed plug flow model, while the mass transfer pattern was described using Linear Driving Force approximation model. The mathematical model was solved by orthogonal collection and by using finite difference method and by assuming: Negligible radial variation in concentration, negligible pressure drop, traces system inverse dependence of the mass transfer coefficient with pressure, and isothermal heat effects. A linear

equilibrium isotherm was assumed. Their model succeeded in making a good representation of experimental results.

A mathematical model that describes Pressure Swing Adsorption separation of CO₂ from a gas mixture of Carbon dioxide (CO₂) and methane (CH₄) was developed by [180]. Both CO₂ and CH₄ have equal proportion by volume. The adsorption medium (adsorbent) was carbon molecular sieve. The flow pattern was described using plug flow model, while the mass transfer pattern was described using LDF approximation model, with a coefficient of mass transfer that is cycle time dependent. The mathematical model was solved using implicit backward finite difference method and, by assuming: Negligible radial variation in concentration, negligible pressure drop within bed, and isothermal heat effects. A Langmuir equilibrium isotherm was assumed. The results provided by the model is reportedly said to be very close to the experimental data used within about 3% margin of error [168]. Cavenati et. al [181] worked on a mathematical model to describe the adsorption separation of a gas mixture of carbon dioxide (CO₂) and methane (CH₄) on Tekada carbon molecular sieve by Vacuum Swing and Pressure Swing (VSA-PSA). The flow pattern was described using axial dispersed plug flow model, while the mass transfer pattern was described using double LDF approximation model. Pressure variation in the system was described using Ergun equation. The PDE's in the mathematical model were solved numerically using method of orthogonal collection for twenty five (25) finite elements, with two collection point per element, after which the evolving ODE's were solved using gPROMS. The following assumptions were made: Negligible transfer of mass, momentum and heat in radial direction, adiabatic and non-isothermal heat effects. A multisite Langmuir equilibrium isotherm was assumed. The mathematical model gave a

qualitative description of the breakthrough experiment and temperature curves. The model had a limitation of how to determine new values of mass transfer coefficient for new runs. Similarly, Ahn and Brandani [182] predicted the dynamics of CO₂ breakthrough on carbon monolith, with different set of assumptions. The flow pattern was also described using axial dispersed plug flow model, while the mass transfer pattern was described using the LDF approximation model. The PDAE's in the mathematical model were solved numerically using gPROMS. The following assumptions were made: Negligible change in concentration in radial direction. A Langmuir equilibrium isotherm was assumed. The mathematical model which accounted for a detailed structure of the adsorbent gave a qualitative description of the breakthrough experiment. It gave results of very close match to the experimental data used. However, another model based on the equivalent channel approach produced wrong results that forecast higher separation efficiency for the system. Hwang et. al [183] described a mathematical model to describe the adsorption separation of CO₂ on activated carbon using helium as the carrier gas. The flow pattern was described using plug flow model, while the mass transfer pattern was described using LDF approximation model. The mass transfer coefficient was lumped i.e. it was determined by fitting the experimental data. The PDE's in the mathematical model were solved numerically using method of lines, after which the evolving ODE's were solved using DIVPAG. The remaining algebraic equations were solved using DNEQNF. The following assumptions were made: Negligible radial velocity, negligible radial variation in temperature and concentration, negligible pressure drop within bed, non-adiabatic, and isothermal heat effects. A Langmuir equilibrium isotherm was assumed. The mathematical model gave a qualitative description of the breakthrough experiment and temperature

curves. The model had a limitation of how to determine new values of mass transfer coefficient for new runs.

The mathematical modeling of the adsorption separation of CO₂ from flue gas (20% CO₂, 80% N₂) on zeolite 13X by Vacuum Swing (VSA) was provided by Chou and Chen [184]. The mixture presents typical dry conditions of flue gas on industrial applications. The flow pattern was described using axial dispersed plug flow model, while the mass transfer pattern was described using local equilibrium model. The PDE's in the mathematical model were solved numerically using method of lines with adaptive grid points, after which an estimate of the flow rate was done using the cubic spline approximation. The evolving ODE's were solved by integration with respect to time of flow in adsorption bed using LSODE from ODEPACK software. The remaining algebraic equations were solved using DNEQNF. The following assumptions were made: Negligible radial variation in temperature and concentration, negligible pressure drop within bed, thermal equilibrium between the gas and the solid particles, and non-isothermal heat effects. An Extended Langmuir equilibrium isotherm was assumed. The mathematical model gave results similar to the experimental data used but with lower values than those of the experiment. This discrepancy was suggested to be due to the use of non-specific isotherm.

Mulgundmath et. al [185] worked on a mathematical model to describe the adsorption separation of binary gas mixtures of carbon dioxide and Nitrogen (90% N₂-10%CO₂), carbon dioxide and Helium (CO₂-He) on zeolite 13X. The flow pattern was described using axial dispersed plug flow model, while the mass transfer pattern was described using LDF approximation model. The PDE's in the mathematical model were solved numerically using method of orthogonal collection for six (6) finite elements, with three (3) collection

point per element, after which the evolving ODE's were solved using gPROMS. The following assumptions were made: Negligible change in temperature and concentration in radial direction, negligible pressure drop and non-isothermal heat effects. Adiabatic and non-adiabatic systems were considered. Langmuir equilibrium isotherm was assumed. The mathematical model gave a qualitative description of the breakthrough experiment for with good accuracy at the temperature break through point. However, the model gave results of lower accuracy for the energy balance in the system.

CO₂ mixture (with CH₄ and H₂)

Doong and Yang [186] described a mathematical model to describe Pressure Swing adsorption separation of CO₂ from a gas mixture of Carbon dioxide (CO₂), methane (CH₄) and Hydrogen (H₂); all of equal proportion by volume. Their adsorption medium (adsorbent) was activated carbon. The flow pattern was described using plug flow model, while the mass transfer pattern was described using local equilibrium model and pore diffusion model. The mathematical model was solved numerically using finite difference method and, by assuming: Negligible radial variation in concentration, negligible pressure drop within bed, and non-isothermal heat effects. A Langmuir-Freundlich equilibrium isotherm was assumed. It was concluded that Knudsen and surface tension model produced results close to the experimental data used, while the ILE model produce results with lower CO₂ concentration with longer break through. They suggested that the latter result may be due to the assumption of infinite rate of pore diffusion.

CO₂ (with Air)

Diagne et. al [187] worked on a mathematical model to describe Pressure Swing Adsorption separation of CO₂ from air using molecular sieves zeolite (13X, 5X, and 4A). The flow pattern was described using plug flow model, while the mass transfer pattern was described using LDF approximation model. The set of equations in the mathematical model was solved by Euler's method. The following assumptions were made: Negligible radial variation in concentration, negligible pressure drop within bed, trace system, and isothermal heat effects. A Langmuir equilibrium isotherm was assumed. The mathematical model gave a qualitative description of the breakthrough experiment and temperature curves. The model showed good agreement with experimental data except for points at which ratio of feed/lean flow rate was less than 2.

CO₂ mixture (CO₂, CO, H₂, and CH₄)

Lee et. al [188] obtained a mathematical model to predict the Pressure Swing Adsorption separation of coke oven gas mixture (i.e. CO₂, CO, N₂, and CH₄) on two different adsorbents (Zeolite 5A and activated carbon). The adsorption bed was made in layers. The flow pattern was described using axial disperse plug flow model, while the mass transfer pattern was described using LDF approximation model. The mass transfer coefficient was lumped. The PDE's in the mathematical model were solved numerically using second order finite difference method (for second order space derivatives) and second order backward difference method (for first order space derivatives). The following assumptions were made: Negligible radial variation in temperature and concentration, thermal equilibrium between gas and solid phase. Effect of pressure drop along bed was taken into account

using the Ergun equation. A Langmuir-Freundlich isotherm equilibrium isotherm was assumed. The LDF model successfully predicted the adsorption and desorption steps and gave good simulation results that agreed with experimental data. It has been reported that the experimental data gave higher gas recovery with error range of 4% [168].

The pressure swing adsorption separation of cracked gas mixture (i.e. CO₂, CO, H₂, and CH₄) on two different adsorbents (Zeolite 5A and activated carbon) was predicted by [189].

In their mathematical model, the adsorption bed was made in layers. The flow pattern was described using axial disperse plug flow model, while the mass transfer pattern was described using LDF approximation model. The mass transfer coefficient was lumped. The PDE's in the mathematical model were solved numerically using backward difference method, after which the evolving ODE's were solved using GEAR method. The following assumptions were made: Negligible radial variation in temperature and concentration, thermal equilibrium between gas and solid phase, negligible pressure drop in axial direction within bed and non-isothermal heat effects. A Langmuir equilibrium isotherm was assumed. The results predicted by the LDF model for a single component system was close to experimental results of adsorption and desorption curves. The model gave a good prediction of the experimental data; however, the model had a limitation of lower residual gas temperature than the one gotten from the experiment. This is due to the neglecting of heat loss to the column end.

CO₂ mixture (with N₂ and O₂)

Choi et. al [159] worked on a mathematical model to describe Pressure Swing Adsorption separation of CO₂ from flue gas (83% N₂, 13% CO₂ and 4% O₂) using zeolite 13X. The

flow pattern was described using plug flow model, while the mass transfer pattern was described using LDF approximation model. The set of equations in the mathematical model was solved by Euler's method. The following assumptions were made: Negligible radial variation in temperature and concentration, negligible pressure drop within bed, and non-isothermal heat effects. An extended Langmuir equilibrium isotherm was assumed. The mathematical model was solved using MATLAB function which was operated on the principle of Sequential Quadratic Programming (SQP). The model gave a close agreement with experimental data, with little differences in the temperature data. Kaguei and Wakao [190] described a mathematical model while working on the theoretical and experimental research on CCS. The adsorption system was a column packed with activated carbon. The flow pattern was described using axial dispersed plug flow model, while the mass transfer pattern was described using pore diffusion model. The mathematical model was solved analytically using Laplace domain, by assuming: semi-infinite column Negligible radial variation in temperature and concentration within column, uniform temperature over column cross section, negligible pressure drop in the axial direction, fixed column wall temperature, and non-isothermal heat effects. A linear equilibrium isotherm was assumed. Their model gave a good prediction of thermal waves at different axial locations.

In order to predict the adsorption separation of CO₂ and CO on activated carbon, Hwang and Lee [191] obtained a mathematical model in which, the flow pattern was described using axial disperse plug flow model. The mass transfer pattern was described using LDF approximation model. The mass transfer coefficient was made pressure dependent. The PDE's in the mathematical model was solved numerically using the method of orthogonal

collection, after which the evolving ODE's were solved using DGEAR through a Gear's stiff method in different orders and step size. The following assumptions were made: Negligible radial variation in concentration, negligible pressure drop within bed and isothermal heat effects. A Langmuir equilibrium isotherm was assumed. The results predicted by the LDF model for a single component system was close to experimental results of adsorption and desorption curves. The mass transfer coefficient and the assumptions gave good results, close the experimental data for adsorption and desorption for multi-component sorption system. Table 2.6 provides detailed review of Adsorption Numerical models including mass isotherm type and mass transfer models. The table gives a detailed account of the mathematical models used in previous studies. The table presents the type of the two most important properties used in the models; namely the adsorption isotherm model and the mass transfer model. Other important consideration such as the heat/energy transfer as well as the pressure drop models are also reviewed up to 2014.

Table 2.6 Detailed review of adsorption numerical models including mass isotherm type and mass transfer models.

#	Year	Authors' names	Application type	Model Dimension	Mass transfer model	Isotherm Type	Energy Model	Pressure and Velocity model	Solution Type
1	1974	Carter and Husain [192]	Modelling of adsorption of Carbon dioxide and water vapour on molecular sieve.	1-D, transient	From experimental data.	Langmuir isotherm.	Isothermal.	Negligible pressure drop.	Numerical solution on Fortran.

2	1989	Kumar [174]	Modelling of blow down of adsorption of CO ₂ from gaseous mixture of; CO ₂ /H ₂ CO ₂ /CH ₄ CO ₂ /N ₂ on Zeolite 5A and BPL carbon by PSA.	1-D, transient .	Local equilibrium model.	Langmuir isotherm.	Non-Isothermal. Adiabatic system Negligible radial temperature gradient.	Negligible pressure gradient across adsorption bed. Flow behaviour: Plug flow	Numerical solution. Finite difference method with the use of IBM 370/165.
3	1994	Hwang and Lee [191]	Modelling of adsorption and desorption of gaseous mixture of CO ₂ and CO on activated carbon by breakthrough experiment.	1-D, transient .	LDF approximation model.	Langmuir isotherm.	Isothermal. Temperature of column wall, adsorbent and gas were all accounted for.	Negligible pressure gradient across adsorption bed. Flow behaviour: Axial dispersed plug flow	Numerical solution with the use of DGEAR commercial code.
4	1995	Chue et. al [22]	Modelling of the adsorption of CO ₂ from CO ₂ /N ₂ mixture on Zeolite 13X and activated carbon by PSA.	1-D, transient .	Adsorbed concentration by IAS model.	Langmuir isotherm.	Non-isothermal. Adiabatic. Thermal equilibrium between gas and solid phase.	Negligible pressure drop in bed. Flow behaviour: Axial dispersed plug flow
5.	1995	Hwang et. al [183]	Modelling of adsorption of gaseous mixture of CO ₂ and CO on activated carbon by breakthrough experiment.	1-D, transient .	LDF approximation model. Lumped mass transfer coefficient.	Extended Langmuir isotherm.	Isothermal. Non-adiabatic and adiabatic systems. Temperature of column wall, adsorbent	Negligible pressure gradient across adsorption bed. Flow behaviour: Plug flow.	Numerical solution. Linear algebras were solved using DIVPAG commercial code while non-linear algebra equations were solved using

							and gas were all accounted for. Negligible radial temperature gradient.	Negligible radial velocity	DNEQNF commercial code.
6	1996	Diagne et. al [187]	Modelling of adsorption of CO ₂ from air by PSA on Zeolite (5A, 13X and 4A).	1-D, transient .	LDF approximation model.	Langmuir isotherm.	Isothermal	Negligible pressure drop. Flow behaviour: Ideal plug flow.	Euler's method.
7	2000	Ding and Alpay [193]	Modelling of adsorption and desorption of CO ₂ on hydrotalcite at high temperature.	1-D, transient .	LDF model based on pore diffusion.	Langmuir isotherm.	Non-isothermal. Negligible radial temperature gradient. Thermal equilibrium between fluid and particles.	Pressure distribution by Ergun's equation. Flow behaviour: Axial dispersed plug flow.	Numerical solution with the use of gPROMS commercial code.
8	2001	Takamura [194]	Modelling of CO ₂ adsorption from gaseous mixture of CO ₂ and N ₂ on Zeolites (Na-X and Na-A) .	1-D, transient .	LDF approximation model.	Langmuir isotherm.	Isothermal	Negligible pressure drop. Flow behaviour: Plug flow. Flow behaviour: Plug flow.	Discretisation of coupled PDEA equations in space and time. Final solution of ODE with variable time step.
9	2003	Choi et. al [159]	Modelling of CO ₂ adsorption from flue gas mixture containing 13% CO ₂ ,	1-D, transient .	LDF approximation model.	Extended Langmuir isotherm.	Non-isothermal. Adiabatic system.	Negligible pressure drop in radial direction.	Numerical solution with the use of MATLAB function.

			83% N ₂ and 4% O ₂ on zeolite 13X by break through experiment and PSA operation.				Negligible temperature gradient in radial direction.	Flow behaviour: Plug flow. Gas flow rate in bed is mainly affected by bed height	
10	2004	Chou and Chen [184]	Modelling of CO ₂ adsorption from flue gas mixture containing 20% CO ₂ and 80% N ₂ on zeolite 13X by VSA.	1-D, transient .	Local equilibrium model.	Extended Langmuir isotherm.	Non-isothermal. Negligible radial temperature gradient. Thermal equilibrium between fluid and particles.	Negligible pressure gradient. Flow behaviour: Axial dispersed plug flow.	Analytical + numerical solution. Solution of spatial derivatives by upwind difference. Solution of flow rates by cubic spline. Solution of temperature, concentration and adsorbed mass by integration with the use of LSODE from ODEPACK commercial code.
11	2004	Cavenati et. al [163]	Modelling of fixed bed adsorption of CO ₂ , CH ₄ and N ₂ on Zeolite 13X at high pressure by breakthrough experiment.	Experimental measurement.	Toth Isotherm and Multisite Langmuir isotherm.	Isothermal	Experimental measurement.	Numerical solution to solve for mass deposited in adsorbent using MATLAB commercial code.
12	2005	Cavenati et. al [181]	Modelling of fixed bed adsorption of CO ₂ from a gaseous mixture of 45% CO ₂ and 55% CH ₄ .	1-D, transient .	A double LDF approximation model.	Multisite Langmuir isotherm	Non-isothermal. Negligible radial temperature gradient.	Pressure distribution by Ergun's equation. Flow behaviour:	Numerical solution with the use of gPROMS commercial code.

			on carbon molecular sieve 3K by PSA					Axial dispersed plug flow.	
13	2005	Ahn and Brandani [182]	Modelling of fixed bed adsorption and desorption of CO ₂ on Carbon Monoliths by break through experiment.	1-D, transient .	LDF approximation model.	Langmuir isotherm.	Isothermal.	Relationship between average velocity and average pressure drop was estimated with the use of equation by Cornish 1928. Flow behaviour: Axial dispersed plug flow.	Numerical solution with the use of gPROMS commercial code.
14	2006	Cavenati et. al [195]	Modelling of fixed bed adsorption of CO ₂ from a gaseous mixture of 20% CO ₂ / 60% CH ₄ / and 20% N ₂ on zeolite 13X by Layered Pressure Swing Adsorption (LPS).	1-D, transient .	Bi-LDF model.	Multicomponent extension of multisite Langmuir.	Non - Isothermal. Temperature of column wall, adsorbent and gas were all accounted for. Negligible radial temperature gradient.	Pressure distribution by Ergun's equation. Flow behaviour: Axial dispersed plug flow.	Numerical solution with the use of gPROMS.
15	2006	Moreira et. al [196]	Modelling of fixed bed adsorption of Helium diluted CO ₂ on hydrotalcite (Al-Mg).	1-D, transient .	LDF approximation model. Calculation of mass transfer coefficient by theoretical correlations.	Langmuir isotherm.	Isothermal.	Negligible pressure drop. Flow behaviour: Axial dispersed plug flow.	Numerical with the use of PDECOL in FORTRAN commercial code.

16	2006, 2007	Delgado [175, 176]	Modelling of fixed bed adsorption of CO ₂ from gaseous mixture of; CO ₂ /He CO ₂ /CH ₄ CO ₂ /N ₂ on Silicalite pellets, sepiolite, and resin using break through experiment .	1-D transient .	LDF approximation model. Lumped mass transfer coefficient.	Extended Langmuir isotherm.	Non-isothermal. Negligible radial temperature gradient.	Pressure distribution by Ergun's equation. Pressure variation in time and space. Flow behaviour: Axial dispersed plug flow.	Numerical solution by PDECOL commercial code.
17	2009, 2010 and 2011	Dantas [132, 165, 197]	Fixed bed adsorption of gaseous mixture of; CO ₂ /N ₂ and CO ₂ /He on zeolites 13X and activated carbon by break through experiment and PSA.	1-D, transient .	LDF approximation model. Lumped mass transfer coefficient.	Toth Isotherm.	Non-Isothermal. Adiabatic and non-adiabatic system. Model accounted for Heat transfer in gas, solid and wall.	Pressure distribution by Ergun's equation. Axial dispersed plug flow.	Numerical solution using gPROMS commercial code.
18	2010	Biswas et. al [198]	Modelling of adsorption separation of gaseous mixture of CO, CH ₄ , H ₂ , CO ₂ on Zeolite 5A and activated carbon.	1-D, transient .	LDF model. Lumped mass transfer coefficient.	Multisite Langmuir model.	Isothermal. Assuming temperature of wall, gas phase and adsorbent are equal.	Pressure distribution by Ergun's equation. Flow behaviour: Axial dispersed plug flow.	Discretisation by Newton based approach. Algebraic solution.

19	2010	Agarwal [199]	Fixed bed adsorption of CO ₂ from gaseous mixture of CO ₂ /N ₂ , 45% CO ₂ /55% H ₂ by PSA.	1-D, transient .	LDF approximation model. Lumped mass transfer coefficient.	Dual site Langmuir isotherm.	Temperature equilibrium between gas phase adsorbent. Constant column wall temperature	Pressure distribution by Ergun's equation. Flow behaviour: Axial dispersed plug flow..	Numerical solution with the use of interior point NPL solver.
20	2011	Krishna and van Baten [23]	Modelling of PSA performance and break through characteristics of zeolites (MFI, JBW, AFX, NaX) and MOFs (MgMOF-74, MOF-177, CuBTri-mmen) for gaseous mixture of CO ₂ /N ₂ .	1-D, transient	Isotherm.	Negligible pressure drop. Assumed flow behaviour: Plug flow.	Molecular simulation with the use of Configuration-Bias Monte Carlo (CBMS).
21	2012	Casas et. al [200]	Fixed bed adsorption of CO ₂ from gaseous mixture of CO ₂ /H ₂ on activated carbon by break through experiment.	1-D, transient .	LDF model. Lumped mass transfer coefficient.	Langmuir and Sip isotherms.	Thermal equilibrium between gas stream and adsorbent. Column wall temperature is accounted for separately.	Pressure distribution by Ergun's equation. Flow behaviour: Plug flow.	Finite volume method and time integration on IMSL DIVPAG commercial package using Gear's method.
22	2012	Mulgund math et. al [185]	Fixed bed adsorption of CO ₂ from gaseous mixture of 10% CO ₂ /90% N ₂ on Ceca 13X by break through experiment.	1-D, transient .	LDF approximation model for external fluid film mass transfer.	Langmuir isotherm.	Non-Isothermal. Temperature of column wall, adsorbent	Negligible pressure drop. Flow behaviour: Axial dispersed plug flow.

							and gas. were all accounted for.		
23	2013	Casas et. al [164]	Mathematical modelling of CO ₂ adsorption from CO ₂ /H ₂ mixture in MOF and UiO-67/MCM-41 by PSA and break through experiment.	1-D, transient .	Mass transfer coefficient determined by fitting of experimental data measured in the range of interest.	Langmuir isotherm.	Non-Isothermal. Adiabatic. Model accounted for Heat transfer in gas, solid and wall. Isotheric heat of adsorption and heat capacities of the fluid and the solid phase.	Pressure distribution by Ergun's equation.	Integration via Gear's method with the use of IMSL DIVPAG (Fortran) commercial code.
24	2013	Sabouni et. al [138]	Modelling of adsorption of CO ₂ From in CPM-5 by breakthrough experiment.	1-D, transient .	Mass transfer coefficient determined by fitting of experimental data.	Langmuir-Freundlich isotherm.	Isothermal.	Negligible pressure drop through column. Constant gas velocity through column.	Numerical solution with the use of COMSOL.
25	2013	Ribeiro et. al [162]	Modelling of CO ₂ adsorption from flue gas by a mixture of Activated carbon honeycomb monolith and Zeolite 13X hybrid system by Electrical Swing Adsorption (ESA).	1-D, transient .	Two different LDF models; one for micro pores and the other for macro pores. Lumped mass transfer parameter for meso pores and micro pores; obtained from Bosanquet equation.	Multisite Langmuir model.	Temperature equilibrium between the solid phases. Negligible temperature gradient in adsorbent.	Pressure distribution by Ergun's equation. Assumed flow behaviour: Axial plug flow.	Numerical solution with the use of gPROMS commercial code.

26	2014	Krishna murthy et. al [201]	Modelling of CO ₂ adsorption from dry flue gas in Zeochem zeolite 13X by break through experiment and VSA.	1-D, transient .	LDF approximation model.	Extended dual site Langmuir model.	Non-Isothermal.	Non Isobaric. Pressure distribution by Darcy's equation.	Numerical solution by stiff ODE solver; ode23s in MATLAB commercial code.

Most of the modelling studies indicated that the gases flow through the bed are treated as one dimensional flow (1D) and the effect of radial direction or 3D simulation still need modelling and performance optimizations investigations. Another point is that the available data obtained by experimental work as adsorption and thermal properties of adsorbent and adsorbate materials could only be used in the modelling to validate the simulation and investigate the adsorption process behaviour and its performance optimization. Therefore, the modelling is restricted by what has been performed by experimentation.

CHAPTER 3

RESEARCH METHODOLOGY

This section is concerned with experimental and simulation methods for CO₂ separation and storage. In the experimental part, the adsorbents, 13X and home-synthesized MOFs, are incorporated with multi-walled carbon nanotubes and characterized by PXRD, adsorption isotherms and breakthrough tests as well as adsorption cycling. In the modeling part, the CO₂ separation and storage numerical codes are developed by using User Define Function (UDF) hooked to Fluent program[202] in pursuit of presenting a multi-dimensional adsorption beds.

3.1 Experimental Methods

3.1.1 Synthesis/Preparation of the Adsorbents

Zeolite 13X

The samples were prepared by adding and mixing small quantities of multi-walled carbon nanotube (MWCNT) into zeolite 13X. The utilized 13X, a commercial adsorbent imported from SORBEAD INDIA as molecular sieve pellets (1.5 mm size), was grinded in order to be an appropriate powder form for consistently mixing with CNT (multi walled). Six samples were made by adding different percentages of MWCNT (0%, 0.1%, 0.25%, 0.5%, 0.75% and 1.5% by weight) to 13X and named as; 13X, XC1, XC2 ,XC3 , XC4 ,and XC5. The increase of MWCNT amounts makes the color of the composite darker as shown in

Figure 3.1. The particle size distribution has been also measured using Particles-Size Analyzer Model S3500.



Figure 3.1 Small samples of CNT/13X compounds.

Mg-MOF-74 synthesis

We have followed a successful procedure for synthesizing Mg-MOF-74 as described in [203]. Briefly, 0.337 g 2,5-dihydroxyterephthalic acid and 1.4 g $\text{Mg}(\text{NO}_3)_2 \cdot 6\text{H}_2\text{O}$ were dissolved in a solution of 135 mL dimethylformamide, 9 mL ethanol, and 9 mL water with sonication for 10 minutes. The resulting stock solution was decanted into twelve 50 mL bottles. The bottles were tightly capped and heated at 398 K for 26 hours. The mother liquor was then decanted, after which the products were washed with methanol, then left immersed in methanol. The products were combined to one bottle and exchanged into fresh methanol daily for 4 days. The activation process was carried out by evacuating the product to dryness and then heated under vacuum at 523 K for 6 hrs.

The MWCNT/Mg-MOF-74 sample designations were based according to the weight percentage of MWCNTs which was physically mixed with Mg-MOF-74 as: Mg-MOF-74, 0.1 wt% MWCNT/Mg-MOF-74, 0.25 wt% MWCNT/ Mg-MOF-74, 0.5 wt% MWCNT/ Mg-MOF-74, and 0.75 wt% MWCNT/ Mg-MOF-74, 1 wt% MWCNT/Mg-MOF-74 and

1.5 wt% MWCNT/Mg-MOF-74 and shortly named as Mg-MOF-74, MFC1, MFC2, MFC3, MFC4, MFC5, and MFC6, respectively.

MIL-100(Fe) synthesis

The synthesis of MIL-100(Fe) were performed in accordance with a previously reported procedure [204]. We firstly dissolved $\text{Fe}(\text{NO}_3)_3 \cdot 9\text{H}_2\text{O}$ (4.04 g, 0.01 mol) in de-ionized water (50.2 mL, 2.8 mol) and the mixture was completely put in a 125 ml Teflon-liner containing BTC (1.4097 g, 0.00671 mol). After that, the Teflon-liner was tightly sealed inside a stainless steel autoclave and kept at 383 K for 14 h. After heating, the autoclave was slowly cooled to ambient temperature, after which the “as-synthesized” dark orange solid was recovered using a centrifuge that was operated at 8000 rpm for about 45 minutes. The as-synthesized MIL-100(Fe) was washed with copious amounts of water and ethanol and finally with an aqueous NH_4F solution for removing any unreacted species. Specifically, the dried solid was first immersed in deionized water (60 mL per 1 g of solid) and the resulting suspension was stirred at 70 °C for 5 h. Again, the suspension was centrifuged and the wash process was repeated using ethanol (60 mL) at 65 °C for 3 h. This two-step purification was repeated until the decanted solvent following centrifugation became completely colorless, after which the solid was immersed in a 700 ml aqueous NH_4F solution and stirred at 70 °C for 5 h. The suspension was again centrifuged and the solid was washed 5 times DI water at 60 °C, and finally dried in air at 75 °C for 2 days followed by 95 °C for 2 days.

The incorporation of MWCNT in the MIL-100(Fe) has produced MIL-100(Fe), 0.1 wt% MWCNT/MIL-100(Fe), 0.25 wt% MWCNT/MIL-100(Fe), and 0.5 wt% MWCNT/ MIL-100(Fe) which were named as MIL-100(Fe), MMC1, MMC2, and MMC3, respectively.

MIL-101(Cr) synthesis

For the synthesis of MIL-101(Cr), the method proposed by Férey et al. [205] has been adopted. Briefly, 4 g chromium nitrate nonahydrate ($\text{Cr}(\text{NO}_3)_3 \cdot 9\text{H}_2\text{O}$), 1.66 g 1,3 benzenedicarboxylic acid (BDC) and 47.4 ml de-ionized water were added to a 125 ml Teflon-liner which was sealed inside a stainless steel autoclave and kept at 220°C for 8 hours. The autoclave was cooled slowly to room temperature, after which the light green solid was recovered using centrifugation at 8000 RPM for 45 minutes. In order to remove the guest molecules, the as-synthesized MIL-101(Cr) was washed twice with 90 ml deionized water and further purified 5 times using an 80% aqueous solution of ethanol, till the decanted solvent following centrifugation became completely colorless. The green solid was then immersed in 30mM aqueous NH_4F solution and stirred at 60°C for 10 hours (1g: 150ml). The suspension was centrifuged, after which the solid was washed 5 times with deionized water at 60°C. The green solid was then washed three times with 70 ml DMF, and 5 times with 75 ml deionized water, and finally dried in air at 75°C for 2 days and 95°C for 2 days.

The first step involved in the synthesis of MWCNT/MIL-101(Cr) composites is the acid-functionalization of MWCNTs in order to attach negatively charged carboxyl (COOH^-) groups on their sidewalls. Typically, 3 g MWCNTs were first dispersed in 200 ml concentrated HNO_3 using ultrasonication. The mixture was then transferred to a 250 ml round bottom flask equipped with a condenser and was refluxed at 120°C for 48 hours. After cooling to room temperature, the mixture was diluted with 500 ml deionized water and then vacuum filtered through a 2.5 μm polymeric membrane. The filtered cake was washed repeatedly with deionized water till the pH of the filtrate reached approximately 5.

The filtered cake was dried at 80°C in air for 24 hours and ground into a fine powder. For the synthesis of MWCNT/MIL-101(Cr) composites, 4 g $\text{Cr}(\text{NO}_3)_3 \cdot 9\text{H}_2\text{O}$ and a pre-determined amount of functionalized MWCNTs (60 mg, 120 mg, 180 mg, and 240 mg) were mixed thoroughly in solid-state until a uniform color of the mixture was achieved. 5 ml of de-ionized water was then added periodically to the mixture and the resulting paste was ultrasonicated till the water was completely vaporized. The dried paste, along with 1.66 g BDC and 47.4 ml de-ionized water, were then transferred completely to a 125 ml Teflon-lined autoclave which was kept at 220°C for 8 hours. The post-synthesis activation procedure was exactly the same as the one adopted for unmodified MIL-101(Cr).

The weight fractions of MWCNTs in each of the synthesized MWCNT/MIL-101(Cr) composites were determined using Elemental Analysis (EA). Sample designations were based according to the weight percentage of MWCNTs in MIL-101(Cr) as: MIL-101(Cr), 2 wt% MWCNT/MIL-101(Cr), 4 wt% MWCNT/MIL-101(Cr), 6 wt% MWCNT/MIL-101(Cr), and 8 wt% MWCNT/MIL-101(Cr).

3.1.2 X-ray Powder Diffraction Analysis

Powder X-Ray diffraction patterns for 13X and MWCNT/Mg-MOF-74 were obtained and collected using a Bruker D8-Advance Diffractometer ($\text{Cu K}_\alpha \lambda=1.54056 \text{ \AA}$) with an operating power of 30 kV/30 mA. The data were recorded by the step-counting method (step = 0.02°, time = 3 s) in the range $2\theta = 3\text{-}45^\circ$ at ambient temperature of 298 K. For MIL-100(Fe) and MIL-101(Cr), the diffraction data were collected between 3 and 45° (2θ) with a total scan time of 3 hours

3.1.3 Gas Sorption Measurements

The first step in the physisorption measurements for CO₂ and N₂ is the sample degassing in order to remove any guest molecules within the pores of each material. Typically, 50-200 mg of each sample was transferred to pre-weighed empty sample cell with a 9 mm diameter and degassing was conducted at 270 °C under vacuum for 24 hours for MWCNT/13X, 150°C under vacuum for about 17 hours for MWCNT/MIL-100(Fe) and MWCNT/MIL-101(Cr), and 220°C under vacuum during about 5 hours for MWCNT/Mg-MOF-74 using an Autosorb degasser equipped with a turbo molecular vacuum pump and controlled heat jackets (Quantachrome Instruments, Inc.). Nitrogen adsorption isotherms at 77 K were firstly recorded to estimate the *Brunauer–Emmett–Teller* (BET) specific surface area (S_{BET}), average pore radius, and total pore volume. The interesting equilibrium adsorption isotherms for CO₂ at different temperatures (273, 298 and 313 K) and for N₂ at ambient temperature (298 K) were recorded. The CO₂ heat of adsorption was evaluated using the adsorption isotherms measured at 273, 298 and 313 K in accordance with the Clausius-Clapeyron equation using a built-in Quantachrome ASiQwin software installed within the Autosorb system.

3.1.4 Binary gas (CO₂+N₂) and Ternary Gas (CO₂+N₂+H₂O) Breakthrough

Experiments

The gas separation capabilities of all the samples were examined using a developed dynamic CO₂/N₂ breakthrough setup as shown in Figure 3.2. The system consists of a fixed adsorbent bed column, feed CO₂ and N₂ cylinders (for simulating a flue gas). The system included two gas regulators with dual pressure gauges and output control valves, two mass

flow controllers (one was calibrated for CO₂ flow and the other was calibrated for N₂), two check valves (to control the flow in one direction) and a bypass line (for calibrating the mass spectrometer from the feed gas mixture). The system also comprised a bourdon absolute pressure, a mass spectrometer (to analyze the output concentration of effluent gases from the bed), heater jacket and vacuum pump (for desorption process to regenerate the adsorbent) and some valves and tubes to control the flow. All pipes and fittings were made of stainless steel to keep off corrosion contaminants. Moreover, a water humidifier was added to validate a numerical simulation in pertinent to a humid flue gas.

The size of the fixed bed for different adsorbents was:

- Inner diameter = 9 mm, Outer diameter = 13 mm and Length = 20 cm filled with CNT/13X compound (about 7 g).
- Inner diameter = 4 mm, Outer diameter = 6 mm and Length = 7 cm) filled with MWCNT/Mg-MOF-74 composite (about 0.26 g), or MWCNT/MIL-100(Fe) composite (about 0.74 g).
- Inner diameter = 4 mm, Outer diameter = 6 mm and Length = 15 cm) filled with the MWCNT/ MIL-101(Cr) composite (about 0.3-0.5 g)

Firstly, the samples were pre-treated by heating (at about 540 K for 13X composites, 423 K for MWCNT/Mg-MOF-74, MIL-101(Cr), and MIL-100(Fe)) under vacuum for 24 hours to remove trapped gases and moisture inside the adsorbent. The experiments were performed at ambient conditions (297 K and 101.3 kPa). The mixed gas flow rate was 100 sccm (20% CO₂ and 80% N₂) for 13X and 10 sccm for MOFs (20% CO₂ and 80% N₂ for Mg-MOF-74 and MIL-101(Cr) and 15% CO₂ and 85% N₂ (vol. %) for MIL-100(Fe)).

A certain amounts of CO₂ and N₂ are allowed to pass mass flowmeter. Then, they are mixing during passing through the mixing tube. After that, the gas mixture feeds the adsorbent bed. The gas exists from the bed is detected by mass spectrometer in molar base. If we need to add some amount of water vapor, the valves of water source are opened to enable the mixture gas (CO₂+N₂) to be wet before feeding the adsorbent bed. The amounts of water vapor added depends on the temperature (ambient temperature) and amount of gas mixture (CO₂+N₂) that passes through the water wet bubbler.

During desorption process, the valve located before the bed is closed while the vacuum pump is switched on. Moreover, a heater jacket could be cover the bed to raise the temperature of the adsorbent material for more evacuating the bed from adsorbed gasses.

The complete breakthrough of CO₂ and N₂ was indicated by the downstream gas composition reaching that of the feed gas. The carbon dioxide adsorption capacity (q_{CO_2}) is estimated using Eq. 1.

$$q_{CO_2} = \frac{\left(\frac{x_{CO_2} Q_F t_{ss} P_s}{R T_s} - \frac{x_{CO_2} V \varepsilon P_{ac}}{R T_{ac}} \right)}{m} \quad (1)$$

where x_{CO_2} is the feed molar fraction of carbon dioxide, Q_F is the feed volumetric flow rate at standard conditions ($m^3 s^{-1}$), V is the bed volume (m^3). P_s and T_s are the pressure and temperature at standard conditions (P in Pa and T in K). P_{ac} and T_{ac} are the pressure and temperature at actual conditions (P in Pa and T in K). R is the gas constant (8.314 J/mol.K), ε is the total bed porosity, m is the mass of the adsorbent (kg), and t_{ss} is the stoichiometric time, which is integrated from the breakthrough curve using the equation below (Eq. 2):

$$tss = \int_0^{\infty} \left(1 - \frac{C(t)}{C_0}\right) dt \quad (2)$$

and $C(t)/C_0$ (C_{outlet}/C_{inlet}) is the concentration ratio of the outlet CO_2 concentration at specific time (t) over the inlet CO_2 concentration.

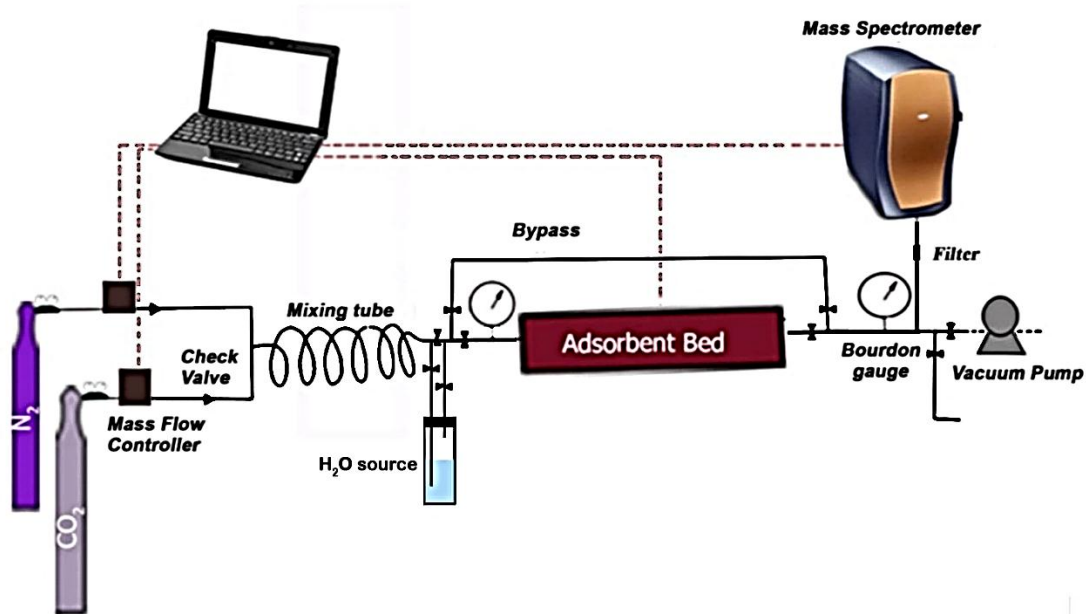


Figure 3.2 Schematic diagram of carbon dioxide adsorption capture breakthrough setup.

3.1.5 Thermal Properties of Adsorbents

The thermal properties including thermal conductivity and heat capacity were so difficult to be measured in our lab. The available systems could measure thermal properties for solid or liquid samples but inaccurate for powders. Therefore, the enhancing CO_2 uptake was referred to improving thermal properties due to dissipation heat quickly.

3.1.6 CO₂ Adsorption Cycling by TSA, and PSA (VSA)

CO₂ cycling adsorption/desorption measurements were recorded using a Dynamic Vapor Sorption Analyzer (DVS Vacuum, Surface Measurement Systems Ltd, London, UK). The samples (13X, XC3, Mg-MOF-74, and MFC4) were firstly pre-treated under vacuum at 250 °C (for 13X, XC3) and 150 °C (for Mg-MOF-74, MFC4) for 6 hrs. prior to commencing the cycling. Thirteen successive cycles were recorded for each sample by TSA (adsorption 25°C/ desorption 120 °C at 101.3 kPa) and VSA (adsorption 101.3 kPa/ desorption under vacuum (~ 2 Pa) at 25 °C) as well as TVSA (adsorption 25 °C and 101.3 kPa/ desorption 120 °C under vacuum (~ 2 Pa)).

3.2 Numerical Modeling Methods

The simulation model is based on the momentum, mass and energy conservation equations. The CFD model has been developed using User Define Function (UDF, written in C language) hooked to Ansys-Fluent software to estimate gases adsorption quantities and adjusting the source terms of mass, momentum and energy equations.

In this context, we extended the models by treating two/three-dimensional behavior instead of one-dimensional behavior.

For all studied cases, the following assumptions are adopted:

- the gas phase obeys ideal gas law,
- the flow is unsteady and laminar,
- the porous media is homogenous,
- the physical properties of the adsorbents are constant, and
- the Linear Driving Force (LDF) model is used to account for the mass transfer rate during the adsorption process.

In addition, the isotherms were accurately fitted from the experimental ones according to the appropriate approaches like Toth, Dual-site Langmuir, and Dubnin-Astakhov.

3.2.1 Mass Conservation Equation

The mass conservation equation calculates the local mass fraction of each species through the solution of the convection-diffusion equation of the all species as the following:

$$\varepsilon \frac{\partial(\rho y_i)}{\partial t} + \nabla \cdot (\rho \vec{v} y_i) = -\nabla \cdot (-\varepsilon \rho D_{disp,i} \nabla y_i) - (1 - \varepsilon) \rho_p M_i \frac{\partial q_i}{\partial t} \quad (3)$$

where ρ (kg m^{-3}) is the gas density, y_i is the mass fraction of species i (CO_2 , N_2 , H_2O , and so on), \vec{v} (m s^{-1}) is the velocity vector, ε is the bed porosity, $D_{disp,i}$ ($\text{m}^2 \text{s}^{-1}$) is the mass dispersion coefficient for species i , M_i (kg mol^{-1}) is the molecular weight of species i , q_i (mmol/g) is the adsorbent amount of component i , and $t(\text{s})$ is the time.

The overall mass balance is

$$\varepsilon \frac{\partial(\rho)}{\partial t} + \nabla \cdot (\rho \vec{v}) = -(1 - \varepsilon) \rho_p \sum_i M_i \frac{\partial q_i}{\partial t} \quad (4)$$

3.2.2 Momentum Conservation Equation

The momentum equation of the gases flow can be expressed as:

$$\varepsilon \frac{\partial(\rho \vec{v})}{\partial t} + \nabla \cdot (\rho \vec{v} \vec{v}) = -\nabla P + \nabla \cdot \bar{\tau} + \rho \vec{g} + S \quad (3)$$

where P (Pa) is the operating pressure, $\bar{\tau}$ (N m^{-2}) is the stress tensor, \vec{g} (m s^{-2}) is the gravity acceleration vector, and S (N m^{-3}) is the momentum source term in the porous media. Its component in i -direction is calculated from Ergun equation including inertia and viscous resistances as:

$$S_i = -\left(\frac{\mu}{\kappa} v_i + C_2 \frac{1}{2} \rho |\vec{v}| v_i\right) \quad (4)$$

where μ (Pa s) is the gas dynamic viscosity, $1/\kappa$ (m^{-2}) is the porous media viscous resistance, C_2 (m^{-1}) is the inertial resistance, $|\vec{v}|$ is the value of the velocity vector, and v_i is the velocity component in i -direction.

3.2.3 Energy Conservation Equation

The energy equation for CO₂ separation and storage shows the balance between the energy stored in the adsorbent bed and the change in energy due to convective flow, pressure work, thermal diffusion and advection as well as the energy released/consumed as a consequence of adsorption/desorption processes. It could be written as:

$$\begin{aligned} \frac{\partial}{\partial t} [\varepsilon \rho E_g + (1 - \varepsilon) \rho_p E_s] + \nabla \cdot [\vec{v} (\rho E_g + P)] \\ = \nabla \cdot \left[k_{\text{eff}} \nabla T - \sum_i h_i \vec{J}_i + \bar{\tau} \cdot \vec{v} \right] + (1 - \varepsilon) \rho_p \sum_i \Delta H_i \frac{\partial q_i}{\partial t} \quad (5) \end{aligned}$$

where E_g (J m⁻³) is the total gas energy, E_s (J m⁻³) is the total adsorbent energy, ΔH (J mol⁻¹) is the heat of adsorption which is different from material to another and sometimes also varies with variation of gas adsorbed amounts, T (K) is the equilibrium temperature, h_i (J kg⁻¹) is the sensible enthalpy ($h = \sum_i y_i h_i$), and \vec{J}_i (kg m⁻² s⁻¹) is the diffusion flux of the gas component i .

The parameter k_{eff} is the effective conductivity of the adsorbent bed and can be expressed as:

$$k_{\text{eff}} = \varepsilon k_g + (1 - \varepsilon) k_s \quad (6)$$

where k_g and k_s (W m⁻¹ K⁻¹) are the thermal conductivity of the gas mixture and adsorbent, respectively.

For the wall metal, the energy equation through the walls depends upon the balance of heat stored in the wall and the heat diffusion through it as follows.

$$\frac{\partial}{\partial t} (\rho_w C_w T_w) = \nabla(k_w \nabla T_w) \quad (7)$$

where ρ_w (kg m^{-3}) is the wall density, C_w ($\text{J kg}^{-1} \text{K}^{-1}$) is the wall heat capacity, T_w (K) is the local temperature of the wall, and k_w ($\text{W m}^{-1} \text{K}^{-1}$) is the thermal conductivity of the wall material.

3.2.4 Adsorption Isotherm and Kinetics Models

The equilibrium adsorption isotherms are presented by different models according to the accuracy of the fitting from the experimental isotherms. Toth and Dual-site Langmuir models are exploited for CO_2 breakthrough and pressure/temperature swing adsorptions while Dubnin-Astakhov model is used for CO_2 storage.

Toth model:

$$q_i^* = \frac{q_{m,i} K_{eq,i} y_i P}{\left(1 + (K_{eq,i} y_i P)^{ni}\right)^{\left(\frac{1}{ni}\right)}} \quad (8)$$

where $q_{m,i}$ (mmol g^{-1}) is the maximum adsorbed amount of species i , $K_{eq,i}$ (Pa^{-1}) is an adsorption constant which can be calculated as a function of temperature (Eq. (9)), and ni is the adsorption constant.

$$(K_{eq,i} = k_0 e^{-\left(\frac{\Delta H}{RT}\right)}) \quad (9)$$

where k_0 (Pa^{-1}) is a temperature-independent constant.

Dual-site Langmuir model:

$$q_i^* = \frac{q_{m,i1} K_{eq,i1} y_i P}{1 + K_{eq,i1} y_i P} + \frac{q_{m,i2} K_{eq,i2} y_i P}{1 + K_{eq,i2} y_i P} \quad (10)$$

where $q_{m,i,1}$ and $q_{m,i,2}$ (mmol g⁻¹) are to present the maximum adsorbed amount of species i , $K_{eq,i,1}$ and $K_{eq,i,2}$ (Pa⁻¹) are adsorption constants that depend on the heat of adsorption and adsorbent temperature.

Dubnin-Astakhov model:

$$q_i^* = q_{m,i} e^{-\left[\frac{RT}{\alpha i + \beta i T} \ln\left(\frac{P_0}{P}\right)\right]^{ni}} \quad (11)$$

where R (J mol⁻¹ K⁻¹) is the universal gas constant, αi (J mol⁻¹) and βi (J mol⁻¹ K⁻¹) are enthalpic and entropic factors, and P_0 (Pa) is the saturation pressure of the pure gas at ambient temperature.

The adsorption kinetics are evaluated by linear driving force (LDF) model as follows.

$$\frac{\partial q_i}{\partial t} = k_{L,i} (q_i^* - q_i) \quad (12)$$

The parameter q_i (mmol g⁻¹) presents the actual adsorbed amount while q_i^* (mmol g⁻¹) is the equilibrium adsorbed amounts. $k_{L,i}$ (s⁻¹) is the adsorption time constant; it is estimated from complex diffusion and concentrations of the species. It is expressed by the film, macroporous, microporous resistances of the gases passing porous materials as:

$$\frac{1}{k_{L,i}} = \frac{r_p q_{0,i}}{3 k_{f,i} C_{0,i}} + \frac{r_p^2 q_{0,i}}{15 \varepsilon_p D_{p,i} C_{0,i}} + \frac{r_c^2}{15 D_{c,i}} \quad (13)$$

where $q_{0,i}$ and $C_{0,i}$ (mol m⁻³) are the values of the concentrations at the solid and gas phases, respectively, r_p (m) is the adsorbent particle radius, ε_p is the particle porosity, and r_c is the adsorbent crystal radius. $k_{f,i}$, $D_{p,i}$ and $D_{c,i}$ are the film mass transfer coefficient, macroporous

diffusion coefficient, and microporous diffusion coefficient, respectively, for a component i . These three coefficients can be evaluated as the following procedure.

The film mass transfer is estimated from Sherwood number (Eq. 14).

$$Sh = \frac{k_{f,i} d_p}{D_{m,i}} = \begin{cases} 2 + 0.6 Re^{\frac{1}{2}} Sc_i^{\frac{1}{3}} & 0 \leq Re \leq 200 \\ 2 + 0.69 Re^{\frac{1}{2}} Sc_i^{\frac{1}{3}} & 20 \leq Re \leq 2000 \end{cases} \quad (14)$$

where d_p (m) is the adsorbent particle size, Sc is Schmidt number ($Sc_i = \frac{\mu}{\rho D_{m,i}}$), Re is Rylonds number $Re = \frac{\rho u d_p}{\mu}$, and $D_{m,i}$ ($m^2 s^{-1}$) is the diffusion coefficient. It, $D_{m,i}$, can be estimated from the molecular diffusion coefficient D_{ij} [206] of binary gases i and j as

$$D_{m,i} = \frac{1 - y_i}{\sum_{j,j \neq i} (y_j / D_{ij})} \quad (15)$$

and

$$D_{ij} = 0.00186 \frac{\left[T^3 \left(\frac{1}{M_i} + \frac{1}{M_j} \right) \right]^{1/2}}{P \sigma_{ij}^2 \Omega_{ij}} \quad (16)$$

where Ω_{ij} is the diffusion collision integral which presents the molecules interaction in the system, σ_{ij} (Å) is collection diameter of gases i and j . For obtain D_{ij} in $cm^2 s^{-1}$, T and P should be in K and bar, respectively.

$$\sigma_{ij} = \frac{1}{2} (\sigma_i + \sigma_j) \quad (17)$$

$$\Omega_{ij} = \frac{A}{B T_{ij}^*} + \frac{C}{\exp(D T_{ij}^*)} + \frac{E}{\exp(F T_{ij}^*)} + \frac{G}{\exp(H T_{ij}^*)} \quad (18)$$

where A, B, C, D, E, F, G, H are constants equal to 1.06036, 0.1561, 0.193, 0.47635, 1.03587, 1.52996, 1.76474, 3.89411, 1.76474, and 3.89411, respectively. The parameter

$T_{ij}^* = \frac{T}{\left(\frac{\varepsilon}{k_\beta}\right)_{ij}}$ and $\left(\frac{\varepsilon}{k_\beta}\right)_{ij} = \sqrt{\left(\frac{\varepsilon}{k_\beta}\right)_i \left(\frac{\varepsilon}{k_\beta}\right)_j}$. The values of σ_i and $\left(\frac{\varepsilon}{k_\beta}\right)_i$ for all

gases are provided by many books of mass transfer [206]. The parameter σ_i has values about 3.941, 3.789 and 2.641 for CO₂, N₂ and H₂O, whereas the values of $\left(\frac{\varepsilon}{k_\beta}\right)_i$ are 195.2, 71.4 and 809.1 for CO₂, N₂ and H₂O, respectively.

Another important parameter used to calculate the macroporous diffusion coefficient is Knudsen diffusion. It is significant when the mean free path of gas molecules is in the same order of adsorbent pore size due to the collision of the gas molecules with the pore walls. It is estimated by Eq. (19).

$$D_{k,i} = 9700 * r_{pore} \left[\frac{T}{M_i} \right]^{0.5} \quad (19)$$

The unit of this equation is cm²s⁻¹ if pore radius, r_{pore} , is taken by cm, T in K, M in g mol⁻¹.

Now the macroporous diffusion coefficient may be written as [206]:

$$D_{p,i} = \frac{\varepsilon}{\tau} \left[\frac{1}{\frac{1}{D_{k,i}} + \frac{1}{D_{m,i}}} \right] \quad (20)$$

where τ is tortuosity. Figure 3.3 explains these parameters in details

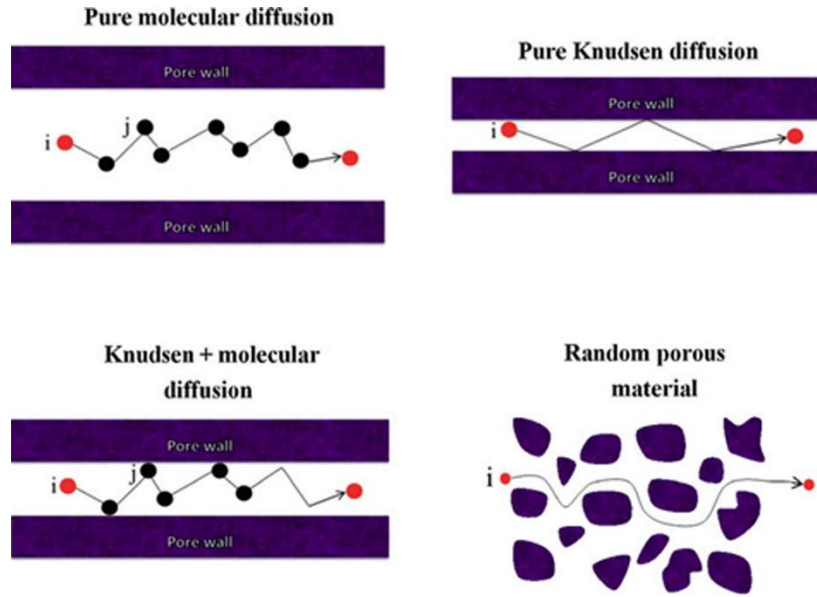


Figure 3.3 Types of macroporous diffusion [206].

The microporous diffusion coefficient $D_{c,i}$ is calculated from experimental kinetic curves. It depends on the adsorption kinetic energy, E (J mol^{-1}), which can be adopted to the Arrhenius equation.

$$D_{c,i} = A_o \exp\left(\frac{-E}{RT}\right) \quad (21)$$

where A_o ($\text{m}^2 \text{s}^{-1}$) is a pre-exponential constant.

3.2.5 General Boundary Condition

In this section, the general boundary conditions are formulated. The specific boundary condition for every case study will be explain later.

External walls

The heat transfer between the bed wall and the ambient can be expressed as

$$k_w \left(\frac{\partial T_w}{\partial n}\right)_w = h_{ext}(T_w - T_{amb}) + \epsilon\sigma(T_w^4 - T_{amb}^4) \quad (22)$$

where n (m) is the normal, h_{ext} ($\text{W m}^{-2} \text{K}^{-1}$) is the external heat transfer coefficient, ϵ is the thermal emissivity, σ is Steffen Boltzmann coefficient.

The heat transfer from the bed wall to the ambient relies on the heat transfer coefficient which may be calculated from Nusselt number using the following correlation [207]:

$$Nu = \frac{h_{ext} D_0}{k_{air}} = \left[0.60 + 0.387 \frac{Ra^{1/6}}{\left[1 + \left(\frac{0.559}{Pr_{air}} \right)^{9/16} \right]^{8/27}} \right]^2 \quad (23)$$

where D_0 (m) is the external wall diameter, k_{air} ($\text{Wm}^{-1} \text{K}^{-1}$) is the thermal conductivity of the air at average temperature (of both the wall and the ambient temperatures), Pr_{air} is the air Prandtl number, Ra is Rayleigh number at average temperature. The simple correlation for a low Reynold numbers less than 100 could be adopted using Eq. (24) [207]

$$Nu = \frac{h_{ext} D_0}{k_{air}} = 1.02 Ra^{0.148} \quad (24)$$

For an adiabatic walls:

$$k_w \left(\frac{\partial T_w}{\partial n} \right)_w = 0 \quad (25)$$

Interfaces between walls and adsorbent

The convection heat transfer through the interface between the bed and wall is estimated by the local heat conduction Eq. (26).

$$k_{eff} \left(\frac{\partial T}{\partial n} \right)_w = h_{int} (T - T_w) = k_{local} \left(\frac{\partial T}{\partial n} \right)_{local} \quad (26)$$

where h_{int} ($\text{W m}^2 \text{K}^{-1}$) is the internal convection heat transfer coefficient calculated automatically by Fluent from the last term in Eq. (26). Also

$$\nabla y_i = 0 \quad (27)$$

Inlet boundary conditions

Mass and heat transfer at the bed inlet could be expressed as the diffusion quantities in a balance to the advection ones.

$$-\varepsilon D_{i,m} \nabla y_i = \vec{v} (y_i|_- - y_i|_+) \quad (28)$$

$$-\varepsilon k_{\text{eff}} \nabla T = \vec{v} \rho (h_i|_- - h_i|_+) \quad (29)$$

Outlet boundary conditions

Mass and heat fluxes at the out let equal to zero.

$$\nabla y_i = 0 \quad (30)$$

$$\nabla T = 0 \quad (31)$$

Centerlines (in 2D) and symmetry planes (in 3D)

Mass and heat fluxes at the axisymmetric axis and symmetry planes are zero.

$$\nabla y_i = 0 \quad (32)$$

$$\nabla T = 0 \quad (33)$$

3.2.6 Materials Properties

The materials used in the models are adsorbents (AC, 13X, Mg-MOF-74, MOF-5, and MOF-177), gases (CO₂, N₂, and H₂O), and stainless steel walls. So that the thermal properties for each species and wall materials have been taken as a polynomial equation

depending on the temperature variation. However, for gas mixture, density has been calculated using ideal gas law, thermal heat capacity has been estimated from mixing-law, and the thermal conductivity and viscosity have been evaluated by mass-weighted-mixing-law. These all properties are shown in the next equations.

Thermal properties for a signal gas are

$$C_{p,i} = A + BT + C T^2 + D T^3 + E T^3 \quad (J \text{ kg}^{-1}K^{-1}) \quad (34)$$

$$k_i = A + BT + C T^2 + D T^3 + E T^3 \quad (W \text{ m}^{-1}K^{-1}) \quad (35)$$

$$\mu_i = A + BT + C T^2 + D T^3 + E T^3 \quad (Pa \text{ s}) \quad (36)$$

The constants of Eqs. (34, 35, and 36) are shown in Table 3.1.

Table 3.1 Polynomial constants for gas components thermal properties.

Thermal properties	Constants of Cp equation	Constants of k equation	Constants of μ equation
CO ₂	A=491.702 B=1.43603 C=-0.0007742 D=0 E=0	A= -0.00694154 B= 7.53746e-05 C= 7.53746e-05 D=0 E=0	A= -1.10128e-06 B= 5.89863e-08 C= -1.74847e-11 D=0 E=0
N ₂	A=938.6992 B=0.3017911 C=-8.109228E-5 D=8.263892E-9 E=-1.537235E-13	A= 0.004737109 B= 0.004737109 C= -1.122018e-08 D= 1.454901e-12 E =-7.871726e-17	A= 7.473306e-06 B= 4.083689e-08 C= 4.083689e-08 D= 1.305629e-15 E = -8.177936e-20
H ₂ O	A=1609.791 B=0.740494 C=-9.129035E-6 D=-3.81392E-8 E=4.80227E-12	A= -0.007967996 B= 6.881332e-05 C= 4.49046e-08 D= -9.099937e-12 E= 6.173314e-16	A= -4.418944e-06 B= 4.687638e-08 C= -5.389431e-12 D= 3.202856e-16 E= 4.919179e-22

For stainless steel material, $\rho = 7941 \text{ kg m}^{-3}$, $C_w = 358.98 + 0.487394 T - 2.65708 \times 10^{-7} T^2 \text{ J kg}^{-1} \text{ K}$, and $k = 15.14 \text{ W m}^{-1} \text{ K}^{-1}$.

The mixture gas heat capacity are expressed by mixing-law.

$$C_p = \sum_i x_i C_i \quad (37)$$

where x_i is the molar fraction of species. Generally, the thermal inertia of the bed is

$$(\rho C_p)_{bed} = (\rho C_p)_{gas} + \rho_s (C_{p,s} + q M C_{p,g}) \quad (38)$$

The last term in Eq. (37) contains the heat capacity of adsorbed amounts, the molecular weight, M , should be taken in kg mol^{-1} .

The thermal conductivity and viscosity of the gas mixture are determined by the following mass-weight-mixing-law.

$$k = \sum_i \frac{x_i k_i}{\sum_j x_j \phi_{ij}} \quad (39)$$

$$\mu = \sum_i \frac{x_i \mu_i}{\sum_j x_j \phi_{ij}} \quad (40)$$

and

$$\phi_{ij} = \frac{\left[1 + \left(\frac{\mu_i}{\mu_j} \right)^{1/2} \left(\frac{M_j}{M_i} \right)^{1/4} \right]^2}{\left[8 \left(1 + \frac{M_i}{M_j} \right) \right]^{1/2}} \quad (41)$$

The mass dispersion coefficient is suggested for laminar low Reynolds number as [132]:

$$D_{disp,i} = 0.508 u \frac{d_p}{Re^{0.02}} \quad (42)$$

If the Reynolds number satisfies the condition of ($Sc Re \varepsilon \geq 0.3$), the appropriate correlation of mass dispersion coefficient is as written in Eq. (43) [208].

$$D_{disp,i} = 1.317 \frac{D_{m,i}}{\varepsilon} (\varepsilon Re Sc)^{1.392} \quad (43)$$

3.2.7 VPSA/TSA and Adsorption Storage Performances

The most important criteria of PSA and TSA is the CO₂ purity and recovery from these separation processes. The CO₂ purity and recovery may be calculated as below.

The CO₂ purity is the amount of pure CO₂ content (molar base) inside the produced CO₂ while CO₂ recovery is the ratio of the amount of produced carbon dioxide to that fed to the adsorbent bed.

$$Purity\ of\ CO_2\ (PSA) = \frac{\int_{t_{blowdown}}^{t_{end\ purge}} F_{CO_2} dt}{\sum_i \int_{t_{blowdown}}^{t_{end\ purge}} F_i dt} \quad (44)$$

$$Purity\ of\ CO_2\ (TSA) = \frac{\int_{t_{heating}}^{t_{cooling}} F_{CO_2} dt}{\sum_i \int_{t_{heating}}^{t_{cooling}} F_i dt} \quad (45)$$

$$Recovery\ of\ CO_2\ (PSA) = \frac{\int_{t_{blowdown}}^{t_{end\ purge}} F_{CO_2} dt}{\int_0^{t_{end\ purge}} F_{CO_2} dt} \quad (46)$$

$$Recovery\ of\ CO_2\ (TSA) = \frac{\int_{t_{heating}}^{t_{cooling}} F_{CO_2} dt}{\int_0^{t_{cooling}} F_{CO_2} dt} \quad (47)$$

and

$$F_i = Q_F C_i \quad (48)$$

where F_i (mol s^{-1}) is the molar flow rate of component i (CO_2 and N_2), C_i (mol m^{-3}) is the component concentration, and Q_F ($\text{m}^3 \text{s}^{-1}$) is the volumetric flow rate at the bed outlet.

For more useful performance analysis, the estimation of CO_2 productivity and PSA consumption energy as well as TSA thermal regeneration energy are conducted as written in Eqs. 49-52.

$$\text{Productivity of } \text{CO}_2 \text{ (PSA)} = \frac{\int_{t_{\text{blowdown}}}^{t_{\text{end purge}}} F_{\text{CO}_2} M_{\text{CO}_2} dt - \int_{t_{\text{rinse}}}^{t_{\text{end rinse}}} F_{\text{CO}_2} M_{\text{CO}_2} dt}{t_{\text{cycle}} m_s} \quad (49)$$

$$\text{Productivity of } \text{CO}_2 \text{ (TSA)} = \frac{\int_{t_{\text{heating}}}^{t_{\text{cooling}}} F_{\text{CO}_2} M_{\text{CO}_2} dt - \int_{t_{\text{rinse}}}^{t_{\text{end rinse}}} F_{\text{CO}_2} M_{\text{CO}_2} dt}{t_{\text{cycle}} m_s} \quad (50)$$

where M_{CO_2} (kg mol^{-1}) is molecular weight of CO_2 , t_{cycle} (hr) the total time of one repeated cycle, and m_s (kg) is the adsorbent mass.

The vacuum pumps and blowers consumed energy is [209].

$$E_{\text{PSA}} = \int \frac{\gamma}{\gamma - 1} \frac{Q_F \varepsilon_{\text{tot}} C R T}{\eta} \left[\left(\frac{P_{\text{max}}}{P_{\text{min}}} \right)^{\frac{\gamma-1}{\gamma}} - 1 \right] dt \quad (51)$$

where η is the vacuum pump or compressor efficiency and assumed to be 0.72, γ is the specific heat capacity of gases. The integration is applied for every step consumed energy and then the total energy consumed during full cycle is the sum of the consumed energy for every step.

The thermal regeneration energy could be estimated as [210, 211]:

$$E_{TSA} = \frac{1}{\eta} \int_{T_{bed,min}}^{T_{bed,max}} (m_s C_{p,s} + m_s q_{CO_2} M_{CO_2} C_{p,CO_2}) dT + \int_{T_{wall,min}}^{T_{wall,max}} m_w C_w dT_w + \int_{q_{min}}^{q_{max}} m_s \Delta H dq \quad (52)$$

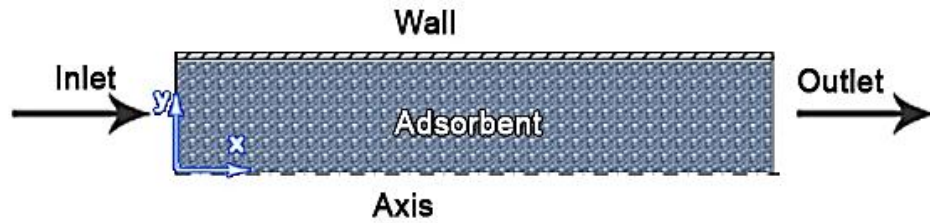
where η is the heat source efficiency and assumed to be 0.8. The first integration is the sensible heat added to the adsorbent material and adsorbed CO₂, the second one is the heat consumed by the bed wall, and the third integration is for the heat consumed due to the desorption heat (isosteric desorption heat).

3.2.8 Breakthrough Case Studies

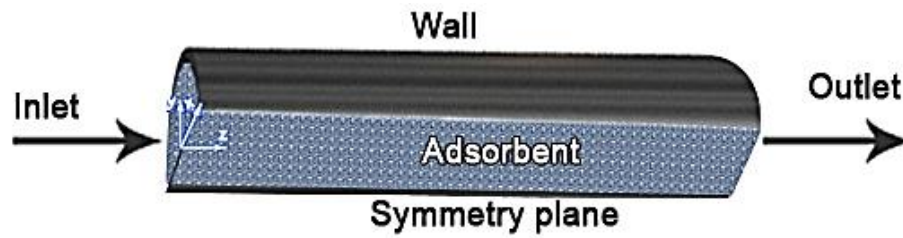
- *Validation*

The first step of breakthrough adsorption simulation is a validation of the numerical models. Therefore, the results of the present model were compared with three experimental works: first case was the experimental work reported by Dantas [165] using activated carbon to separate CO₂ from CO₂/N₂ mixture at 101.3 kPa and 423 K, the second one is 2D and 3D models compared to the present experimental CO₂/N₂ separation using Mg-MOF-74 at 101.3 kPa and 297 K, and the third validation is comparing the 2D model with experimental CO₂ separation in the present work from CO₂/N₂/H₂O mixture using 13X at 101.3 kPa and 297 K.

The used adsorbent bed was a cylinder filled with adsorbent material as shown in Figure 3.4.



(a) 2D Adsorbent bed



(b) 3D adsorbent bed

Figure 3.4 Adsorbent beds used for CO₂ separation.

The beds and system properties for the validation cases are described in below tables (Table 3.2 -Table 3.6).

Table 3.2 Bed, adsorption , and thermal properties of AC bed [165].

Properties	Value
Bed length, L	0.171 m
Bed diameter, D	0.022 m
Bed wall thickness	0.0015 m
Bed density, ρ_s	546.24 kg m ³
Adsorbent specific heat capacity, $C_{p,s}$	880 J kg ⁻¹ K ⁻¹
Adsorbent thermal conductivity	0.63 W m ⁻¹ K ⁻¹
Particle density, ρ_p	1138 kg m ⁻³
Adsorbent particle size, d_p	0.0038 m

Bed porosity, ϵ	0.52
Inlet velocity, u	0.00131 ms ⁻¹
Inlet temperature	423 K
Outlet pressure, p	0 Pa (gauge)
Ambient temperature, T_{amb}	298 K (the bed was adiabatic)
CO ₂ inlet molar fraction	0.2
N ₂ inlet molar fraction	0.8
CO ₂ adsorption time constant coefficient, k_{L,CO_2}	0.032 s ⁻¹
N ₂ adsorption time constant coefficient, k_{L,N_2}	0.128 s ⁻¹
CO ₂ adsorption heat, ΔH_{CO_2}	-21840 J mol ⁻¹
N ₂ adsorption heat, ΔH_{N_2}	-16310 J mol ⁻¹

The equilibrium isotherm parameters in accordance to Toth model is shown in Table 3.3

Table 3.3 Equilibrium isotherm parameters for AC [165].

Gas species	q_m (mmol/g)	K_0 (Pa ⁻¹)	n
CO ₂	10.05	7.62e-10	0.678
N ₂	9.74	6.91e-10	0.518

Table 3.4 Bed, adsorption, and thermal properties of Mg-MOF-74 bed.

Properties	Value
Bed length, L	0.07 m
Bed diameter, D	0.004 m
Bed wall thickness	0.001 m
Bed density, ρ_s	230.1 kg m ³

Adsorbent specific heat capacity, $C_{p,s}$	900 J kg ⁻¹ K ⁻¹
Adsorbent thermal conductivity	0.3 W m ⁻¹ K ⁻¹
Particle density, ρ_p	911 kg m ⁻³
Adsorbent particle size, d_p	0.0002 m
Bed porosity, ϵ	0.7417
Inlet flow rate, Q_F	10 sccm
Inlet temperature	297 K
Outlet pressure, p	0 Pa (gauge)
Ambient temperature, T_{amb}	297 K (the bed was adiabatic)
CO ₂ inlet molar fraction	0.2
N ₂ inlet molar fraction	0.8
CO ₂ adsorption time constant coefficient, k_{L,CO_2}	0.1182 s ⁻¹
N ₂ adsorption time constant coefficient, k_{L,N_2}	0.3043 s ⁻¹
CO ₂ adsorption heat, ΔH_{CO_2}	-42492.6 q + 3973.75 q ² - 959.838 q ³ + 69.1208 q ⁴ J mol ⁻¹ [26]
N ₂ adsorption heat, ΔH_{N_2}	-18000 J mol ⁻¹ [26]

The equilibrium isotherm parameters in accordance to Toth model at 297 K is shown in Table 3.5.

Table 3.5 Equilibrium isotherm parameters for Mg-MOF-74.

Gas species	q_m (mmol/g)	K_0 (Pa ⁻¹)	n	$-\Delta H$ (J mol ⁻¹)
CO ₂	11.4048	3.089e-11	0.4217	42000
N ₂	6.7072	9.36e-10	1	18000

Table 3.6 Bed, adsorption , and thermal properties of 13X bed.

Properties	Value
Bed length, L	0.2 m
Bed diameter, D	0.009 m
Bed wall thickness	0.002 m
Bed density, ρ_s	533.8 kg m ³
Adsorbent specific heat capacity, $C_{p,s}$	900 J kg ⁻¹ K ⁻¹
Adsorbent thermal conductivity	0.2 W m ⁻¹ K ⁻¹
Particle density, ρ_p	1230 kg m ⁻³
Adsorbent particle size, d_p	0.0015 m
Bed porosity, ϵ	0.566
Inlet flow rate, Q_F	10 sccm
Inlet temperature	297 K
Outlet pressure, p	0 Pa (gauge)
Ambient temperature, T_{amb}	297 K (the bed was adiabatic)
CO ₂ inlet molar fraction	0.19466
N ₂ inlet molar fraction	0.7786
H ₂ O inlet molar fraction	0.0267 (RH=0.9)
CO ₂ adsorption time constant coefficient, k_{L,CO_2}	0.006 s ⁻¹
N ₂ adsorption time constant coefficient, k_{L,N_2}	0.601 s ⁻¹
H ₂ O desorption time constant coefficient, k_{L,H_2O}	0.000058 s ⁻¹

CO ₂ adsorption heat, ΔH_{CO_2}	-30731 J mol ⁻¹ [163]
N ₂ adsorption heat, ΔH_{N_2}	-14935 J mol ⁻¹ [163]
H ₂ O adsorption heat, ΔH_{H_2O}	-53289 J mol ⁻¹

The equilibrium isotherm parameters in accordance to Toth model is shown in Table 3.7.

Table 3.7 Equilibrium isotherm parameters for 13X.

Gas species	q _m (mmol/g)	K ₀ (Pa ⁻¹)	n	Ref.
CO ₂	9.842	6.86e-9	0.658*(0.0013* T)	[163]
N ₂		8e-10	1	[163]
H ₂ O	15.4849	1.68e-10	0.5536	present

- *Effect of water vapor on the CO₂ adsorption uptake*

The water effect on the CO₂ uptakes using AC, 13X and Mg-MOF-74 at 300 K has been investigated by breakthrough tests. Adsorption breakthrough at different relative humidity has also been modeled for Mg-MOF-74 at 323 K. Moreover, the effect of water vapor on Mg-MOF-74 when the bed reaches H₂O saturated adsorption has been studied at 373 K. All these cases (12) are tabulated in Table 3.8.

Table 3.8 Case studies of effect of water on the CO₂ separation.

Case	Material	T (K)	CO ₂ (vol.%)	N ₂ (vol.%)	H ₂ O (vol.%)	RH%
1	Mg-MOF-74	323	15	85	0	0.0
2	Mg-MOF-74	232	15	82	3	24.8
3	Mg-MOF-74	232	15	79	6	49.6
4	Mg-MOF-74	232	15	76	9	74.7
5	Mg-MOF-74	232	15	73	12	99.2
6	Mg-MOF-74	300	15	85	0	0.0
7	Mg-MOF-74	300	15	82	3	86.0
8	Mg-MOF-74	373	15	76	9	9.1
9	AC	300	15	85	0	0.0
10	AC	300	15	82	3	86.0
11	13X	300	15	85	0	0.0
12	13X	300	15	82	3	86.0

The bed used in modeling dry and humid CO₂/N₂ separation by different adsorbents had a geometry as Length = 0.07 m, Inter Diameter = 0.004 m, and Wall Thickness = 0.001 m. The inlet flow rate is 20 ml min⁻¹ for the all cases at 300 K and 101.325 kPa. The adsorption and thermal properties are the same to those mentioned in Table 3.4 and Table 3.5 except those vary with temperature specified in Table 3.9 for AC and 13X and Table 3.10 and Table 3.11 for Mg-MOF-74.

Table 3.9 LDFadsorption time constnt of AC and 13X.

Properties	Value
For AC	
CO ₂ adsorption time constant coefficient, k_{L,CO_2}	0.068 s ⁻¹
N ₂ adsorption time constant coefficient, k_{L,N_2}	0.67s ⁻¹
H ₂ O adsorption time constant coefficient, k_{L,H_2O}	none-adsorptive

For 13X	
CO ₂ adsorption time constant coefficient, k_{L,CO_2}	0.006 s ⁻¹
N ₂ adsorption time constant coefficient, k_{L,N_2}	0.6 s ⁻¹
H ₂ O adsorption time constant coefficient, k_{L,H_2O}	0.000056 s ⁻¹

For Mg-MOF-74 cases, the operation temperature values were about 300, 323 and 373 K, so that Dual-site Langmuir model have been used for predicting gases equilibrium adsorbed amounts at different temperatures as suggested by Manson [26]. Table 3.10 shows the Dual-site Langmuir parameters required for estimating equilibrium CO₂ adsorbed values. Toth model has been used to evaluate those values for N₂ and H₂O. The packed density used was about 297 kg m⁻³, so that the accordance porosity was about 0.674.

Table 3.10 Equilibrium isotherm parameters for Mg-MOF-74 [26].

Gas species	$q_{m,1}$ (mmol/g)	$q_{m,2}$ (mmol/g)	$K_{0,1}$ (Pa ⁻¹)	$K_{0,2}$ (Pa ⁻¹)	n	$-\Delta H_1$ (J mol ⁻¹)	$-\Delta H_2$ (J mol ⁻¹)
CO ₂	6.8	9.9	2.44e-11	1.39e-10	-	42000	24 000
N ₂	14	-	4.96e-10	-	1	18000	-
H ₂ O	39.5701	-	1.677e-10	-	0.5536	48991	-

The LDF adsorption time constant diffusion are calculated using Eq. (13) and tabulated in Table 3.11.

Table 3.11 LDF adsorption properties of Mg-MOF-74 at different temperatures.

Species	K_L at 300 K (s^{-1})	K_L at 323 K (s^{-1})	K_L at 373 K (s^{-1})
CO ₂	0.12130	0.1373	0.1704
N ₂	0.30550	0.3129	0.3263
H ₂ O	0.00123	0.0051	0.0503

3.2.9 Pressure and Temperature Swing Adsorption Cases

- *Validation*

Pressure Swing Adsorption (PSA) model has been validated with the experimental work of Dantas et. al [151] for a column bed filling with zeolite 13X. Four steps have been carried out to present a full PSA cycle namely: pressurization, feed, blowdown and purge. All-important parameters and column properties are shown in

Table 3.12. The pressurization process (consumed 20 s) was mainly targeted to raise the pressure of the bed up to 1.3 bar by pure N₂ using compressor or blower. Then, the feed process takes place with a mixture flow that contains CO₂/N₂ (15% CO₂, 85% N₂ by volume) at 1.3 bar and 323 K. After a stipulated feed time (100 s), the CO₂ desorption was performed by blowdown process (for 70 s) in which the pressure was minimized to about 0.1 bar. During the blow down process, the majority of captured CO₂ has been removed from the bed. The remaining amounts of adsorbed CO₂ could, moreover, be reduced by

counter-current flow purge process (by applying 0.5 liter/min of pure N₂) at about 0.187 bar and 323 K for about 70 s. The detailed boundary conditions are shown in Figure 3.5.

A complete PSA cycle (1st cycle) for both of experimental and 1D simulation modeling [151] and the present 2D and 3D laminar and turbulent simulations are studied. The turbulent model has been solved by standard k - ϵ model to explore the effect of turbulent flow on the PSA when the Reynolds number is greater than 10 similar to the case of the feed step (Re=16.26). The modeled transport equations for standard turbulence kinetic energy (k) and its rate of dissipation (ϵ) are:

k-equation:

$$\frac{\partial}{\partial t}(\rho k) + \frac{\partial}{\partial x^j}(\rho k u_j) = \frac{\partial}{\partial x^j} \left[\left(\mu + \frac{\mu_t}{\sigma_k} \right) \frac{\partial k}{\partial x^j} \right] + G_k - \rho \epsilon + Y_M \quad (53)$$

and ϵ -equation:

$$\frac{\partial}{\partial t}(\rho \epsilon) + \frac{\partial}{\partial x^j}(\rho \epsilon u_j) = \frac{\partial}{\partial x^j} \left[\left(\mu + \frac{\mu_t}{\sigma_\epsilon} \right) \frac{\partial \epsilon}{\partial x^j} \right] + C_{1\epsilon} \frac{\epsilon}{k} G_k - C_{2\epsilon} \rho \frac{\epsilon}{k} \quad (54)$$

where, G_k represents the generation of turbulence due to mean velocity gradient. Y_M represents the contribution of the fluctuating dilatation in compressible flow to the overall dissipation rate. $C_{\epsilon 1}$ and $C_{\epsilon 2}$ are constants. σ_k and σ_ϵ are the turbulent Prandtl numbers for k and ϵ , respectively. More details about the standard k - ϵ model are described in Fluent documentations [202]. The turbulent intensity and turbulent viscosity ratios have been taken as 5 and 10, respectively

Table 3.12 Properties of the bed column and adsorbent (13X) used in the experimental work [151] and the current simulation.

Properties	Value
Bed Length, L	0.83 m
Bed diameter, d_{int}	0.021 m
Column wall thickness, l	0.0041 m
Column wall specific heat capacity, C_w	$500 \text{ J kg}^{-1} \text{ K}^{-1}$
Column wall density	8238 kg m^{-3}
Particle density, ρ	1228.5
Bed void fraction, ε	0.62
Solid Specific heat, C_s	$920 \text{ J kg}^{-1} \text{ K}^{-1}$
CO ₂ maximum adsorbed concentration (q_m)	5.09 mol kg^{-1}
N ₂ maximum adsorbed concentration (q_m)	3.08 mol kg^{-1}
Toth constant n (CO ₂)	0.429
Toth constant n (N ₂)	0.869
Toth constant Ko (CO ₂)	$4.31\text{e-}9 \text{ Pa}^{-1}$
Toth constant Ko (N ₂)	$8.81\text{e-}10 \text{ Pa}^{-1}$
CO ₂ adsorption heat ΔH	$-29380 \text{ J mol}^{-1}$
N ₂ adsorption heat ΔH	$-17190 \text{ J mol}^{-1}$

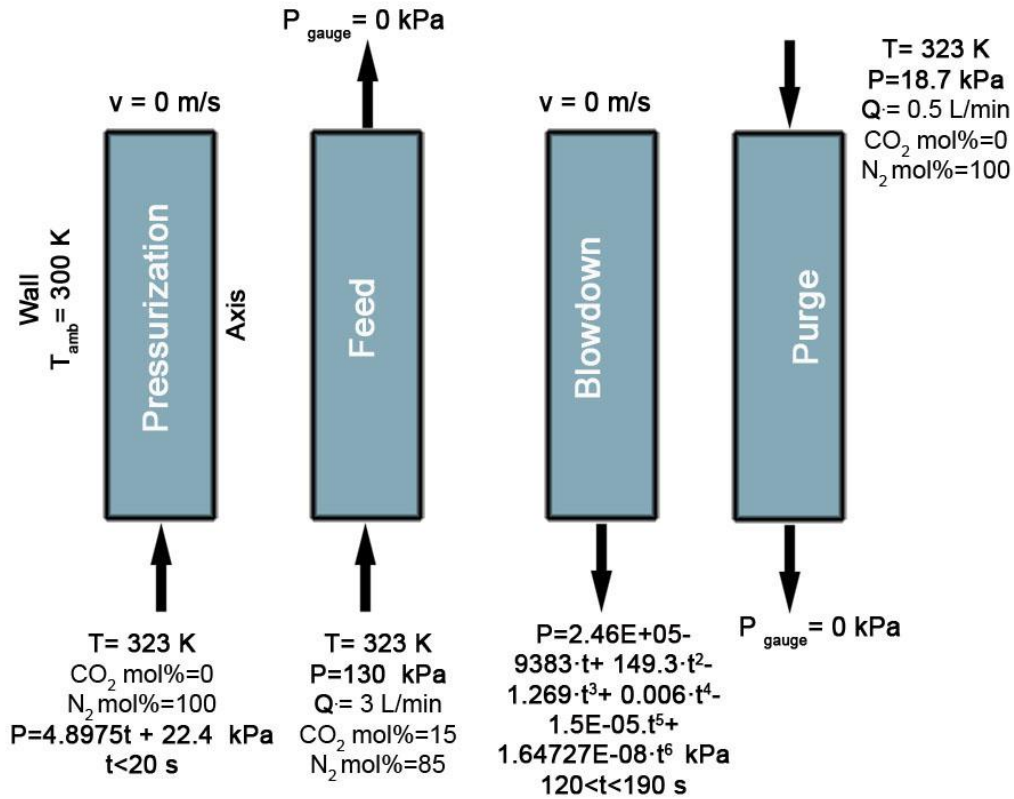


Figure 3.5 Boundary conditions for the 4 steps of the 1st cycle of PSA according to the experimental work [151].

- *Vacuum Pressure Swing Adsorption (VPSA)*

The similar bed used in adsorption breakthrough of Mg-MOF-74 have been exploited for PSA. A single bed was adopted to simulate five steps of PSA, namely: pressurization, feed, rinse, blowdown and purge. The pressurization process (consumed 20 s) was mainly targeted to raise the pressure of the bed from 2 kPa up to 130 KPa by pure N_2 . Then, the feed process took place with a mixture flow contains CO_2/N_2 (15% CO_2 , 85% N_2 (vol. %)) at 1.3 bar and 323 K. After a stipulated feed time (250 s), the pure CO_2 has been introduced to the bed to rinse the remaining N_2 inside the bed void for about (40 s). The devoted times for feed and rinse processes were fixed through all cases to avoid the violation of the

adsorption breakpoint, the point at which the outlet concentration is less than 5% from the that of inlet, and its effect on releasing the CO₂ to the ambient. In blowdown process, CO₂ was desorbed from the bed by evacuating the bed to about 2 kPa. During the blow down process, the majority of captured CO₂ has been removed from the bed. The remaining amounts of adsorbed CO₂ could, moreover, be reduced by counter-current flow purge process (by applying 10 ml/min of pure N₂). Blowdown and purge steps have been investigated for the optimal operation time as described in Table 3.13. The detailed boundary conditions of the five steps are shown in Figure 3.6. Mg-MOF-74 isotherms and LDF properties are described in Table 3.10 and Table 3.11. The pressure was changing with time for the pressurization step and the beginning of blowdown step. For illustration, the operating pressure of the case 2 during at the first three cycles is shown in Figure 3.7. The first cycle of all cases was devoted to fill the bed with CO₂ up to breakpoint by feed and rinse processes, therefore the feed time of the first cycle was greater than that of the others.

Table 3.13 VPSA study cases.

Case	Blowdown Time (s)	Purge time (s)
1	150	50
2	150	100
3	150	150
4	100	100
5	200	100

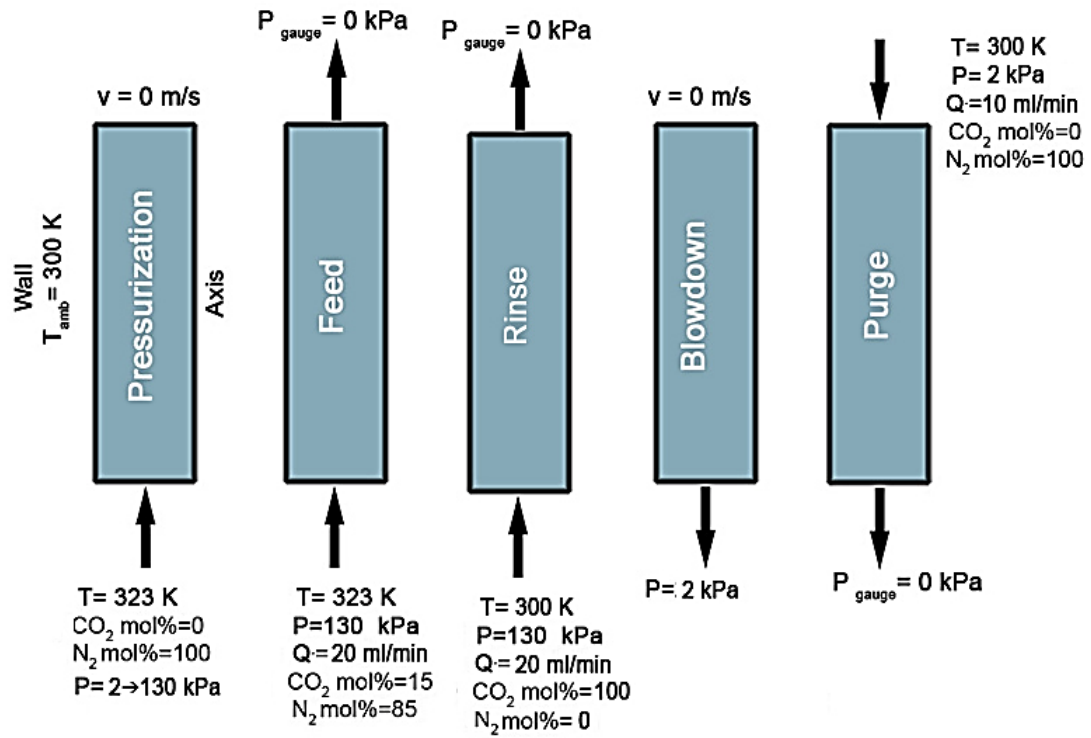


Figure 3.6 Boundary conditions for five steps of VPSA.

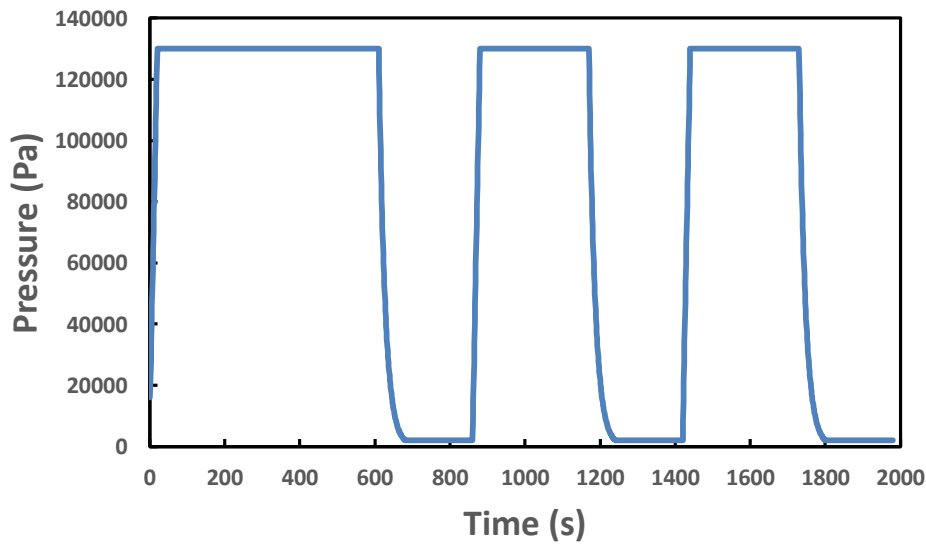


Figure 3.7 Operating pressure of the case 2 during the first three cycles.

- *Temperature Swing Adsorption (TSA)*

Temperature swing adsorption have been investigated using Mg-MOF-74 as adsorbent and the same bed configuration of PSA. A single bed was implemented for numerically modeling four steps of TSA, namely: feed, rinse, heating and cooling. The feed process consumed 250s to feed the adsorbent bed with a mixture flow contains CO₂/N₂ (15% CO₂, 85% N₂ (vol. %)) at 101.3 kPa and 323 K. After bed feeding, the pure CO₂ was introduced into the bed to rinse remaining N₂ inside the bed void for about (40 s). The devoted times for feed and rinse processes were fixed to avoid the violation of the adsorption breakpoint and a consequence emission of the CO₂ to the ambient. During the heating process, CO₂ was desorbed from the bed by increasing the bed temperature up to 393 K. Therefore, a significant amount of CO₂ have been removed from the bed. Before starting the next feed, the bed should be cooled down by a certain cooling process. The cooling step here have been carried out by natural convection and radiation with the ambient. Heating and cooling were investigated for the optimal operation times as described in Table 3.14. The detailed boundary conditions of the four steps are shown in Figure 3.8. Mg-MOF-74 isotherms and LDF properties are described in Table 3.10 and Table 3.11. The first cycle of the all cases was devoted to fill the bed with CO₂ up to breakpoint by feed and rinse processes, therefore the feed time of the first cycle is greater than that of the others.

Table 3.14 TSA study cases.

Case	Heating time (s)	Cooling time (s)
1	200	200
2	250	200
3	300	200
4	200	300
5	200	400

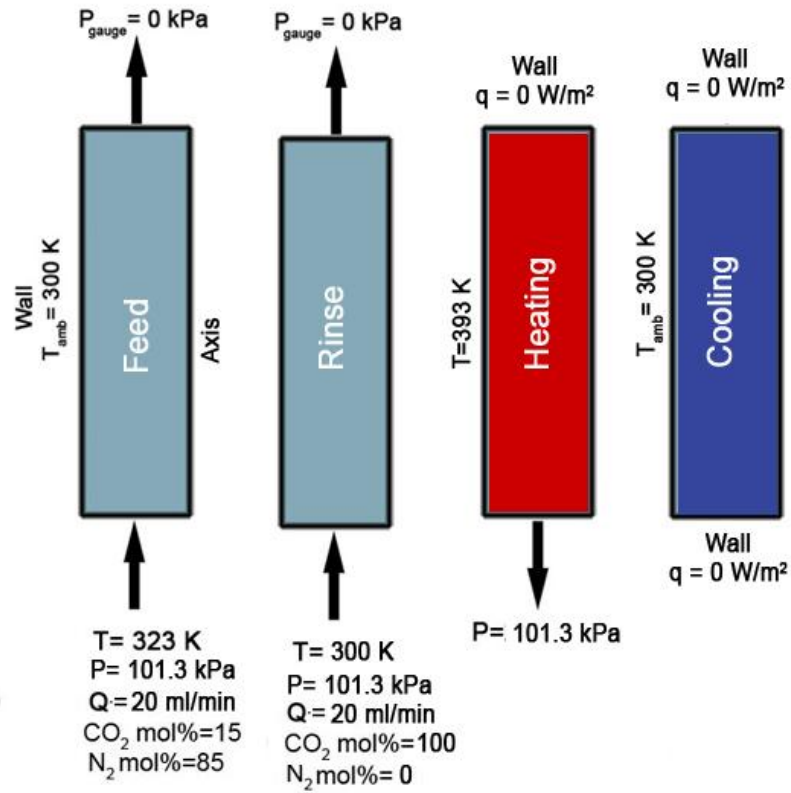


Figure 3.8 Boundary conditions for four steps of TSA.

3.2.10 Carbon dioxide Adsorptive Storage Cases

- *Validation*

In order to validate the numerical modeling of a gas adsorptive storage in a 2D and 3D tank, we compared the present model with the experimental results of H₂ adsorptive storage using activated carbon, Ye et al. [212]. The storage tank is shown in Figure 3.9 with small inlet tube for feeding the gas to the receiver. The tank, activated carbon, and H₂ properties are described in Table 3.15. The inlet mass fluxes during tank charging, dormancy, discharging and dormancy are shown in Table 3.16.

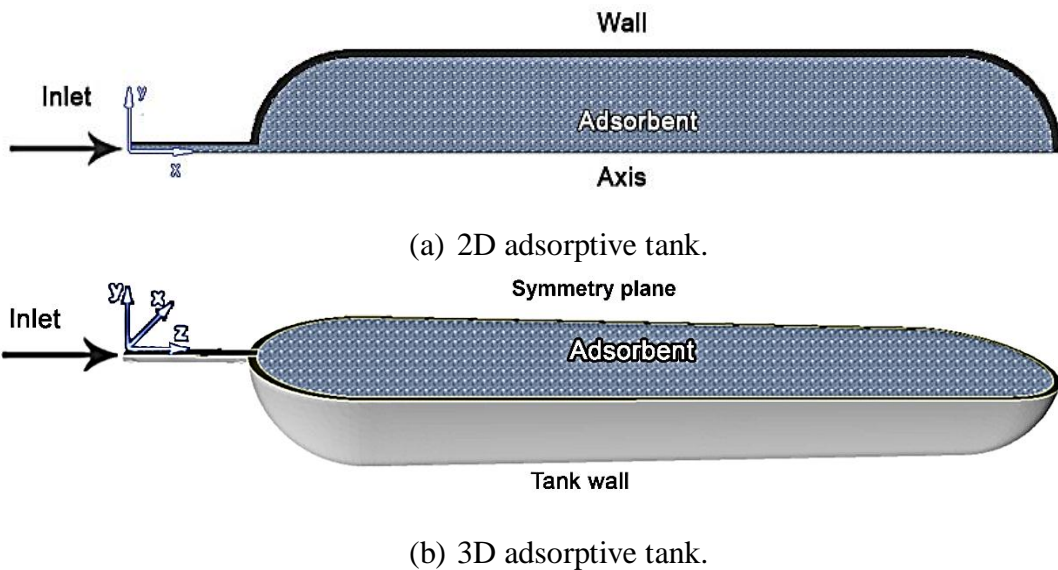


Figure 3.9 Scheme of adsorptive tank.

Table 3.15 Tank, AC, and H₂ properties used in the numerical modeling at the same conditions of the experimental work [212].

Tank diameter (m)	0.0928	Pipe diameter (m)	0.008
Tank wall thickness (m)	0.0039	Pipe wall thickness (m)	0.001

Tank length (m)	0.4	Pipe length (m)	0.05375
Wall density (kg m ⁻³)	7830	Wall specific heat (J kg ⁻¹ K ⁻¹)	468
Wall thermal conductivity (W m ⁻¹ K ⁻¹)	13	Activated carbon density (kg m ⁻³)	517.6
AC specific heat capacity (J kg ⁻¹ K ⁻¹)	825	AC thermal conductivity (W m ⁻¹ K ⁻¹)	0.646
Bed porosity	0.49	H ₂ specific heat capacity (J kg ⁻¹ K ⁻¹)	14700
H ₂ thermal conductivity (W m ⁻¹ K ⁻¹)	0.206	H ₂ viscosity (Pa s)	8.411e-6

The isotherm model used here is Dubnin-Astackov (Eq. 11). The main parameters of this model for AC is shown in Table 3.17. LDF coefficient was taken as 0.15 s⁻¹ [212].

Table 3.16 Inlet mass flux of PSA validation [212].

Time (s)	Mass flux (kg s ⁻¹ m ⁻²)
0 - 442	0.866399
442 - 3046	0
3046 - 3907	-0.43489069
3907 - 6000	0

Table 3.17 Dubnin-Astackov parameters for H₂ isotherms of AC.

Gas species	q _m (mmol/g)	P ₀ (MPa)	α (J mol ⁻¹)	β (J mol ⁻¹ K ⁻¹)	n	ΔH (J mol ⁻¹)	Ref.
H ₂	71.6	1408	3080	18.9	2	3185	[212]

- *Carbon dioxide storage in MOF-5*

The same tank used in validation case filled with MOF-5 in order to simulate the pressure effect on the CO₂ adsorptive storage. Thermal properties of MOF-5, isotherms [213], and LDF model is shown in Table 3.18. The heat transfer from the cylinder wall to the ambient was by free convection and radiation while the inlet tube wall was adiabatic.

Table 3.18 Thermal and adsorptive properties of MOF-5/CO₂.

Properties	Value
Particle density, ρ	621 [214]
Bed void fraction, ε	0.31
Solid Specific heat, C _s (J kg ⁻¹ K ⁻¹)	750 [215]
LDF coefficient	0.025 [213]
CO ₂ adsorption heat ΔH (J mol ⁻¹)	-34000 [213]
q _m (mmol/g)	23
P ₀ (MPa)	72.14
α (J mol ⁻¹)	20
β (J mol ⁻¹ K ⁻¹)	37.8
n	7

Bed density (kg m ⁻³)	428.5
MOF-5 thermal conductivity (W m ⁻¹ K ⁻¹)	0.32 [216]

Six cases have been investigated by changing the inlet pressure as 5, 10, 20, 30, 40, and 50 bar as shown in Figure 3.10. The first 500 s are dedicated for CO₂ charging process, while the remains are for dormancy.

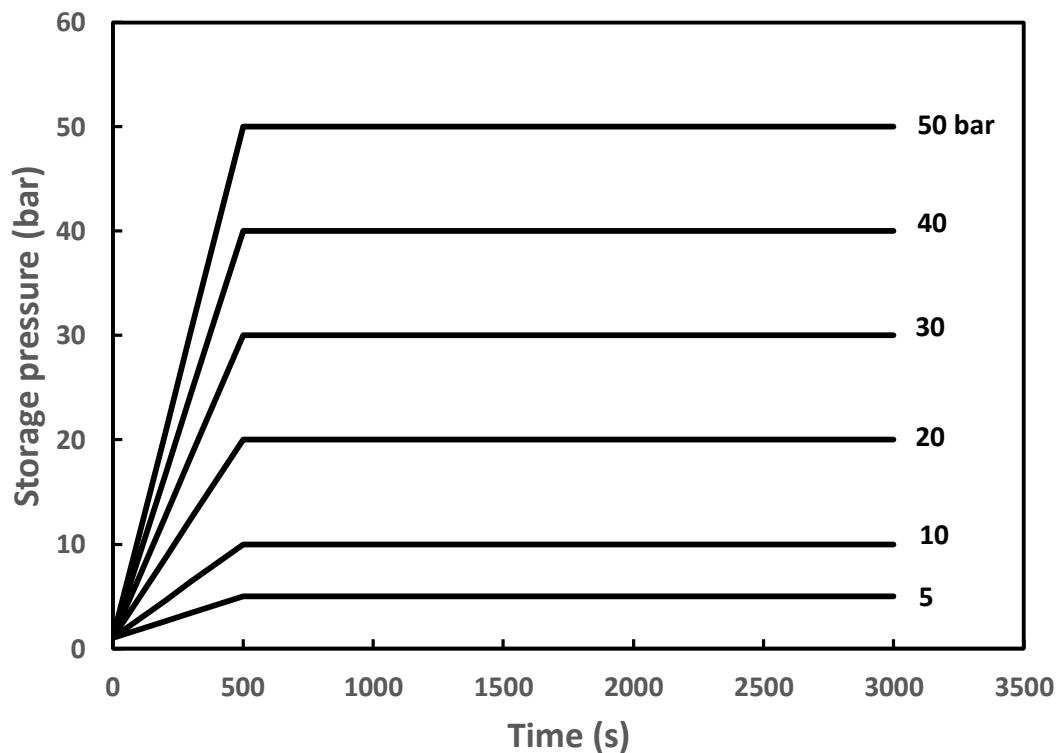


Figure 3.10 Inlet pressure for MOF-5/CO₂ adsorption storage.

- *Carbon dioxide storage in MOF-177*

MOF-177 used for CO₂ adsorptive storage and has been simulated for the same cases and bed configuration mentioned before with MOF-5. The important thermal properties of MOF-177, CO₂ isotherms [213], and LDF models are tabulated in Table 3.19.

Table 3.19 Thermal and adsorptive properties of MOF-177/CO₂.

Properties	Value
Particle density, ρ	477 [214]
Bed void fraction, ε	0.44
Solid Specific heat, C_s (J kg ⁻¹ K ⁻¹)	490 [217]
LDF coefficient	0.1597 [218]
CO ₂ adsorption heat ΔH (J mol ⁻¹)	-14000 [26]
qm (mmol g ⁻¹)	37.4
P0 (MPa)	72.14
α (J mol ⁻¹)	100
β (J mol ⁻¹ K ⁻¹)	34.8
n	7
Bed density (kg m ⁻³)	239.1
MOF-177 thermal conductivity (W m ⁻¹ K ⁻¹)	0.3

Like MOF-5, six cases have been investigated by changing the inlet pressure as 5, 10, 20, 30, 40, and 50 bar as shown in Figure 3.10.

CHAPTER 4

EXPERIMENTAL RESEARCH RESULTS AND

DISCUSSION

4.1 Carbon Nanotubes/Zeolite 13X Composites

To show the features of the physical mixture of MWCNT/13X compounds, we have captured some optical microscopic photos for all samples as shown in Figure 4.1. As evident, the MWCNT (black-color) appears more as its percentage increases. The density of CNT is about 0.12 g/cc compared to about 0.5 g/cc for 13 X, so that adding CNT quantities up to 1.5 is sufficient to investigate the adsorption behavior. Figure 4.2 shows the particle size distributions for all MWCNT/13X composites. They are close to each other for all the compounds; the majority of particles lay between 200 and 400 μm and between 800 and 1200 μm . The exception is that the XC4 composite has larger particle size distribution between 800 and 1400 μm . Also the particle distribution of XC2 shows almost similar amounts of particles existing in the range of 1000-1400 μm . The similar distribution of the grain sizes because the pure 13X pellets was grinded firstly and then the all samples were composed by mixing the new powder of the pristine 13X with MWCNT. The grinding method could significantly control the grain size distribution. However, the large grain sizes can preferably be packed to the adsorbent bed with increasing bed porosity and then minimizing the packing bed density. The high packed density could increase the pressure drop through the bed.

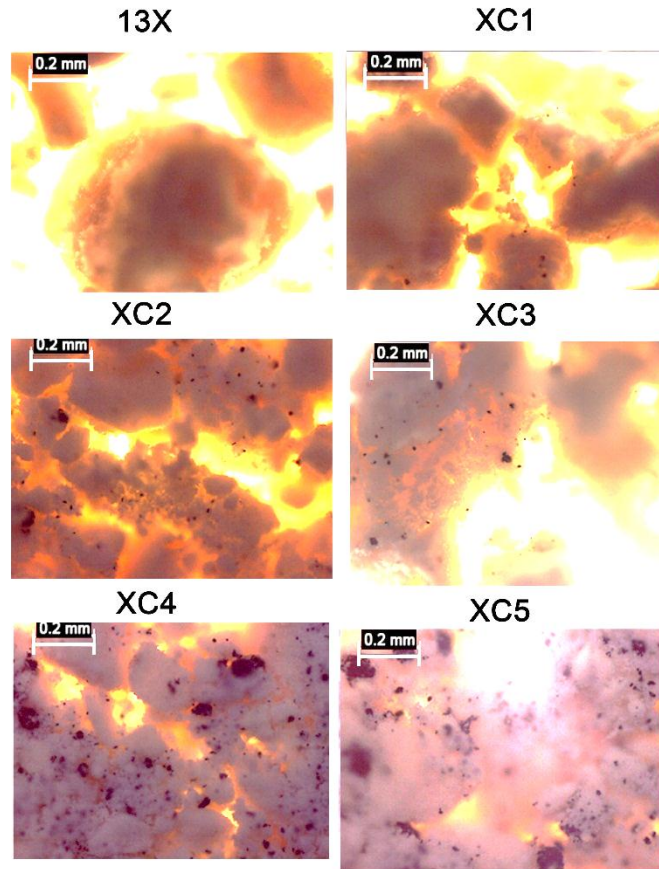


Figure 4.1 Optical microscopic photos of MWCNT/13X compounds.

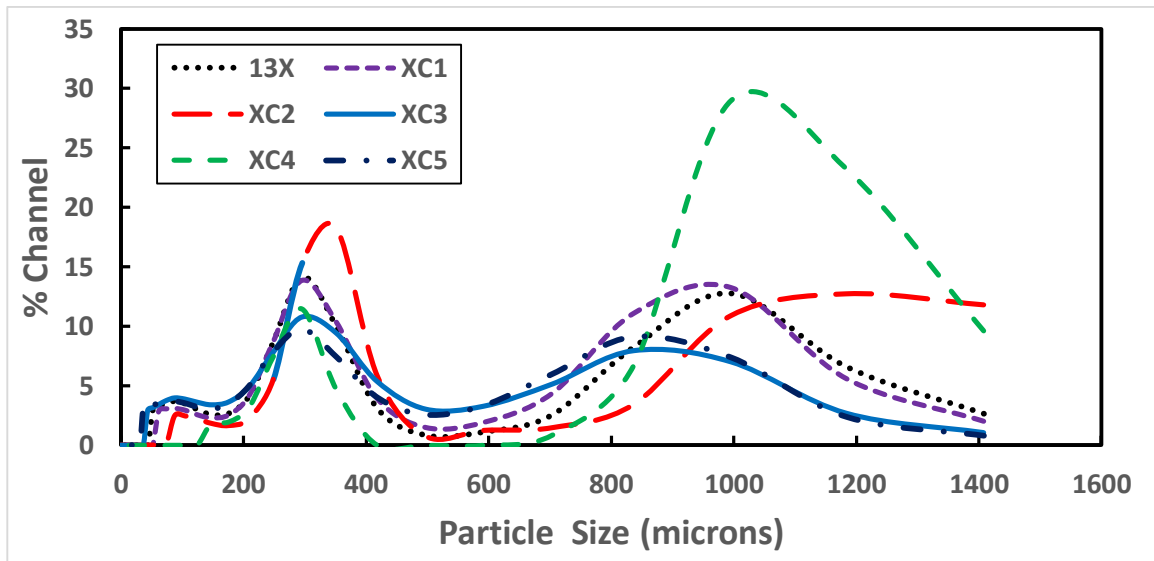


Figure 4.2 Particle size distribution of MWCNT/13X compounds.

4.1.1 Powder X-Ray Diffraction Analysis

Figure 4.3 illustrates the PXRD patterns of the seven samples (5 of MWCNT/13X compounds and 2 of pure 13X and pure MWCNT). All the samples (excluded pure CNT) approximately show the same intensity peaks locations which are in good agreement with the pure 13X synthesized by Zheng et. al [219]. The effect of MWCNT inside the MWCNT/13X compounds was observed to disappear due to two principal reasons. Firstly, the MWCNT percentages inside the compounds are very small (less than 1.5% by weight) so the diffracted X-ray beam really emits from the crystalline cell's planes of 13X. The other reason is that the MWCNT has almost one or two small intensity peaks in the same range of operating angles (two-theta = 3 - 45°) as shown in Figure 4.3.

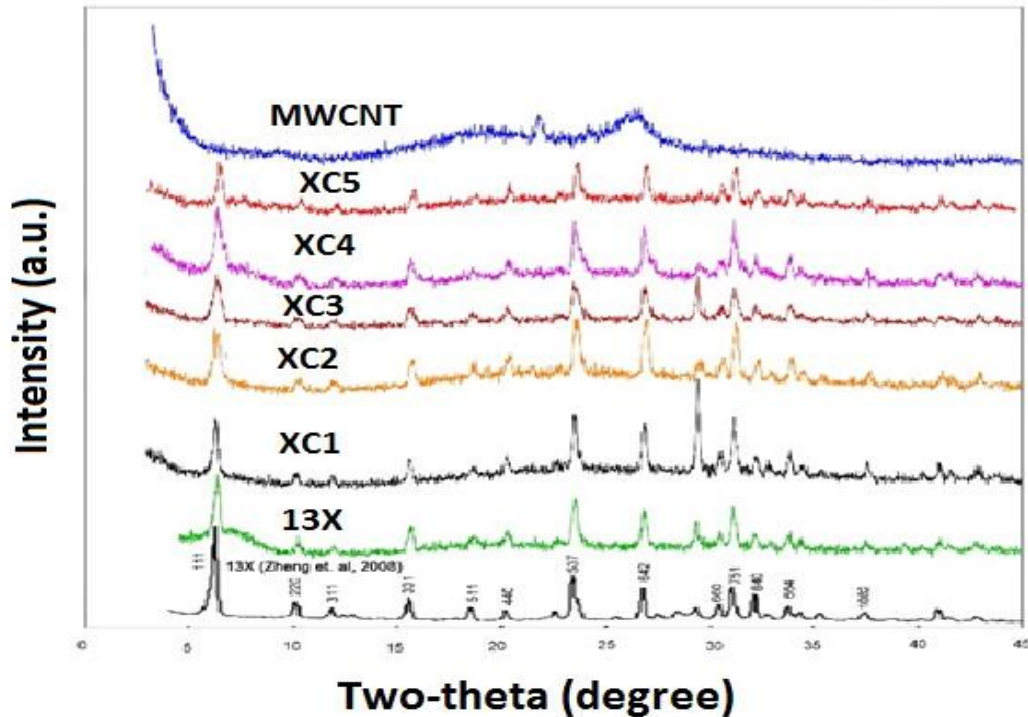


Figure 4.3 Powder X-ray diffraction (PXRD) data of MWCNT/13X compounds and pure materials (13X and MWCNT).

4.1.2 Adsorption Equilibrium Isotherms of Carbon Dioxide and Nitrogen

The adsorption isotherms of N₂ at 77 K are shown in Figure 4.4. The tested samples exhibit almost slight linear increase for N₂ adsorbed amounts in the pressure range between 0-101 kPa. 13X shows the highest equilibrium adsorption values. Then, the adsorbed values decline sharply by about 40% for XC3, which is still having better adsorption values than those of the remaining MWCNT/13X compounds attributable to maintain the same pore size (Table 26). Moreover, CO₂ adsorption isotherms are collected at 273 K as shown in Figure 4.5. The differences between CO₂ adsorbed amounts by pure 13X and XC3 are small compared with those of the others. Therefore, 13X and XC3 have the best adsorption equilibrium values under the all applied pressure values (e.g. larger than 5 and 6.5 mmol/g could be adsorbed at P=20 kPa and 126 kPa, respectively). Table 4.1 summarizes BET surface areas (for N₂ at 77 K and CO₂ at 273 K), average pore size, and porous volume (for N₂ at 77 K) for all the samples.

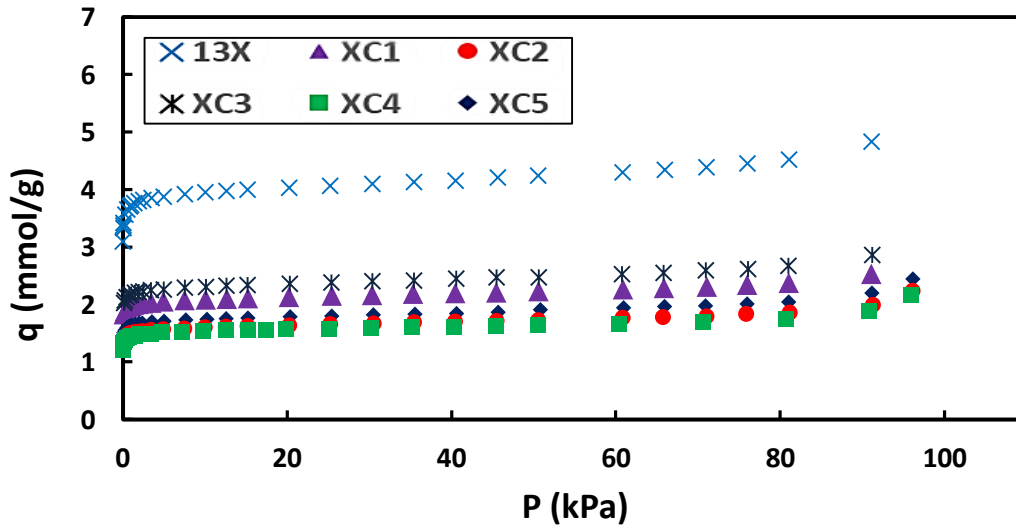


Figure 4.4 N₂ adsorption isotherms of MWCNT/13X compounds at 77K.

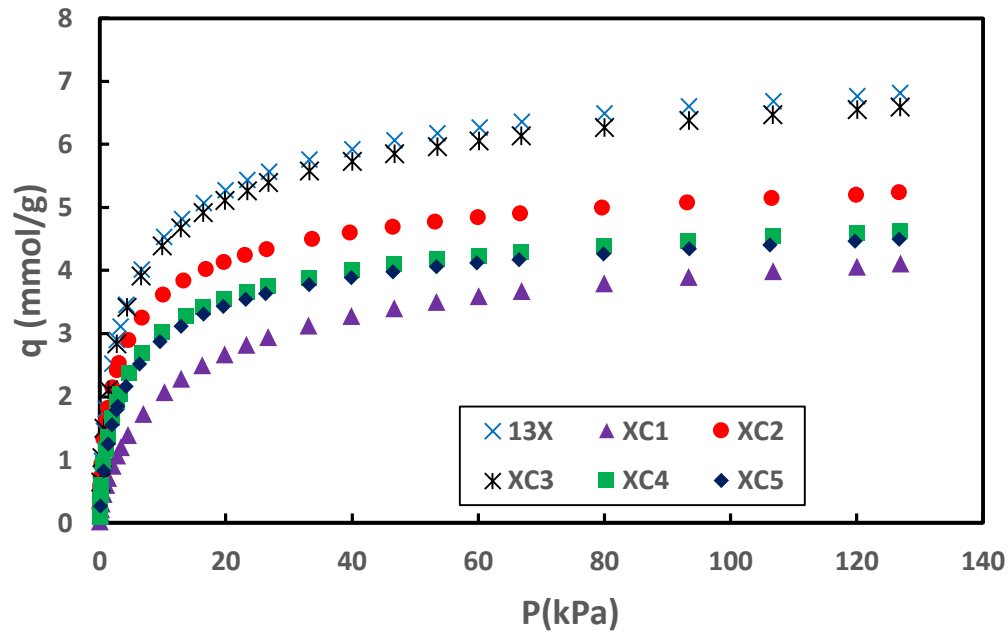


Figure 4.5 CO₂ adsorption isotherms of MWCNT/13X compounds at 273K.

The highest BET surface area is associated with 13X (about 1300 m²/g for N₂ and 573 m²/g for CO₂). The next highest BET is for XC3 (727 m²/g for N₂ and 552 m²/g for CO₂). In addition, the pore size is almost the same for the both cases (13X and XC3) by around 18.4 Å while the other MWCNT/13X compounds have almost close values to each other by about 20.75 Å. In terms of the pore volume, the maximum value associates 13X (about 0.6 cc/g) whereas all MWCNT/13X compounds have a pore capacity of about 0.3 cc/g, which could be interpreted as the low-size MWCNT particles less than 13X pore size may easily penetrate inside the 13X macropores.

Table 4.1 Pores characterization of the 13X incorporated with MWCNT.

Characterizations	13X	XC1	XC2	XC3	XC4	XC5
BET (m²/g) @ 77 K for N₂	1304	685.24	575.34	727.04	528.1	519.46
BET (m²/g) @273 K for CO₂	573.75	385.2	364.58	552.07	381.02	378.46
Average pore radius (Å)	9.189	10.14	10.57	9.3	10.53	10.26
Pore volume (cc/g)	0.599	0.243	0.304	0.257	0.278	0.267

The interesting adsorption isotherms have been collected for CO₂ and N₂ at ambient temperature (298 K) as shown in Figure 4.6 and Figure 4.7. Again, XC3 illustrates competitive adsorption values compared with pure 13X and better than the other CNT/13X mixtures attributable to maintain the same pore size of 13X (Table 26). CO₂ adsorption values, generally, are more selective than N₂. For instance, CO₂ adsorbed amount is about 3.7 mmol/g for XC5 at P=1.2 bar, while adsorbed quantity of N₂ at the same conditions is about 0.16 mmol/g. Consequently, 13X-based materials are considered as an excellent materials for CO₂ separation from flue gases. Another advantage of 13X (with/without MWCNTs) is an asymptotic trend of CO₂ adsorption values against the pressure indicating that high adsorption values could be obtained at low pressure, such as a partial pressure of CO₂ in a flue gas (between 10 - 20%).

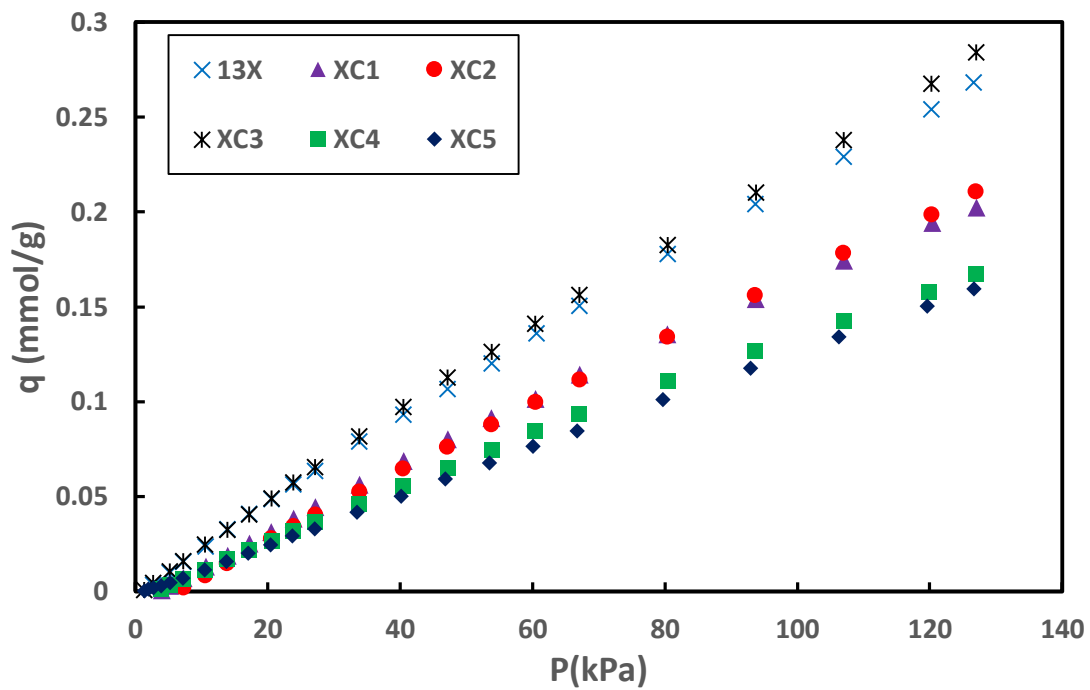


Figure 4.6 N₂ adsorption isotherms of CNT/13X compounds at 298 K.

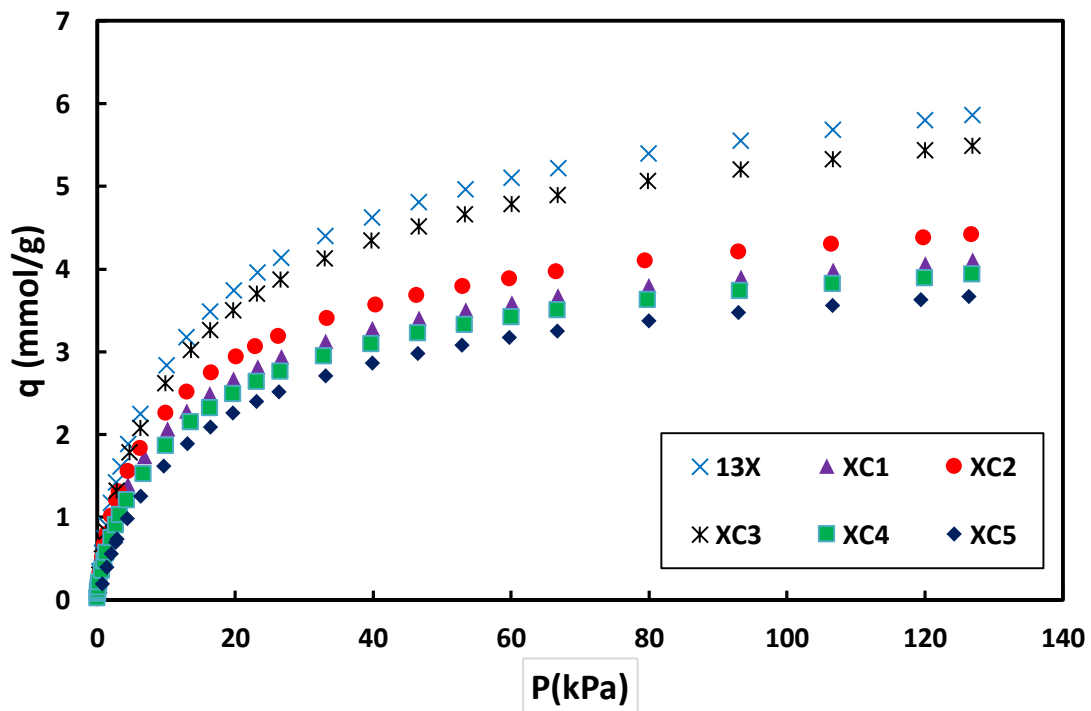


Figure 4.7 CO₂ adsorption isotherms of CNT/13X compounds at 298 K.

Figure 4.8 depicts the adsorption heat of CO₂ against the equilibrium adsorbed amounts for the all tested samples. The heat of adsorption is calculated using the Clausius-Clapeyron approach by the software associated with Autosorb (Quantachrome ASiQwin). The adsorption heat values trends are almost linear against CO₂ adsorbed amounts as shown in Figure 4.8. The highest values of adsorption heat are obtained during adsorbing CO₂ by XC3 ($\Delta H(\text{mean})=42.8$ kJ/mol), whereas 13X, XC1, XC2, XC4, and XC5 have average values of 36, 37.4, 31.9, 32.1, and 42.2 kJ/mol, respectively.

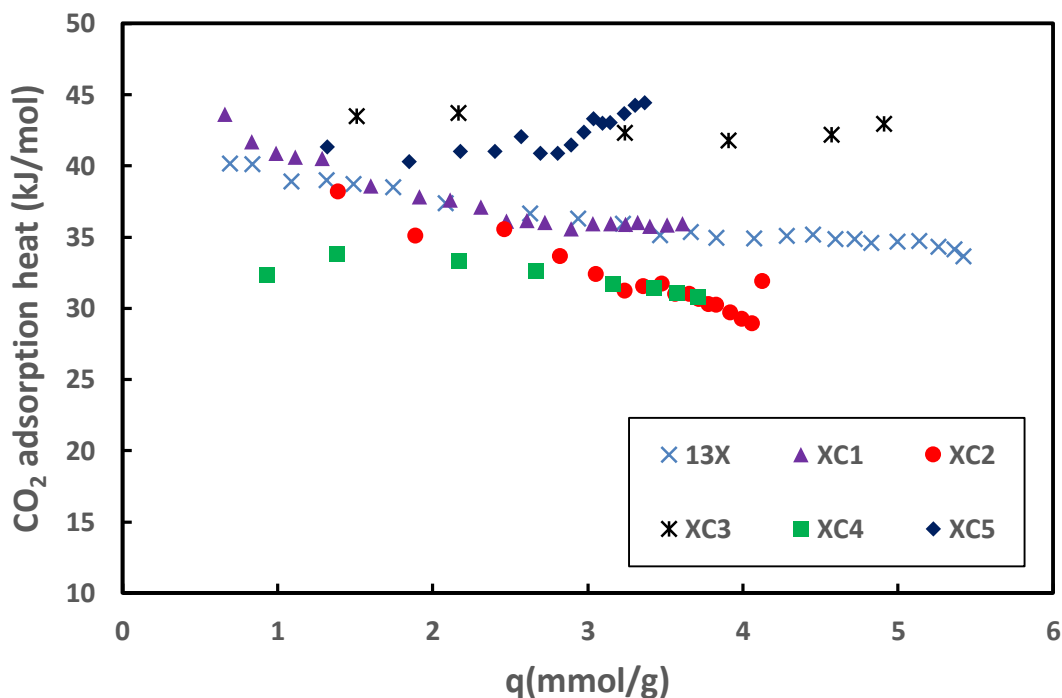


Figure 4.8 CO₂ heat of adsorption (ΔH) for CNT/13X compounds.

4.1.3 Experimental Adsorption Breakthrough of Test MWCNT/13X

In order to investigate the enhancements of the adsorption capacity and the carbon dioxide separation due to adding small amounts of MWCNT to the adsorbent (13X), breakthrough

experiments are carried out. For this purpose, 6 samples of MWCNT/13X compounds have been put inside a stainless steel bed (Length $L=20$ cm, Inner diameter $\varnothing=9$ mm); the bed is tested in ambient temperature of 297 K and other conditions mentioned earlier.

The first records of breakthrough curves for MWCNT/13X composites are shown in Figure 4.9. Indeed, there was a pressure drop may be caused by wrong packing. The pressure drops were monitored about 0.25, 0.38, 0.6, 0.7 and 0.75 bar and the samples densities were 0.462, 0.501, 0.503, 0.502, and 0.459 g/cc for 13X, XC1, XC2, XC3, and XC4, respectively. As shown by the CO₂ isotherms, the CO₂ adsorbed amounts increase dramatically by increasing the pressure values, especially for the partial pressure of CO₂ below 30 kPa. This includes the breakthrough inlet pressure (P_{CO_2} is about 20 kPa at 0.2 molar fraction of the inlet pressure). Therefore, we tried to keep the same operating condition for all the MWCNT/13X compounds. Moreover, the degassing process, before the adsorption process, was carried out at 423 K for 5 hours which is not sufficient to evacuate the adsorbent from any guest gases. For these types of experimental errors, we cannot consider the breakthrough curves, shown in Figure 4.9, sufficient to evaluate the effect of the incorporation of MWCNT with 13X. Therefore, we have repeated the experiments with new samples until reaching the most systematic one. In this case, the pressure drop is minimized to almost zero as optically observed by two bourdon gauges before and after the bed. The bed was filled with a constant packing density of about 0.553 cm³ cc/g for all the MWCNT/13X compounds. The samples pre-treated by heating process have been prolonged to be 20 hours at about 540 K under vacuum. The curves of the systematic experimental adsorption breakthrough test are exhibited in Figure 4.10. In these curves, the outlet concentration ratios of the both gases (CO₂/N₂) are plotted against the

operating time. For each sample, the concentration ratio of CO₂ remains at zero at the bed outlet for the first 15-20 minutes (depends on the sample) while the concentration ratio values of N₂ rise up to about 1.25 due to the absence of CO₂ which is being adsorbed into the MWCNT/13X bed. Eventually, the CO₂ concentration ratio increases up to 1 and decreases down to 1 that of N₂ after 15-20 minutes. It is noted from Figure 4.10 that a breakpoint, a level at which the concentration ratio is less than 5% at the bed outlet; has an optimal value (about 21 minutes) for XC3 compound. This value is consecutively followed by that of XC5, XC1, XC2 and XC4.

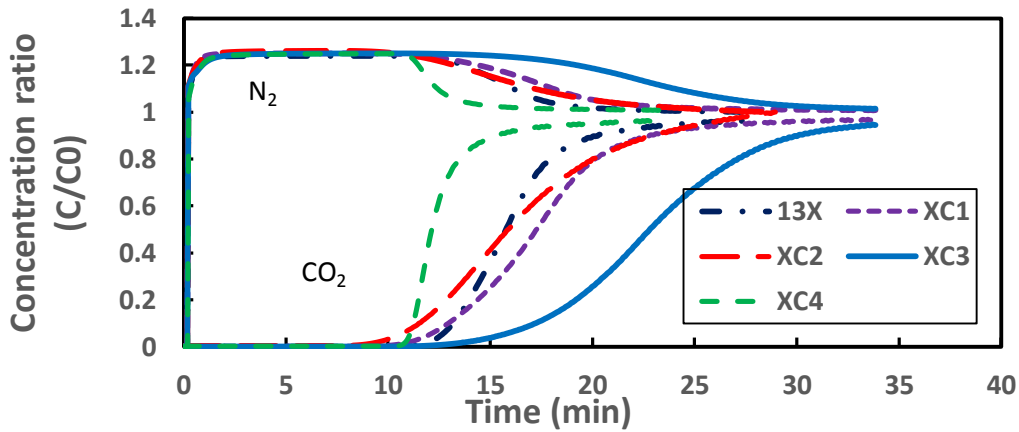


Figure 4.9 CO₂/N₂ breakthrough curves of MWCNT/13X compounds at 297 K with variable packing density, noticeable pressure drop and non-sufficient degasification process.

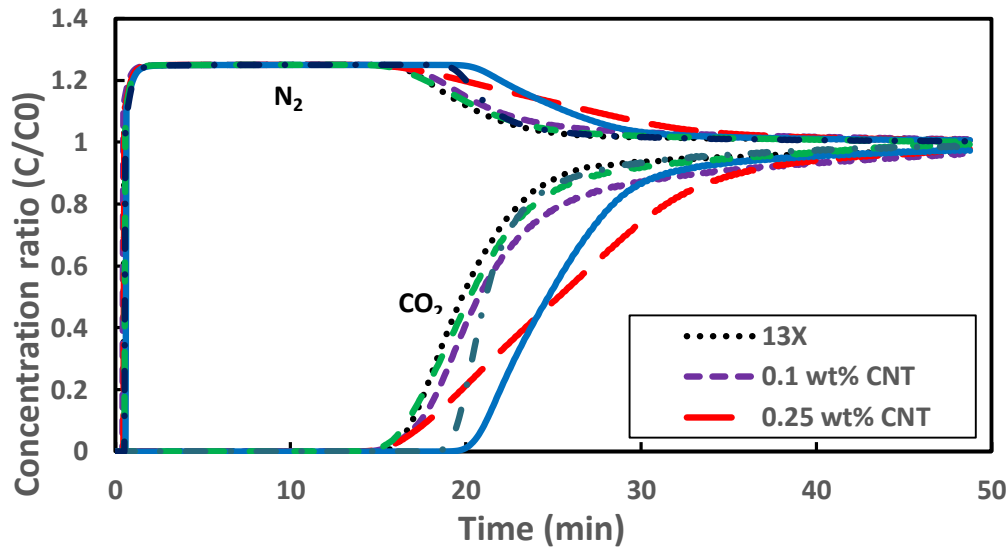


Figure 4.10 CO₂ breakthrough curves of MWCNT/13X compounds at 297K and 101.3kPa for the same amounts of adsorbents.

There is a noticeable variation of curves trends between breakpoints and saturation level, especially for XC2, XC3 and XC5; it is steeper for XC5, steady for XC2, and almost the same for 13X and XC3. This variation in the adsorption trends could be caused by many parameters such as; particle size, diffusion resistances, or thermal resistances. In general, large particle size or/and small diffusion coefficient slow down the breakthrough trend. For 13X, XC2, XC3 and XC5, we have estimated the diffusion time constant (D/rc^2 (s⁻¹): D is the inter-particle diffusivity (m²/s), rc is the adsorbent crystal radius (m)) from CO₂ kinetic curves measured by Dynamic Vapor Adsorption (DVS) for pressure range between 0-20 kPa and temperature of 298 K. The main results of the diffusion time constant and the average particle size are shown in Figure 4.11. The value of the diffusion time constant of XC2 is higher than that of 13X which may indicate to higher CO₂ uptake being adsorbed by XC2, while the larger value of the average particle size could be responsible for the decline of XC2 breakthrough curve compared with the trends of the other composites. For XC3, D/rc^2 has almost the same value of 13X indicating that the diffusion properties is

similar for both cases while the little bit smaller particle sizes for XC3 could make the breakthrough curve slightly steeper. The change in adsorption capacity for 13X and XC3 might be referred to the change in the thermal resistances. The particle size of XC5 has the smallest values which could make the breakthrough curve steepest, however, the low value of the diffusion time was expected to slow the trend. It is clear that there is sometimes interferences between the effects of the particle size and the diffusion resistance on the breakthrough trends.

The calculated adsorbed amounts of CO₂ from experimental breakthrough curves using Eq. 1 are displayed in Figure 4.12 as the ratio of improving the carbon dioxide adsorption capacity and separation breakpoint for all the MWCNT/13X compounds compared to the base sample (13X).

The improvement in the adsorption capacity values (Figure 4.12) shows that the XC2 has an optimum value of 22.6 % followed by about 21.6% for XC3. The carbon dioxide separation breakpoint enhancement gives all advantages to XC3 by about 25.3%. This value is followed by 17.1% associated with XC5. Consequently, XC3 has the resultant optimal values (adsorption capacity + adsorption breakpoint). It might be worth mentioning here that the higher value of the breakpoint, the greater value of adsorption heat as shown in Figure 4.8 and Figure 4.12. This is attributed to a higher quantity of adsorbed CO₂ that releases more heat during the adsorption process before it appears in the outlet.

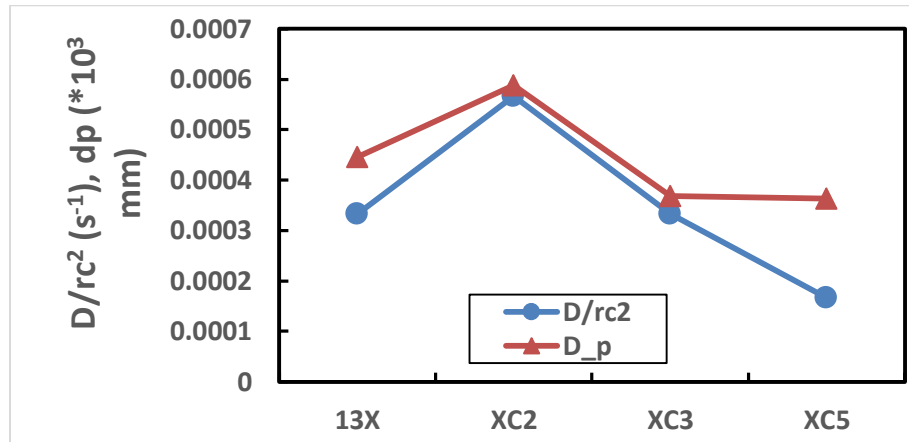


Figure 4.11 The average particle size (dp) and diffusion time constant (D/rc^2) for 13X, XC2, XC3 and XC5.

It is also believed that the enhancement in the carbon dioxide adsorption capacity and separation has been caused by improving the thermal conductivity of 13X after adding MWCNT to 13X [220-222]. The thermal conductivity of MWCNT is considerably very high; about 2000-5000 W/m.K [223], so that the effective thermal conductivity of MWCNT/13X composites could be improved accordingly.

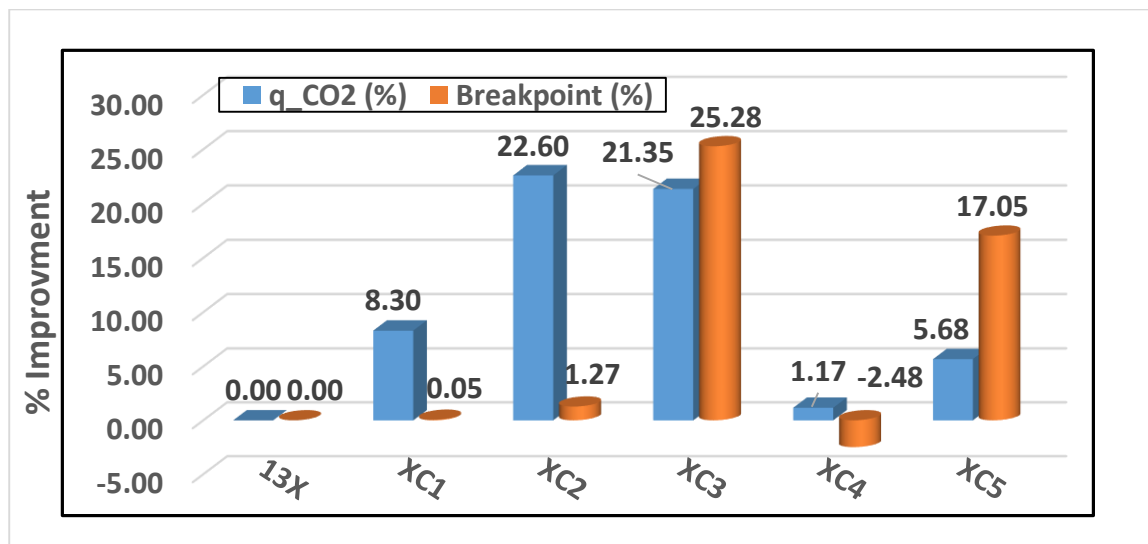


Figure 4.12 Carbon dioxide adsorption capacity (cubic bars) and separation breakpoint (cylindrical bars) improvements (percent) for MWCNT/13X compounds at 297 K and 1.013 bar.

4.2 Carbon Nanotubes/Mg-MOF-74 and Carbon Nanotubes/MIL-100(Fe) Composites

4.2.1 Powder X-ray Diffraction (PXRD) Analysis

Figure 4.13 shows the PXRD patterns of MWCNT/Mg-MOF-74 compounds with various weight fractions of MWCNTs as well as MIL-100(Fe). It can be seen (Figure 4.13(a)) that the PXRD pattern of MWCNT/Mg-MOF-74 and Mg-MOF-74 samples are in good agreement with the simulated pattern. The incorporation of MWCNTs does not result in any noticeable peak shift or decrease in the crystallinity of the framework, as all the characteristic peaks representative of the Mg-MOF-74 structure can also be observed in the patterns shown for each category of MWCNT/Mg-MOF-74 composite. Hence, it can be concluded that the incorporation of MWCNTs up to 1.5 wt. % using physical mixing preserves the characteristic lattice structure of the Mg-MOF-74 framework. The same conclusion was drawn for MWCNT/MIL-100(Fe) as reported in the recent work [224]. Figure 4.13(b) is to exhibit that the synthesized MIL-100(Fe) is in good agreement with the simulated pattern and to that reported in the literature [225].

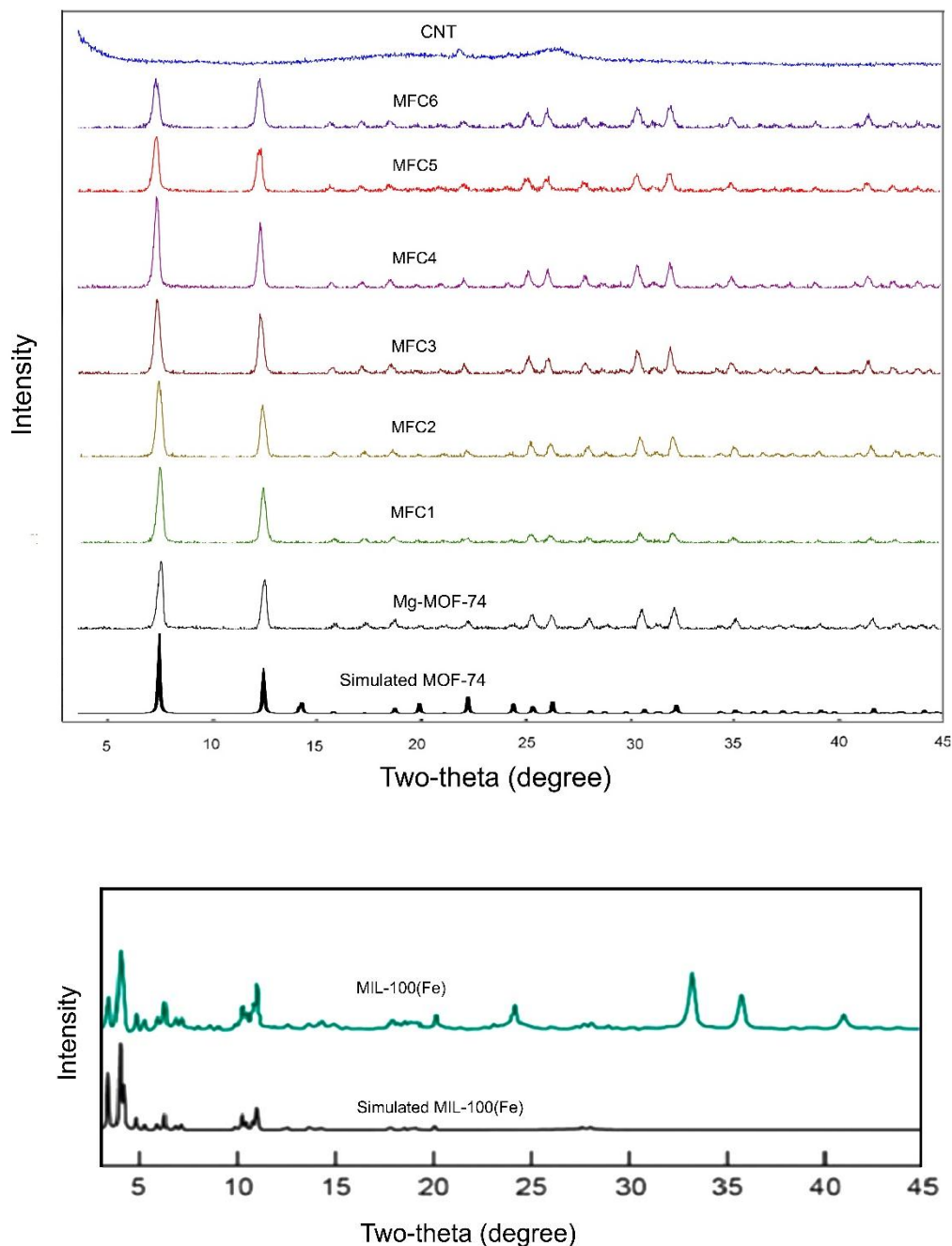


Figure 4.13 PXRD patterns for (a) MWCNT/Mg-MOF-74 and (b) MIL-100(Fe).

4.2.2 Adsorption Equilibrium Isotherms of Carbon Dioxide and Nitrogen

The N₂ equilibrium isotherms for the MWCNT/Mg-MOF-74 and MWCNT/MIL-100(Fe) composites have been measured at 77 K. Table 4.2 lists the important porosity-related

parameters estimated from the N₂ adsorption data MWCNT/Mg-MOF-74 and MWCNT/MIL-100(Fe) composites. The measured BET surface area was almost close to each other in MWCNT/Mg-MOF-74 compounds between 1470 and 1590 m²/g. In addition, the total pore volume measured at 95% relative pressure (P/P₀) and the pore size measured were determined to be almost the same for all the samples by around 0.63-0.71 cc/g and 19 Å, respectively. The Mg-MOF-74 BET surface area and total pore volume values are in good agreement with those reported in the literature [203, 226, 227]. It can be deduced from the data shown in Table 4.2 that the addition of MWCNTs does not result in substantial differences concerning its influence on the porosity-related parameters evaluated for the MWCNT/Mg-MOF-74 compounds. Likewise, the incorporation of MWCNTs with MIL-100(Fe) was not substantially changed the porosity-related parameters. There are almost slight increase in the surface area from 1083 m²g⁻¹ for base MIL-100(Fe) to 1464 m²g⁻¹ for MMC2. The total pore volume at 0.95 relative pressure was around 0.61 and 0.69 cc/g for MMC1 and MMC2, respectively, in comparison to 0.55 cc/g for the pristine MIL-100(Fe). Regarding the pore size, it is clearly that the pore diameter for all the MIL-100(Fe) and composite samples was around 20 Å. These porous-property values are close to those reported for MWCNT/MIL-100(Fe) composites [224].

The CO₂ adsorption isotherms for MWCNT/Mg-MOF-74 and MWCNT/MIL-100(Fe) composites, measured at 273, 298 and 313 K, are exhibited in Figure 4.15 and Figure 4.15. It is obvious that the adsorption uptake increases sharply in the region below 15 kPa and increases gradually with increasing adsorption pressure greater than 20 kPa. This behavior gives a good advantage for CO₂ capturing in low-pressure applications including the CO₂ separation from the flue gas (P_{CO₂}=10-20 kPa). However, as expected, an increase in the

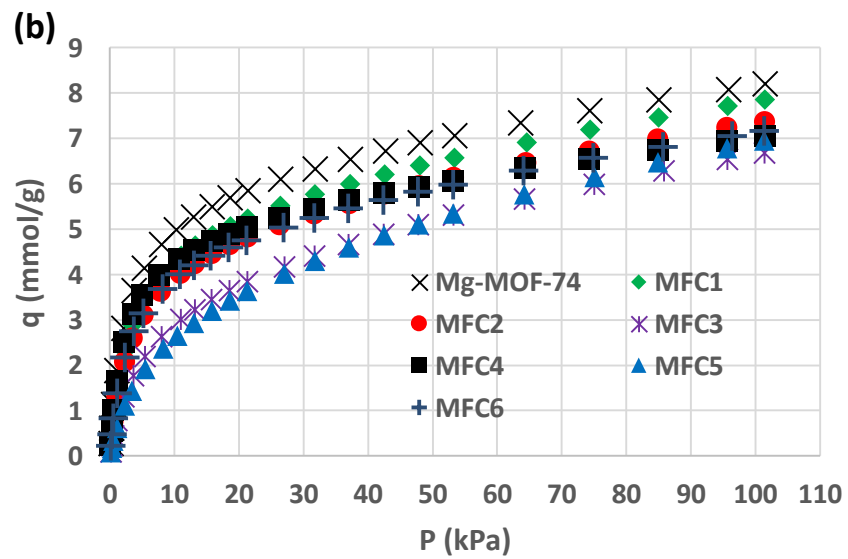
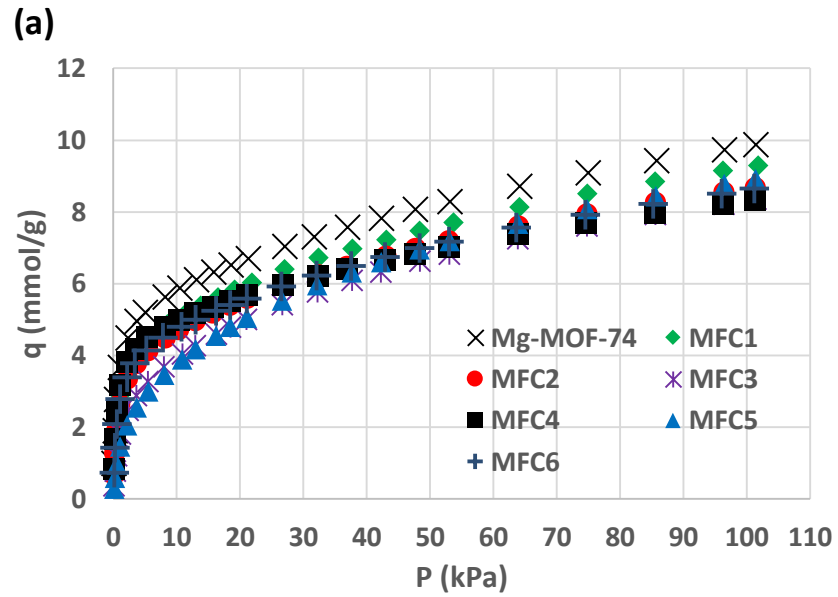
measured temperature shows an adverse effect on the recorded uptakes for each material. As obvious from, the highest CO₂ uptake has been measured for pristine Mg-MOF-74 followed by MFC1 at all the measured temperatures (273, 298, and 313 K). For MWCNT/MIL-100(Fe) compounds (Figure 4.15), the adsorption uptake increases more or less linearly with increasing adsorption pressure.

Table 4.2 Pores characterization of the MWCNT/Mg-MOF-74 and MWCNT/MIL-100(Fe) composites for N₂ at 77 K.

Characterizations	S_{BET} (m²/g)	Pore volume (cc/g)	Average pore radius (Å)
Mg-MOF-74	1518	0.63	8.31
MFC1	1545	0.66	8.55
MFC2	1525	0.65	8.51
MFC3	1579	0.67	8.51
MFC4	1562	0.71	8.51
MFC5	1586	0.69	8.73
MFC6	1477	0.63	8.52
MIL-100(Fe)	1083	0.55	10.07
MMC1	1248	0.61	9.74
MMC2	1464	0.69	9.52
MMC3	1060	0.58	10.94

It is obvious that MMC2 shows optimal adsorbed amounts, and MMC1 resulted in the second highest uptake even greater than the pristine MIL-100(Fe) and MMC3 composites as shown in Figure 4.15(a-c). It is worth mentioning here that the CO₂ uptake for

MWCNT/Mg-MOF-74 composites is much higher than that adsorbed by MWCNT/MIL-100(Fe) compounds.



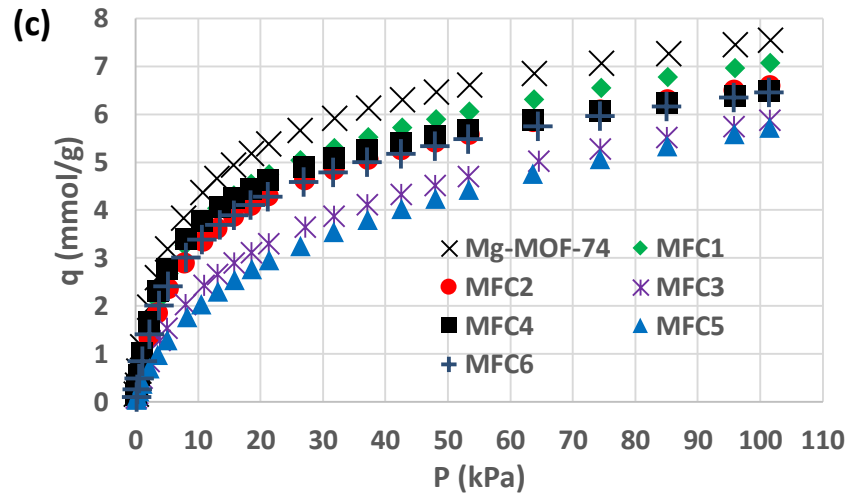
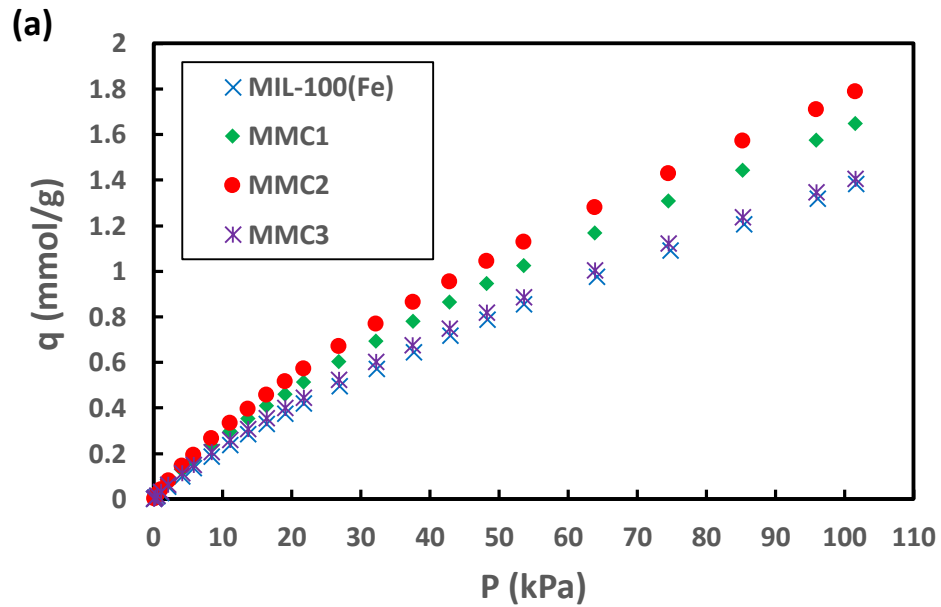


Figure 4.14 CO₂ adsorption isotherms of MWCNT/Mg-MOF-74 composites at: (a) 273 K, (b) 298 K, and (c) 313 K.



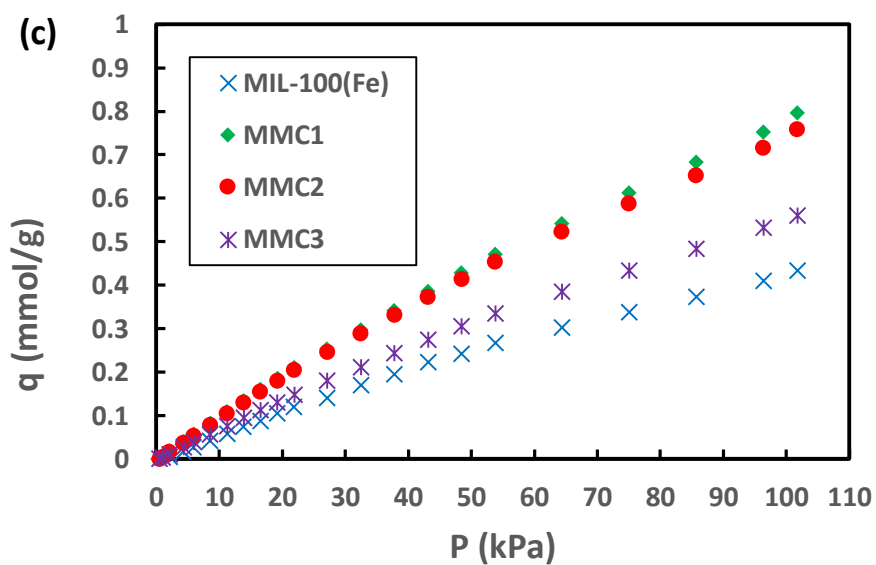
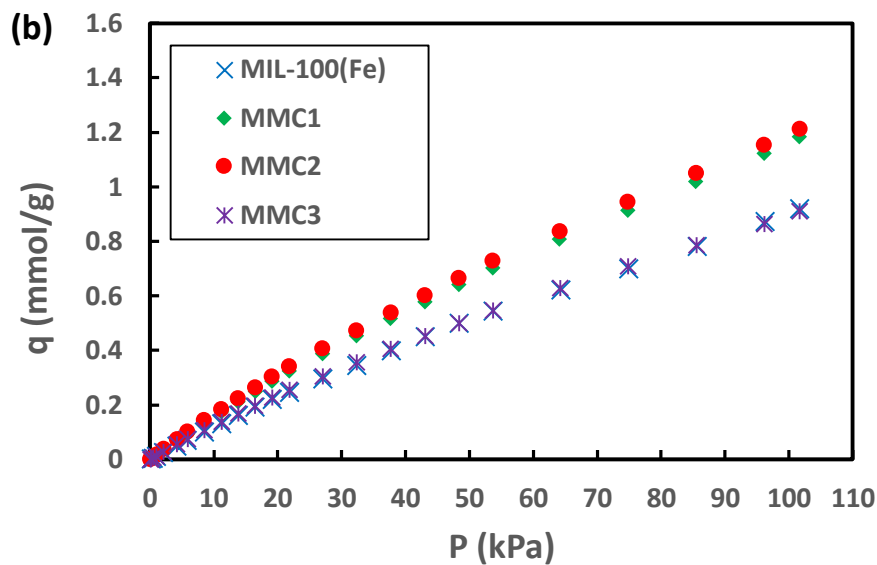


Figure 4.15 CO₂ adsorption isotherms of MWCNT/MIL-100(Fe) composites at: (a) 273 K, (b) 298 K, and (c) 313 K.

The N₂ adsorption isotherms for MWCNT/Mg-MOF-74 composites, measured at 298 K, are displayed in Figure 4.16(a). It is evident that the pristine Mg-MOF-74 exhibits the largest uptake amount, followed by MFC4, MFC1, MFC6, MFC2, MFC5, and MFC3, respectively. Figure 4.16(b) shows N₂ uptake by MWCNT/MIL-100(Fe) compounds. It is

clear that MMC1 has higher adsorbed values in comparison to the other compounds. For both adsorbent composites (MWCNT/Mg-MOF-74 and MWCNT/MIL-100(Fe)), the maximum uptake measured for N₂ is observed to be significantly smaller than that measured earlier for CO₂. In other words, all the samples have been noticed to exhibit preferential selectivity of CO₂ over the N₂.

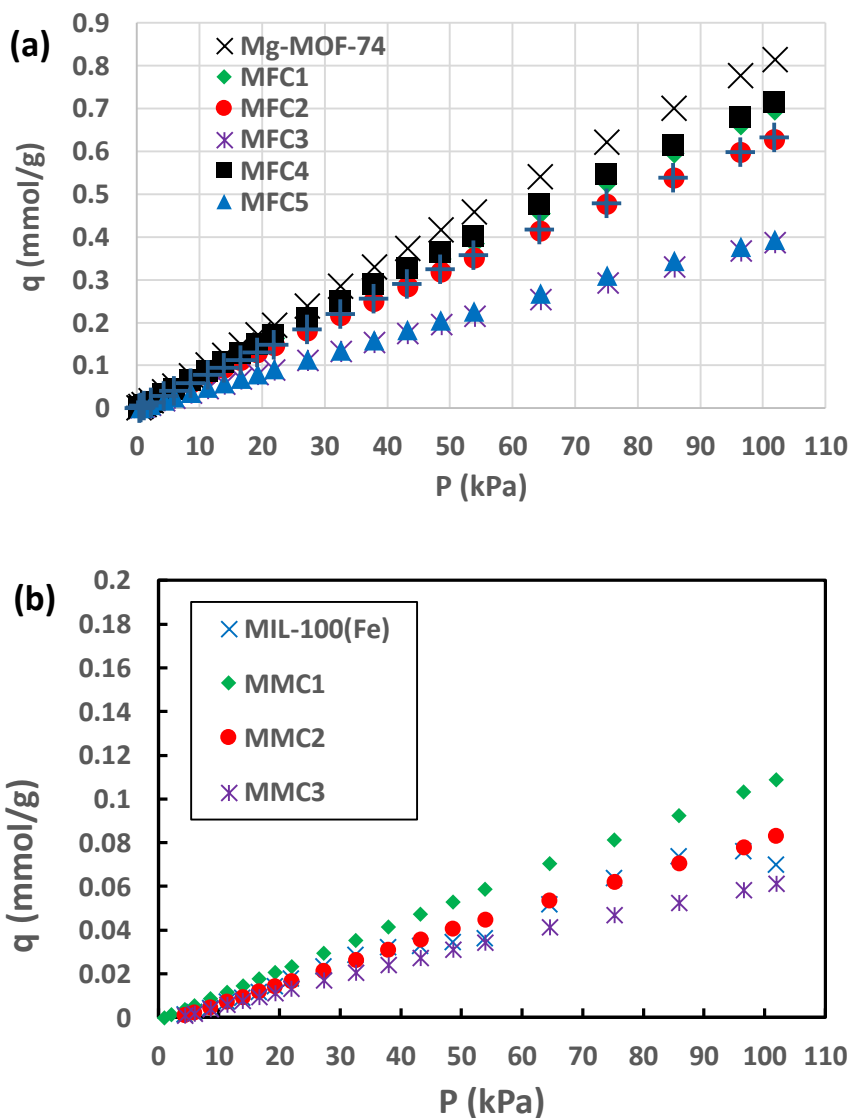
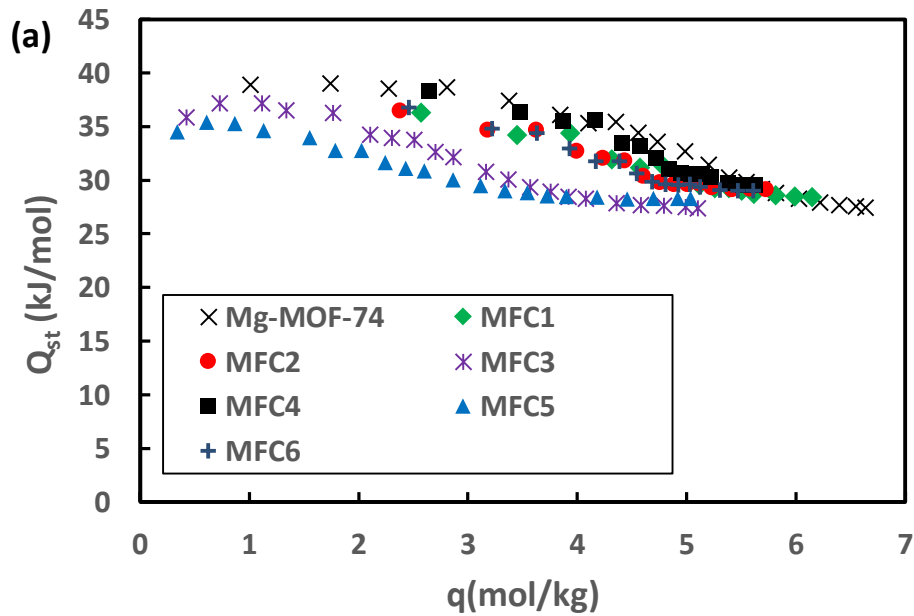


Figure 4.16 N₂ adsorption isotherms at 298 K for (a) MWCNT/Mg-MOF-74 and (b) MWCNT/MIL-100(Fe) composites.

Figure 4.17(a and b) depicts the variation of heat of adsorption for CO₂, Q_{st} , against the instantaneous CO₂ uptake for MWCNT/Mg-MOF-74 and MWCNT/MIL-100(Fe) composites. For MWCNT/Mg-MOF-74, the Q_{st-CO_2} values are observed to exhibit a more or less curvilinear correlation with the instantaneous CO₂ uptake as shown in Figure 4.17(a). In general, Q_{st-CO_2} values locate between 25 and 40 kJ/mol; the high values are sequentially associated with Mg-MOF-74, MFC4, MFC2, and MFC5. In contrast, MFC5 and MCF3 show lower values of CO₂ adsorption heat. The MWCNT/MIL-100(Fe) composites have CO₂ adsorption heat values recorded between 15 and 48 kJ/mol (Figure 4.17(b)); the highest values were measured for MIL-100(Fe) about 24 kJ/mol (for $q > 0.2$ mmol/g) and the lowest obtained by MMC1 about 15 kJ/mol (for $q > 0.18$ mmol/g).



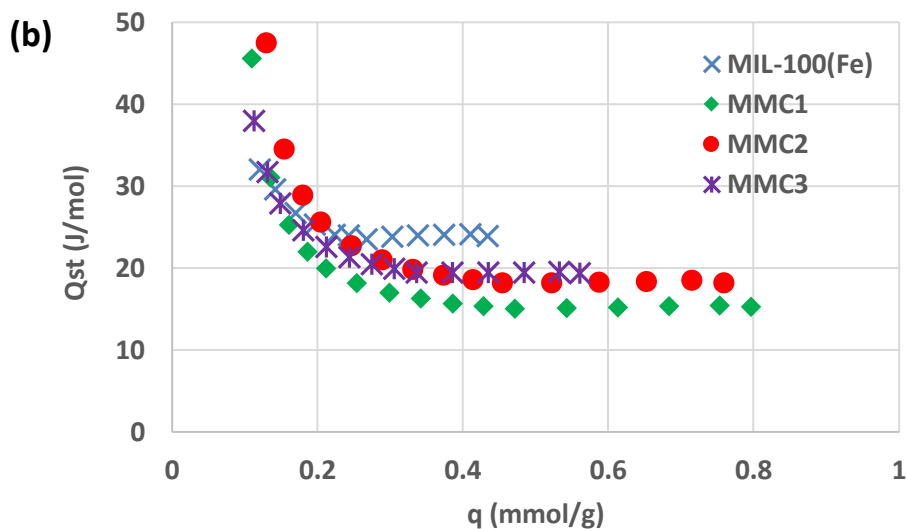


Figure 4.17 CO₂ heat of adsorption (Q_{st}) (a) MWCNT/Mg-MOF-74 and (b) MWCNT/MIL-100(Fe) composites.

4.2.3 Experimental Adsorption Breakthrough Test for MWCNT/Mg-MOF-74 and MWCNT/MIL-100(Fe) Composites

Breakthrough experiments have been performed for the binary gas (CO₂/N₂) in order to quantify the improvements in CO₂ adsorption uptake and breakpoint as a result of the incorporation MWCNTs inside Mg-MOF-74 and MIL-100(Fe). In a typical procedure, predetermined amounts of MWCNT/Mg-MOF-74 and MWCNT/MIL-100(Fe) composite samples are first transferred to a stainless steel tube (Length L=7 cm, Inner diameter Ø=4 mm). All breakthrough experiments have been performed at ambient temperature of 297 K.

For systematic tests, the pressure drop is minimized to almost zero as optically observed by two bourdon gauges before and after the bed. The bed was filled with almost constant packing density about 0.292±0.005 and 0.842±0.002 g/cc for MWCNT/Mg-MOF-74 and

MWCNT/MIL-100(Fe) compounds, respectively. The samples have been pre-treated by heating process for 20 hours at about 423 K under vacuum. The experimentally measured CO₂ and N₂ adsorption breakthrough curves for MWCNT/Mg-MOF-74 and MWCNT/MIL-100(Fe) composites are displayed in Figure 4.18. As evident, the outlet concentration ratios calculated each of these two gases have been plotted against the measurement time. In general, it was observed in all the tested samples that the concentration ratio evaluated for CO₂ at the bed outlet keeps constant at zero for some time (e.g. about 6-7 min for MWCNT/Mg-MOF-74 and 2-3 min for MWCNT/MIL-100(Fe) compounds), whereas the concentration ratio for N₂ increased up to about 1.3 owing to the absence of CO₂ which was pre-adsorbed into the Mg-MOF-74 or MIL-100(Fe) composite adsorbent bed. Following the first adsorption minutes of measurement time, the CO₂ concentration ratio was observed to increase up to 1, whereas the concentration ratio of N₂ was evaluated to gradually drop to a value close to 1. For MWCNT/Mg-MOF-74 composites, the optimal value of the breakpoint, a time at which the concentration ratio of the bed outlet is evaluated to be less than 5%, was measured to be about 8.16 minutes for MFC6. This is followed by the value measured for MFC4 of about 8.1 minutes, and then by 7.96 minutes for MFC1 (Figure 4.18(a)). In the same manner, the highest breakthrough breakpoint obtained by MWCNT\MIL-100(Fe) is associated with MMC2 by about 3.21 minutes (Figure 4.18(b)). The next breakthrough point is obtained by MMC1 at about 3.19 minutes, and, then, by pristine MIL-100(Fe) at about 2.9 minutes.

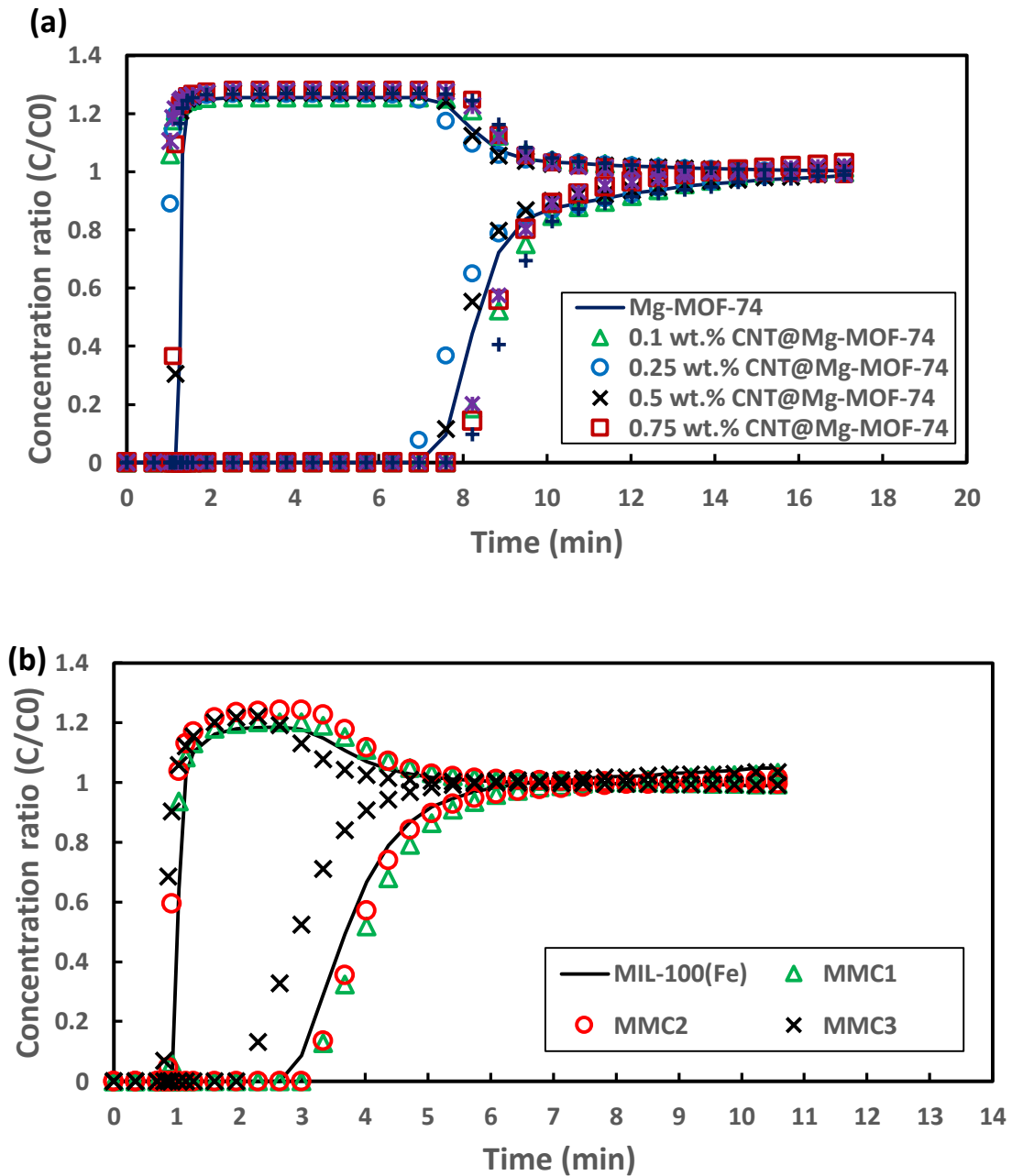


Figure 4.18 Breakthrough curves for (a) MWCNT/Mg-MOF-74 composites for CO₂/N₂ (0.2/0.8 v/v) and (b) MWCNT/MIL-100(Fe) composites for CO₂/N₂ (0.15/0.85 v/v), measured at 297 K and 101.3 kPa.

In order to evaluate the improvement in CO₂ adsorption capacity and breakpoint by adding MWCNT to Mg-MOF-74 and to MIL-100(Fe), the adsorbed amounts of CO₂ have been calculated from the experimental breakthrough curves using Eq. 1. The maximum CO₂

adsorption capacity for base Mg-MOF-74 and MIL-100(Fe) calculated from the respective breakthrough curve were estimated to be about 5.46 and 0.33 mmol/g, respectively. The maximum CO₂ uptakes along with the adsorption breakpoint ratios for Mg-MOF-74 as well as each of the six MWCNT/Mg-MOF-74 composites are displayed in Figure 4.19(a). As evident, each of the six composites, except MFC2 and MFC3, exhibit a good improvement over pristine Mg-MOF-74 with regards to both the adsorption capacity and the adsorption breakpoint ratio values. More specifically, the most optimum combination of adsorption capacity and breakpoint ratio values have been evaluated for MFC6 which has shown an improvement of 7.4% and 8.0% over pristine Mg-MOF-74 for adsorption capacity and breakpoint ratio, respectively. This pair of statistics is followed by MFC1, MFC4 and MFC5 composites for which the corresponding improvements in adsorption capacity and breakpoint values over pristine Mg-MOF-74 have been evaluated to be 4.4% and 5.7%, 2.2% and 7.3%, and 1.5% and 5.0%, respectively. It is worth mentioning here that each of the MFC6, MFC1 and MFC4 composites has already been characterized for lower values of heat of adsorption for CO₂ in comparison with pristine Mg-MOF-74 as shown earlier in Figure 4.17(a). This, theoretically, implies that each of these composites should not only exhibit higher CO₂ uptake values than pristine Mg-MOF-74, but also require comparatively lower energy for regeneration process (recycling recovery).

Figure 4.19(b) shows the improvement in both adsorption capacity and breakpoint due to adding MWCNT to the pristine MIL-100(Fe). As evident, MMC1 exhibit an optimal improvement reaches 12.0% and 9.2% for CO₂ adsorption capacity and breakpoint, respectively. This improvement is followed by MMC2 measured adsorption uptake and breakpoint of about 8.7% and 9.5%, respectively, comparing with the base adsorbent (MIL-

100(Fe)). On the contrary, the evaluated adsorption uptake and breakpoint improvement values for MFC2, MFC3 and MMC3 show lower performance than the base adsorbents. This attribute indicates that there is no a uniform improvement can be obtained for the incorporation of CNT with MOFs. The detected improvement in the CO₂ adsorption capacity and breakpoint primarily refers to an improvement in the thermal properties of Mg-MOF-74 and MIL-100(Fe) frameworks upon the incorporation of MWCNTs [220-222]. The thermal conductivity of MWCNT is considerably very high about 2000-5000 W/m.K [223], so that the effective thermal conductivity of MWCNT/Mg-MOF-74 and MWCNT/MIL-100(Fe) composites could be improved accordingly.

In the literature, chemists use the adsorption isotherm data to compare the CO₂ capacities of different adsorbents. However, we found out by carrying both adsorption isotherm measurements and adsorption breakthrough experiments that they can give different ratings of adsorption capacity. Keeping in mind that adsorption isotherm measurements are taken under constant temperatures while the breakthrough measurements are not, as the breakthrough bed is allowed to vary its temperature due to the heat dissipation from the adsorbent to the ambient or surrounding environments. The most accurate adsorption capacity if we are joining to use a PSA/VSA/TSA is that measured in a breakthrough set-up.

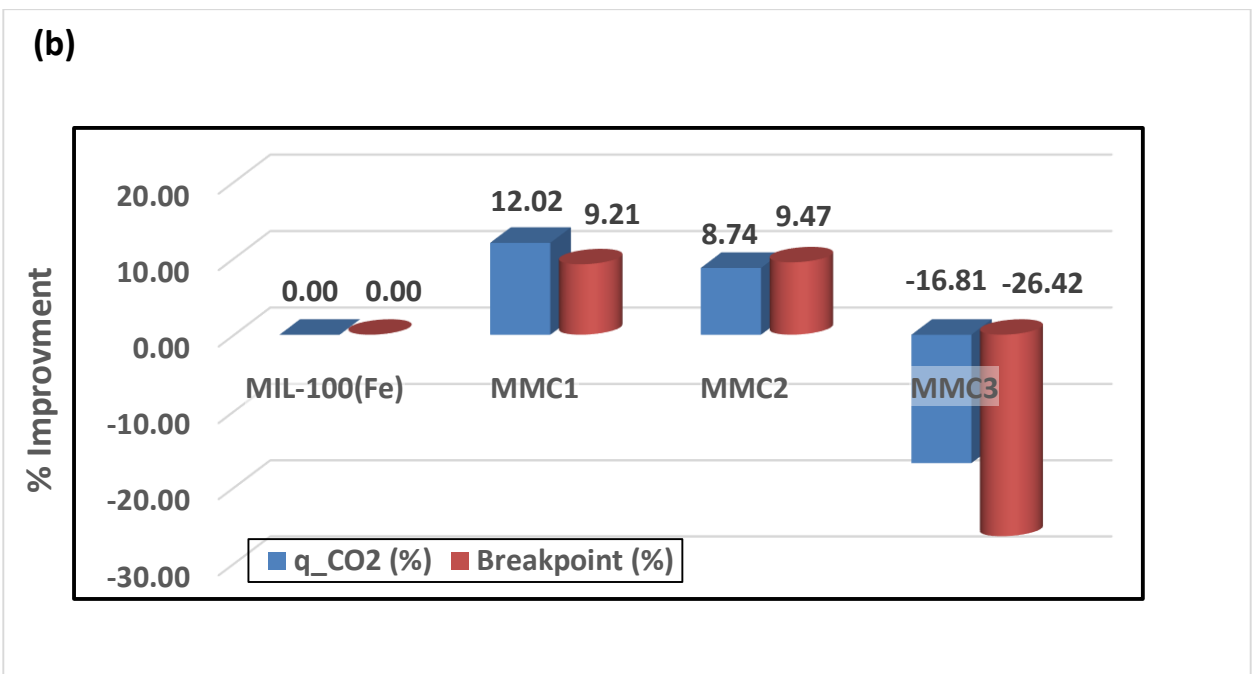
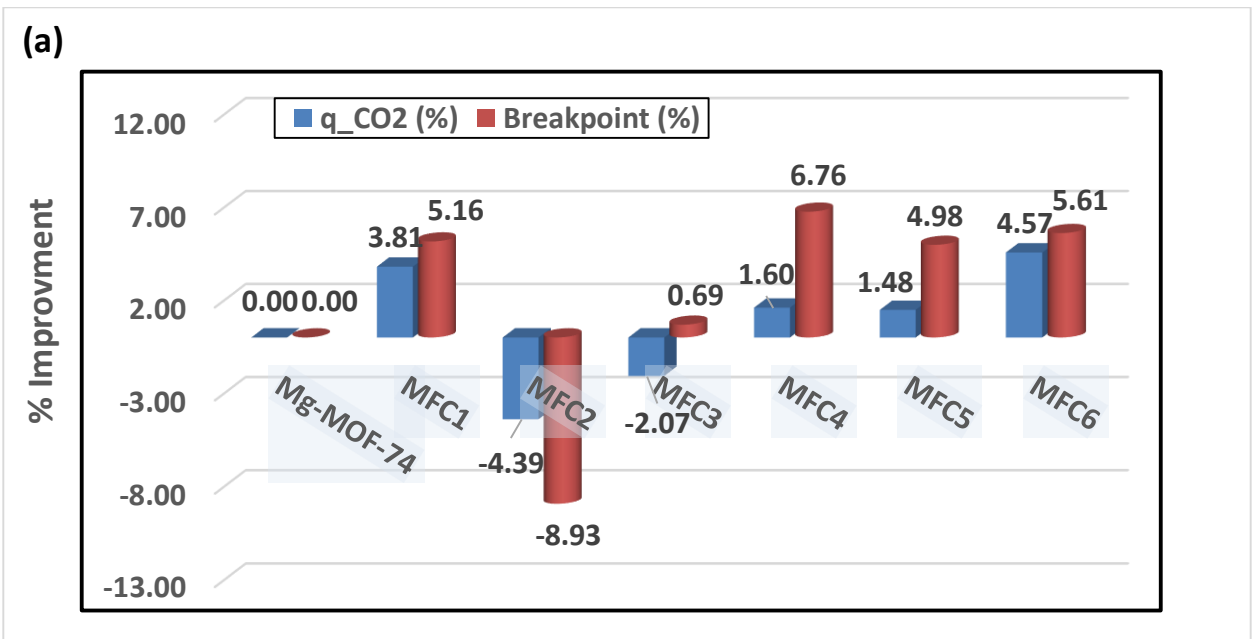


Figure 4.19 Carbon dioxide adsorption capacity (cubic bars) and breakpoint (cylindrical bars) improvements (percent) for (a) MWCNT/Mg-MOF-74, and (b) MWCNT/MIL-100(Fe) composites measured at 297 K.

4.3 Carbon Nanotubes/MIL-101(Cr) Composites

4.3.1 Powder X-ray Diffraction (PXRD) Analysis

Table 4.3 shows the PXRD profiles of MWCNT/MIL-101(Cr) composite with various weight fractions of MWCNTs. The PXRD profile of acid-treated MWCNTs has also been added as the benchmark. It can be seen that the PXRD pattern of MIL-101(Cr) is in good agreement with the simulated pattern and the one reported in literature for similar method used for synthesis [225]. The incorporation of MWCNTs does not result in any noticeable peak shift or decrease in the crystallinity of the framework, as all the characteristic peaks representative of the MIL-101(Cr) structure can also be observed in the patterns shown for each category of MWCNT/MIL-101(Cr) composite. Hence, it can be concluded that the incorporation of MWCNTs up to 8 wt% using an *in-situ* synthesis method preserves the characteristic lattice structure of the MIL-101(Cr) framework.

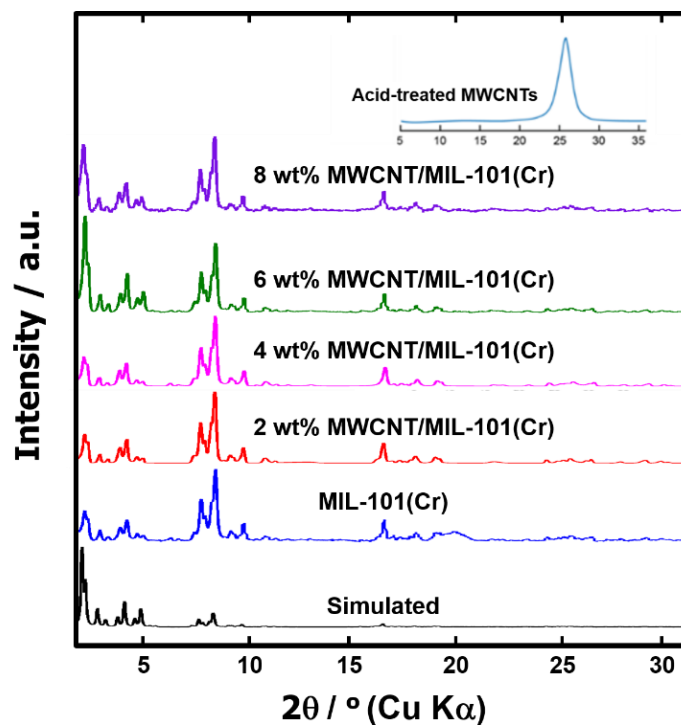


Figure 4.20 PXRD patterns for MIL-101(Cr) and MWCNT/MIL-101(Cr) composites.

4.3.2 Adsorption Equilibrium Isotherms of Carbon Dioxide and Nitrogen

The N_2 physisorption isotherms for MIL-101(Cr) and the MWCNT/MIL-101(Cr) composites have been measured at 77 K. Table 4.3 lists the important porosity-related parameters evaluated from the N_2 adsorption/desorption data for MIL-101(Cr) and each of the four MWCNT/MIL-101(Cr) composites. The highest BET surface area was measured for 4 wt% MWCNT/MIL-101(Cr) of about $4004 \text{ m}^2/\text{g}$, followed by pristine MIL-101(Cr) which showed almost $3750 \text{ m}^2/\text{g}$. This value of the pristine adsorbent is close to the reported values for MIL-101(Cr) [228, 229]. The lowest BET surface area was evaluated for 8 wt% MWCNT/MIL-101(Cr) composite showing almost 35% lower surface area than pristine MIL-101(Cr). In contrast, the highest total pore volume, at a relative pressure of $P/P_0 = 0.95$, was measured for the 4 wt.% MWCNT/MIL-101(Cr) composite of about 2.1

cc/g, which is an improvement of 5.9% over pristine MIL101(Cr), while the three remaining composites exhibited lower pore volume values. The average pore size measured in terms of diameter was determined to be almost the same for all the samples around 20.9 Å. Hence, it can be deduced from the data shown in Table 4.3 that the addition of MWCNTs does not result in a well-defined trend concerning its influence on the porosity-related parameters evaluated for the MWCNT/MIL-101(Cr) composites.

The CO₂ adsorption/desorption isotherms for MIL-101(Cr) and the MWCNT/MIL-101(Cr) composites, measured at 273, 298 and 313 K, are shown in Figure 4.21 - Figure 4.23. It is obvious that the adsorption uptake increases more or less linearly with increasing adsorption pressure. However, as expected, an increase in the measurement temperature shows an adverse effect on the recorded uptakes for each material. As obvious from Figure 4.21 - Figure 4.23, the highest CO₂ uptake has been measured for the 2 wt.% MWCNT/MIL-101(Cr) composite at 273 K. The pristine MIL-101(Cr) resulted in the second highest uptake, followed by 4, 6, and 8 wt% MWCNT/MIL-101(Cr) composites respectively. For instance, the uptake amounts recorded at 298 K and 20 kPa are observed to be about 1.2, 1, 0.65, 0.58, and 0.51 mmol/g for 2, 4, 6, and 8 wt% MWCNT/MIL-101(Cr) composites, respectively.

Table 4.3 Pores characterization of the MWCNT/MIL-101(Cr) composites for N₂ at 77 K.

Characterizations	S_{BET} (m²/g)	Pore volume (cc/g)	Average pore radius (Å)
MIL-101(Cr)	3745	1.95	10.5
2 wt% MWCNT/MIL-101(Cr)	3146	1.63	10.4
4 wt% MWCNT/MIL-101(Cr)	4004	2.07	10.3
6 wt% MWCNT/MIL-101(Cr)	3307	1.77	10.7
8 wt% MWCNT/MIL-101(Cr)	2446	1.26	10.3

The N₂ adsorption isotherms for MIL-101(Cr) and MWCNT/MIL-101(Cr) composites, measured at 298 K, are displayed in Figure 4.24. It is evident that a loading of 2 wt.% MWCNTs in MIL-101(Cr) exhibits the largest uptake amount, followed by pristine MIL101(Cr), 4 wt.%, 6 wt.%, and 8 wt.% MWCNT/MIL-101(Cr) composites, respectively. It is worth mentioning here that the same sequence was previously observed regarding CO₂ uptake at 298 K, except the fact that the maximum uptake measured for N₂ is observed to be significantly smaller than that measured earlier for CO₂. In other words, all the samples have been noticed to exhibit preferential selectivity of CO₂ over N₂.

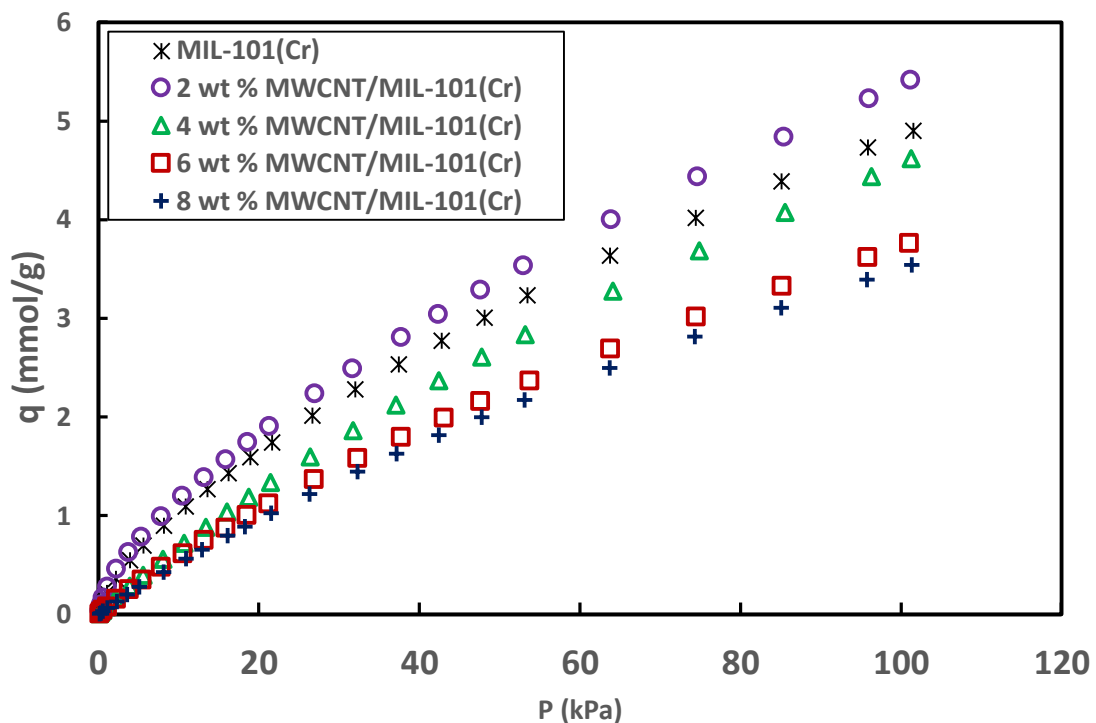


Figure 4.21 CO₂ adsorption isotherms of MWCNT/MIL-101(Cr) composites at 273K.

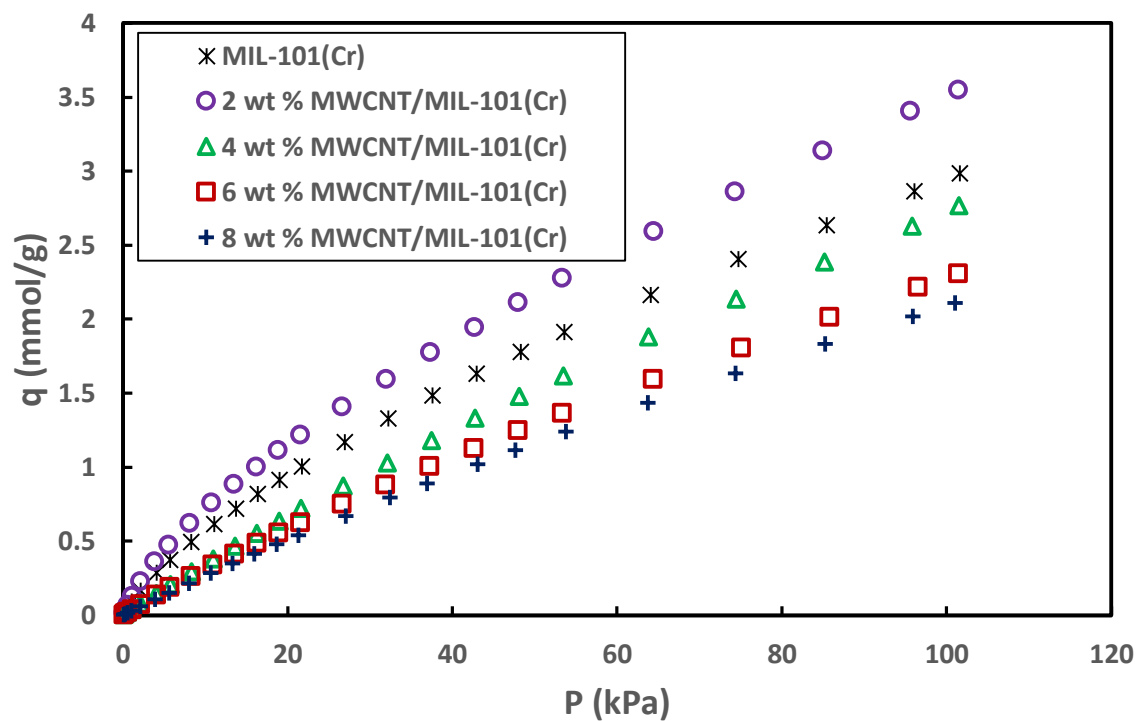


Figure 4.22 CO₂ adsorption isotherms of MWCNT/MIL-101(Cr) composites at 298 K.

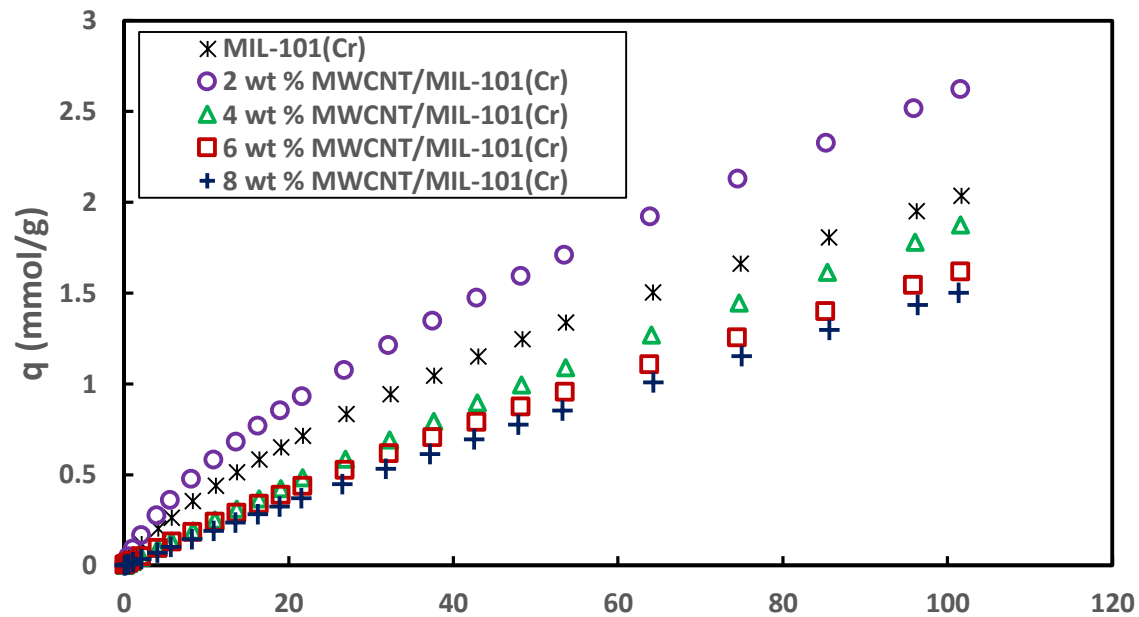


Figure 4.23 CO₂ adsorption isotherms of MWCNT/MIL-101(Cr) composites at 313 K.

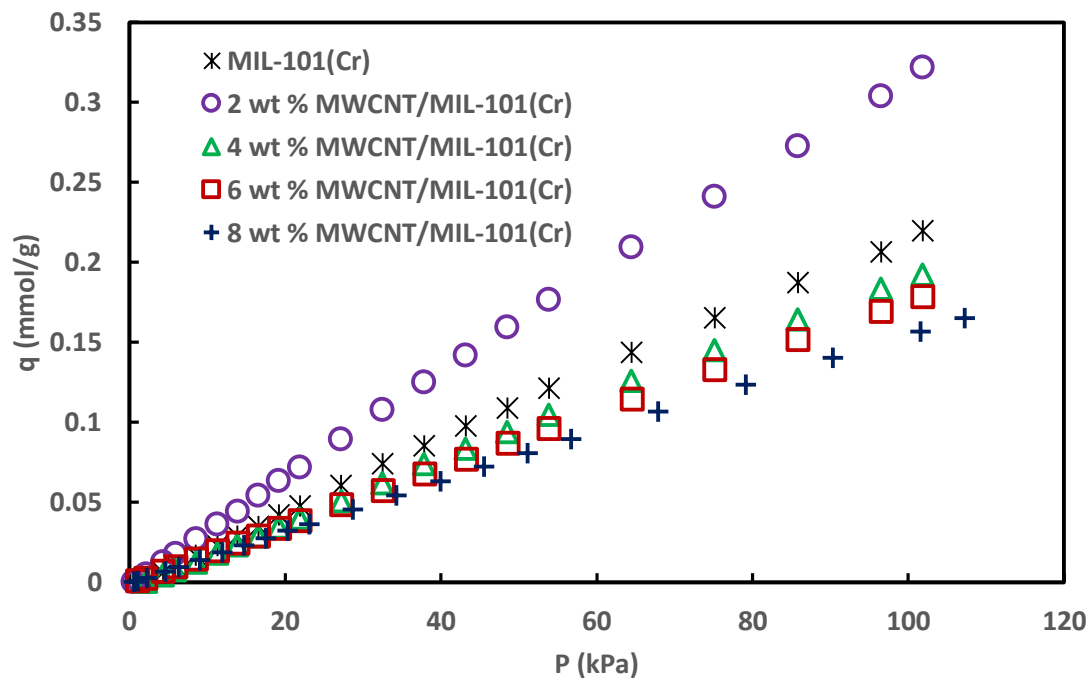


Figure 4.24 N₂ adsorption isotherms of MWCNT/MIL-101(Cr) composites at 298 K.

Figure 4.25 depicts the variation of heat of adsorption for CO₂, Q_{st} , against the instantaneous CO₂ uptake for MIL-101(Cr) and MWCNT/MIL-101(Cr) composites. For MIL-101(Cr), the Q_{st} values are observed to exhibit a more or less linear correlation with the instantaneous CO₂ uptake as shown in Figure 4.25. In contrast, the MWCNT/MIL-101(Cr) composites, after a steep initial increase in Q_{st} till an uptake of almost 0.2 mmol/g, result in a more or less constant value of Q_{st} of about 23 kJ/mol for all values of instantaneous uptake higher than 0.2 mmol/g. In a nutshell, the pristine MIL-101(Cr) results in increasingly higher heat of adsorption values for CO₂ than MWCNT/MIL-101(Cr) composites with steadily increasing values of the instantaneous uptake when the Clausius-Clayperon equation is employed for the heat of adsorption calculation.

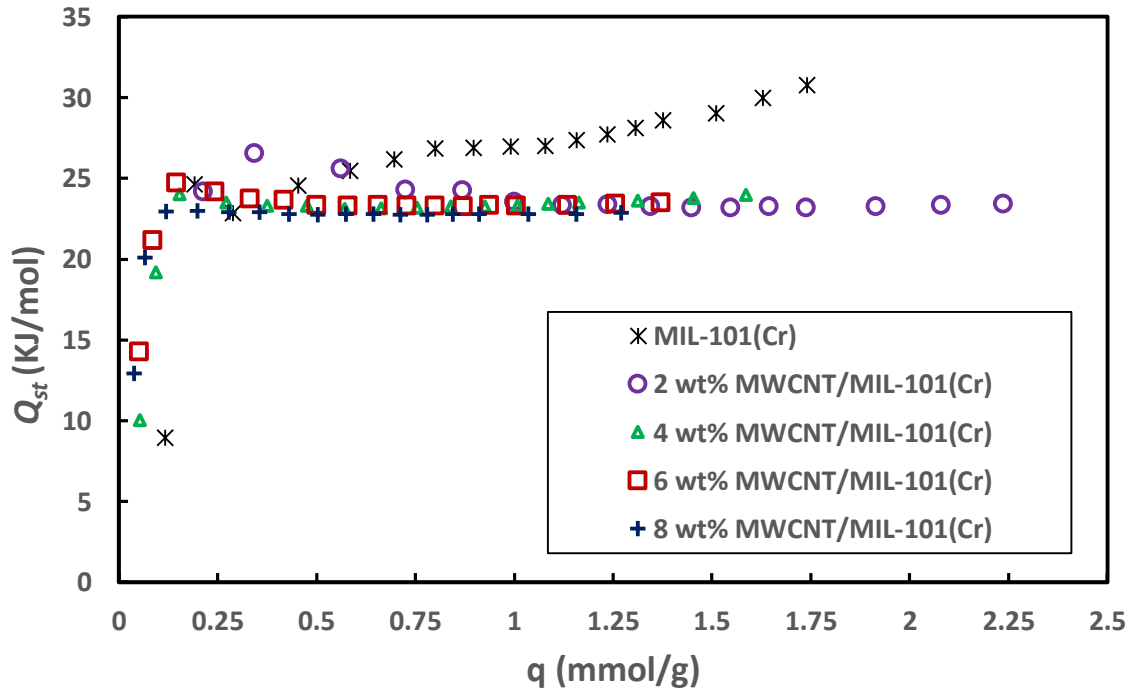


Figure 4.25 CO₂ heat of adsorption (Q_{st}) for MWCNT/MIL-101(Cr) composites.

4.3.3 Experimental Adsorption Breakthrough Test for MIL-101(Cr) and MWCNT/MIL-101(Cr) Composites

In order to quantify the improvements of in CO₂ adsorption capacity as well as breakpoint during CO₂/N₂ separation as a result of the incorporation MWCNTs inside MIL-101(Cr), CO₂ breakthrough experiments have been performed. In a typical procedure, predetermined amounts of MIL-101(Cr) and MWCNT/MIL-101(Cr) composite samples are first transferred to a stainless steel tube (Length L=14 cm, Inner diameter \varnothing =4 mm). All breakthrough experiments have been performed at ambient temperature of 297 K.

The experimentally measured CO₂ and N₂ adsorption breakthrough curves for MIL-101(Cr) and MWCNT/MIL-101(Cr) composites are displayed in Figure 4.26. The outlet concentration ratios calculated each of these two gases have been plotted against the measurement time Fig. 13(b). In general, it was observed for all the tested samples that the concentration ratio evaluated for CO₂ at the bed outlet keeps constant at zero for the first 2.5-3.4 minutes Figure 4.26, whereas the concentration ratio for N₂ increased up to about 1.3 owing to the absence of CO₂ which was pre-adsorbed into the MWCNT/MIL-101(Cr) composite adsorbent bed. Following the first 2.5-3.4 minutes of measurement time, the CO₂ concentration ratio was observed to increase up to 1, whereas the concentration ratio of N₂ was evaluated to gradually drop to a value close to 1. The optimal value of the breakpoint, which is defined as the time at which the concentration ratio at the bed outlet is evaluated to be less than 5%, was measured to be about 3.38 minutes for 6 wt.% MWCNT/MIL-101(Cr) composite as shown in Figure 4.26. This is followed by the value measured for 8 wt. % MWCNT/MIL-101(Cr) composite of about 3.36 minutes, and then by that measured for pristine MIL-101(Cr) of about 3.2 minutes. However, since these

breakpoint values correspond to a variable adsorbent mass in accordance with the added proportion of MWCNTs in each of the four composite samples, the re-calculated normalized optimal CO₂ adsorption breakpoint for 2 wt% MWCNT/MIL-101(Cr) composite was observed to be about 8.91 minutes per gram of adsorbent. Accordingly, the corresponding values evaluated for MIL-101(Cr) and 4, 6, and 8 wt.% MWCNT/MIL-101(Cr) composites were recorded to be 6.7, 8.9, 8.2, and 7.1 minutes per gram of adsorbent, respectively.

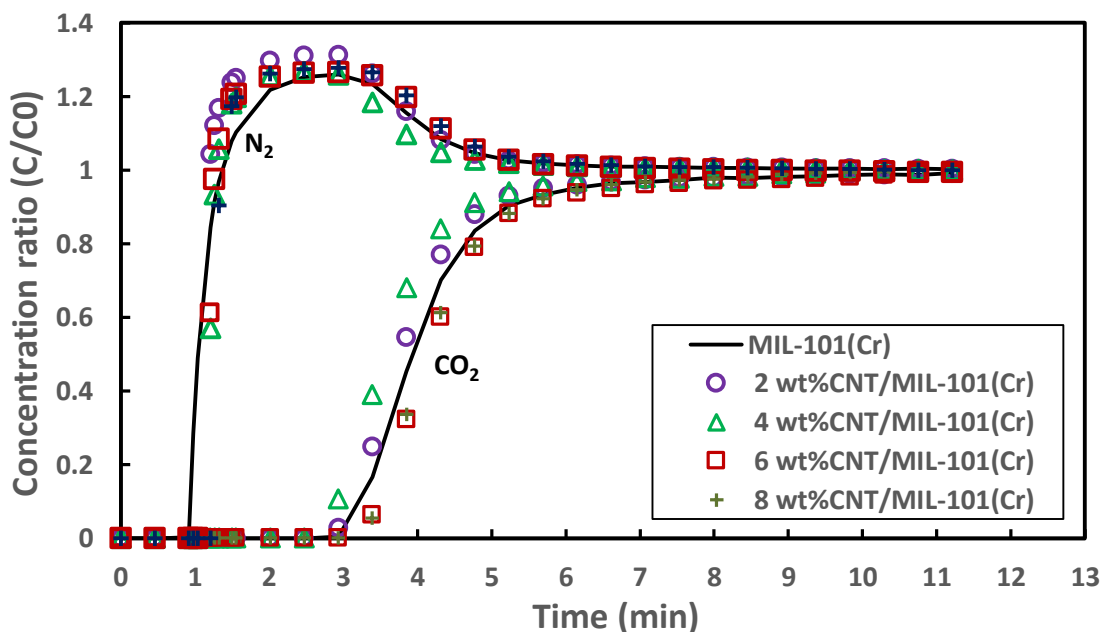


Figure 4.26 CO₂/N₂ breakthrough curves at 297 K and 101.3 kPa as concentration ratios of MWCNT/MIL-101(Cr) composites. The adsorbent masses are 0.475, 0.33, 0.32, 0.41, and 0.477 g for MIL-101(Cr), 2 wt% MWCNT/MIL-101(Cr), 4 wt% MWCNT/MIL-101(Cr), 6 wt% MWCNT/MIL-101(Cr), and 8 wt% MWCNT/MIL-101(Cr), respectively.

In order to evaluate the improvement in adsorption uptake by virtue of MWCNT incorporation in MIL-101(Cr), the adsorbed amounts of CO₂ have been calculated from the experimental breakthrough curves using Eq. 1. The maximum CO₂ uptake for MIL-101(Cr)

calculated from the respective breakthrough curve was estimated to be about 0.76 mmol/g at 0.2 molar fraction of 10 sccm, 297 K, and 101 kPa. The maximum CO₂ uptakes along with the adsorption breakpoint ratios for MIL-101(Cr) as well as each of the four MWCNT/MIL-101(Cr) composites are displayed in Figure 4.27. As evident, each of the four composites exhibit a substantial improvement over pristine MIL-101(Cr) with regards to both the adsorption capacity and the adsorption breakpoint ratio values. More specifically, the most optimum combination of adsorption capacity and breakpoint ratio value have been evaluated for 2 wt. % MWCNT/MIL-101(Cr) composite which has shown an improvement of 37.7 % and 32.1% over pristine MIL-101(Cr) for adsorption capacity and breakpoint ratio, respectively. This pair of statistics is followed by the 4, 6 and 8 wt. % MWCNT/MIL-101(Cr) composites for which the corresponding improvements in adsorption capacity and breakpoint values over pristine MIL-101(Cr) have been evaluated to be 33.1 % and 32.1%, 21.9 % and 22.1%, and 3.1% and 4.7%, respectively. It is worth mentioning here that each of the four MWCNT/MIL-101(Cr) composites have already been characterized for lower values of heat of adsorption for CO₂ in comparison with pristine MIL-101(Cr) as shown earlier in Figure 4.25, which theoretically implies that each of these composites should not only exhibit higher CO₂ uptake values than pristine MIL-101(Cr), but also require comparatively lower energy for regeneration process (recycling recovery).

The observed enhancement in the CO₂ adsorption capacity and breakpoint is primarily attributable to an improvement in the thermal properties of MIL-101(Cr) framework upon the incorporation of MWCNTs [220-222]. In a similar fashion, a MWCNT-incorporated 13X/CaCl₂ composite has been reported to show higher thermal conductivity and

adsorption capacity values than those measured for 13X/CaCl₂ and pure 13X [220, 221]. More recently, a comparatively higher water-stability and adsorption capacity have also been recorded for MIL101-68 (Al) following the incorporation of MWCNT into the framework [222].

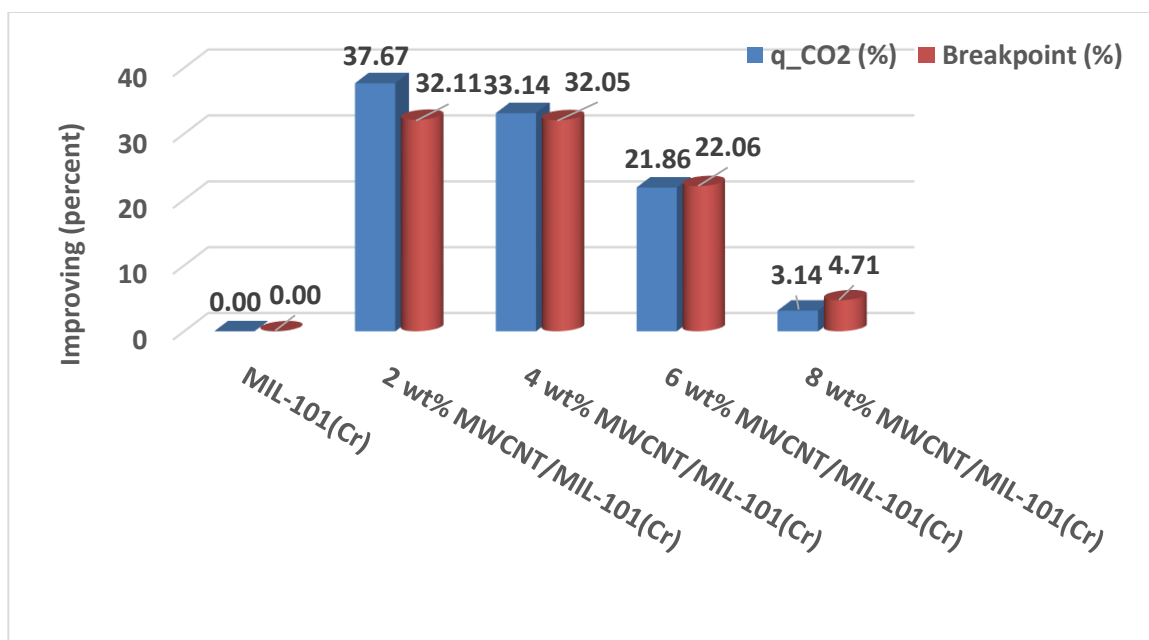


Figure 4.27 Carbon dioxide adsorption capacity (cubic bars) and breakpoint (cylindrical bars) improvements (percent) for MWCNT/MIL-101(Cr) composites over pristine MIL-101(Cr) measured at 297 K and 1.013 bar (gas mixture pressure).

4.3.4 Comparison amongst Investigated Adsorbents and Literature

The present work shows a comparative CO₂ adsorption capacity comparing with some adsorbents reported in the literature as shown in Table 29. The MIL-100(Fe) shows the lowest values of adsorption in a comparison to AC, 13X and Mg-MOF-74, while Mg-MOF-74 and MFC6 have the highest CO₂ uptake. 13X and XC3 also show a good CO₂ adsorption capacities. Mg-MOF-74, MIL-100(Fe) and MIL-101(Cr) are reticular materials while AC and 13X are porous materials. The affinity of CO₂/adsorbent is supreme for Mg-MOF-74

and good for 13X while MIL-100(Fe) has the lowest affinity. That means the bonding energy between Mg-MOF-74 and CO₂ is low.

Table 4.4 Dynamic CO₂ adsorption capacity of adsorbents.

Adsorbent	Temperature(K)	CO₂ vol%	CO₂ Capacity (mmol/g)	Ref.
Mg-MOF-74	298	15	4.06	[203, 227]
Mg-MOF-74	297	20	5.46	This work
MFC6	297	20	5.86	This work
AC	301	20	0.734	[165]
MIL-101(Cr)	298	10	0.49	[230]
MIL-101(Cr)	298	20	0.76	This work
MIL-101(Cr)	298	20	1.04	This work
13X	301	20	2.35	[132]
13X	297	20	2.56	This work
XC3	297	20	3.11	This work
MIL-100(Fe)	297	15	0.33	This work
MMC1	297	15	0.37	This work

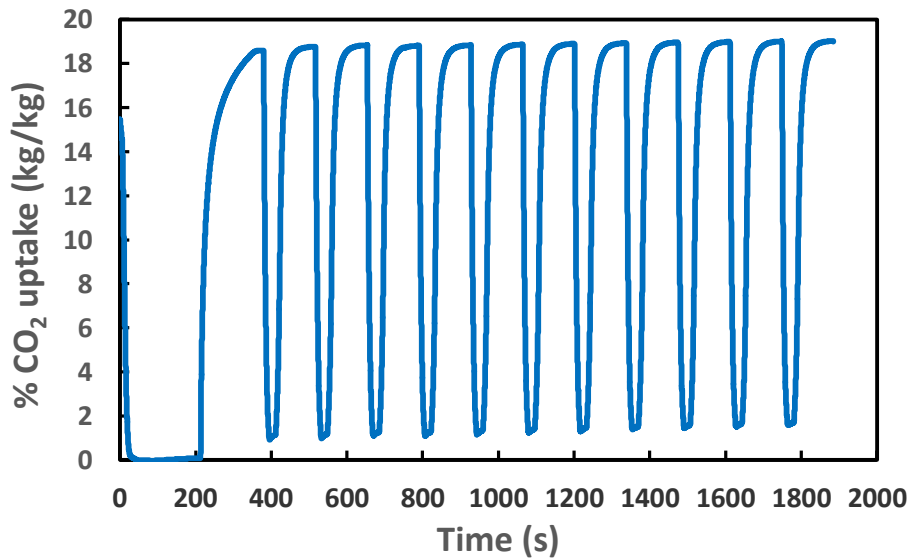
4.4 CO₂ Adsorption Cycling for Selective Composites

Seeing that MWCNT/Mg-MOF-74 and MWCNT/13X have the highest CO₂ adsorption capacity amongst the other adsorbents studied in this work. The pristine and MWCNT incorporated with these adsorbents have been investigated for CO₂ cycling. TSA, VSA, and TVSA are the techniques exploited in this research for CO₂ cycling purpose. For TSA, desorption process has been carried out by heating up the adsorbent up to 120 °C (for Mg-MOF-74 composites) or 150 °C (for 13X composites). For VSA, desorption has been executed by vacuum (around 2 Pa) for all the investigated adsorbents while TVSA method used both heating and vacuum for regeneration process.

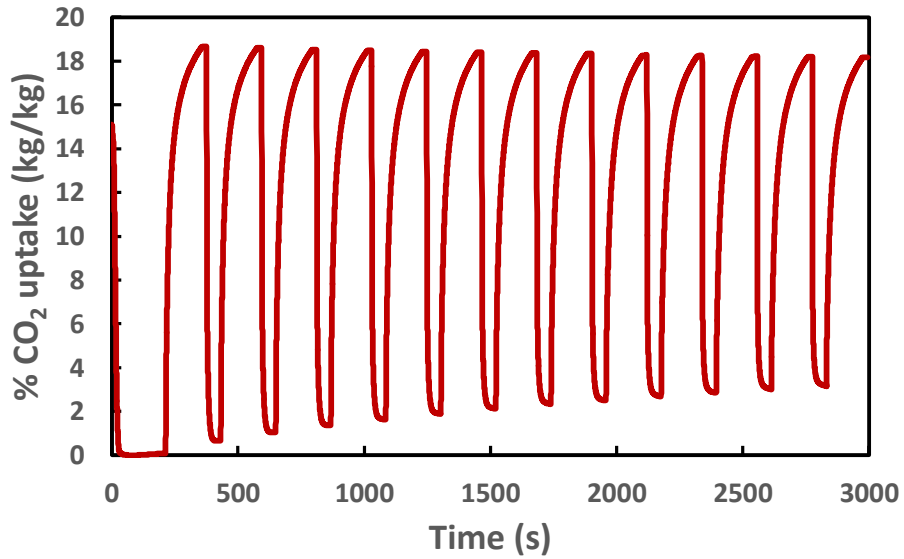
Zeolite 13X and XC3 (0.5 wt% CNT/13X) have been selected to adsorb/desorb CO₂ for about 13 cycles of TSA/VSA/TVSA. The cycles are shown in Figure 4.28 and Figure 4.29.

Moreover a comparison of CO₂ adsorption cycling stability between 13X and XC3 are tabulated in Table 4.5. It is clear that less than 1.5% of CO₂ uptake is reduced at steady state cycles comparing to the 2nd cycle of TSA. However, the reduction increases up to 13% for VSA using 13X and about 23% for XC3 by using VSA technique. Oppositely, the TVSA seems to maintain the same CO₂ uptake through all cycles. The reduction of CO₂ adsorption in VSA case is due to the utilizing the vacuum alone for desorption process which is not able to overcome all the attraction forces between CO₂ and 13X or XC3, so that some layers of CO₂ are still attracted to the adsorbent.

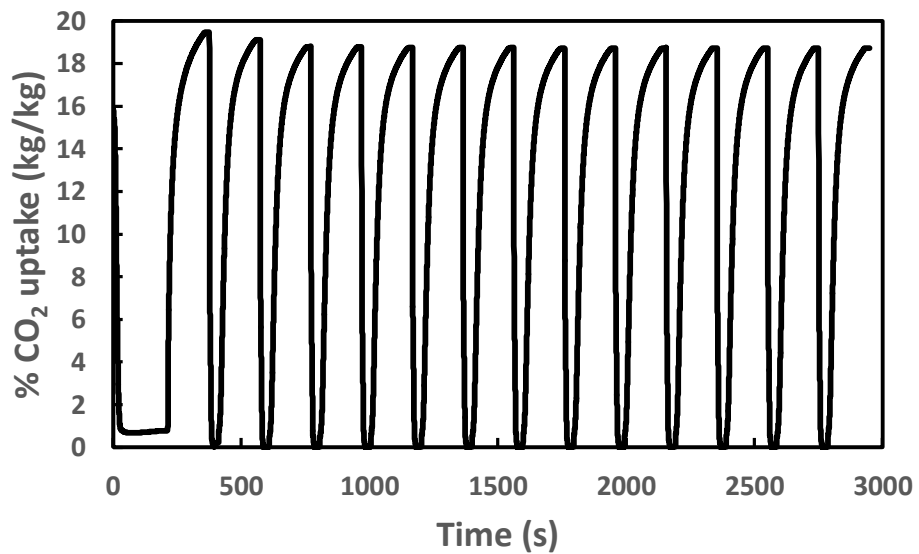
Table 4.5, Figure 4.28 and Figure 4.29 show that the adsorption/desorption cycles are stable for TSA more than that for VSA. VSA needs around 8 cycles to reach stability with lower CO₂ uptake comparing to TSA. The optimal uptake recycled is associated with TVSA due to the evacuation of the majority of adsorbed amounts.



(a) TSA of 13X.



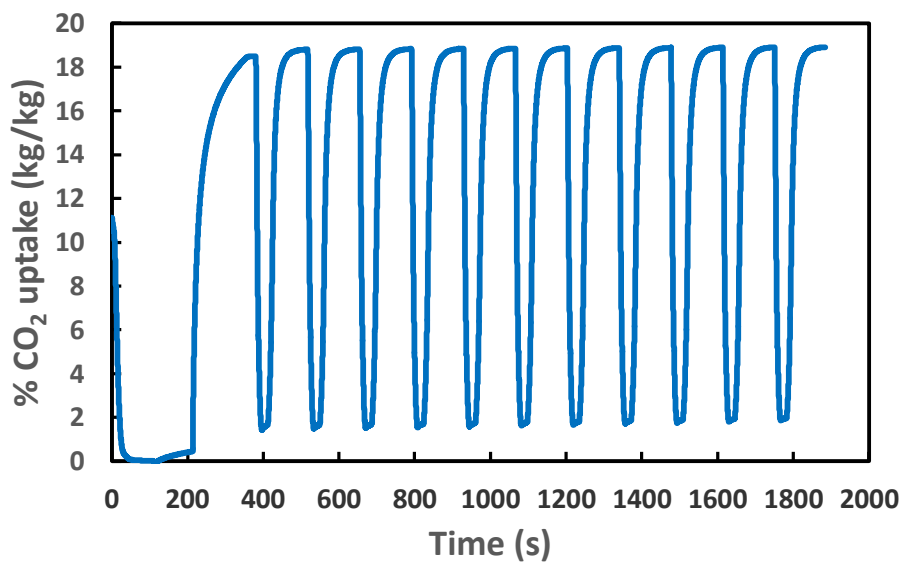
(b) VSA of 13X.



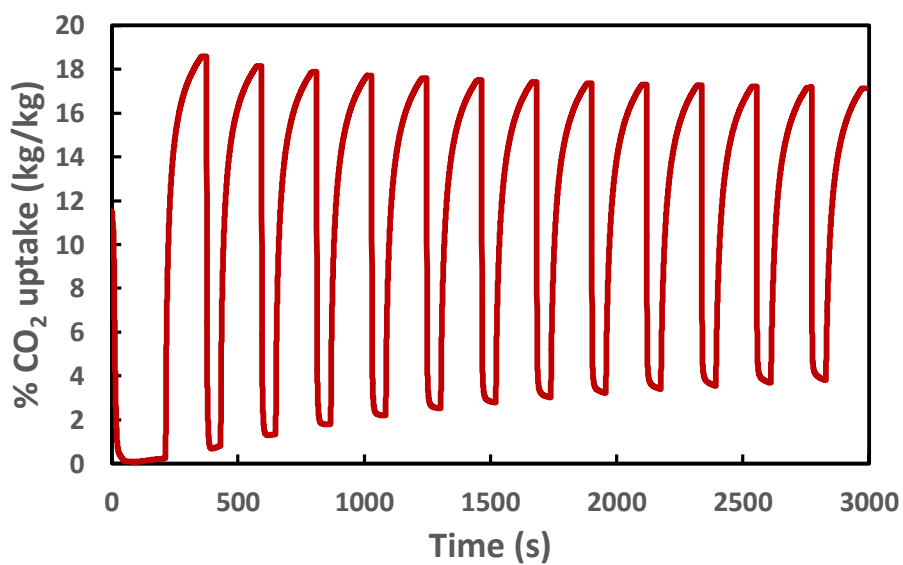
(c) TVSA of 13X.

Figure 4.28 CO₂ adsorption/desorption cycles of 13X.

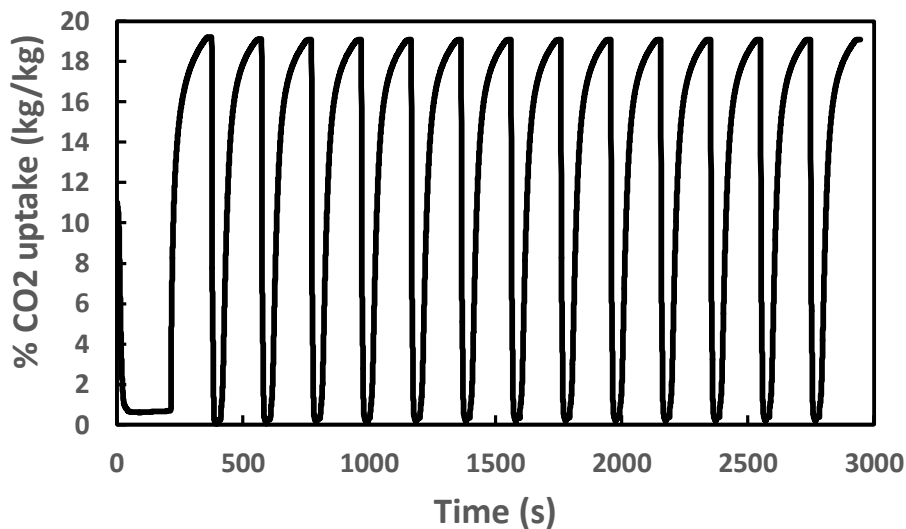
It is noticed that the CO₂ adsorption is successfully recycled through 13X and XC3 by all regeneration methods. Another point is no degradation of materials occurs due to adsorption/desorption cycles.



(a) TSA of XC3 (0.5 wt% MWCNT/13X).



(b) VSA of XC3 (0.5 wt% MWCNT/13X).



(c) TVSA of XC3 (0.5 wt% MWCNT/13X).

Figure 4.29 CO₂ adsorption/desorption cycles of XC3 (0.5 wt% CNT/13X).

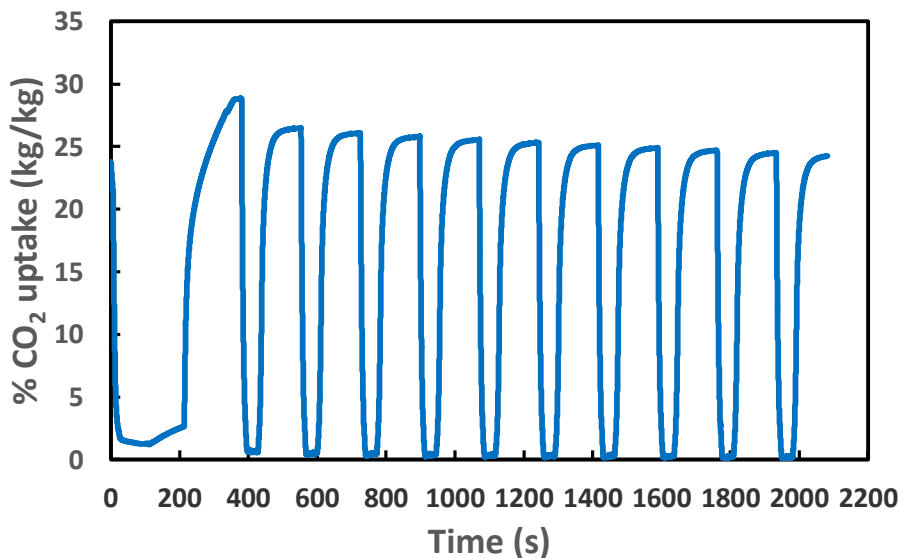
Table 4.5 shows CO₂ adsorption/desorption cycling as a comparison between 13X and XC3. It is clear that less than 1.5% of CO₂ uptake has reduced at steady state cycles compare to the 2nd cycle of TSA. However, the CO₂ uptake reduction increases up to 13% for VSA using 13X and about 23% for XC3 by using VSA technique. Oppositely, the TVSA seems to maintain the same CO₂ uptake through all cycles. The reduction of CO₂ adsorption in VSA case is due to the utilizing the vacuum alone for desorption process which is not able to overcome all the attraction forces between CO₂ and 13X/XC3, so that some layers of CO₂ are still attracted to the adsorbent.

The recycling behavior of MOFs and MWCNT/MOFs are close to that of 13X except that the cycling stability of 13X is superior. Figure 4.30 and Figure 4.31 show the cycling stability of Mg-MOF-74 and MFC4 (0.75 wt% CNT/Mg-MOF-74) by the three methods (TSA, VSA, TVSA). All methods have exhibited CO₂ adsorption stability with a certain

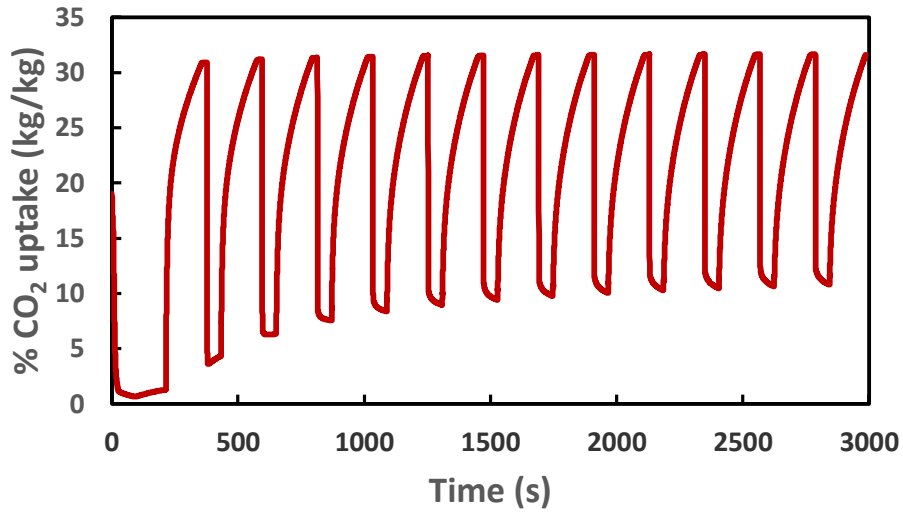
value of CO₂ uptake for each method. It is high for VTSA (Figure 4.30(c) and Figure 4.31(c)) follows by TSA (Figure 4.30(a) and Figure 4.31(a)) and then VSA (Figure 4.30(b) and Figure 4.31(b)) for the same reasons discussed earlier.

Table 4.5 CO₂ adsorption/desorption cycling comparison between 13X and XC3.

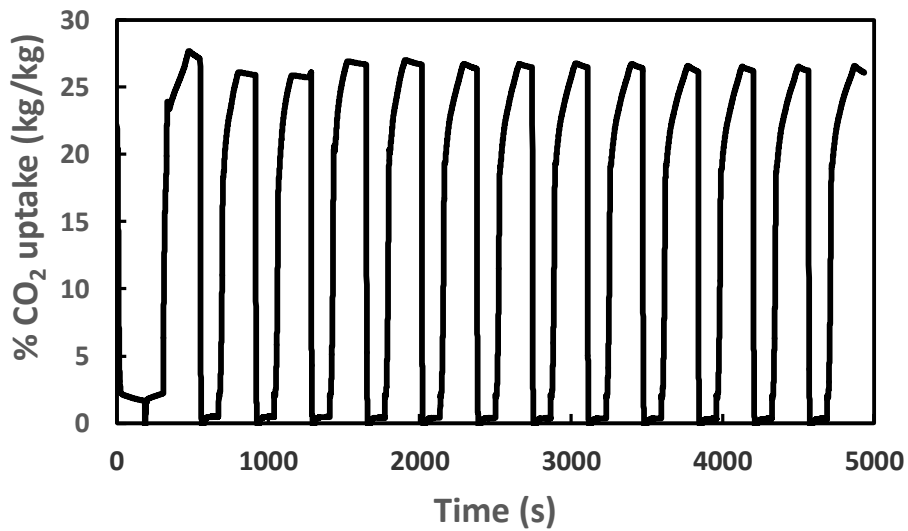
Method	13X			XC3 (0.5 wt% MWCNT/13X)		
	Cycle	% uptake (kg/kg)	%Difference	Cycle	% uptake (kg/kg)	%Difference
TSA	2	17.17	-0.76	2	17.19	1.34
	11	17.30		11	16.96	
VSA	2	17.56	12.59	2	17.41	22.57
	11	15.35		11	13.48	
TVSA	2	18.89	1.01	2	19.04	0.74
	11	18.70		11	18.90	



(a) TSA of Mg-MOF-74.



(b) VSA of Mg-MOF-74.

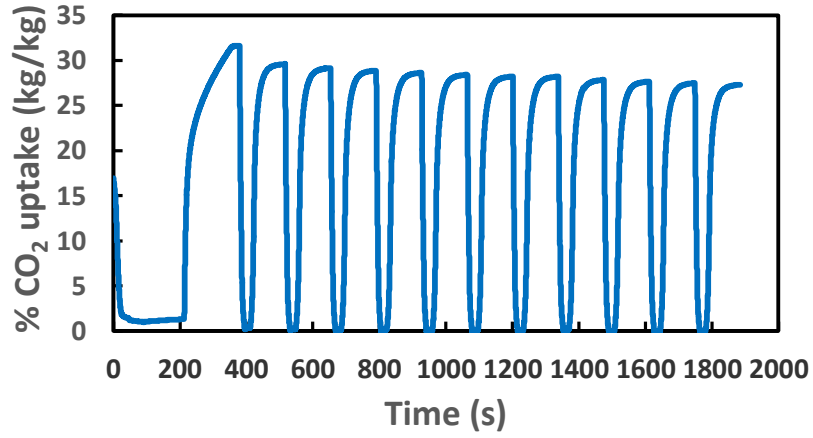


(c) TVSA of Mg-MOF-74.

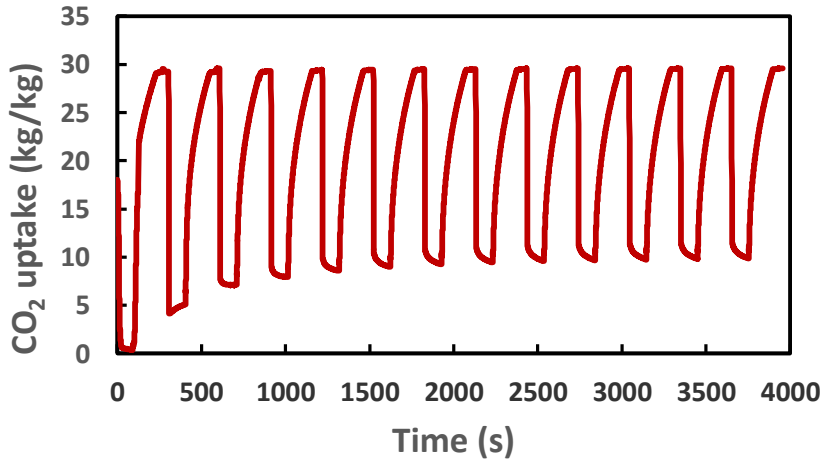
Figure 4.30 CO₂ adsorption/desorption cycles of Mg-MOF-74.

Actually, VTSA and TSA showed that the CO₂ recycling capability of MFC4 is higher than that of Mg-MOF-74 while the opposite is correct for VSA. It may be interpreted as the thermal diffusion enhancement have been increased by adding MWCNT to Mg-MOF-74

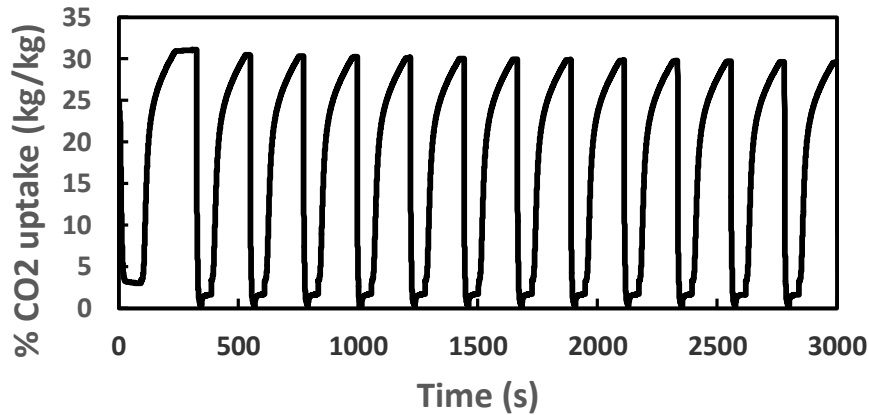
for both thermal methods (TSA, TVSA). Comparing to 13X composites, VSA reaches steady state earlier for Mg-MOF-74 composites (after the 3rd cycle), Figure 4.31(b).



(a) TSA of MFC4 (0.75 wt.% MWCNT/Mg-MOF-74).



(b) VSA of MFC4 (0.75 wt.% MWCNT/Mg-MOF-74).



(c) TVSA of MFC4 (0.75 wt.% MWCNT/Mg-MOF-74).

Figure 4.31 CO₂ adsorption/desorption cycling of MFC4 (0.75 wt.% CNT/Mg-MOF-74).

Table 4.6 illustrates the recycled CO₂ uptake differences between pristine Mg-MOF-74 and that incorporated with MWCNT *via* the three regeneration methods. The CO₂ uptake was stable through TSA with a reduction about 6.5% for both Mg-MOF-74 and MFC4. This CO₂ uptake reduction raised to about 20.5 and 24% for MFC4 and Mg-MOF-74, respectively, for VSA. TVSA showed more stability with CO₂ uptake reduction less than 4.1% for MFC4 and fully regeneration occurs for Mg-MOF-74. The TVSA, again, is recommended for such cycles in terms of CO₂ uptake, However, TSA could have a good amount of recycled CO₂ uptake with optimal energy consumption by using cheap and efficient heat sources.

Table 4.6 CO₂ adsorption/desorption cycling comparison between Mg-MOF-74 and MFC4.

Method	Mg-MOF-74			MFC4 (0.75 wt% MWCNT/Mg-MOF-74)		
	Cycle	% uptake (kg/kg)	%Difference	Cycle	% uptake (kg/kg)	%Difference
TSA	2	25.85	6.74	2	29.48	6.48
	11	24.11		11	27.57	
VSA	2	27.55	24.03	2	24.90	20.48
	11	20.93		11	19.80	
TVSA	2	26.64	-2.21	2	30.34	4.09
	11	27.23		11	29.10	

CHAPTER 5

SIMULATION MODELING RESULTS AND

DISCUSSION

5.1 Adsorption Breakthrough for Dry and Humid CO₂/N₂

For showing the reliability of UDF-Fluent CFD, the code results have been compared to those of experimental works and then the effect of water on CO₂ adsorption from CO₂/N₂ mixture has been investigated.

5.1.1 Mesh Independence

The 2D adsorbent bed domain was meshed using structure quadrilateral elements. Grid independency was carried out using Mg-MOF-74 as adsorbent at 300 K and 101.3 kPa for the adsorbent bed shown in Figure 3.4. The thermal and adsorption properties are described in Table 3.4 and Table 3.5. Figure 5.1 shows CO₂/N₂ concentration ratio profiles for four different number of cells (1120, 1320, 1600, and 1980 cells). It is clear that all selected grids have shown the same concentration ratio values indicating that any mentioned cell number was enough to present an accurate simulation. For 3D bed, the cell size have been taken as that in 2D.

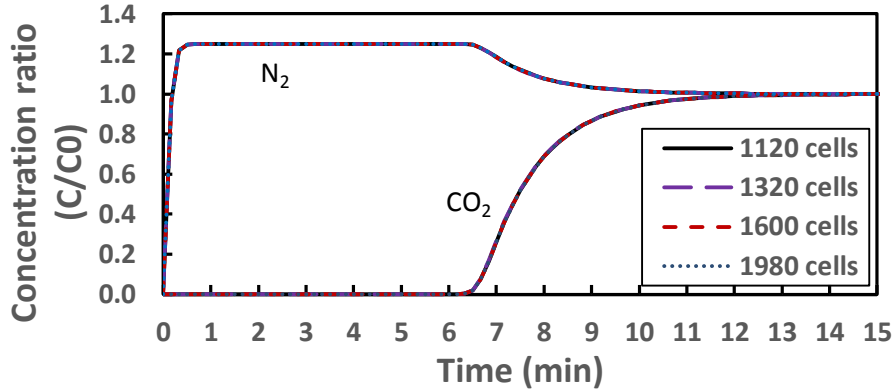


Figure 5.1 Mesh independency as a comparison of concentration ratio profiles for 1120, 1320, 1600, and 1980 cells.

5.1.2 Model Validation

The present numerical models were compared to three experimental breakthrough curves. The first validation case described in Table 3.2 is concerned with separation of CO₂ from CO₂/N₂ mixture at high temperature (423 K) using activated carbon. The breakthrough curves of CO₂ and N₂ against the time at the bed outlet for both experimental work [165] and present numerical modeling are shown in Figure 5.2. It can be seen that the N₂ concentration profile has compared well with the experimental data, while the CO₂ concentration profile showed a slight discrepancy; the good agreement indicates that the Fluent with the developed UDF code is a feasible tool to investigate such systems. It is clear that the concentration ratio of CO₂ was zero at the bed outlet for the first 7 minutes, while the concentration ratio value of N₂ rose up to approximately 1.22 due to the absence of CO₂, which adsorbed onto the adsorbent material. Thus, the concentration ratio increased up to 1 for CO₂ and decreases down to 1 for N₂ at approximately 30 minutes.

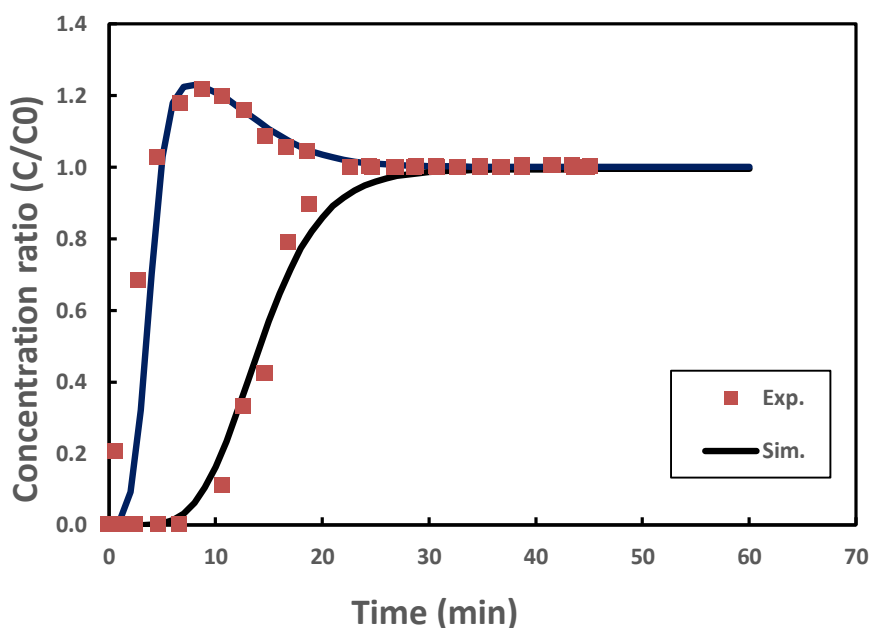


Figure 5.2 Breakthrough concentration ratio curves of CO₂ separation at the bed outlet during the adsorption process using AC as a comparison of the modeled concentration ratio with the experimental values at 301 K.

- *Validation multidimensional bed*

Figure 5.3 shows the concentration ratio of CO₂/N₂ separation at the bed outlet using Mg-MOF-74 (described in section 3.2.8 (Table 3.4 and Table 3.5)) as a comparison between the experimental work and 1D simulation work (using MATLAB) as well as 2D and 3D simulations (using UDF-Fluent). The CO₂/N₂ curves revealed an excellent agreements between the experimental results and UDF-Fluent simulations. The differences between 2D and 3D concentration ratio values are not significantly important. Therefore, the 2D UDF-Fluent simulation is enough to carry out adsorption breakthrough simulations under geometry selected. The small discrepancy of agreements between the 1D simulation and the experimental work is mainly due to ignoring the thermal diffusion term in the adsorbent

energy equation. Moreover, this discrepancy is due to some additional factors such as mass and thermal diffusion in the other dimensions.

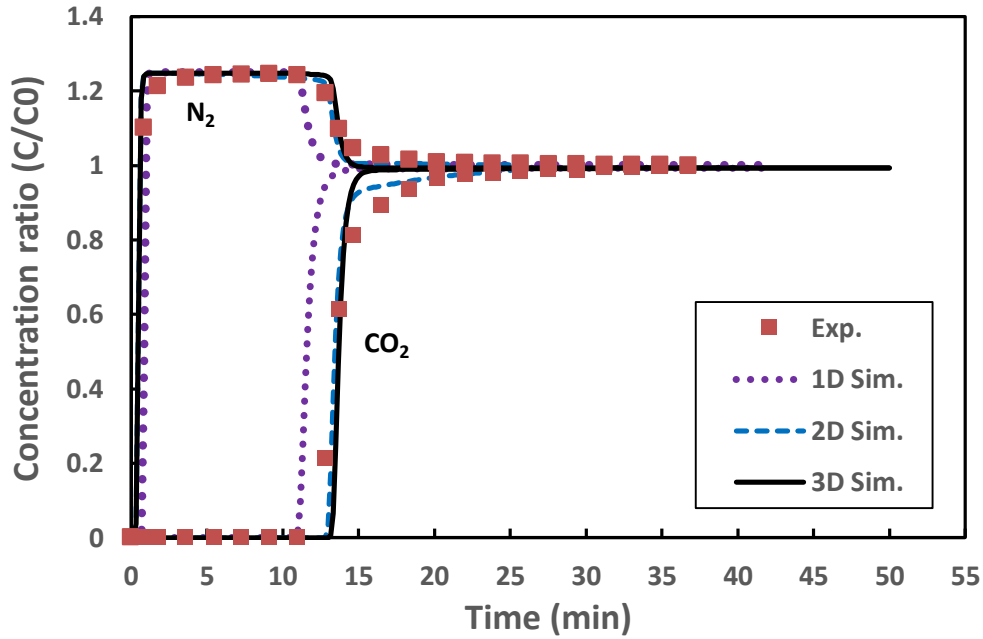


Figure 5.3 Breakthrough concentration ratio curves of CO₂ separation at the bed outlet during the adsorption process using Mg-MOF-74 as a comparison of the 1D, 2D, and 3D modeled concentration ratio with the present experimental values at 301 K and 101.3 kPa.

For highlighting the differences between 2D and 3D simulations, Figure 5.4 -Figure 5.6 show interesting 2D and 3D contours for temperature, CO₂ mass fraction, and CO₂ uptake for some selective times (30, 180, 330, 540, 720, and 870 s) of adsorption breakthrough. The temperature contours (Figure 5.4) shows the hot zone transfer from the inlet at 30s to the outlet at 870s due to the CO₂ adsorption process and rolling-up effect. As the adsorption process is exothermic, the hottest zones confirm the CO₂ adsorption regions. It is shown also in Figure 5.4, the temperature difference between 2D and 3D is as small as 1-2 K.

History of CO₂ adsorption rolling-up is, moreover, shown in Figure 5.5 in term of the CO₂ mass fraction. The bed was almost empty of CO₂ at 30s and full at 870 s by around 0.28 mass fraction (almost 0.2 molar fraction). Again, the values of CO₂ mass fraction were almost similar for both 2D and 3D models. Figure 5.6 exhibits the CO₂ uptake by Mg-MOF-74 for both the 2D and 3D simulation modeling at 297 K and 101.3 kPa. The CO₂ uptake took place at the bed inlet at 30s and reached the bed middle between 330 and 540 s and then filled the bed after 850 s. Both the 2D and 3D showed similar values of CO₂ uptake.

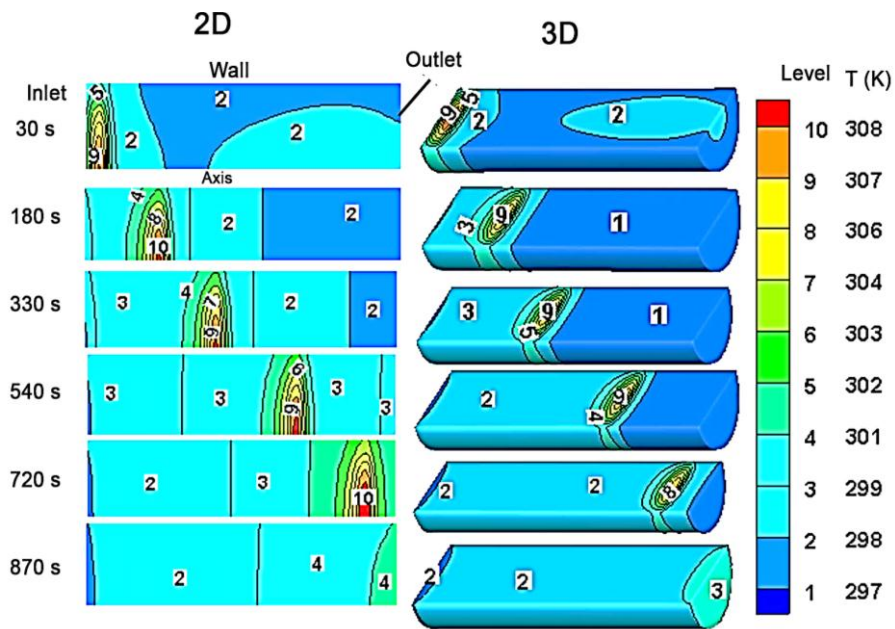


Figure 5.4 2D and 3D temperature contours of bed using Mg-MOF-74 at 101.3 kPa.

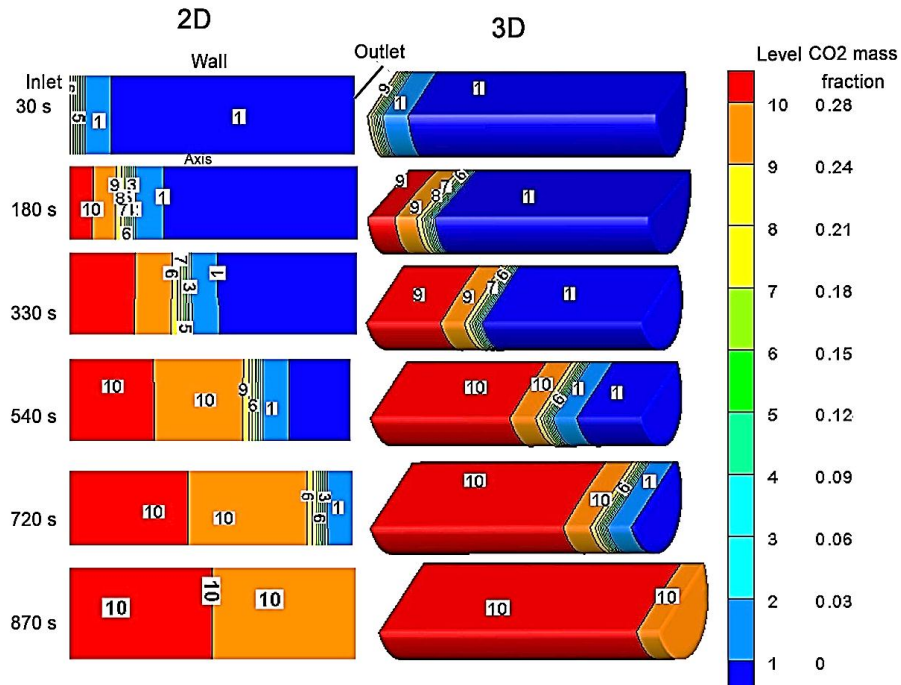


Figure 5.5 2D and 3D CO₂ mass fraction during CO₂/N₂ separation process using Mg-MOF-74 at 297 K, 101.3 kPa.

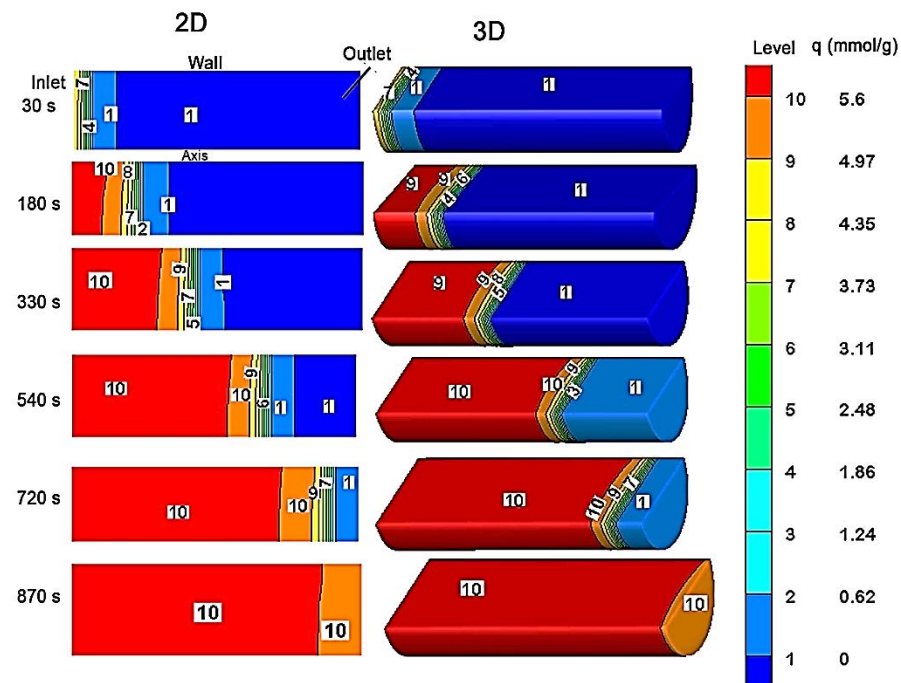


Figure 5.6 2D and 3D CO₂ adsorbed amounts during CO₂/N₂ separation process using Mg-MOF-74 at 297 K, 101.3 kPa.

- Validation humid CO₂/N₂ breakthrough

Humid CO₂/N₂ separation using 13X described in section 3.2.8 (Table 3.6 and Table 3.7) is shown in Figure 5.7 for both experimental and numerical simulation works. It is obvious that the CO₂/N₂/H₂O concentration ratio values of the simulation modeling match well with those of the experimental work. As evident, the model can easily be used for handling an adsorption of many species.

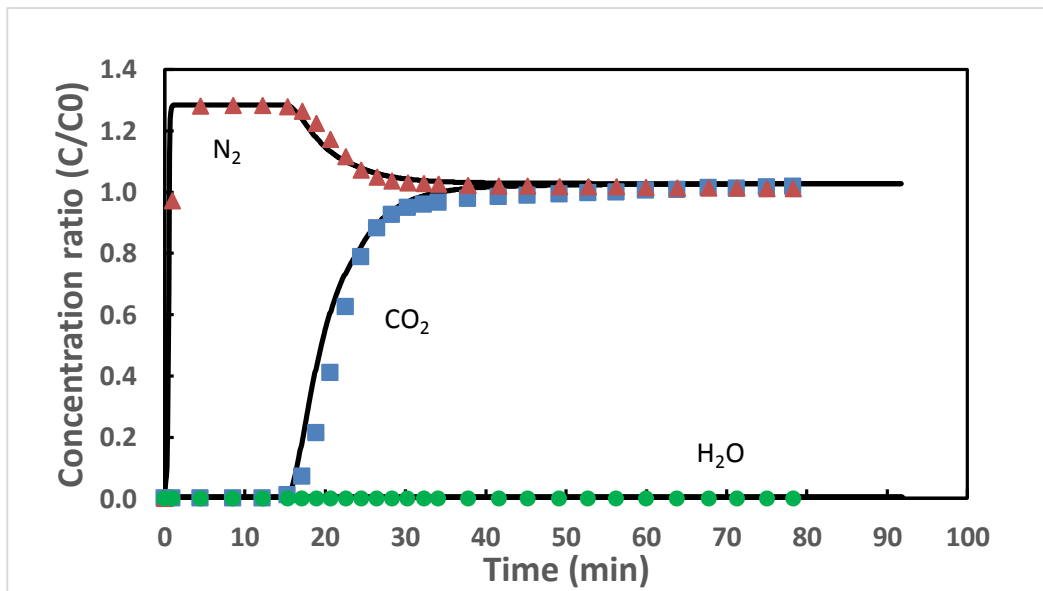


Figure 5.7 CO₂/N₂/H₂O breakthrough curves of concentration ratio using 13X at 92% RH, 297 K and 101.3 kPa. Symbols are experimental results and lines are numerical ones.

5.1.3 Parametric Study of Adsorption Breakthrough of Dry and Humid CO₂/N₂

This section discusses the effect of water vapor on CO₂ separation utilizing different adsorbents such as AC, 13X and Mg-MOF-74.

The adsorbent bed configuration and adsorption and thermal properties have been described well in section 3.2.8. The adsorption behavior of dry and wet CO₂/N₂ mixtures using activated carbon at 300 K and 101.3 kPa (cases 9 and 10 in Table 3.8) is shown in

Figure 5.8 -Figure 5.10. The dry and humid (86% RH) CO₂/N₂ adsorption breakthrough curves are illustrated in Figure 5.9. It is shown that the dry CO₂ reached adsorption saturation with values higher than those of humid case. This is because of the H₂O was not adsorbed into the AC and left the bed from the beginning. After CO₂ adsorbed to saturation point (> 4 min) for humid case, the molar fraction at the out bed for all species were close to those at the bed inlet, so that the CO₂ concentration ratios values of humid case was lower than those of dry case. Another point is that the CO₂ concentration values of the both dry and humid cases did not reach 1 (the exact values of CO₂ concentration at the inlet) due to the low diffusion resistance of AC under the operating velocity.

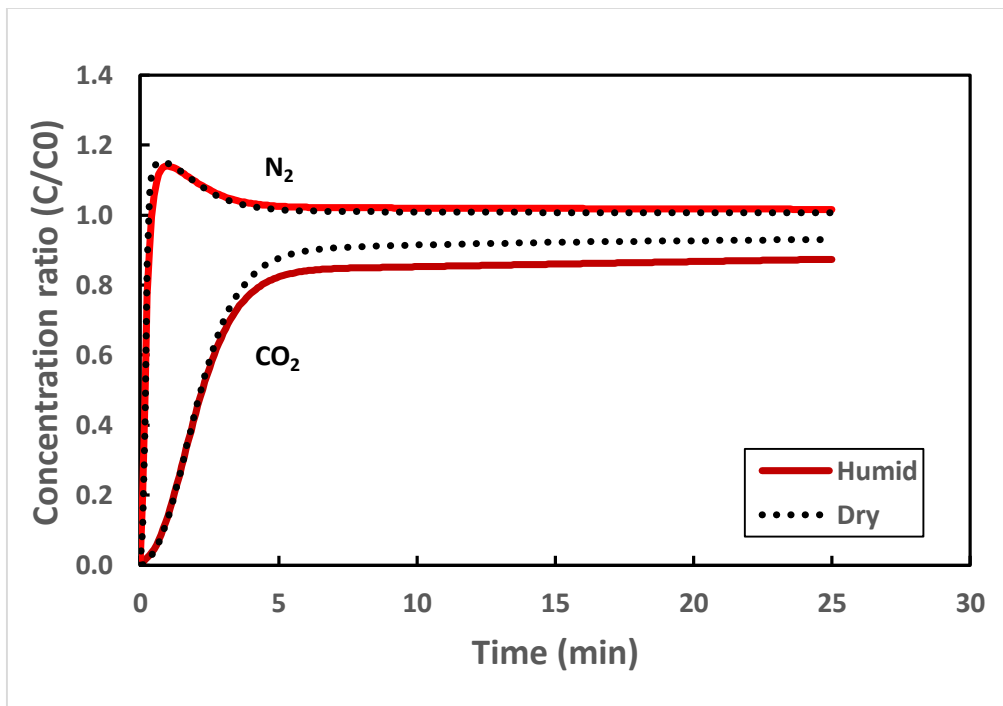


Figure 5.8 Dry and humid CO₂/N₂ adsorption breakthrough curves of concentration ratio for AC at 86% RH, 300 K, and 101.3 kPa.

The temperature profiles at the bed outlet shown in Figure 5.9 indicate to slightly higher values of outlet temperature in the dry case than those in the humid case. This is because

of non-adsorptive water vapor onto AC which carries some energy since the heat capacity of water vapor is considerably high. The temperature difference between the values at starting adsorption process up to those at adsorption saturation was very small by about 1.7 K due to the low amounts of CO_2/N_2 were adsorbed to the bed as shown in Figure 5.10. The amounts of N_2 adsorbed were around the half of those of CO_2 indicating to a bad CO_2 separation selectivity of AC. Moreover, the humid case revealed the CO_2/N_2 uptakes were slightly lower than those of dry one due the absence of water vapor.

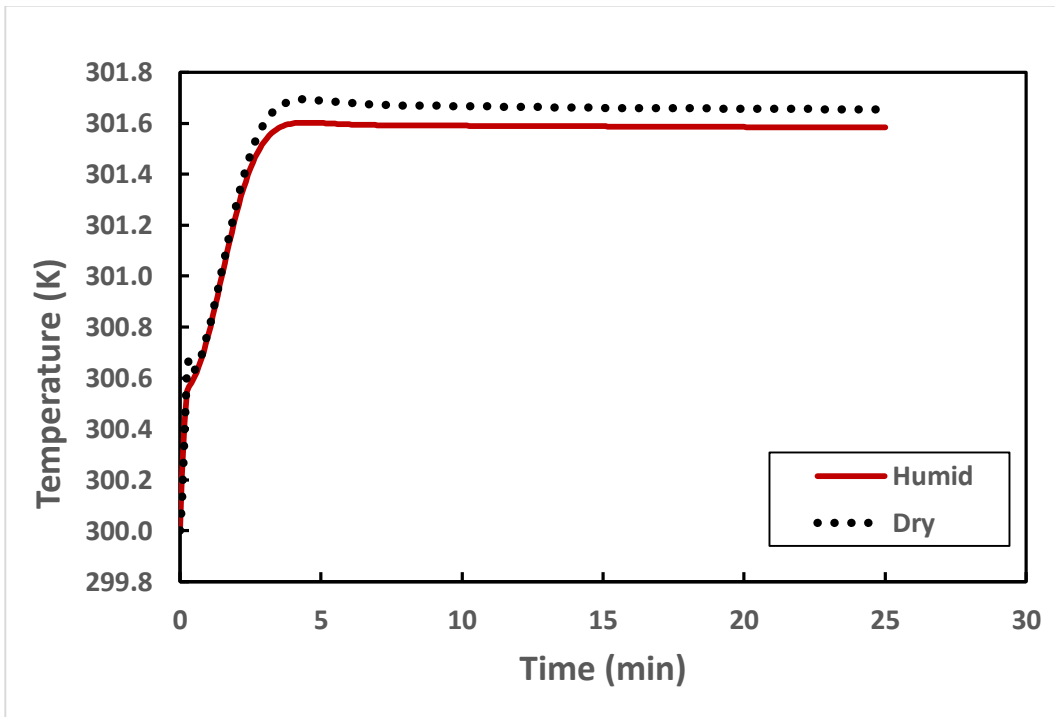


Figure 5.9 Temperature profiles at the bed outlet during dry and humid CO_2/N_2 separation process for AC at 86% RH, 300 K, and 101.3 kPa.

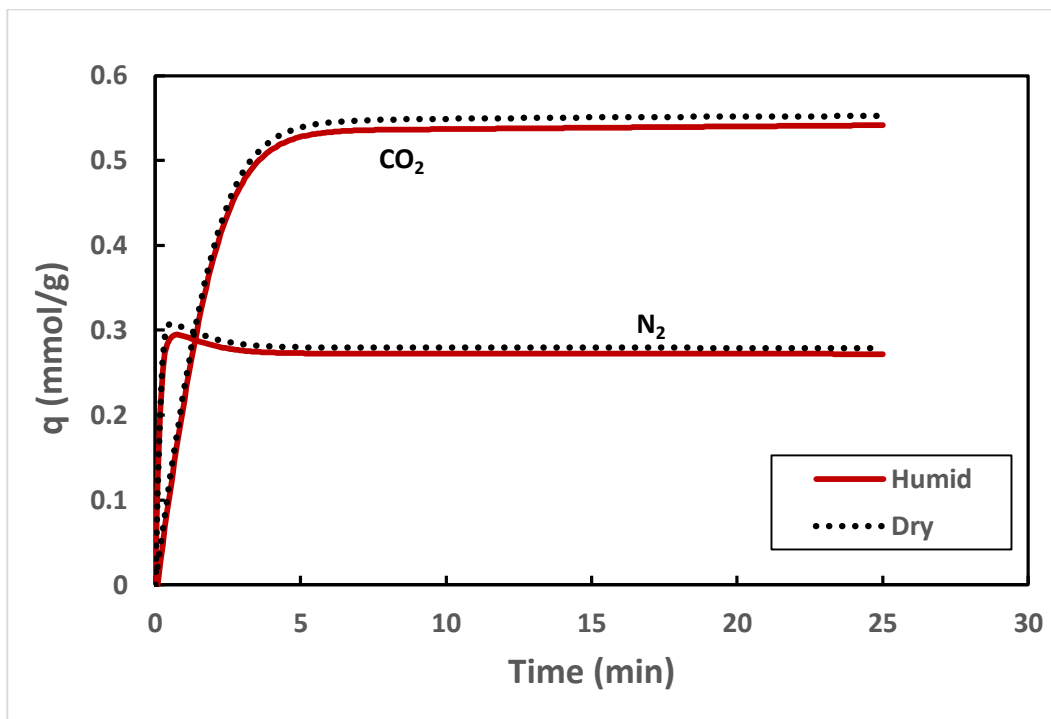


Figure 5.10 CO₂/N₂ adsorbed amounts during the dry and humid CO₂ separation process for AC at 86% RH, 300 K, and 101.3 kPa.

The adsorption breakthrough of dry and humid CO₂/N₂ using 13X (as described in case 11 and 12 of Table 3.8) are shown in Figure 5.11 -Figure 5.13. The adsorption concentration breakthrough curves of CO₂/N₂ at 300 K, 101.3 kPa for dry and humid (86% RH) are shown in Figure 5.11. Firstly, the CO₂ adsorption time of 13X was much higher than that of AC (Figure 5.8). The CO₂/N₂ concentration ratio values were a little higher in the humid case compared to those of the dry case. This trend is caused by the fact that water vapor is an adsorptive species in zeolite 13X, so that the outlet CO₂/N₂ concentration values at the saturation region (> 13 minutes) are compensated by the values of H₂O which is being adsorbed to the bed during the entire studied time. The temperature values at the bed outlet were higher for the humid case compared to those of the dry gas due to the extra heat released by the water adsorption process, Figure 5.12. By the adsorption saturation time (>13 minutes), the CO₂ uptake was almost 2.5 for both dry and humid cases while N₂ uptake values were around

0.21 mmol/g. This means that the 13X is substantially selective for CO₂ separation from CO₂/N₂ mixtures. The water vapor adsorption was continuously increasing in linear trend for the whole investigated time showing no effect on the CO₂ uptake at this time.

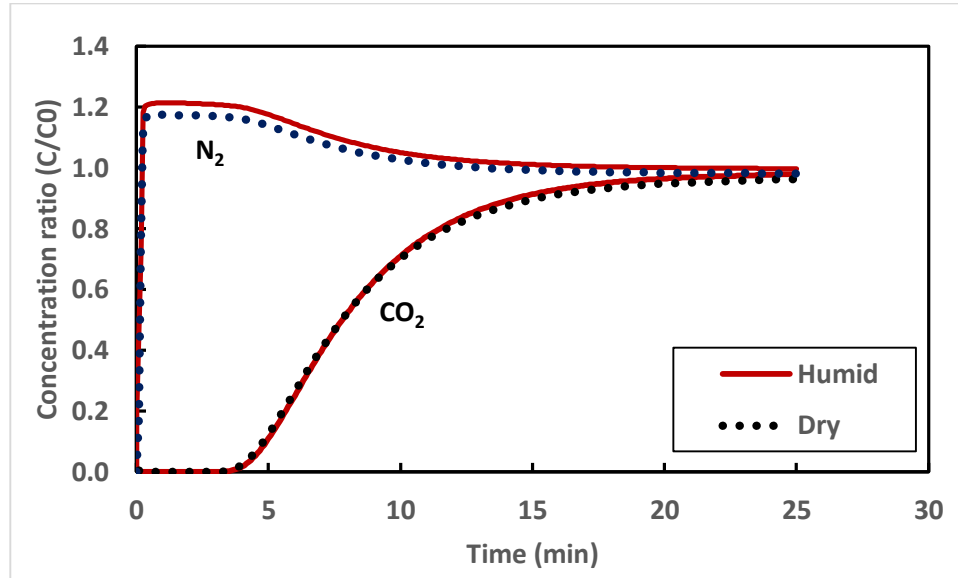


Figure 5.11 Dry and humid CO₂/N₂ adsorption breakthrough curves of concentration ratio for 13X at 86% RH, 300 K, and 101.3 kPa.

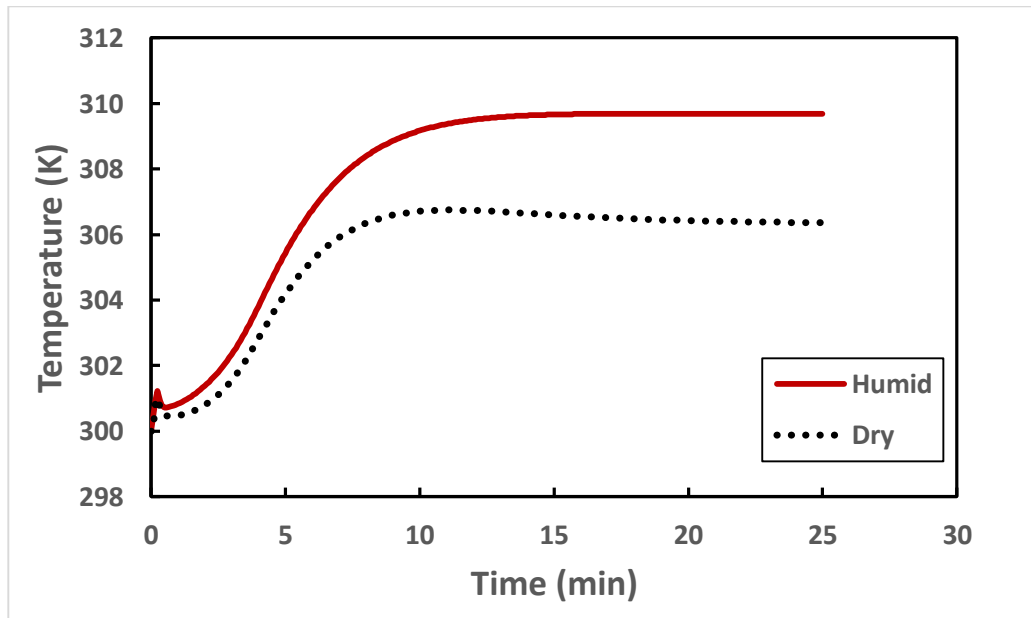


Figure 5.12 Temperature profiles at the bed outlet during dry and humid CO₂/N₂ separation process for 13X at 86% RH, 300 K, and 101.3 kPa.

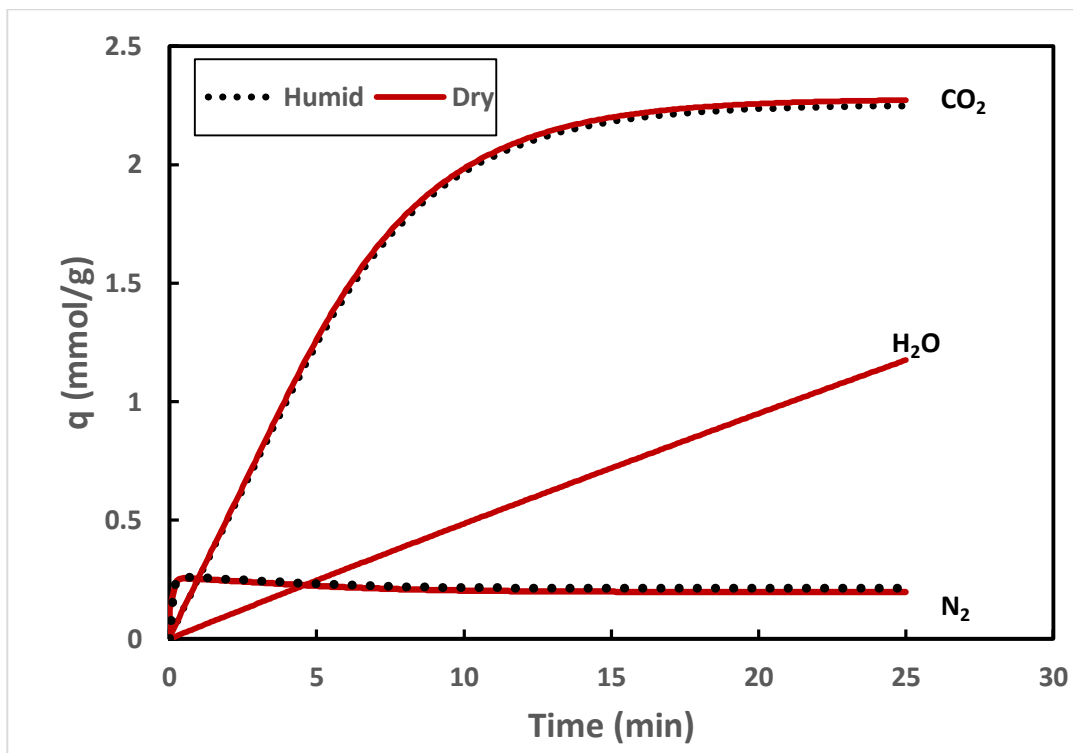


Figure 5.13 CO₂/N₂/H₂O adsorbed amounts during the dry and humid CO₂ separation process for 13X at 86% RH, 300 K, and 101.3 kPa.

The interesting adsorption breakthrough curves of dry and humid CO₂/N₂ are found with using Mg-MOF-74 as adsorbent as shown in the below figures. The simulation data for Mg-MOF-74 at 300 K and 101.1 kPa have been mentioned in section 3.2.8 (Table 3.8, cases 6 and 7) whereas the concentration ratio results shown in Figure 5.14. The adsorption breakthrough curves of dry and humid (86% RH) CO₂/N₂ by Mg-MOF-74 have displayed the best adsorption time comparing to those of AC and 13X. The adsorbent adsorbed more CO₂ in dry CO₂/N₂ mixture in comparison to the humid one due to that Mg-MOF-74 has a tendency to adsorb H₂O. For the saturation period (>15 minutes), the outlet concentration ratios of CO₂/N₂ were higher than those of dry case as a result of the water vapor is being adsorbed to the bed while the outlets were only CO₂ and N₂. It is worth mentioning here

that the concentration curves trends of Mg-MOF-74 are steepest amongst other adsorbents (AC, and 13X) caused by the differences of diffusion and thermal resistances.

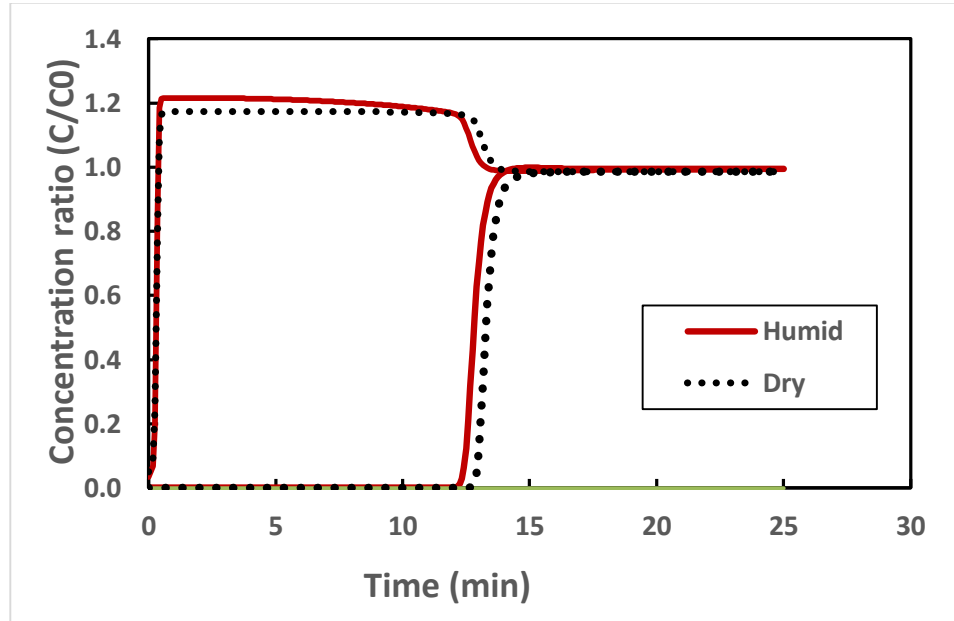


Figure 5.14 Dry and humid CO₂/N₂ adsorption breakthrough curves of concentration ratio for Mg-MOF-74 at 86% RH, 300 K, and 101.3 kPa.

The bed outlet temperature during the adsorption breakthrough is shown in Figure 5.15 for both dry and humid cases. Generally, the maximum temperature values were recorded at about 13 minutes, at which the adsorption took place at the bed outlet, as 320 and 311 K for both humid and dry cases, respectively. The tremendous increasing in temperature values for humid case is a consequence of the water vapor adsorption process which release temperature more than those of CO₂ and N₂. In another word, the heat of adsorption of water vapor is greater than those of CO₂ and N₂ (Table 3.10) leading to raise the bed temperature from this exothermic reaction.

The CO₂/N₂/H₂O uptake by Mg-MOF-74 at 300 K are shown in Figure 5.16 for both humid (86% RH) and dry conditions. CO₂ and N₂ uptakes were higher for dry conditions than

those of humid mixture due to the absence of water vapor which being adsorbed to the bed, leading to block some sites inside MOF frameworks, resulting in minimizing the CO₂ and N₂ uptakes. Comparing CO₂ uptake (almost 6 mmol/g at saturation) with N₂ uptake (about 0.7 mmol/g) provides a good evidence of substantial selectivity of separating CO₂ from CO₂/N₂ mixture.

The water vapor has been adsorbed linearly in the investigated breakthrough time pointing to a good potential for H₂O uptake.

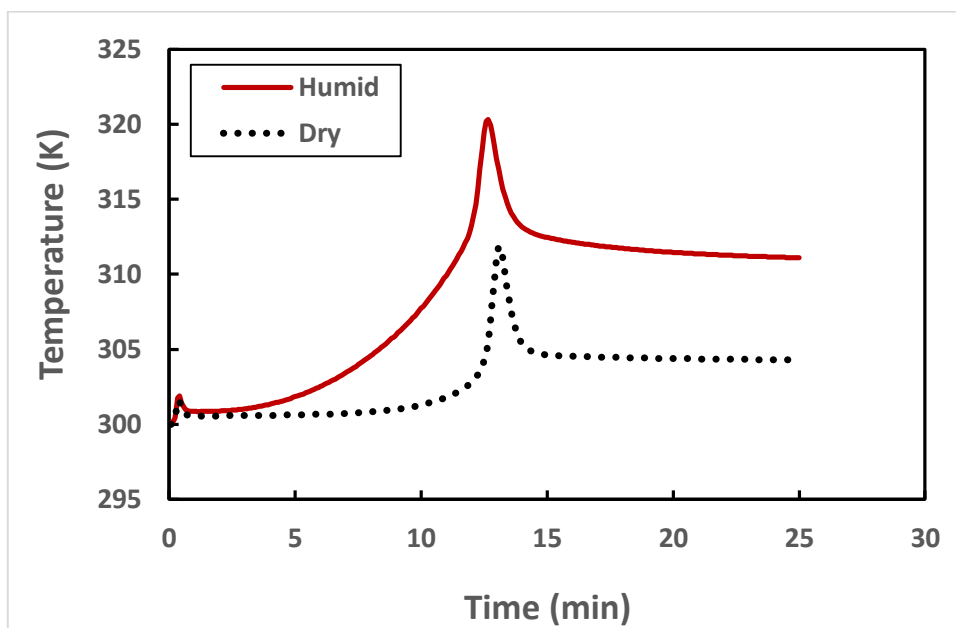


Figure 5.15 Temperature profiles at the bed outlet during dry and humid CO₂/N₂ separation process for Mg-MOF-74 at 86% RH, 300 K, and 101.3 kPa.

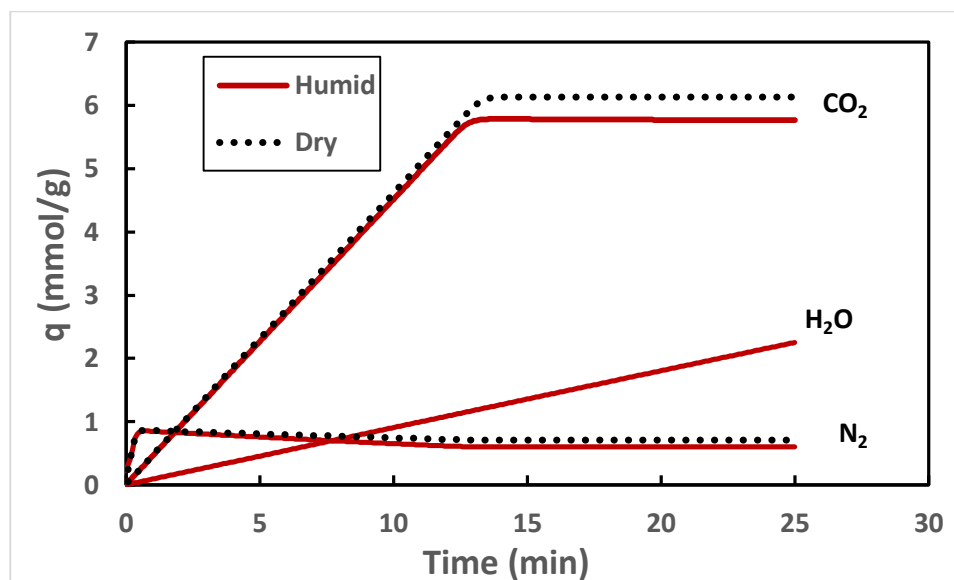


Figure 5.16 CO₂/N₂/H₂O adsorbed amounts during the dry and humid CO₂ separation process for Mg-MOF-74 at 86% RH, 300 K, and 101.3 kPa.

A comprehensive modeling of humid CO₂/N₂ mixture at different H₂O relative humidity values (0%, 24.8%, 49.6%, 74.4% and 99.2% RH) for 323 K are shown in Figure 5.17 - Figure 5.19 for the data described in section 3.2.8 (cases 1-5, Table 3.8).

Figure 5.17 shows the concentration ratio values of CO₂/N₂ at different humidity ratio values. It is clear that the breakpoints were minimized by existing higher amounts of water vapor which have been adsorbed to the adsorbent. In addition, the increase of concentration values of CO₂/N₂ after saturation (> 12 minutes) is due to the absence of H₂O at the outlet for all relative humidity cases. It is clear, also, that Mg-MOF-74 is more hydrophilic than 13X.

Figure 5.18 presents the temperature profiles at different H₂O relative humidity values. The higher relative humidity, the higher temperature profile values. After CO₂ saturation region, the temperature values increased from steady trend for low RHs to dramatic increase for high RHs attributed by the multiplication of H₂O adsorption. Figure 5.19

illustrates the adsorption uptakes of CO₂/N₂/H₂O at different relative humidity values. As evidence, the CO₂ uptake at 25 minutes was about 4.3 mmol/g and that minimized to about 3.4 mmol/g (20%) for 99.2% RH case. Also, the CO₂ adsorption capacity reduction was about 9.4 % when the CO₂ reached saturation point. The H₂O uptakes were linearly increasing while the CO₂ uptake values were decreasing accordingly.

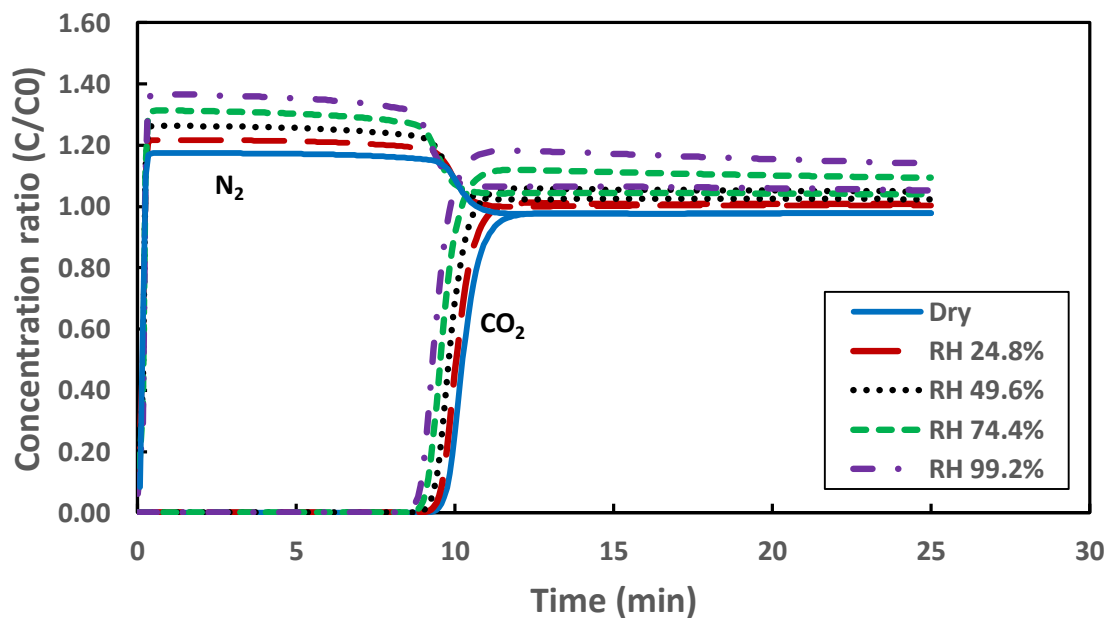


Figure 5.17 Dry and humid CO₂/N₂ adsorption breakthrough curves of concentration ratio for Mg-MOF-74 at different RH, 323 K, and 101.3 kPa.

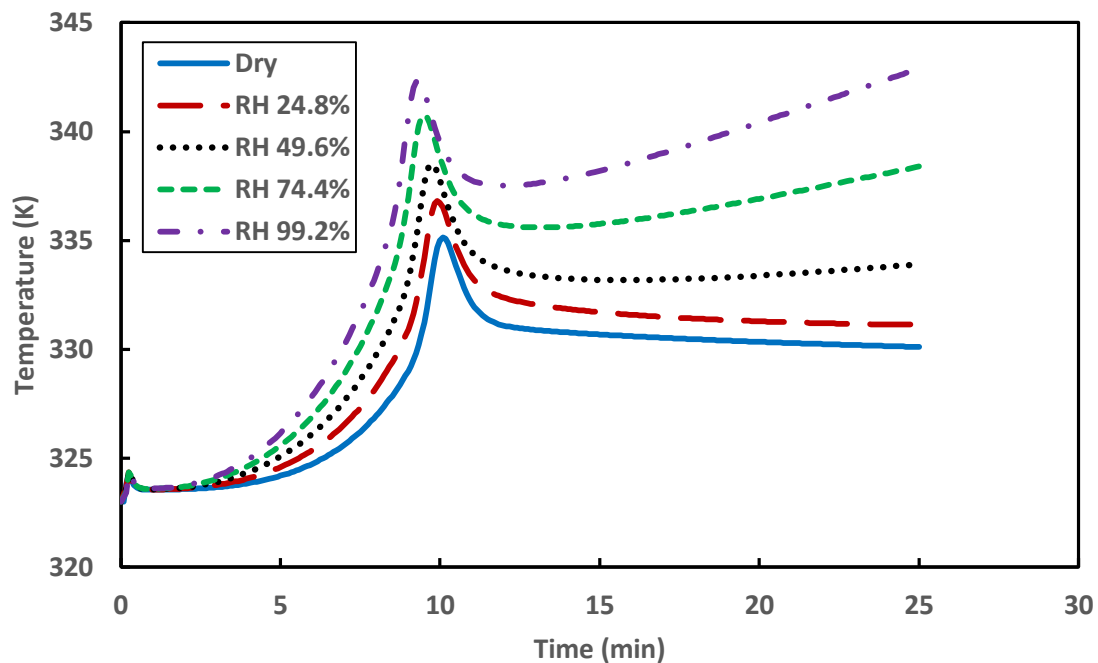


Figure 5.18 Temperature profiles at the bed outlet during dry and humid CO₂/N₂ separation process for Mg-MOF-74 at different RH, 323 K, and 101.3 kPa.

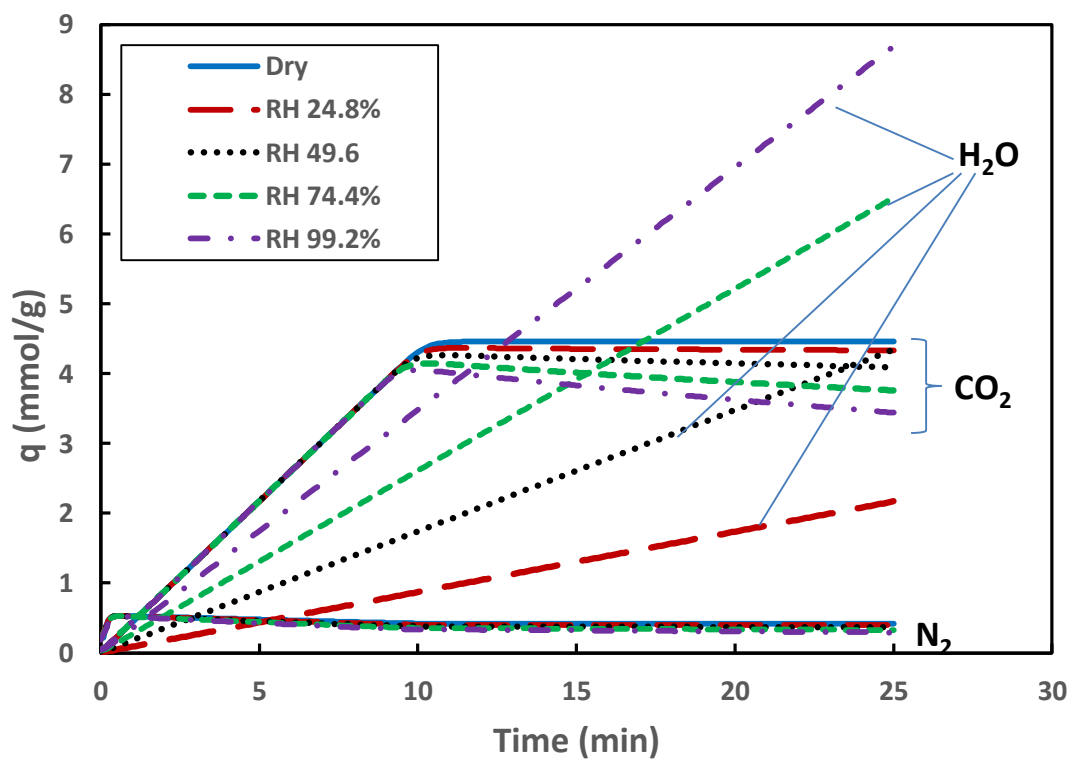


Figure 5.19 CO₂/N₂/H₂O adsorbed amounts during the dry and humid CO₂ separation process for Mg-MOF-74 at different RHs, 323 K, and 101.3 kPa.

For putting in view the effect of water vapor on CO₂ uptake when H₂O reaches adsorption saturation point, case 8 in Table 3.8 have been dedicated to explore and evaluate the maximum reduction of CO₂ uptake. Figure 5.20 shows the breakthrough ratio curves of dry and humid CO₂/N₂ at 373 K. The relative humidity is about 9.1% to present 9% of molar fraction of the CO₂/N₂/H₂O mixture. The adsorption saturation point of H₂O was so long (about 100 minutes) in comparison to CO₂/N₂ (about 5 minutes). Figure 5.21 shows the temperature profile during CO₂/N₂/H₂O adsorption processes. The CO₂ adsorption raised the bed outlet temperature to about 377 K at the beginning of CO₂ adsorption saturation while this value has sharply increased to about 408 K at H₂O saturation period. Mg-MOF-74 could adsorb about 20 mmol/g of H₂O at 373 K and 9 vol.%. This huge amount of H₂O could block MOF sites and accordingly reduced the CO₂ uptake by around 47.0%. For this reason, it is recommended that the CO₂ separation process should be delayed after a condensation pre-process to remove water vapor from the flue gas.

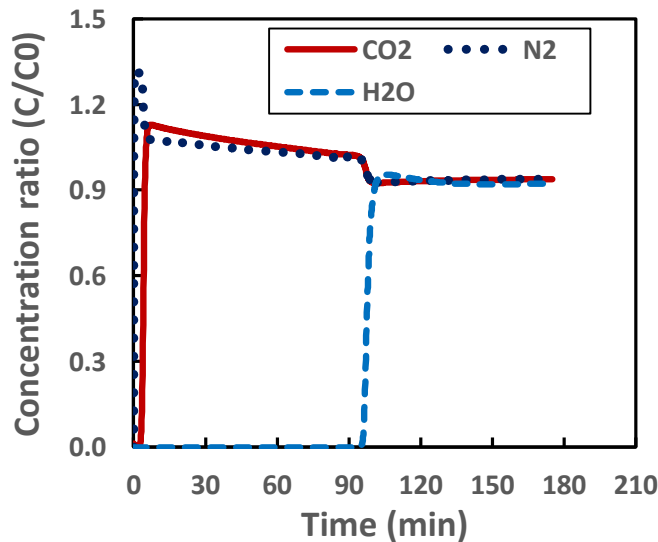


Figure 5.20 Humid CO₂/N₂ adsorption breakthrough curves of concentration ratio for Mg-MOF-74 at 9.1% RH, 373 K, and 101.3 kPa.

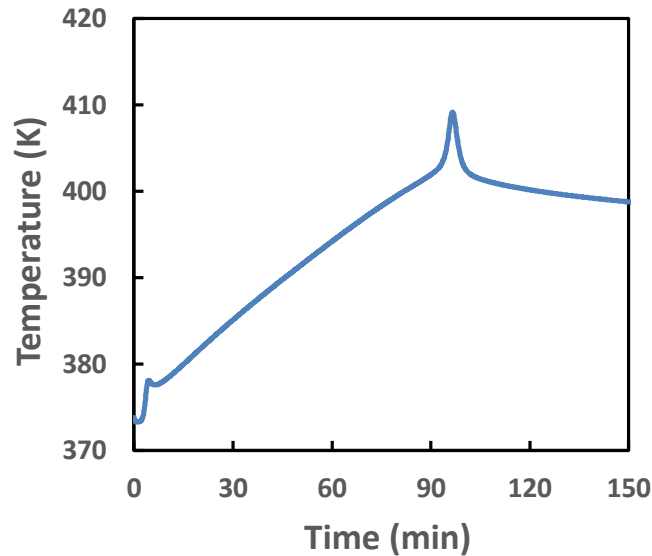


Figure 5.21 Temperature profile at the bed outlet for humid CO₂/N₂ mixture during separation process using Mg-MOF-74 at 9.1% RH, 373 K, and 101.3 kPa.

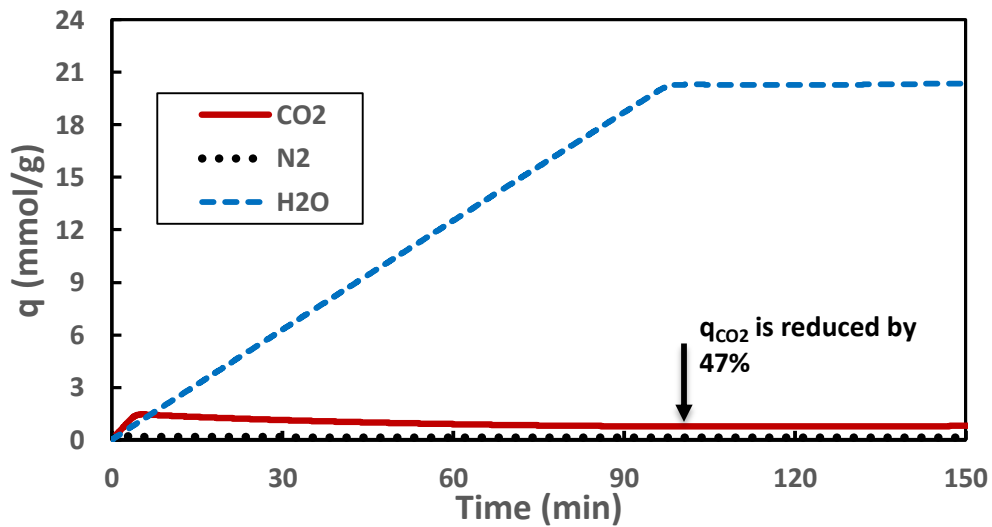


Figure 5.22 CO₂/N₂/H₂O adsorbed amounts during the humid CO₂ separation process for Mg-MOF-74 at 9.1% RH, 373 K, and 101.3 kPa.

5.2 Vacuum/Pressure Swing Adsorption

For practical applications of CO₂ capture, Pressure Swing Adsorption (PSA) is an important method for adsorption and desorption processes by changing the applied pressure through some steps in purpose of a continuous adsorption/desorption operation.

5.2.1 PSA Validation

As described in Table 3.12 and Figure 3.5, the PSA model have been validated by the experimental work [151] for one cycle with an operating pressures varies during pressurization, feed, blowdown, and purge steps as shown in Figure 5.23. Figure 5.24 shows CO₂ molar flow rate of a complete PSA cycle (1st cycle) for both of experimental and 1D simulation modeling [151] and the present 2D laminar and turbulent models as well as 3D simulation study. The results shown in Figure 5.24 confirm that the CO₂ molar flow rate of both the laminar and the turbulent flow overlaps during all PSA steps, indicating that the laminar flow is sufficient under the studied boundary conditions. Additionally, The CO₂ molar flow rate values of the 2D and 3D simulations have a much better agreement with those of the experimental [151] in comparison with the results of 1D simulation. This can be attributed to the existence of the radial diffusion of both mass and heat transfer in the 2D and 3D models and involves the thermal diffusion term of the porous bed energy equation.

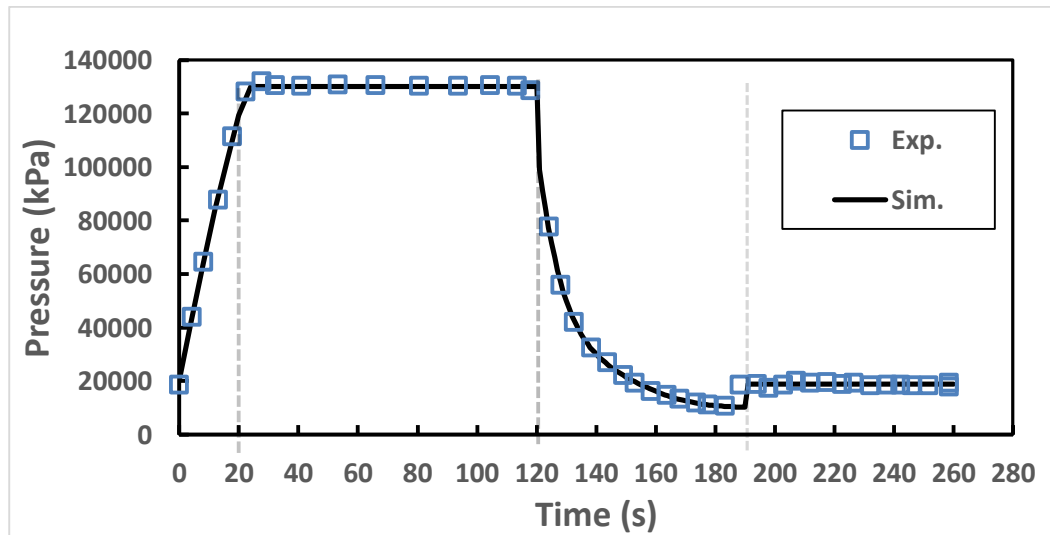


Figure 5.23 Variation of the bed pressure (Pa) with the 1st cycle time of the experimental work [151] and the present simulation.

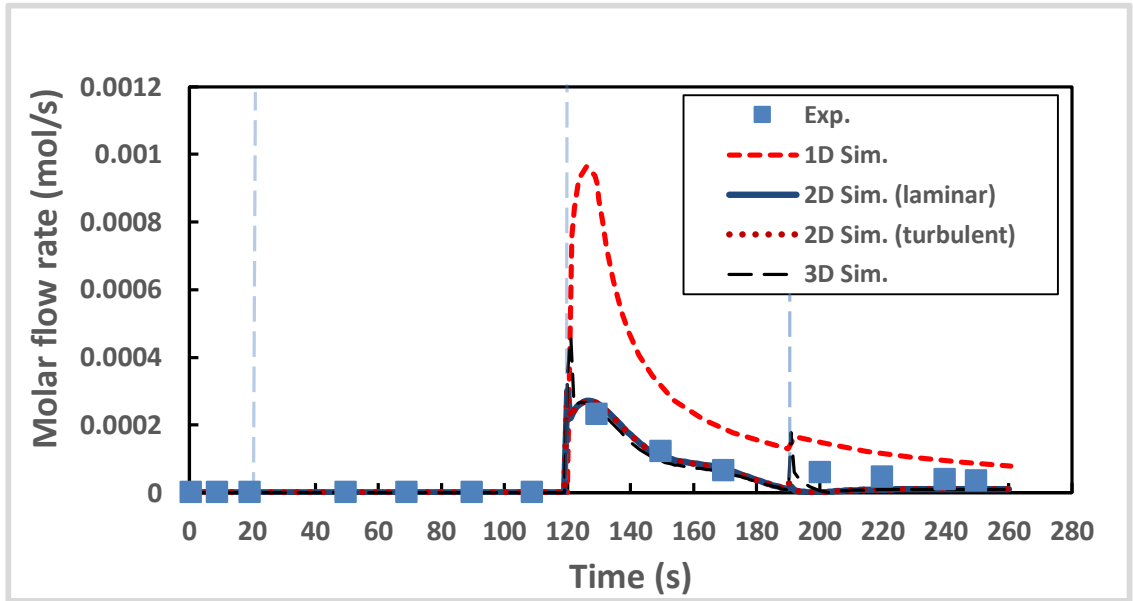


Figure 5.24 A comparison of the CO₂ molar flow rate history between the experimental work, the 1D simulation [151] and the present 1D, 2D (laminar and turbulent) and 3D simulations during a full PSA 1st cycle.

5.2.2 Comparison between VPSA of 2D and 3D Simulations

A comparison between 2D and 3D vacuum pressure swing adsorptions have been investigated for the thermal and adsorption conditions depicted in section 3.2.9. VPSA has included five steps named: pressurization, feed, rinse, blowdown, and purge for about 20, 250, 40, 100, 40 seconds, respectively. Figure 5.25 shows the molar flow rate history at the bed outlet during the first three cycles for both 2D and 3D simulations. The molar flowrate values of 2D simulation overlapped with those of the 3D. As a whole, carbon dioxide molar flow rate values were almost zero during pressurization, feed and rinse steps and then increased to the maximum levels during the blowdown process due to the desorption process. For blowdown process, there were two thorns of CO₂ molar flow rate values. The first one is due evacuating the gas from the bed void at the beginning of blowdown process by decreasing the pressure whereas the second one is due to minimizing the pressure to the

lowest level (2 kPa abs.) leading to rise the outlet velocity and hence increases the CO₂ molar flow rate. Reaching to the minimum pressure evacuated a considerable amount of adsorbed CO₂. The purge process followed the blowdown process to release more CO₂ from the bed *via* purging some amounts of N₂. The CO₂ uptake during the first three cycles are shown in Figure 5.26. As evident, the bed could adsorb about 7.6 mmol/g of CO₂. However, it could only recycle about 4.5 mmol/g under the operating pressure (130 kPa – 2 kPa).

Figure 5.27 shows the temperature distribution along the bed at selective times (at 1200, 1220, 1350, 1470, 1510, 1560, 1610, and 1650s) during all VPSA steps of one steady state cycle. Obviously, the bed temperature increased for few degrees during pressurization process while the temperature of the hottest zone of the bed column raised up to almost 307 K during feed process due to CO₂ adsorption process. Then the temperature have grown up again to about 309 K in rinse process due to adsorbing more amounts of CO₂ since the CO₂ has entered the bed at 100% molar fraction. Throughout the blowdown process, the temperature dropped down to almost 299 K at the last third zone and about 297 K in the remaining zone of the column due to the huge drop in the pressure values, and also because of the desorption process which consumed some energy. The temperature continually decreased during the purge process as a result of desorbing some CO₂ from the bed under purging N₂ at a low pressure (2 kPa).

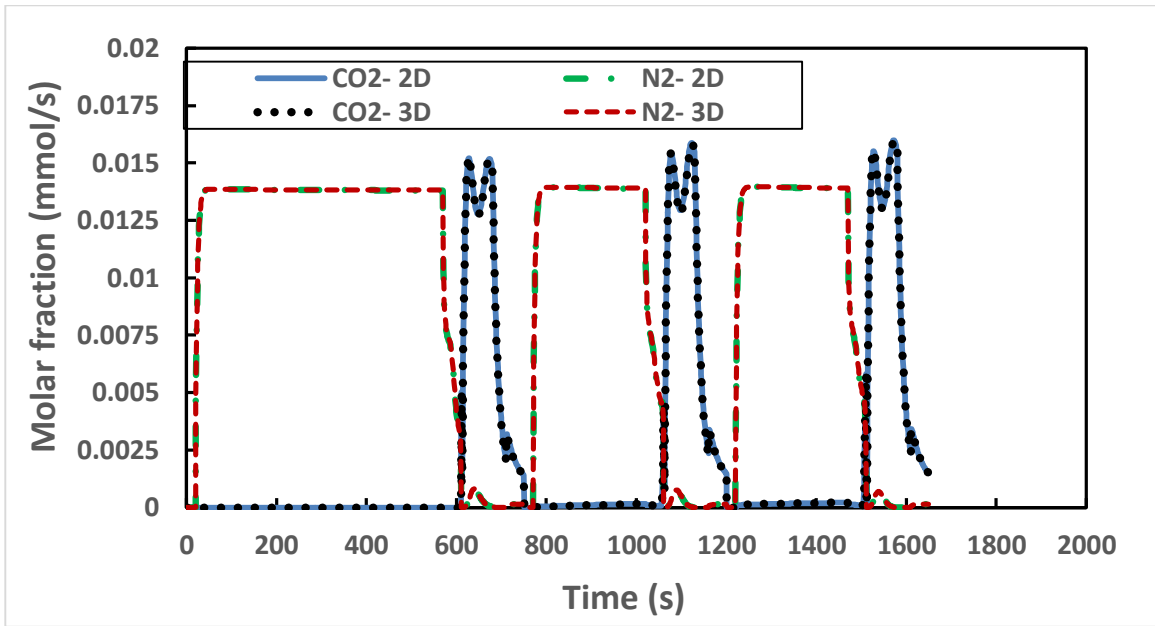


Figure 5.25 A comparison of molar flowrate between 2D and 3D VPSA during 3 cycles.

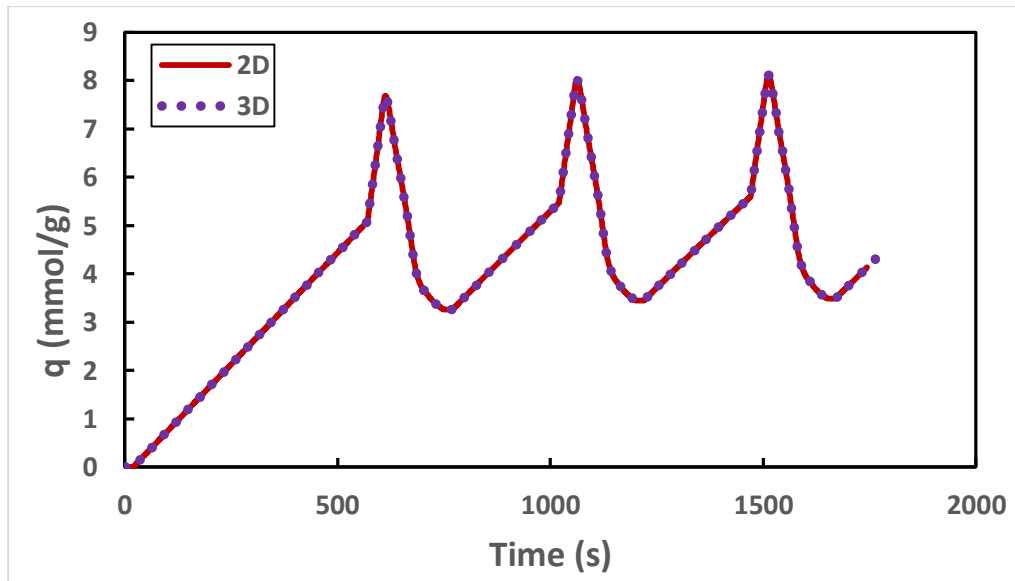


Figure 5.26 A comparison of CO₂ adsorbed amounts between 2D and 3D VPSA during 3 cycles.

The minimum temperature recorded during the desorption process was about 296 K. Figure 5.28 exhibits the CO₂ mass fraction at the same selective times discussed early in Figure 5.27. The mass fraction at the beginning of pressurization step was high due to the fact that the beginning time of pressurization process presented the end process of a purge

step of the previous cycle. At the end of pressurization step, the CO₂ mass fraction was about zero due to filling the bed with pure N₂. During the feed process, the CO₂ molar fraction (about 0.28) was marching through the bed with advancing time. This parameter (CO₂ molar fraction) has increased up to 1 in the rinse step under feeding pure CO₂ at the bed inlet. This value (CO₂ mass fraction=1) remained constant in the majority of the left over steps due to the absence of N₂. The CO₂ uptake contours are shown in Figure 5.29. Evidently, the minimum CO₂ through the bed was about 3.4 and raised during the feed and rinse steps consecutively due to feeding CO₂ at the bed inlet. This amounts decreased in the blowdown and purge steps as effect of the desorption processes.

Again, the 2D and 3D simulation could give a similar results with slight differences, so that the 2D modeling is enough for predicting such cases.

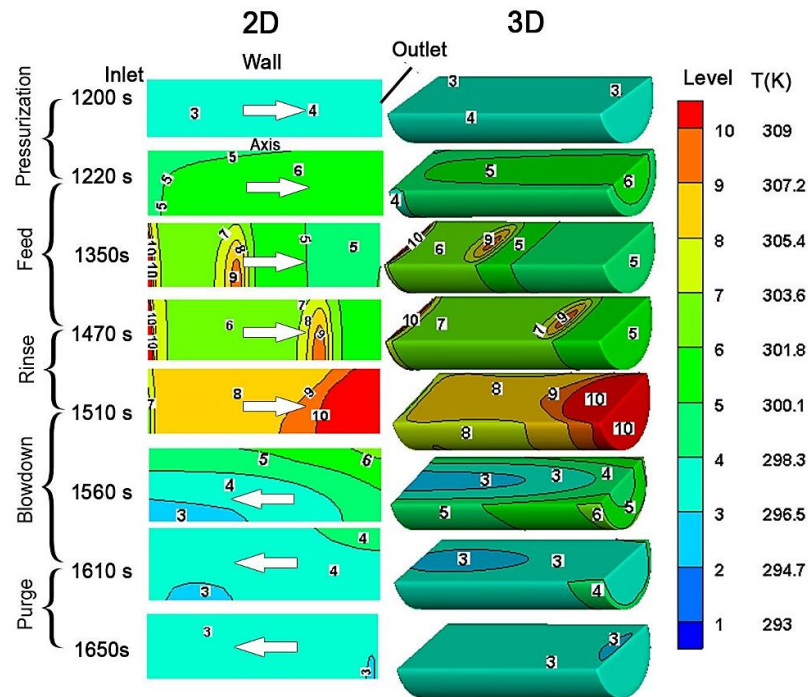


Figure 5.27 A comparison of temperature contours of the bed between 2D and 3D VPSA during a steady state cycle.

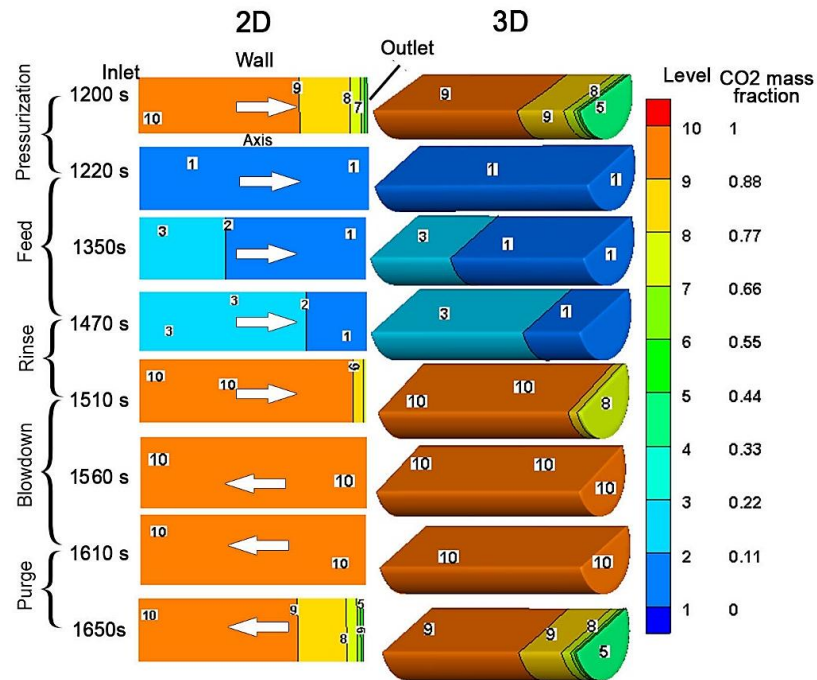


Figure 5.28 A comparison of CO₂ molar fraction between 2D and 3D VPSA during a steady state cycle.

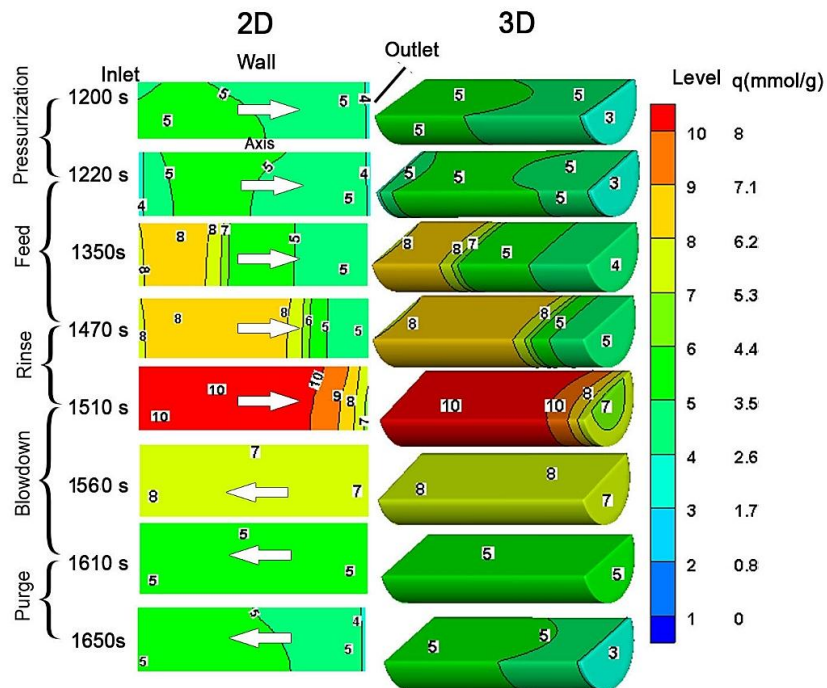


Figure 5.29 A comparison of CO₂ adsorbed amounts between 2D and 3D VPSA during a steady state cycle.

5.2.3 VPSA Cases

Vacuum pressure swing adsorption, for the same 2D bed shown in section 3.2.9 (Figure 3.6) using 5 steps including pressurization, feed, rinse, blowdown, and purge for about 20, 250, 40, 100, 40 seconds, respectively; was studied for 11 cycles to show the cycling stability. Figure 5.30 shows the average bed pressure during 11 repeated cycles for the 5 steps. The pressure values fluctuates between 130 kPa and 2 kPa during adsorption and desorption processes, respectively. The history of CO₂/N₂ molar flow rates are shown in Figure 5.31. All in all, nitrogen has appeared at the bed outlet during the feed and rinse steps while the CO₂ is dominant during the blowdown and purges processes due to applying the vacuum which leads to suck some adsorbed CO₂ amounts. It is clear that the steady state cycles have started from the third one.

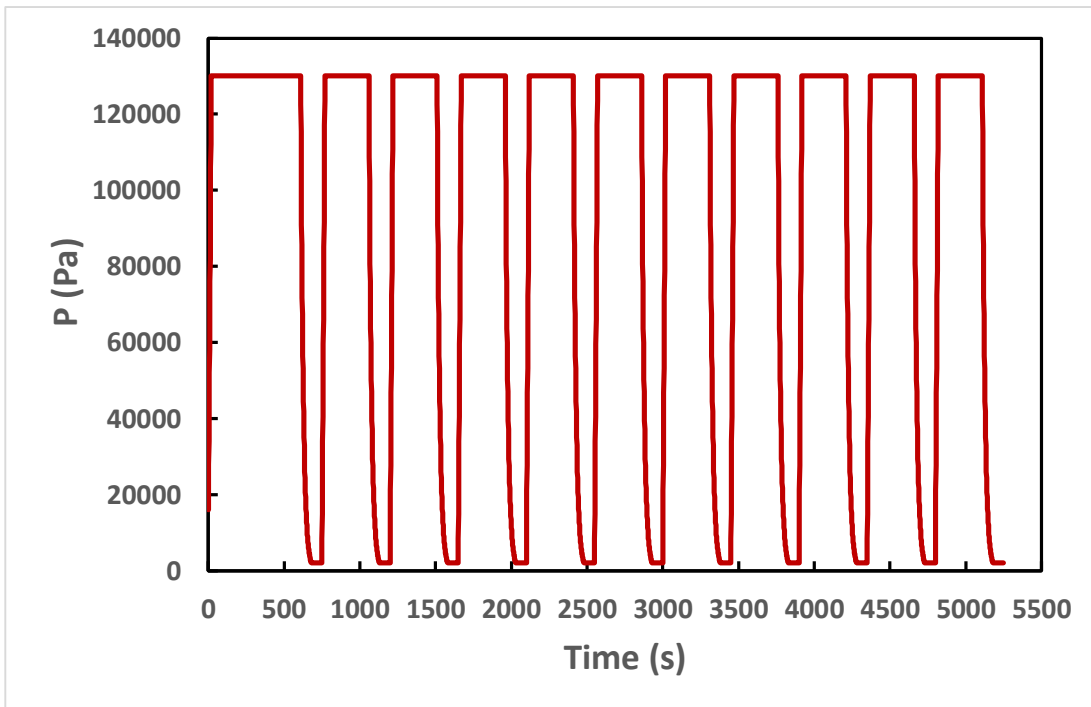


Figure 5.30 Pressure history of 11 VPSA cycles (Pressurization=20s, feed=250s, rinse=40s, blowdown=100s, and purge=40s).

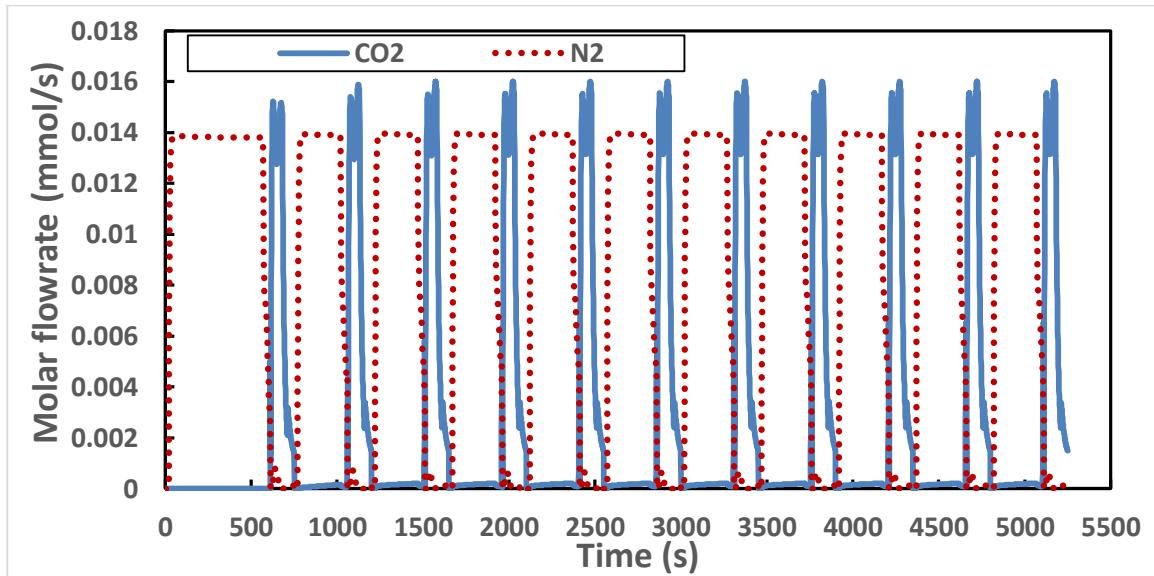


Figure 5.31 CO₂/N₂ molar flow rate of 11 VPSA cycles (Pressurization=20s, feed=250s, rinse=40s, blowdown=100s, and purge=40s).

Figure 5.32 shows the history of CO₂ uptake during 11 cycles. Almost 4.6 mmol/g is successfully recycled under the operating pressure range (130-2 kPa). The sharp lines during the adsorption process was the CO₂ uptake throughout the rinse step owing to the CO₂ adsorption process have been occurred at high CO₂ pressure (130 kPa) compared to those during the feed step (19.5 kPa).

In order to investigate the effect of blowdown and purge times on the VPSA performance, 5 cases (Table 3.13) have been compared in terms of CO₂ purity, recovery, and productivity as well the energy consumed during the process with assuming that the efficiency of compressors and vacuum pumps are 0.72. The comparison was taken when the cycles have attained steady state for every case. Figure 5.33 gives emphasis to the CO₂ purity recovery and productivity for blow down times between 100 and 300 seconds.

The increase of the blowdown time has somehow improved the CO₂ recovery (from 89.45% to 98.6%) and decreased the purity (from 97.3% to 97.1%). Actually these minor changes in the CO₂ purity and recovery are not significant anymore inferring the lowest

time (100 s) is sufficient to blowdown processes. The CO₂ productivity values have supported the smallest investigated period (100 s) for blowdown time since the time increasing has shrunk the productivity. This is because of adding more time without desorbing a significant amounts of CO₂.

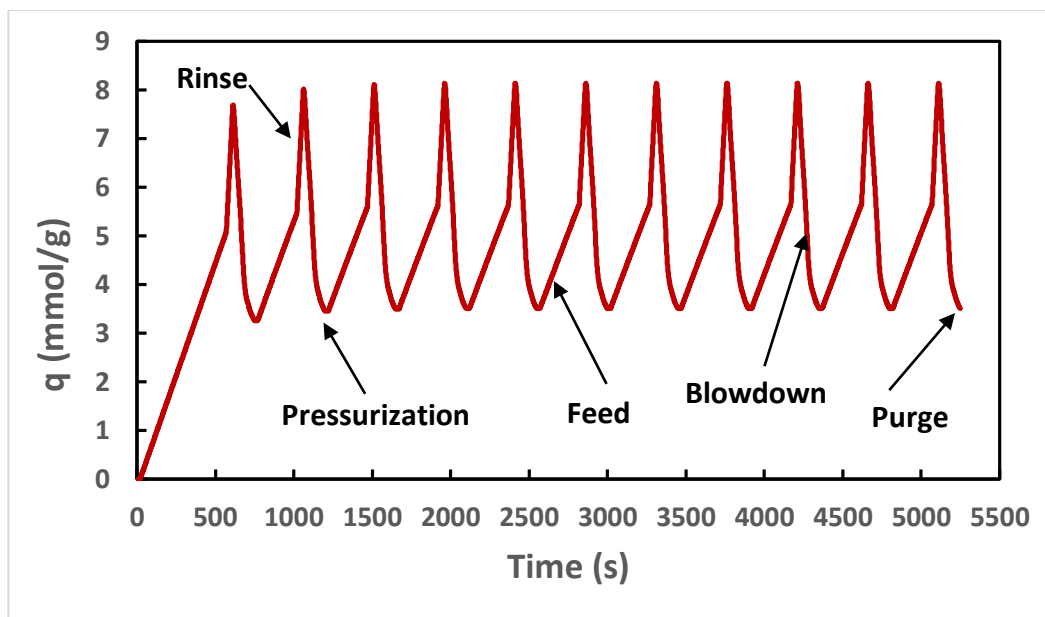


Figure 5.32 CO₂ uptake of 11 VPSA cycles (Pressurization=20s, feed=250s, rinse=40s, blowdown=100s, and purge=40s).

The effect of purge time on the VPSA performance is shown in Figure 5.34. It is clear that increasing the purge time (from 50 s to 150 s) has increased the CO₂ productivity (from 97.2% to 99.1%), and dropped both the CO₂ purity (from 98.1 to 96.4) and productivity (from 0.67 to 0.58 kg-CO₂ hr⁻¹ kg-MOF⁻¹). Therefore, the trivial increase of the CO₂ recovery values due to increasing the purge time was sacrificed to give the advantages to the CO₂ purity and productivity. The interesting calculated power consumption of CO₂ separation utilizing VPSA is shown in Figure 5.35 for both blowdown and purging times. The power consumption required for increasing the blowdown time is almost the same (67 kWh/ tonne-CO₂) for all the blowdown investigated times (100, 150, and 200 s). This trend

is because the time increased balances out the CO₂ desorbed amounts during the extended times. On the other hand, the increase of purge time has increased the power consumption from 64 to about 70 kWh/tonne-CO₂ for 50 and 150s, respectively. The extending purge time have raised the energy consumption without desorbing substantial amounts of CO₂ as well as increased the whole time of the VPSA cycle. The optimal case may be taken from the investigated cases for blowdown time about 150s and purge time about 50s. The CO₂ purity, recovery, productivity, and the power consumption have estimated about 98.1%, 97.3%, 0.67 (kg-CO₂ hr⁻¹ kg-MOF⁻¹), and 64.2 kWh/tonne-CO₂, respectively. However, selecting blowdown and purge times as 100s and 40s (the same case shown in Figs. 5.30-5.32) revealed the optimal CO₂ purity, recovery, productivity, and power consumption by about 98.3%, 95.7%, 0.731 (kg_CO₂ hr⁻¹ kg_MOF⁻¹), and 63.89 kWh tonne_CO₂⁻¹, respectively. Decreasing purge time less than 40s will drop the CO₂ productivity less than 95% which is not preferable.

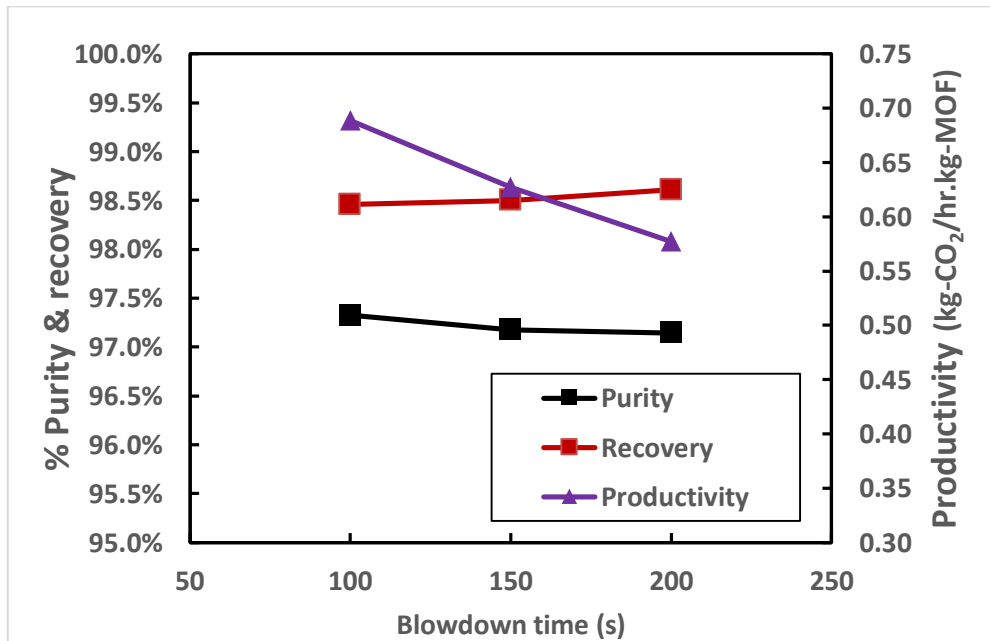


Figure 5.33 Effect of blowdown time on CO₂ purity, recovery and productivity of VPSA (Pressurization=20s, feed=250s, rinse=40s, and purge=100s).

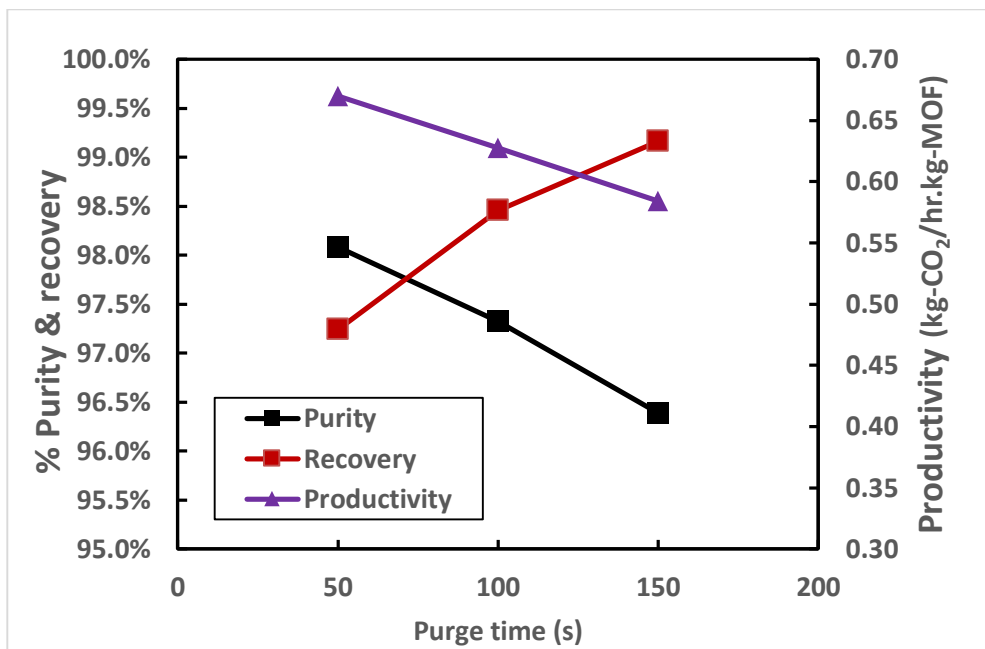


Figure 5.34 Effect of purge time on CO₂ purity, recovery and productivity of VPSA (Pressurization=20s, feed=250s, rinse=40s, and blowdown=150s).

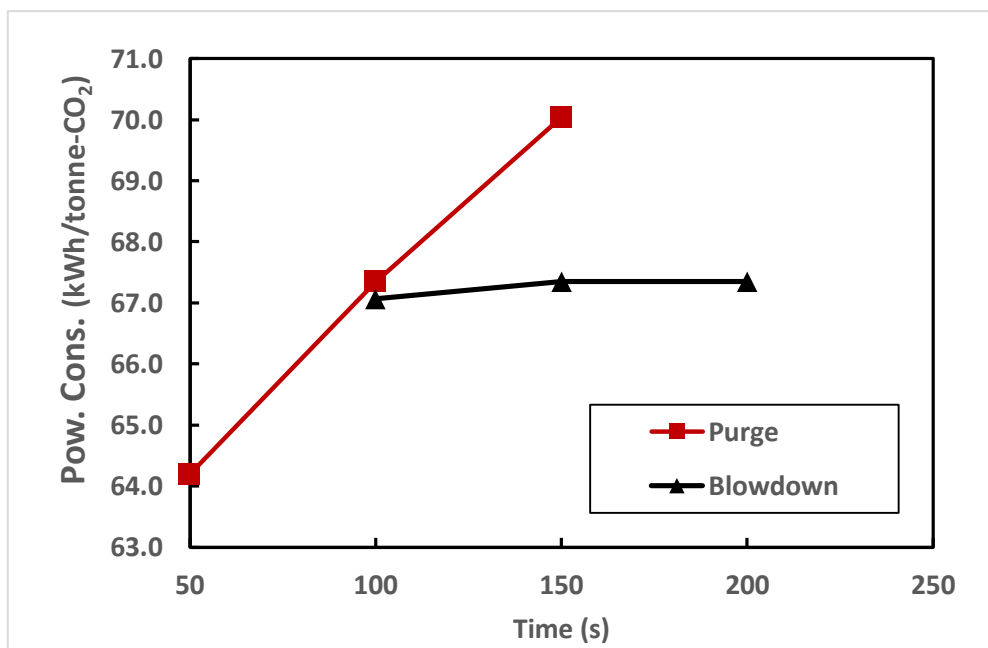


Figure 5.35 Effect of blowdown and purge times on VPSA power consumption (Pressurization=20s, feed=250s, rinse=40s).

5.3 Temperature Swing Adsorption

Temperature swing adsorption is another important technology for CO₂ adsorption. It takes its merits from the capability to supply the needed regeneration heat from cheap sources like waste heat.

5.3.1 Comparison between TSA 2D and 3D Simulations

The 2D and 3D beds described in section 3.2.9 (Table 3.14 and Figure 3.8) have been investigated to perform TSA for CO₂ separation from CO₂/N₂ mixture. TSA was presented by 4 steps namely: feed, rinse, heating, and cooling. The molar flow rates (Figure 5.36) and CO₂ uptake (Figure 5.37) showed a superior closeness between 2D and 3D simulation modeling. Figure 5.36 shows CO₂/N₂ molar flow rate values for two stable TSA cycles. Heating method was devoted for CO₂ desorption process. It is clear that the CO₂ desorbed amounts during heating period was higher than those of N₂ confirming a good CO₂ purity. The recycled CO₂ uptake profile is shown in Figure 5.37 for both 2D and 3D simulations. About 3.3 mmol/g was successfully recycled at 393 K comparing to about 4.6 mmol/g by applied vacuum (2 kPa) during blowdown and purge steps of VPSA.

Figure 5.38 is dedicated to show 2D and 3D temperature contours for one repeated cycle of TSA during selective times (at 2683, 2816, 2936, 2976, 3056, 3176, 3326, and 3476 seconds) for all steps. During the feed process (at 323 K), the cooled bed by previous cooling step was cooled down again (from about 324 K to about 314 K) due to keeping the bed exposed to the ambient. The temperature values increased for some degrees during the rinse step as a result of adsorption more CO₂. The heating process raised the bed temperature up to 393 K in pursuit of extracting the majority of an adsorbed CO₂ from the

bed. After that, the cooling process has taken place to cool down the bed before starting a new feed process. It is noticed that there was a small difference between 2D and 3D temperature contours due to respecting the thermal diffusion through the three dimensions in 3D simulation. However, this small difference in temperature values does not impinge on the TSA performance. Figure 5.39 demonstrates the CO₂ mass fraction through the bed at selective times. It has increased to high values by the end of the rinse process due to feed pure CO₂, and then the CO₂ mass fraction amounts have persisted at high levels during heating and cooling processes by means of the absence of N₂. The carbon dioxide contours (2D and 3D) are shown in Figure 5.40. The adsorbent (Mg-MOF-74) could be filled by about 5 mmol/g at the end of the feed process, and increased to the maximum level (about 7.6 mmol/g) at the end of the rinse process. The heat process was, then, able to minimize the values of CO₂ uptake to about 3.4 mmol/g).

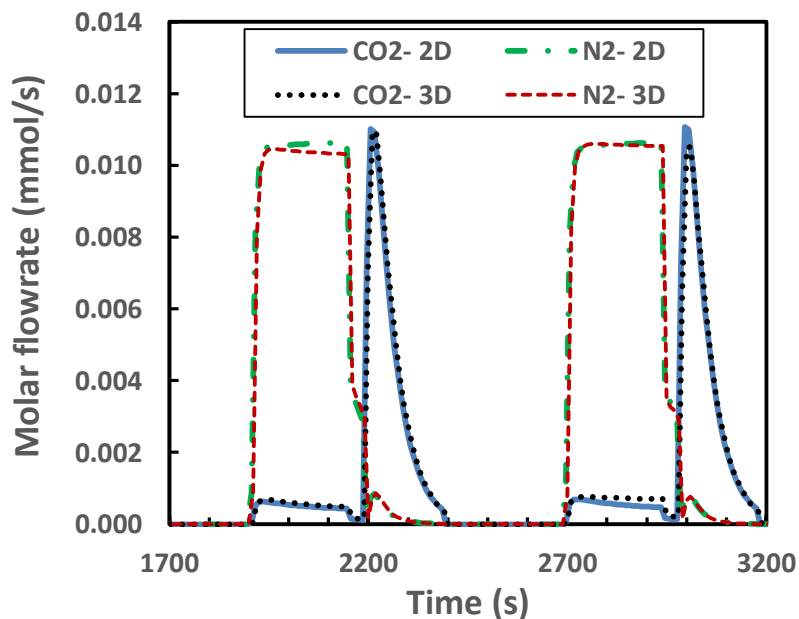


Figure 5.36 A comparison of molar flowrate between 2D and 3D TSA during 2 cycles.

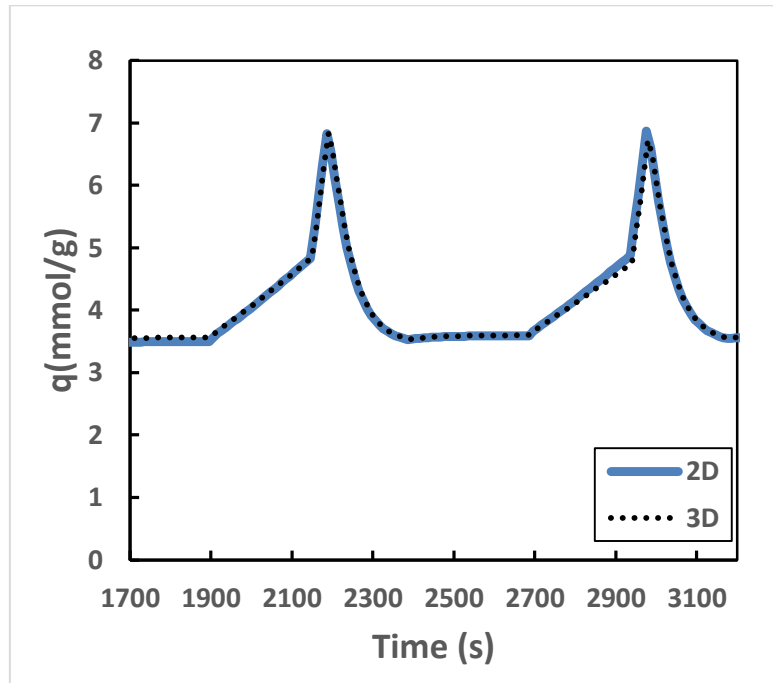


Figure 5.37 A comparison of CO₂ uptake between 2D and 3D TSA during 2 cycles.

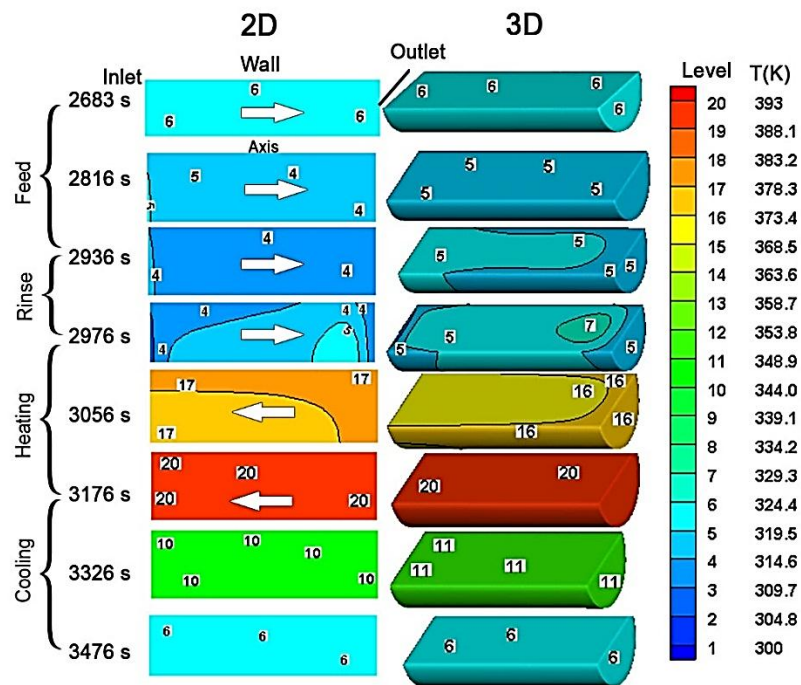


Figure 5.38 A comparison of temperature contours of the bed between 2D and 3D TSA during a steady state cycle.

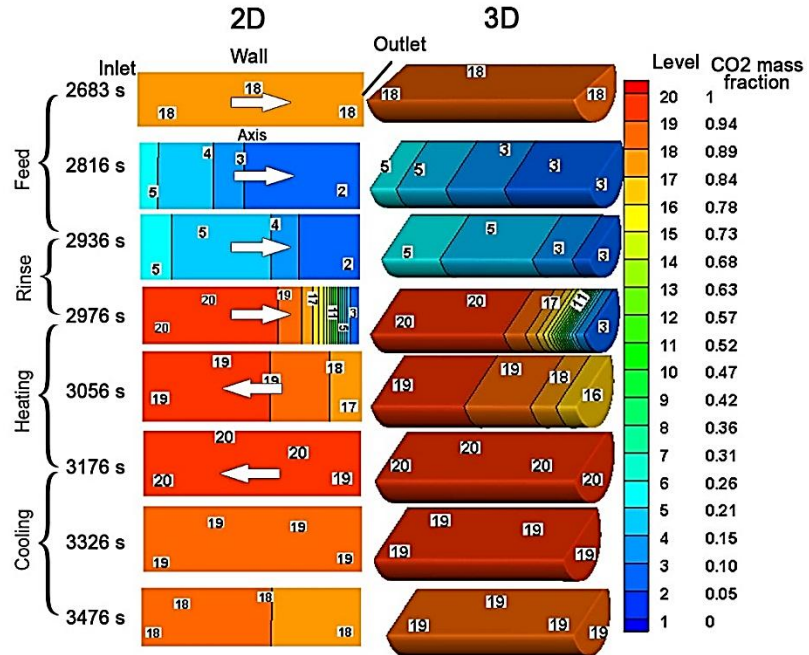


Figure 5.39 A comparison of CO₂ mass fraction between 2D and 3D TSA during a steady state cycle.

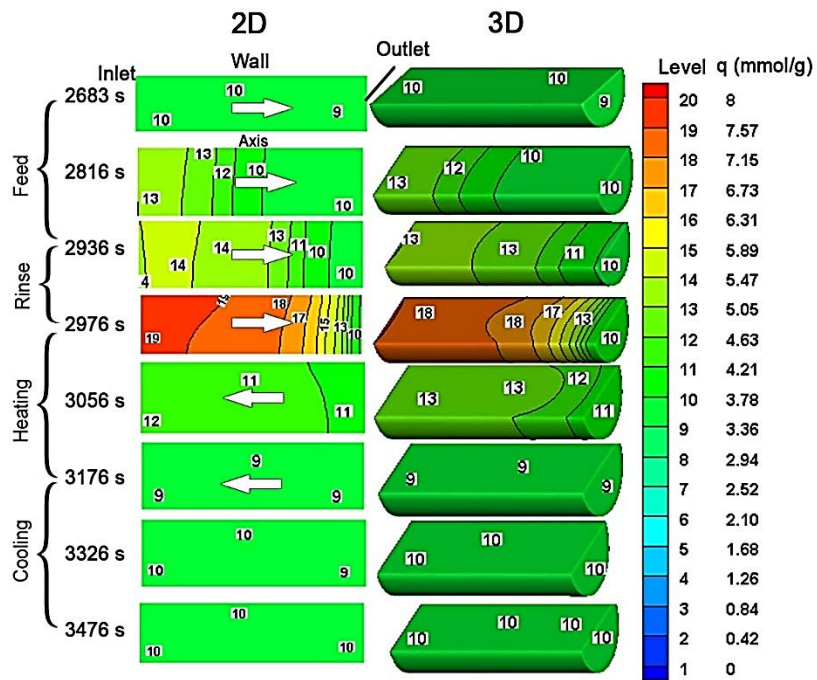


Figure 5.40 A comparison of CO₂ uptake contours between 2D and 3D TSA during a steady state cycle.

5.3.2 TSA Cases

Temperature swing adsorption is studied for 11 cycles to demonstrate the CO₂ cycling stability using the same 2D bed shown in section 3.2.9 (Figure 3.8) applying 4 steps including feed, rinse, heating, and cooling for about 250, 40, 200, 400 seconds, respectively. Figure 5.41 shows the temperature profile at the middle of the bed during 11 repeated cycles. The temperature values increased to about 313 K during 1st rinse and then increased again to about 391 K at the end of the heating process and subsequently cooled down to about 324 K at the end of cooling processes. Temperature values dropped to about 313 K after the feed and rinse processes as the bed cooled down by the surrounding ambient. Generally, the temperature values fluctuated between 393 kPa and 313 K during all the TSA cycles. The steady state cycles are announced from the sixth cycle. The history of CO₂/N₂ molar flow rates are shown in Figure 5.42. The N₂ has appeared at the bed outlet during feed and rinse steps while the CO₂ was dominant during the heating processes due to the desorption process.

Figure 5.43 exhibits the history of CO₂ uptake during 11 cycles. Almost 3.3 mmol/g was successfully recycled. The sharp lines during adsorption process was the CO₂ uptake at the rinse step due to the CO₂ adsorption process have been occurred at high CO₂ pressure (101.3 kPa) compared to those during the feed step (15.2 kPa).

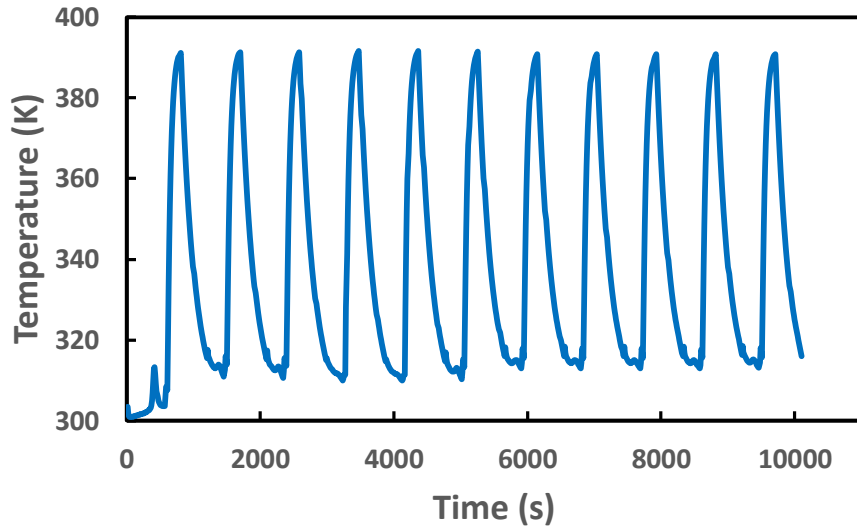


Figure 5.41 Temperature profile at the middle of the bed for 11 TSA cycles (feed=250s, rinse=40s, heating=200s, and cooling=400s).

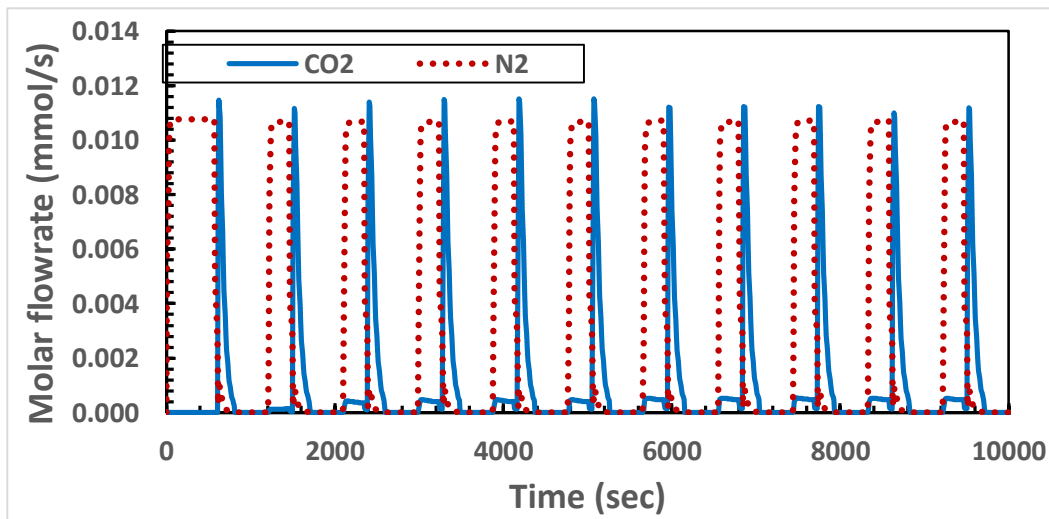


Figure 5.42 CO_2/N_2 molar flowrate of 11 TSA cycles (feed=250s, rinse=40s, heating=200s, and cooling=400s).

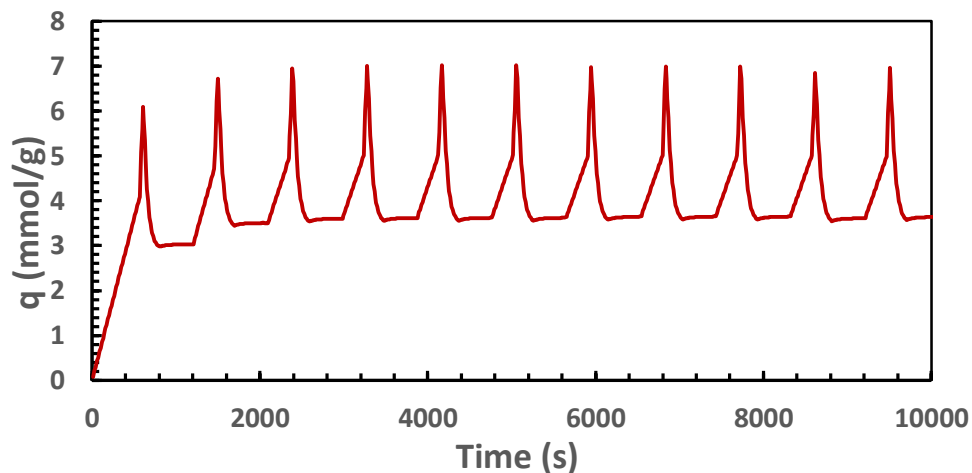


Figure 5.43 CO₂ uptake of 11 TSA cycles (feed=250s, rinse=40s, heating=200s, and cooling=400s).

In order to investigate the impact of heating and cooling times on the TSA performance, 5 cases (Table 3.14) are compared in terms of CO₂ purity, recovery, and productivity as well the energy consumed during the regeneration process with assuming that the efficiency of the heat source is 0.8. The comparison have been taken when the cycles reached steady state for every case. Figure 5.44 shows the CO₂ purity, recovery and productivity for different heating times between 200 and 300 seconds.

The increase of heating time to some extent improved the CO₂ recovery (from 85.8% to 86.3%) and dropped off the purity (from 95.5% to 94.8%). Actually these minor changes in the CO₂ purity and recovery is not significant at all, indicating to the lowest time (200 s) is sufficient to heating processes. The CO₂ productivity values have supported the period of 100s for heating time since the extended time reduces the productivity. This is because of adding more time without desorbing a significant amounts of CO₂.

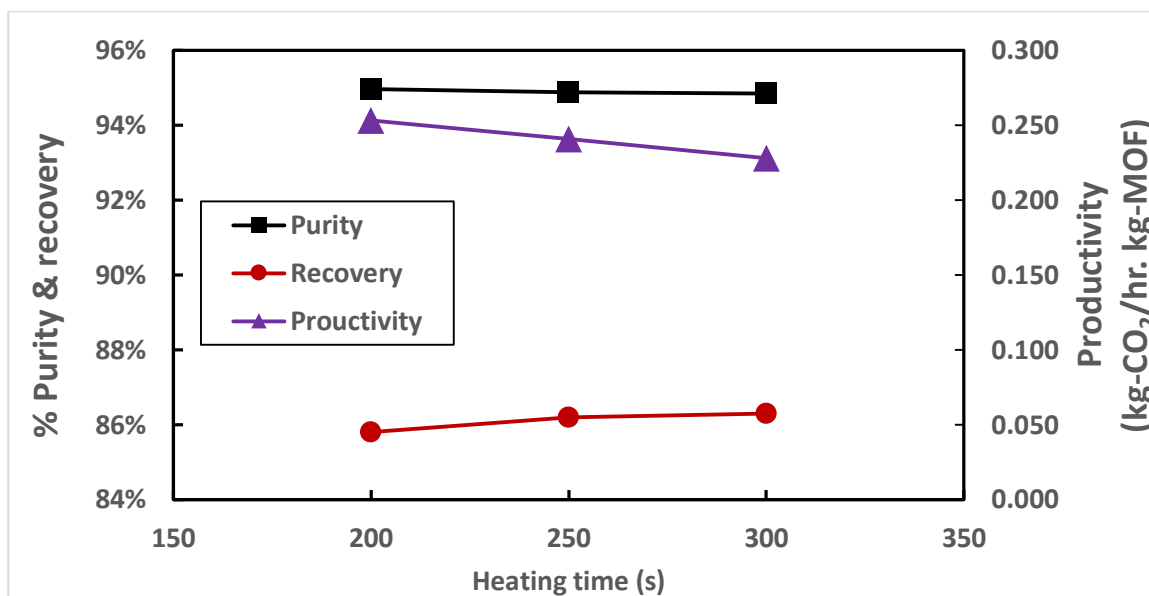


Figure 5.44 Effect of heating time on CO₂ purity, recovery and productivity of TSA (feed=250s, rinse=40s, and cooling=300s).

The effect of cooling time on the TSA performance is shown in Figure 5.45. It is obvious that increasing the cooling time (from 200 s to 400 s) have grown the CO₂ recovery (from 87% to 87.5%), and raised both the CO₂ purity (from 94.2% to 95.2%) and productivity (from 0.221 to 0.24 kg-CO₂ hr⁻¹ kg-MOF⁻¹). The interesting calculated regeneration energy and power consumption of CO₂ separation utilizing TSA are shown in Figure 5.46 - Figure 5.49 for both heating and cooling times. The energy of regeneration values per kilogram of produced CO₂ have escalated marginally by increasing the heating periods (Figure 5.46) and significantly decreased by extending the cooling time (Figure 5.47) due to enhancing the CO₂ production with cooled bed. The most important point in this scenario is that the regeneration energy for the adsorbent/adsorbate was much lower than that consumed by the metal walls due to high wall thermal inertia. Therefore, it is recommended here to use low thermal capacity metals for wall with low density as well as low wall thickness.

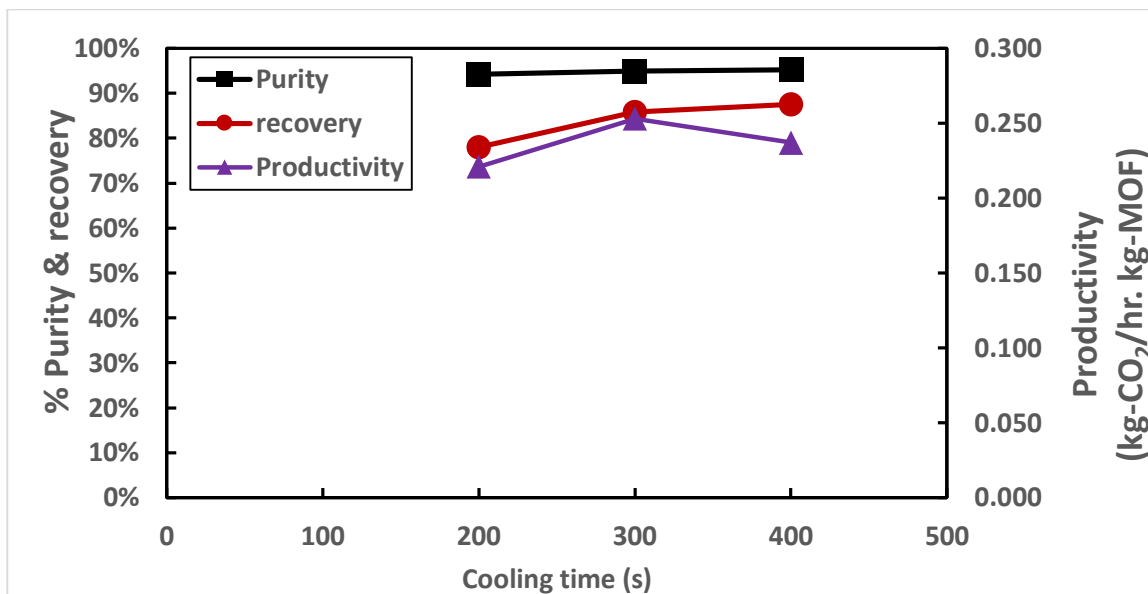


Figure 5.45 Effect of cooling time on CO₂ purity, recovery and productivity of TSA (feed=250s, rinse=40s, and heating=200s).

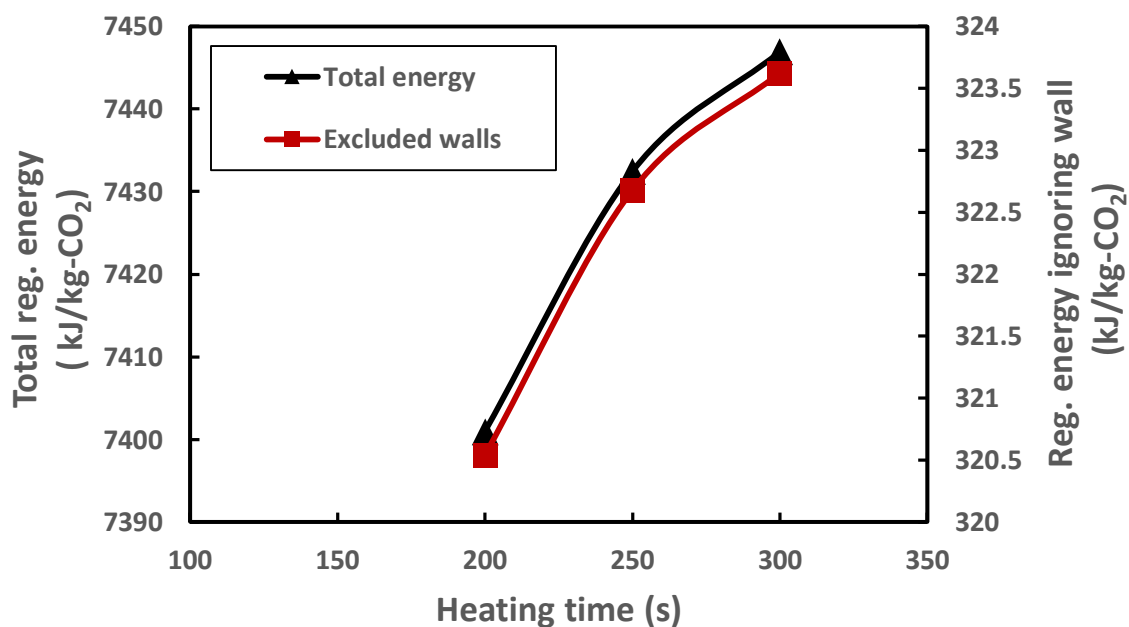


Figure 5.46 Effect of Heating time on TSA regeneration energy (feed=250s, rinse=40s, and cooling=300s).

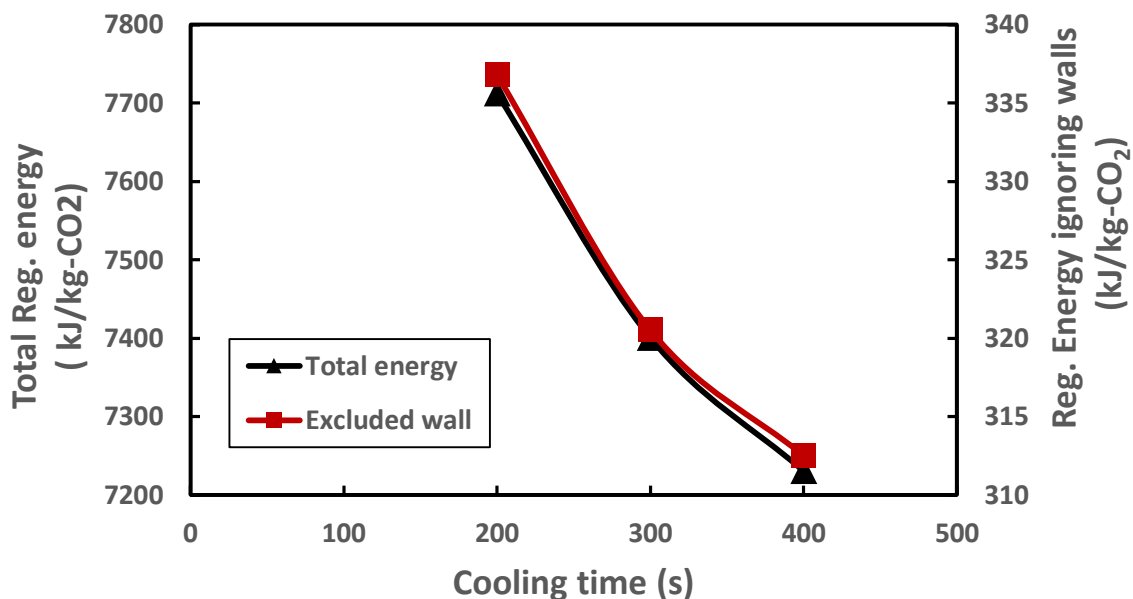


Figure 5.47 Effect of cooling time on TSA regeneration energy (feed=250s, rinse=40s, and heating=200s).

The energy consumed by increasing the heating times was almost constant 0.11 MWh/tonne-CO₂ as shown in Figure 5.48 (if we ignored the heat consumed by the metal wall). That is because the adding more heat could balance the produced CO₂ amounts. Figure 5.49 depicts the energy consumed due to extending the cooling time. The values of the power consumed have declined a little as a reason of building up the CO₂ production by broadening the cooling time. Again, the difference between total power consumption and that ignored the power consumption of the metal walls was very large about 22 times. Therefore, optimization of wall thickness is utmost needed. The wall thickness (1 mm) to internal diameter (4 mm) ratio of the studied bed was about 0.25 which is available in market for stainless steel quarter inch tubes. However, this ratio is very small in large diameter tubes. Another wall thickness have, moreover, been investigated as 0.5 mm, then the wall thickness to internal diameter ratio was 0.125.

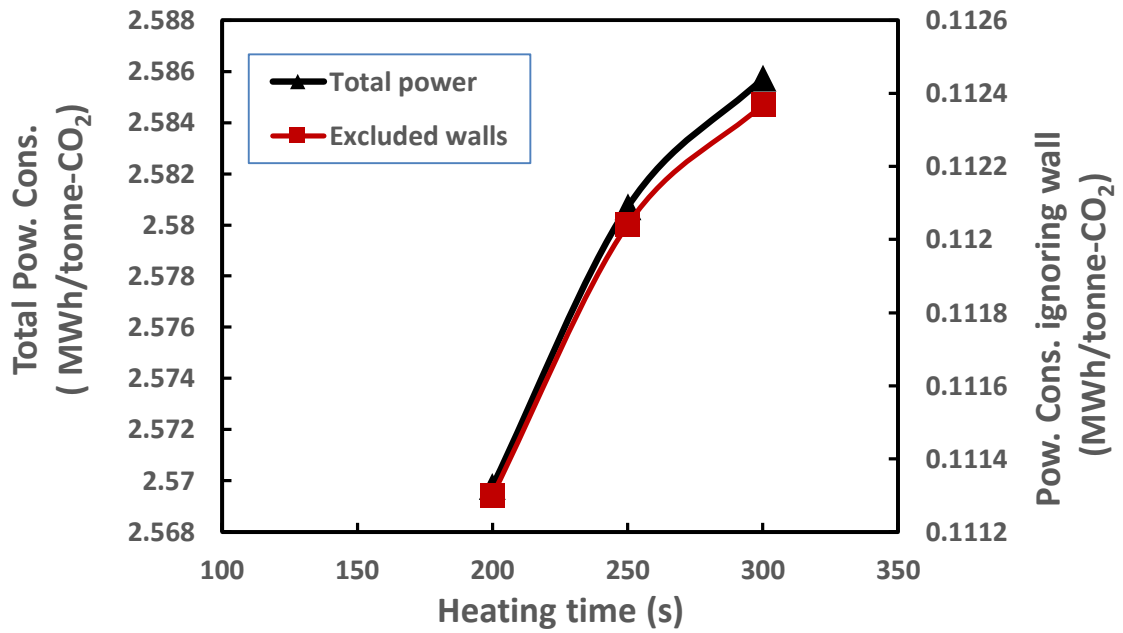


Figure 5.48 Effect of heating time on TSA power consumption (feed=250s, rinse=40s, and cooling=300s).

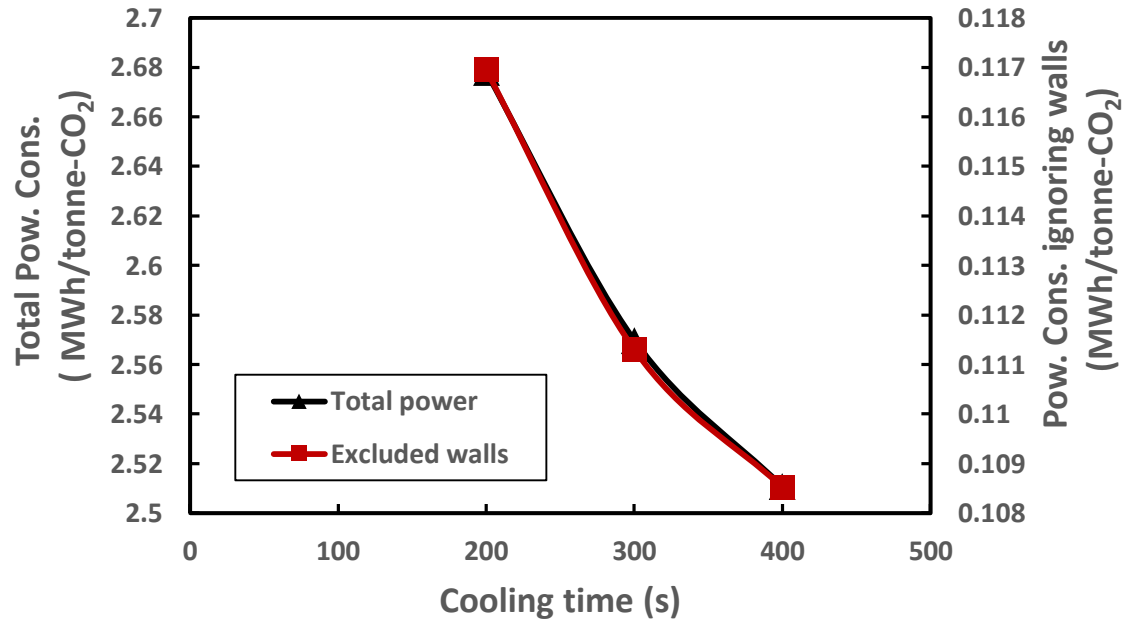


Figure 5.49 Effect of cooling time on TSA power consumption (feed=250s, rinse=40s, and heating=200s).

It is shown in Figure 5.50 that the increase of wall thickness decreased CO₂ purity, recovery and productivity. Figure 5.51 confirms that the power consumption is about 0.664 MWh/tonne-CO₂ for 0.125 $t_{\text{wall}}/D_{\text{in}}$. However the consumption has been magnified to about 2.5 MWh/tonne-CO₂ for the highest thickness due to increasing the thermal inertia of the bed wall.

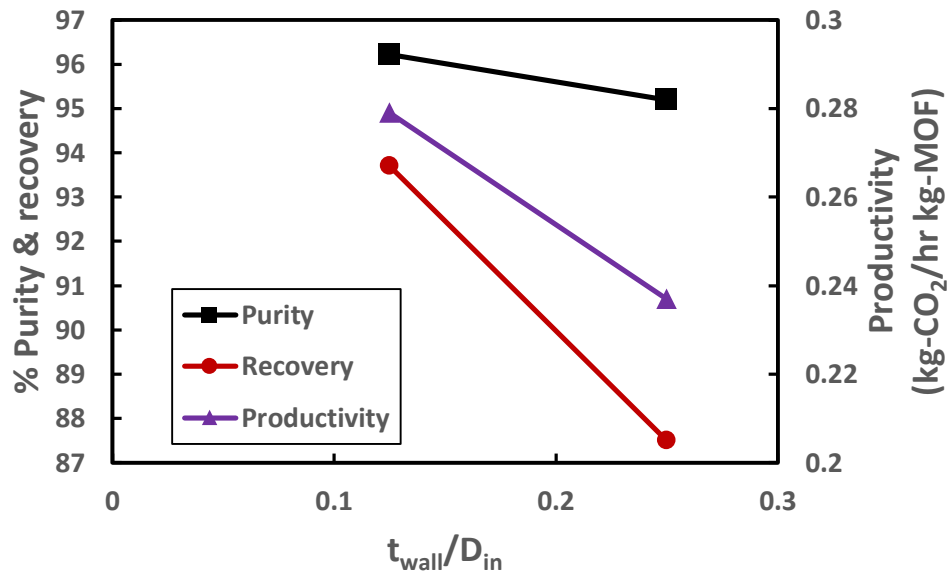


Figure 5.50 Effect of wall thickness to internal diameter of the bed on CO₂ purity, recovery and productivity for TSA (feed=250s, rinse=40s, and heating=200s).

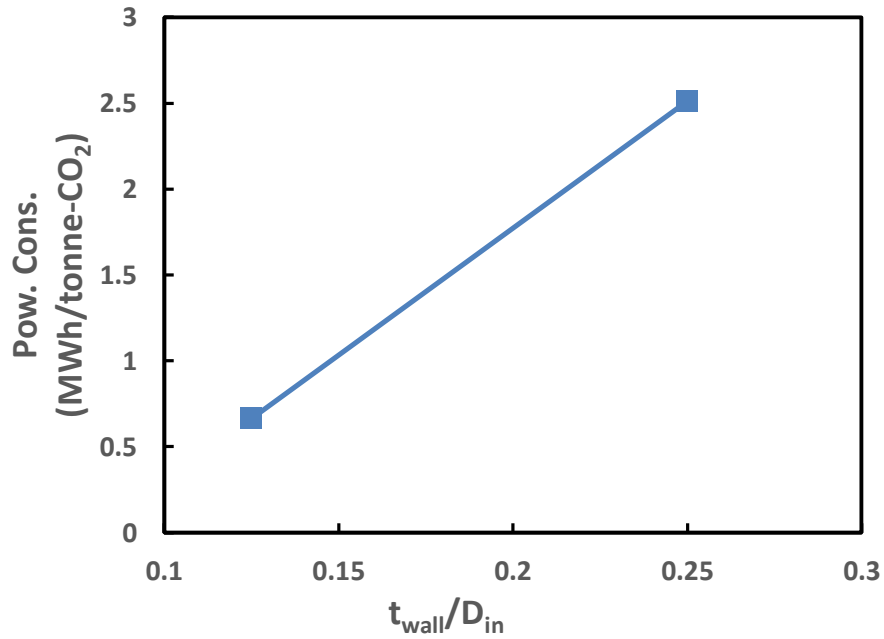


Figure 5.51 Effect of wall thickness to internal diameter of the bed on TSA power consumption (feed=250s, rinse=40s, and heating=200s).

Table 5.1 brings to light a comparison of CO₂ separation performances between the present VPSA and TSA and some reported in the literature. The present VPSA gives an advanced improvement in CO₂ capture applications due to main two reasons: 1st one is because of utilizing Mg-MOF-74 as adsorbent which adsorbs/desorbs plenty amounts of CO₂, and the 2nd reason is the optimization of the regeneration times.

Table 5.1 Comparison of CO₂ separation performances amongst different processes.

Adsorbent	Process	CO ₂ (vol. %)	%Purity	% Recovery	Productivity (kg-CO ₂ hr ⁻¹ kg-Adsorbent ⁻¹)	Energy consumption (kJ kg-CO ₂ ⁻¹)	Study	Ref
13XApG	VPSA	15.5-16.5	95.6	73-82.3	0.0387	1790-2140	Exp.	[155]
AC	VPSA	15	95.3	74.4	0.035	723.6	Sim.	[231]
13X	PSA	10.5	99	80	-	2300-2800	Exp.	[232]
5A	TSA	10	>94	75-85	0.052	6120-6460	Exp.	[233]
Mg-MOF-74	TSA	15	97.36	93.7	0.279	1921.3	Sim.	This work
Mg-MOF-74	VPSA	15	98.1	97.3	0.67	231.2	Sim.	This work

5.4 Carbon Dioxide Adsorptive Storage

The produced CO₂ from separation processes should be stored to be utilized later for different applications (such as enhancing oil production by CO₂ sequestration process). The best way to store more quantities of CO₂ in a confined container is adsorbing it into a high CO₂ capacity adsorbent like MOF-5 and MOF-177. In this context, a numerical modeling has been developed for CO₂ adsorptive storage processes. Firstly, the 2D and 3D CFD models were compared to the experimental work [212] that carried out for storing hydrogen into activated carbon at almost 100 bar. The adsorbed bed parameters and adsorbent/adsorbate characterization are described in section 3.2.10 (Table 3.15 - Table 3.17). The measured parameters as the average operating pressure (Figure 5.52) and the temperature (Figure 5.53) at the bed center point ($z=0.27875$ m, $x=0$ m, $y=0$ m) have compared well with those of the present 2D and 3D simulations for the all stages: charging, dormancy, discharging, and dormancy. This confirms that the UDF-Fluent modeling could efficiently predict the adsorption storage behaviors.

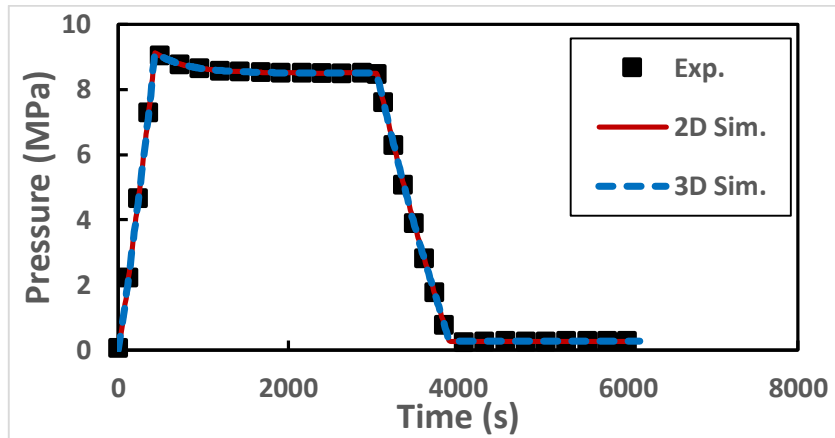


Figure 5.52 A comparison of storage pressure between experimental work [212] and present 2D and 3D simulation for H₂ adsorptive storage.

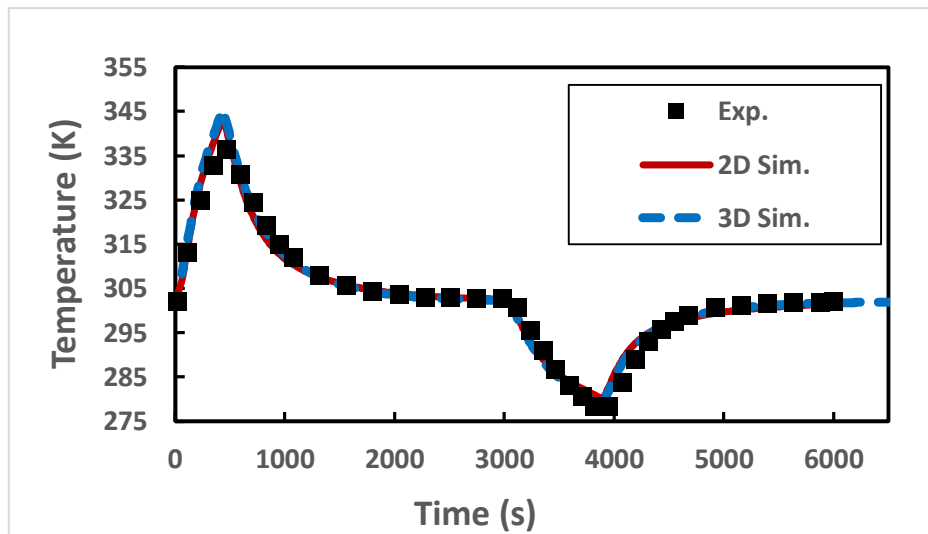


Figure 5.53 A comparison of temperature history of the bed (at $z=0.27875$ m, $x=0$ m, $y=0$ m) between experimental work [212] and present 2D and 3D simulation for H₂ adsorptive storage.

Figure 5.54 displays the temperature contours of the 2D and 3D simulation during charging and cooling stages at selective times (110, 290, 500, 1010, 2000, and 2990s). The temperature values have gone up as the pressure values escalated along with the increase of H₂ uptake. The maximum temperature (about 340 K) have been addressed at the end of the charging time (about 500 s) and then the storage tank cooled down to about 300 K by the surrounding ambient during 2500 seconds. The temperature difference between 2D and 3D modeling was not significant. That difference has happened due to respecting the

thermal diffusion in the all three dimensions for 3D case. Hydrogen uptake contours are presented in Figure 5.55. It is obvious that the adsorbed H_2 amounts have grown gradually from the start of CO_2 charging to the end of the same process. Then, during the cooling process, the H_2 amounts kept almost constant (about 8 mmol/g) due to no H_2 entered or left the tank. A little increase in H_2 uptake values occurred when the bed cooled down was because of the H_2 in the tank void was being adsorbed again.

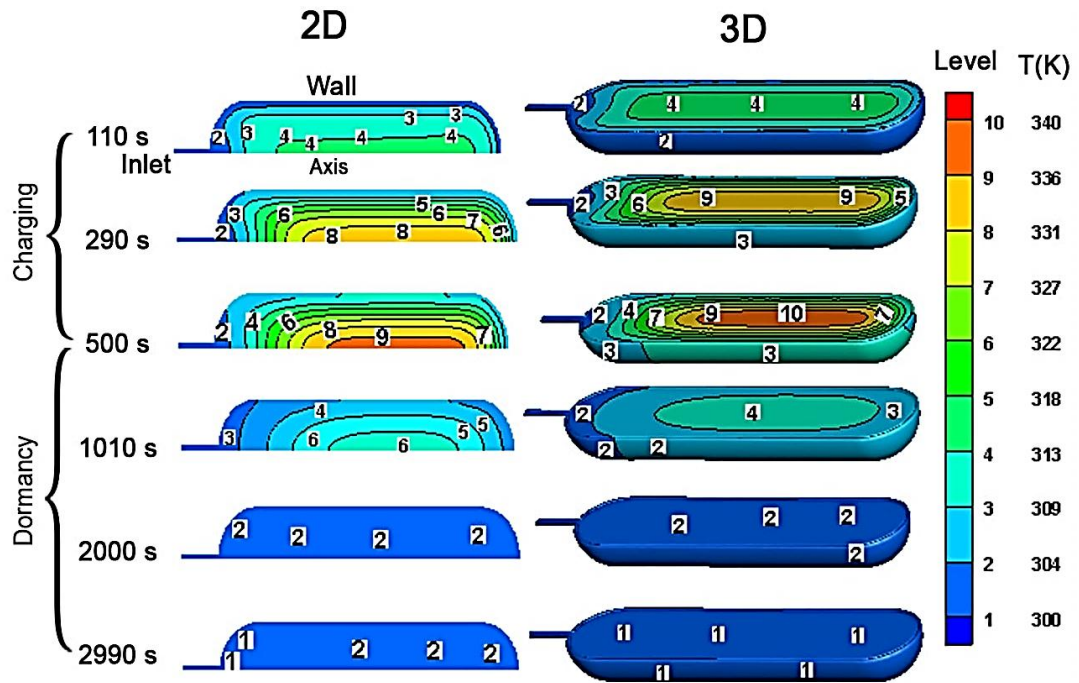


Figure 5.54 2D and 3D temperature contours of H_2 adsorptive storage tank for AC.

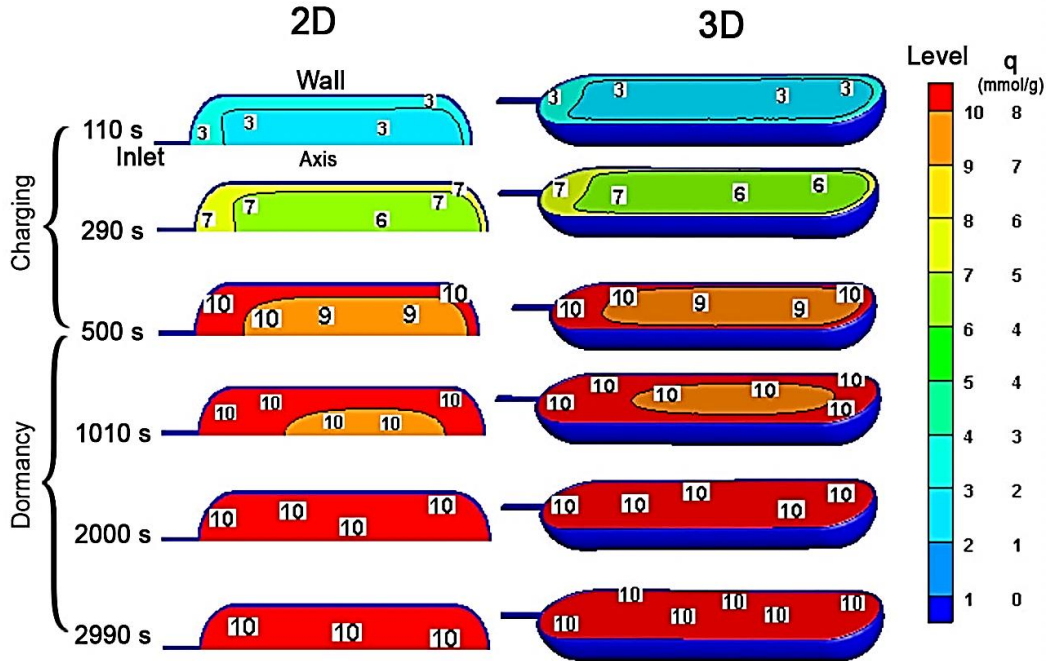


Figure 5.55 2D and 3D H₂ uptake of the AC adsorptive storage tank.

5.4.1 CO₂ Adsorptive Storage Using MOF-5

Adsorbent MOF-5 exhibits a substantial CO₂ capacity at high storage pressures, so that this section will investigate the CO₂ adsorptive storage using this materials (MOF-5) at different pressures. The bed (2D), MOF-5, and CO₂ adsorption and thermal characterizations are described in section 3.2.10 (Table 3.18 and Figure 3.10). The charging process has taken place at 500 seconds followed by cooling process for about 2500 seconds for all investigated adsorptive pressures (5, 10, 20, 30, 40, and 50 bar) as shown in Figure 3.10.

Figure 5.56 shows temperature profiles at the middle of the tank for all studied pressure values. The maximum climb temperature has been associated with the highest storage pressure due to the increase of CO₂ adsorbed amounts within MOF-5 which in turn leads to high heat generation source from the exothermic reaction. Oppositely, the temperature

values in the middle of the tank have cooled down more for higher pressures (as case of 50 bar) in a comparison to those of lower pressure (as cases of 20 bar). This effect is due to the central region of the tank reaches adsorption saturation and hence stopping the adsorption for the high pressure cases, while a little amounts of CO₂ were still being adsorbed to the adsorbent from the tank void regarding to the low pressure cases leading to slow down the bed cooling. Figure 5.57 explains the CO₂ uptake for all aimed storage pressures. The CO₂ adsorbed amounts have increased sharply for 5, 10 and 20 bar and then the CO₂ uptake values gone up slowly for 30, 40, 50 bar due to the CO₂ adsorption saturation phenomena of MOF-5 that characterized by adsorption isotherms [213]. The adsorption capacity of CO₂ for MOF-5 has grown slightly after 20 bar [213]. Figure 5.58 exhibits the percentage of adsorbed CO₂ amounts per kilogram of the adsorbent (MOF-5). It is shown that the case 5 bar has only enabled the adsorbent to adsorb about 0.13 kg/kg while that increased sharply to about 0.93 kg/kg for 30 bar case. The CO₂ uptake has slowly reached 0.99 kg/kg at 50 bar. Moreover, the power consumption due to adsorptive storage has standing up from 119 kJ/tonne-CO₂ for 5 bar to about 231 kJ/tonne-CO₂. Followed by a little increase in the regeneration energy from 231 kJ/tonne-CO₂ to about 255 kJ/tonne-CO₂ for 50 bar. All these figures recommend that the adsorptive pressure 30 bar is sufficient for CO₂ adsorptive storage in MOF-5 with a good thermal and storage performance.

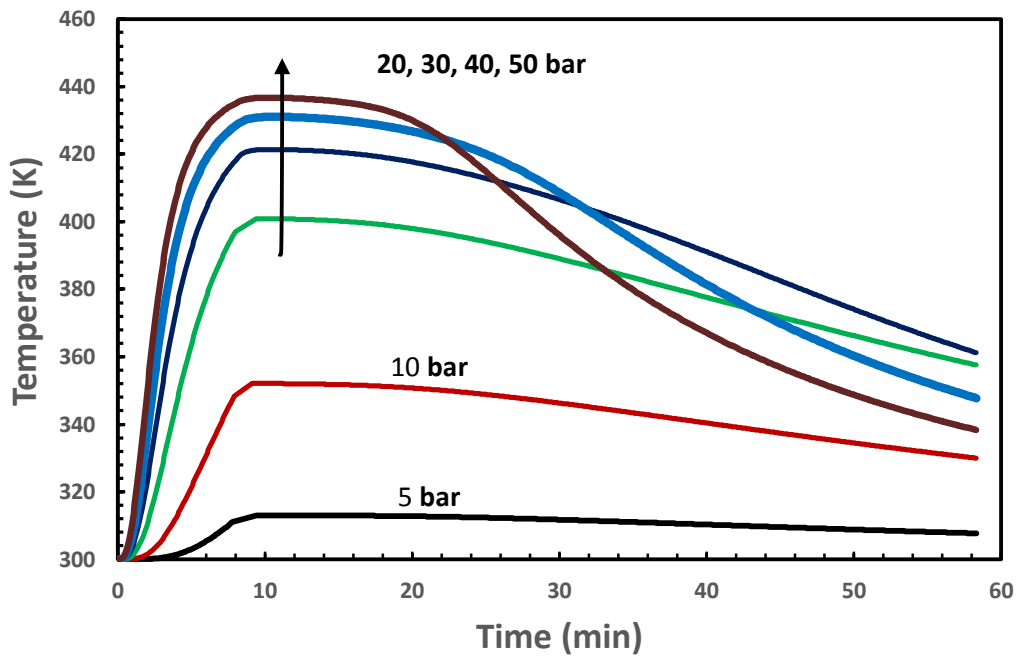


Figure 5.56 Temperature profiles of CO₂ adsorptive tank at the tank center for different storage pressures for MOF-5.

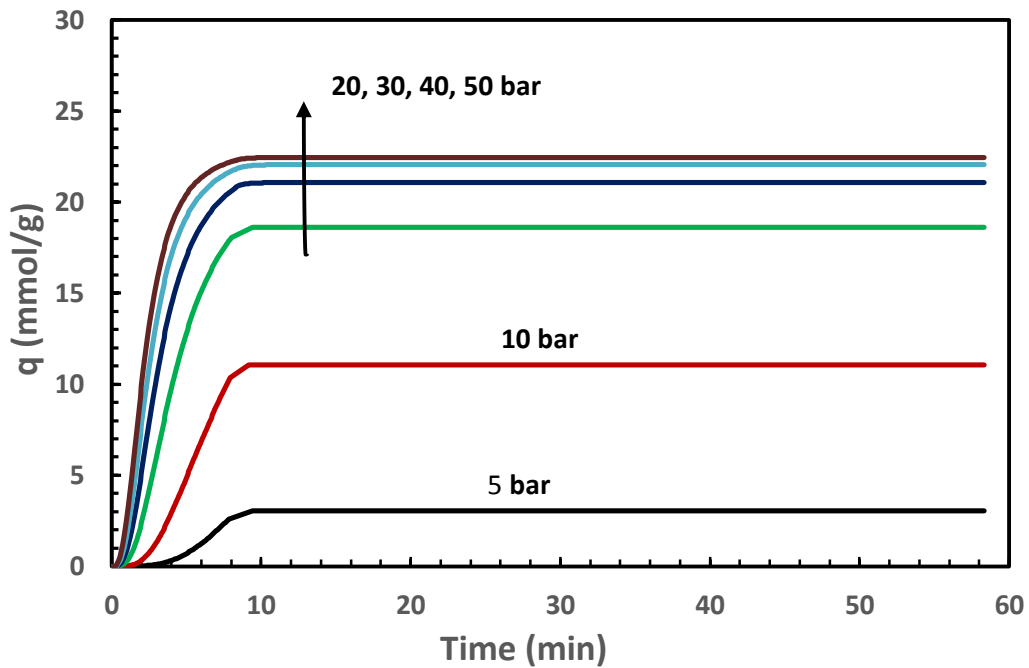


Figure 5.57 CO₂ uptake of different storage pressures for MOF-5.

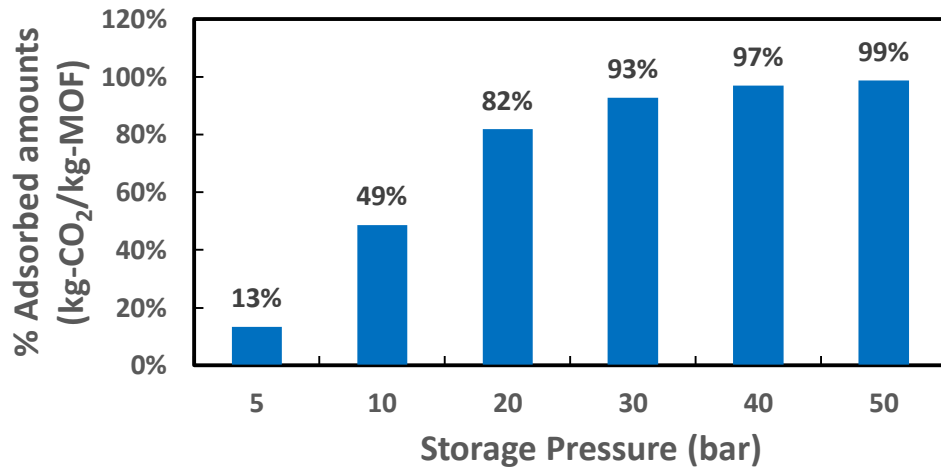


Figure 5.58 Adsorbed CO₂ amounts per MOF-5 amounts ratio for different storage pressures.

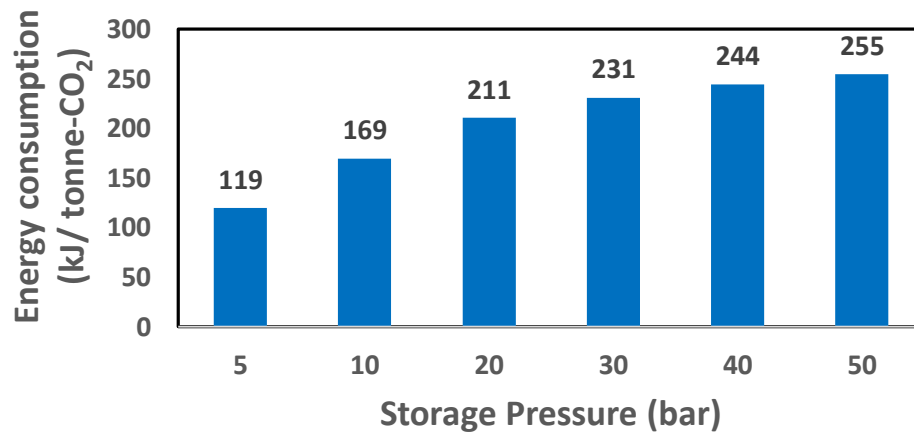


Figure 5.59 CO₂ storage energy consumption for different storage pressures for MOF-5.

5.4.2 CO₂ Adsorptive Storage Using MOF-177

Metal organic framework, MOF-177, exhibits an excellent CO₂ adsorption capacity at high pressures [213], so that it is exploited in this numerical modeling to investigate the optimal storage pressure can accomplish the best CO₂ adsorption capacity and energy performances. The 2D tank, MOF-177, and CO₂ adsorption and thermal properties are mentioned in section 3.2.10 (Figure 3.10 and Table 3.19).

The temperature profiles at the middle of the tank for all studied pressure values are plotted in Figure 5.60. The maximum values of temperature have been addressed with the high storage pressures as a result of the increase of adsorbed CO₂ amounts within MOF-177 which in turn leads to high heat generation source from the exothermic reaction. On contrast, the temperature in the middle of the tank has rapidly cooled down more for higher pressure cases (as case of 50, 40, and 30 bar) than those of lower pressure (as cases of 20 bar). This effect is due to the central region of the tank reaches the adsorption saturation limits hence stopping CO₂ adsorption and starting cooling (for high pressure cases), while a few amounts of CO₂ have still being adsorbed from the tank void to MOF-177 leading to slowing down the cooling process for the low pressure cases. Figure 5.61 explains the CO₂ uptake for all aimed storage pressures. The CO₂ adsorbed amounts increases dramatically for 5, 10 and 20 bar and then those have grown steadily for 30, 40, 50 bar due to the CO₂ adsorption saturation limit of MOF-177 characterized by the adsorption isotherms [213]. Figure 5.62 exhibits the percentage of CO₂ adsorbed amount per kilogram of the adsorbent (MOF-177). It is shown that the case 5 bar has only allowed the adsorbent to adsorb about 0.07 kg/kg while that has escalated harshly to about 1.45 kg/kg for 30 bar. The CO₂ uptake had a slight increase after 30 bar reaching 1.58 kg/kg at 50 bar. In addition, the power consumption due to the adsorptive storage have grown from 121 kJ/tonne-CO₂ for 5 bar to about 233 kJ/tonne_CO₂ for 30 bar, Figure 5.63. This has been followed by a little increase in the energy consumption from about 231 kJ/tonne-CO₂ to about 255 kJ/tonne-CO₂ for 30 and 50 bar, respectively. All these figures recommend that the adsorptive pressure 30 bar is sufficient for CO₂ adsorptive storage with an excellent thermal and storage performances. It is clear, also, that MOF-177 is a superior to CO₂ storage purposes

more than those of MOF-5 especially at high pressure values. Nevertheless, the storages performances at low pressure conditions (< 5 bar) are higher for MOF-5.

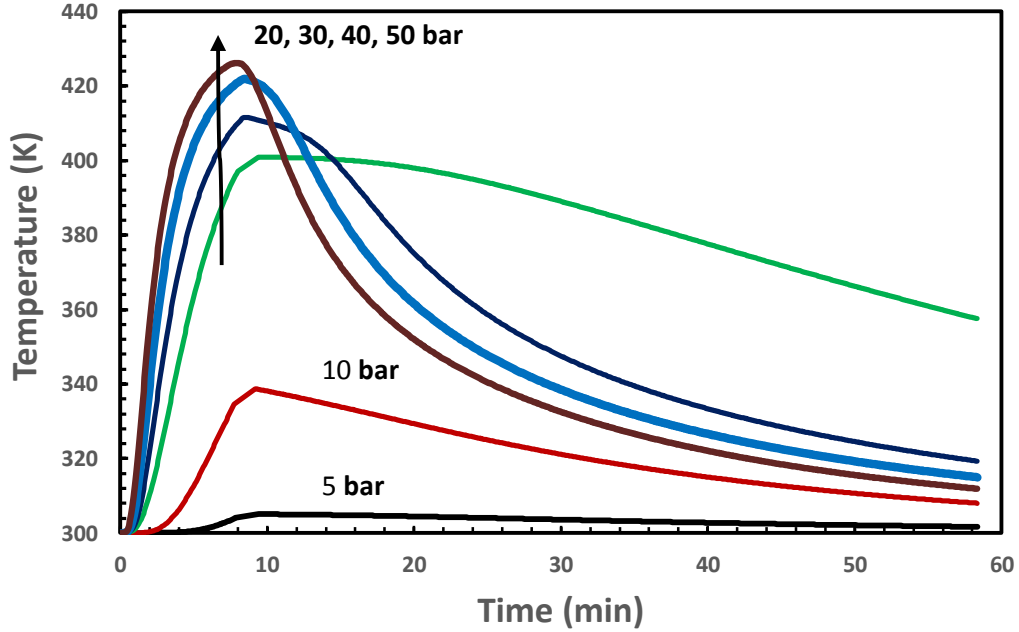


Figure 5.60 Temperature profiles of CO₂ adsorptive tank at the tank center for different storage pressures for MOF-177.

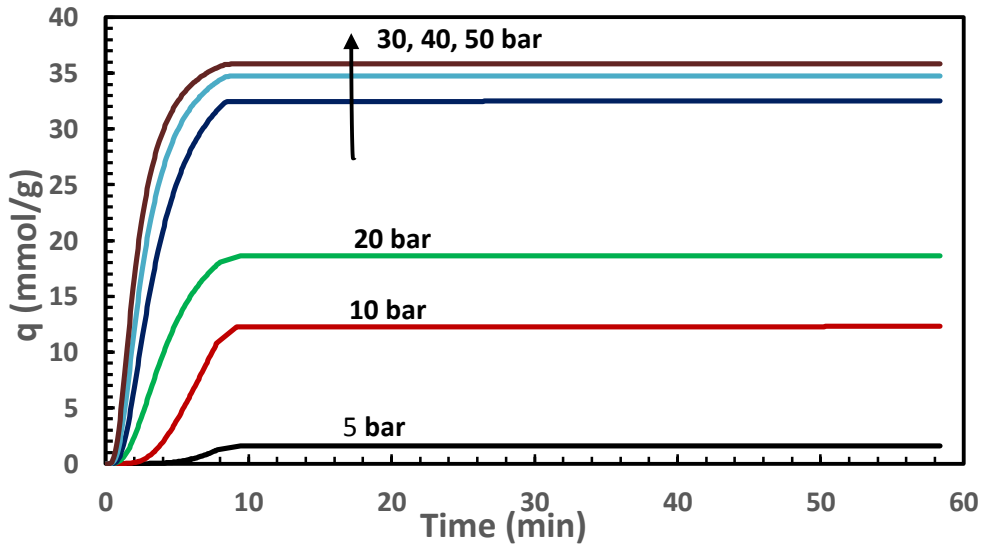


Figure 5.61 CO₂ uptake for different storage pressures for MOF-177.

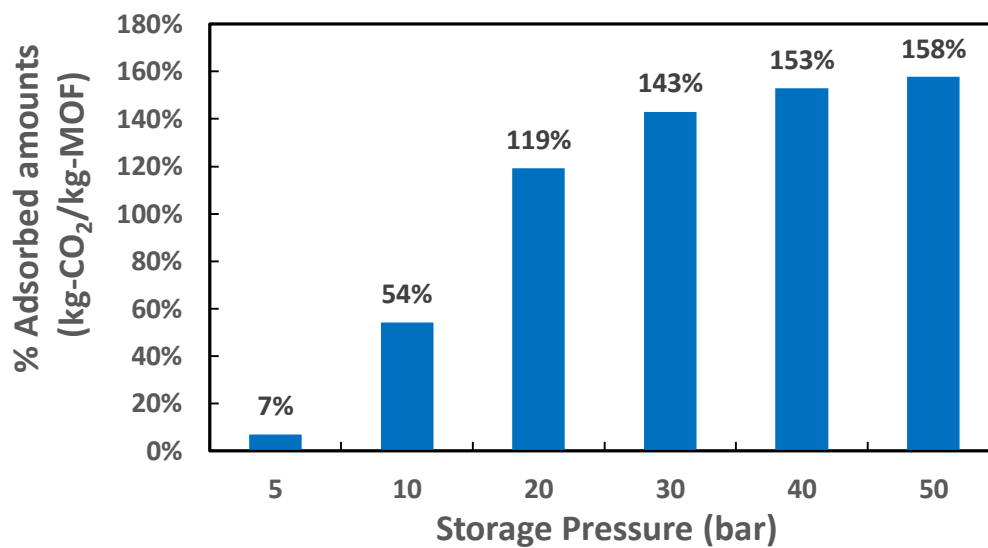


Figure 5.62 CO₂ adsorptive amounts per MOF-177 amounts for different storage pressures.

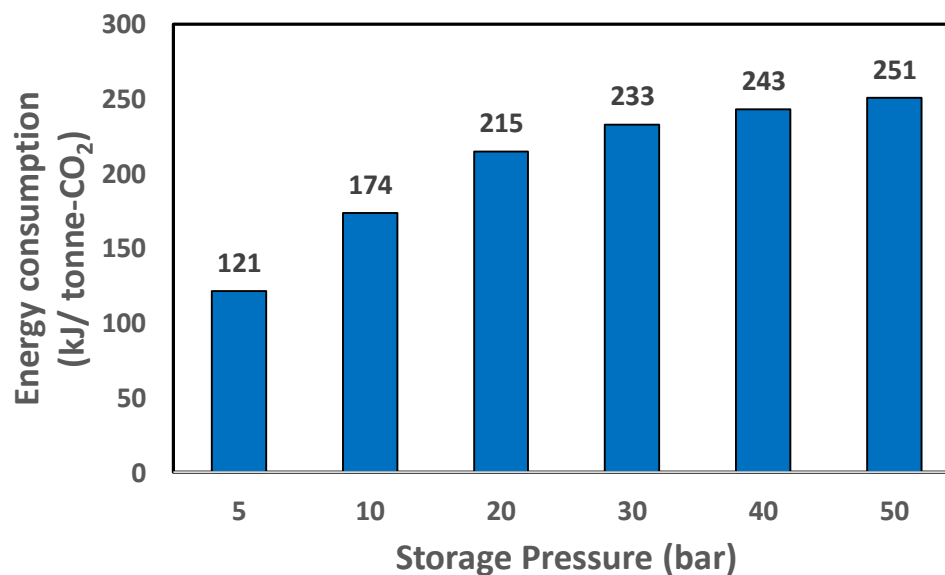


Figure 5.63 CO₂ storage energy consumption for different storage pressures for MOF-177.

CHAPTER 6

CONCLUSIONS AND RECOMMENDATIONS

In this work, the carbon dioxide separation by physical adsorption processes have been investigated and represented experimentally and numerically through using novel materials as Metal Organic Framework (MOFs) as well as well-known materials (as zeolite 13X). Furthermore, the research have explored the enhancements of CO₂ uptake by incorporating carbon nanotubes with the pristine adsorbents.

6.1 Conclusions

The concluded remarks drawn by the experimental work are:

- 1- The effect of adding carbon nanotubes to zeolite 13X on CO₂ adsorption separation and capacity has been investigated. Experimental methods have included XRD characterization, adsorption isotherms and dynamic adsorption breakthrough. Six MWCNT/13X mixture samples are investigated: pure 13X, XC1, XC2, XC3, XC4, and XC5. The equilibrium isotherms show that the adsorption quantities for CO₂ and N₂ of XC3 (0.5 wt% MWCNT/13X) are close to those of pure 13X while the others samples have lower adsorption values. XRD patterns have shown that all the samples have almost the same peaks as pure 13X due to less amounts of MWCNT added to the base adsorbent. The key results are represented by the breakthrough curves in which the optimal adsorption behavior of CO₂ separation and capacity (together) resulted from adding 0.5% by weight of MWCNT to 13X. The

improvements are approximately 21.4% of the adsorption capacity and nearly 25.3% of the separation breakpoint compared to the base case (pure 13X).

- 2- Mg-MOF-74 was synthesized and incorporated with MWCNTs. In total, seven compounds of Mg-MOF-74 materials containing 0, 0.1, 0.25, 0.5, 0.75, 1 and 1.5 wt% MWCNTs have been characterized for the degree of crystallinity, intrinsic porosity, CO₂ adsorption capacity and separation, and dynamic adsorption breakthrough tests. The powder X-ray diffraction patterns as well as the porosity-related parameters for each of the composites do not include any substantial variation in peak intensities and peak locations, BET surface area, and pore volume and size. The crystal lattice and chemical structure are unaffected by the incorporation of MWCNTs using the physical mixing method.

Equilibrium adsorption isotherms of CO₂ measured at 273, 298, and 313 K, and N₂ adsorption isotherms measured at 298 K confirm that the highest adsorption capacities for each of these two gases are exhibited by Mg-MOF-74. Overall, the MWCNT/Mg-MOF-74 composites have much larger adsorption uptake values than those of others.

The key performance evaluation of the MWCNT/Mg-MOF-74 composites have been achieved through the measurement of actual time-variant CO₂ breakthrough curves, which have revealed a good improvement in CO₂ adsorption capacity as well as adsorption breakpoint due to the incorporation of MWCNTs in the Mg-MOF-74 frameworks. The most optimum combination of these characteristics has been observed for an incorporation of 1.5 wt % MWCNTs in Mg-MOF-74, MFC6,

which has resulted in improvements of about 7.4% and 81% over pristine Mg-MOF-74 for CO₂ adsorption capacity and breakpoint, respectively.

- 3- MIL-100(Fe) was also synthesized and incorporated with MWCNTs. Four compounds of MIL-100(Fe) involving 0, 0.1, 0.25 and 0.5 wt% MWCNT have been characterized for intrinsic porosity, CO₂ adsorption capacity and separation, and dynamic adsorption breakthrough tests. BET surface area, and pore volume and size indicate that MIL-100(Fe) structure has not substantially been changed due to incorporating MWCNT.

Equilibrium adsorption isotherms of CO₂ measured at 273, 298, and 313 K, and N₂ adsorption isotherms measured at 298 K confirm that the highest adsorption capacities for each of these two gases are exhibited by 0.25 wt% MWCNT/MIL-100(Fe) (MMC2). A good performance of MWCNT/MIL-100(Fe) composites has been accomplished through the measurement of the dynamic CO₂ breakthrough curves, which have shown a good improvement in CO₂ adsorption capacity as well as adsorption breakpoint due to the incorporation of MWCNTs in MIL-100(Fe) frameworks. The incorporation of 0.1 wt% MWCNTs in MIL-100(Fe), MMC1, improves the adsorption capacity and adsorption breakpoint over pristine MIL-100(Fe) by about 12.0% and 9.2%, respectively.

- 4- A novel MWCNT/MIL-101(Cr) composite has been synthesized using a molecular level approach which involves *in-situ* incorporation of MWCNTs within the MIL-101(Cr) framework. The as-synthesized and activated MOF materials containing 0, 2, 4, 6, and 8 wt% CNTs have been characterized for degree of crystallinity, microstructure, thermal stability, intrinsic porosity, CO₂ adsorption capacity and

separation, and dynamic adsorption breakthrough characteristics. Preliminary characterization conducted on the sample materials indicates that the intrinsic morphology of the MIL-101(Cr) framework is preserved upon the incorporation of MWCNTs, and that the MWCNTs are properly implanted into the MOF crystals in accordance with the protocol proposed for the synthesis of MWCNT/MIL-101(Cr) composites. The powder X-ray diffraction patterns for each of the four composites do not include any extraneous peaks, noticeable peak shifts, or chemical functionalities indicating that the characteristic MIL-101(Cr) crystal lattice and chemical structure are unaffected by the incorporation of MWCNTs using the proposed method of synthesis. The porosity characterization data obtained from the nitrogen physisorption isotherms measured at 77 K for the synthesized and activated MOF materials reveal the highest BET specific surface area evaluated for pristine MIL-101(Cr), with the incorporation of MWCNTs resulting in surface area reduction of about 15.6%, 44.6%, 11.3% and 34.4% measured for 2, 4, 6, and 8 wt% CNT/MIL-101(Cr) composites, respectively. Equilibrium adsorption isotherms of CO₂ measured at 273, 298, and 313 K, and N₂ adsorption isotherms measured at 298 K confirm that the highest adsorption capacities for each of these two gases are exhibited by the 2 wt% CNT/MIL-101(Cr) composite, followed by the pristine MIL-101(Cr).

The performance evaluation of the synthesized CNT/MIL-101(Cr) composites has been achieved through the breakthrough curves, which have brought to light a significant improvement in CO₂ adsorption capacity as well as adsorption breakpoint due to the incorporation of MWCNTs in the MIL-101(Cr) framework.

The most optimum combination of these characteristics has been observed for an incorporation of 2 wt % MWCNTs in MIL-101(Cr) which has resulted in measured improvements of about 37.7% and 32.1% over pristine MIL-101(Cr) for CO₂ adsorption capacity and breakpoint, respectively.

- 5- The regeneration processes including temperature swing adsorption (TSA, $T > 120^{\circ}\text{C}$ for MOFs, and $> 150^{\circ}\text{C}$ for 13X), vacuum swing adsorption (VSA, $P < 2\text{ Pa}$) and temperature-vacuum swing adsorption (TVSA) have shown a successful repetition for CO₂ adsorption/desorption cycles. TVSA could repeat the adsorption/desorption cycles with attaining the all CO₂ uptake. Moreover, TSA could repeat the majority of CO₂ adsorption capacity during CO₂ cycling while VSA trims down the CO₂ capacity by about 13% for 13X, 23% for XC3 (0.5 wt% CNT/13X), 24.0% for Mg-MOF-74, and 20.5% for MFC4 (0.75 wt% CNT/Mg-MOF-74).

The concluded remarks drawn by the numerical modeling work are:

- 1- The results of developed models by UDF (written in C language) hooked to Ansys-Fluent program have accurately been validated by CO₂ separation and storage experimental works including dry and humid CO₂/N₂ breakthrough curves, pressure swing adsorption (PSA), and CO₂ adsorptive storage.
- 2- Two and three dimensional simulation models show similar thermal and adsorption performances for CO₂ adsorption breakthrough separation, VPSA, TSA, and adsorptive storage.
- 3- Water vapor could significantly reduce CO₂ adsorption capacity at high H₂O molar fractions ($> 5\%$) while the CO₂ uptake unaffected for low water vapor contents in

the CO₂/N₂ mixtures. For instance, the CO₂ uptake reduction for separating CO₂ from humid (86% RH, about 3% molar fraction) CO₂/N₂ mixture was low at ambient conditions (300 K, and 101.3 kPa) for AC, 13X, and Mg-MOF-74. However, the CO₂ adsorption capacity reduction have increased substantially at high temperatures and high relative humidity values; the reduction was almost 9% at 323 K and 99.2% RH (12% H₂O (vol. %)) for using Mg-MOF-74 as adsorbent. That happens when CO₂ reached adsorption saturation point. In addition, the CO₂ uptake reduction could be grown up to 47.0% when H₂O has been adsorbed up to its adsorption saturation point for 373 K and 9.1% RH using Mg-MOF-74.

- 4- The optimal performance of vacuum pressure swing adsorption could be addressed by 5 steps: pressurization (20 s), feed (250 s), rinse (40 s), blowdown (100 s), and purge (40 s). The accomplished CO₂ purity, recovery and productivity were about 98.3%, 95.7%, and 0.73 kg-CO₂/hr kg-MOF, respectively. In addition, the energy consumption was about 63.9 kWh/tonne-CO₂ showing a substantial improvement in comparison to those reported in literature.
- 5- The optimal performance for temperature swing adsorption have been achieved by 4 steps including feed (250 s), rinse (40 s), heating at 393 K (200 s), cooling by free convection (400 s). Carbon dioxide purity, recovery, and productivity have been reported to be about 96.2%, 93.7%, and 0.28 kg-CO₂/hr. kg-MOF, respectively. These values were less than those of VPSA. Moreover the energy consumed by the TSA process was 663.8 kWh/tonne-CO₂.
- 6- Carbon dioxide adsorption capacity has increased at high storage pressures.

- 7- Adsorbent MOF-5 has exhibited a good performance of CO₂ adsorptive capacity and energy consumption at high pressures. For the optimal pressure (about 30 bar), the CO₂ uptake and energy consumption were about 0.93 kg-CO₂/kg-MOF and about 231 kJ/tonne-CO₂, respectively.
- 8- Adsorbent MOF-177 has revealed a high CO₂ adsorption capacity about 1.43 kg-CO₂/kg-MOF with a reasonable energy consumption by about 233 kJ/tonne-CO₂ at 30 bar.
- 9- MOF-5 is the best choice for CO₂ storage at low pressures less than 5 bar, while MOF-177 is the perfect adsorbent to store CO₂ at high pressures (> 10 bar).

6.2 Recommendations

For further investigation in the field of CO₂ adsorption separation and storage, it is recommended to:

- 1- explore the effect of water vapor on CNT/adsorbent composites at different temperatures,
- 2- incorporate other secondary materials like graphene with different adsorbents to improve thermal and adsorption characteristics,
- 3- study the effect of incorporating secondary materials with functionalized adsorbents (chemical adsorption),
- 4- carry out a thermodynamic analysis (1st and 2nd laws) for breakthrough tests, swing adsorption processes, and CO₂ adsorptive storage, and
- 5- carry out 2D and 3D numerical modeling for CO₂ separation from actual flue gas including all species.

References

1. Lee, S.-Y. and Park, S.-J., *A review on solid adsorbents for carbon dioxide capture*. Journal of Industrial and Engineering Chemistry, 2015. **23**: p. 1-11.
2. Guardian. *antarctic-ship-stranding-delights-climate-change-sceptics*. 2014; Available from: www.theguardian.com.
3. D'Alessandro, D.M. and McDonald, T., *Toward carbon dioxide capture using nanoporous materials*. Pure and Applied Chemistry, 2010. **83**(1).
4. IPCC, *Special Report on Carbon Dioxide Capture and Storage*, O.D. Ed. B. Metz, H. Coninct, M. Loos and L. Meyer, Editor. 2005.
5. GCEP, *Global Climate & Energy Project An Assessment of Carbon Capture Technology and Research Opportunities*. 2005, Stanford University.
6. Herzog, H., Meldon, J., and Hatton, A., *Advanced post-combustion CO2 capture*. Clean Air Task Force, 2009: p. 1-39.
7. Li, H., Ditaranto, M., and Yan, J., *Carbon capture with low energy penalty: Supplementary fired natural gas combined cycles*. Applied Energy, 2012. **97**: p. 164-169.
8. global-ccs-institute. 2015; Available from: (<http://www.globalccsinstitute.com>).
9. Ben-Mansour, R., Habib, M.A., Bamidele, O.E., Basha, M., Qasem, N.A.A., Peedikakkal, A., Laoui, T., and Ali, M., *Carbon capture by physical adsorption: Materials, experimental investigations and numerical modeling and simulations – A review*. Applied Energy, 2016. **161**: p. 225-255.
10. Songolzadeh, M., Ravanchi, M.T., and Soleimani, M., *Carbon dioxide capture and storage: a general review on adsorbents*. World Academy of Science, Engineering and Technology, 2012. **70**: p. 225-232.
11. Li, J.-R., Ma, Y., McCarthy, M.C., Sculley, J., Yu, J., Jeong, H.-K., Balbuena, P.B., and Zhou, H.-C., *Carbon dioxide capture-related gas adsorption and separation in metal-organic frameworks*. Coordination Chemistry Reviews, 2011. **255**(15-16): p. 1791-1823.
12. Dong, R., Lu, H., Yu, Y., and Zhang, Z., *A feasible process for simultaneous removal of CO2, SO2 and NOx in the cement industry by NH3 scrubbing*. Applied Energy, 2012. **97**: p. 185-191.
13. Lv, Y., Yu, X., Jia, J., Tu, S.-T., Yan, J., and Dahlquist, E., *Fabrication and characterization of superhydrophobic polypropylene hollow fiber membranes for carbon dioxide absorption*. Applied Energy, 2012. **90**(1): p. 167-174.
14. Lv, Y., Yu, X., Tu, S.-T., Yan, J., and Dahlquist, E., *Experimental studies on simultaneous removal of CO2 and SO2 in a polypropylene hollow fiber membrane contactor*. Applied Energy, 2012. **97**: p. 283-288.
15. Song, C.F., Kitamura, Y., and Li, S.H., *Evaluation of Stirling cooler system for cryogenic CO2 capture*. Applied Energy, 2012. **98**: p. 491-501.
16. van Benthum, R.J., van Kemenade, H.P., Brouwers, J.J.H., and Golombok, M., *Condensed Rotational Separation of CO2*. Applied Energy, 2012. **93**: p. 457-465.

17. Zhang, M. and Guo, Y., *Rate based modeling of absorption and regeneration for CO₂ capture by aqueous ammonia solution*. Applied Energy, 2013. **111**: p. 142-152.
18. Yan, S., Fang, M., Wang, Z., and Luo, Z., *Regeneration performance of CO₂-rich solvents by using membrane vacuum regeneration technology: Relationships between absorbent structure and regeneration efficiency*. Applied Energy, 2012. **98**: p. 357-367.
19. Nakamura, T., Senior, C., Olaizola, M., Bridges, T., Flores, S., Sombardier, L., and Masutani, S., *Recovery and sequestration of CO₂ from stationary combustion systems by photosynthesis of microalgae (Final Report, Contract No. DEFC2600NT40934)*. US Department of Energy, 2005: p. 220.
20. Li, J.-R., Sculley, J., and Zhou, H.-C., *Metal–Organic Frameworks for Separations*. Chemical Reviews, 2012. **112**(2): p. 869-932.
21. Ho, M.T., Allinson, G.W., and Wiley, D.E., *Reducing the Cost of CO₂ Capture from Flue Gases Using Pressure Swing Adsorption*. Industrial & Engineering Chemistry Research, 2008. **47**(14): p. 4883-4890.
22. Chue, K.T., Kim, J.N., Yoo, Y.J., Cho, S.H., and Yang, R.T., *Comparison of Activated Carbon and Zeolite 13X for CO₂ Recovery from Flue Gas by Pressure Swing Adsorption*. Industrial & Engineering Chemistry Research, 1995. **34**(2): p. 591-598.
23. Krishna, R. and van Baten, J.M., *A comparison of the CO₂ capture characteristics of zeolites and metal–organic frameworks*. Separation and Purification Technology, 2012. **87**: p. 120-126.
24. Krishna, R., *Adsorptive separation of CO₂/CH₄/CO gas mixtures at high pressures*. Microporous and Mesoporous Materials, 2012. **156**: p. 217-223.
25. Clause, M., Bonjour, J., and Meunier, F., *Adsorption of gas mixtures in TSA adsorbents under various heat removal conditions*. Chemical Engineering Science, 2004. **59**(17): p. 3657-3670.
26. Mason, J.A., Sumida, K., Herm, Z.R., Krishna, R., and Long, J.R., *Evaluating metal–organic frameworks for post-combustion carbon dioxide capture via temperature swing adsorption*. Energy & Environmental Science, 2011. **4**(8): p. 3030.
27. Amrollahi, Z., Ertesvåg, I.S., and Bolland, O., *Thermodynamic analysis on post-combustion CO₂ capture of natural-gas-fired power plant*. International Journal of Greenhouse Gas Control, 2011. **5**(3): p. 422-426.
28. Ball, R., *Using the second law first: Improving the thermodynamic efficiency of carbon dioxide separation from gas streams in an Endex calcium looping system*. Applied Thermal Engineering, 2015. **74**: p. 194-201.
29. Lara, Y., Martínez, A., Lisbona, P., Bolea, I., González, A., and Romeo, L.M., *Using the second law of thermodynamic to improve CO₂ capture systems*. Energy Procedia, 2011. **4**: p. 1043-1050.
30. Calbry-Muzyka, S. and Edwards, C.F., *Thermodynamic Benchmarking of CO₂ Capture Systems: Exergy Analysis Methodology for Adsorption Processes*. Energy Procedia, 2014. **63**: p. 1-17.

31. Raynal, L., Bouillon, P.-A., Gomez, A., and Broutin, P., *From MEA to demixing solvents and future steps, a roadmap for lowering the cost of post-combustion carbon capture*. Chemical Engineering Journal, 2011. **171**(3): p. 742-752.
32. McGlashan, N.R. and Marquis, A.J., *Availability analysis of post-combustion carbon capture systems: Minimum work input*. Proceedings of the Institution of Mechanical Engineers, Part C: Journal of Mechanical Engineering Science, 2007. **221**(9): p. 1057-1065.
33. Mansouri, M.T. and Mousavian, S., *Exergy-based analysis of conventional coal-fired power plant retrofitted with oxy-fuel and post-combustion CO₂ capture systems*. Proceedings of the Institution of Mechanical Engineers, Part A: Journal of Power and Energy, 2012. **226**(8): p. 989-1002.
34. Iribarren, D., Petrakopoulou, F., and Dufour, J., *Environmental and thermodynamic evaluation of CO₂ capture, transport and storage with and without enhanced resource recovery*. Energy, 2013. **50**: p. 477-485.
35. Sathre, R. and Masanet, E., *Prospective life-cycle modeling of a carbon capture and storage system using metal–organic frameworks for CO₂ capture*. RSC Advances, 2013. **3**(15): p. 4964.
36. Li, J.-R., Kuppler, R.J., and Zhou, H.-C., *Selective gas adsorption and separation in metal–organic frameworks*. Chemical Society Reviews, 2009. **38**(5): p. 1477.
37. Akhtar, F., Andersson, L., Keshavarzi, N., and Bergström, L., *Colloidal processing and CO₂ capture performance of sacrificially templated zeolite monoliths*. Applied Energy, 2012. **97**: p. 289-296.
38. Choi, S., Drese, J.H., and Jones, C.W., *Adsorbent Materials for Carbon Dioxide Capture from Large Anthropogenic Point Sources*. ChemSusChem, 2009. **2**(9): p. 796-854.
39. Zhao, D., Yuan, D., Krishna, R., van Baten, J.M., and Zhou, H.-C., *Thermosensitive gating effect and selective gas adsorption in a porous coordination nanocage*. Chemical Communications, 2010. **46**(39): p. 7352.
40. Zhao, D., Yuan, D., Yakovenko, A., and Zhou, H.-C., *A NbO-type metal–organic framework derived from a polyyne-coupled di-isophthalate linker formed in situ*. Chemical Communications, 2010. **46**(23): p. 4196.
41. Sun, R., Li, Y., Liu, H., Wu, S., and Lu, C., *CO₂ capture performance of calcium-based sorbent doped with manganese salts during calcium looping cycle*. Applied Energy, 2012. **89**(1): p. 368-373.
42. Wang, J., Manovic, V., Wu, Y., and Anthony, E.J., *A study on the activity of CaO-based sorbents for capturing CO₂ in clean energy processes*. Applied Energy, 2010. **87**(4): p. 1453-1458.
43. Feng, B., An, H., and Tan, E., *Screening of CO₂ Adsorbing Materials for Zero Emission Power Generation Systems †*. Energy & Fuels, 2007. **21**(2): p. 426-434.
44. Yamaguchi, T., Niitsuma, T., Nair, B.N., and Nakagawa, K., *Lithium silicate based membranes for high temperature CO₂ separation*. Journal of Membrane Science, 2007. **294**(1-2): p. 16-21.
45. Ochoa-Fernández, E., Rusten, H.K., Jakobsen, H.A., Rønning, M., Holmen, A., and Chen, D., *Sorption enhanced hydrogen production by steam methane reforming using Li₂ZrO₃ as sorbent: Sorption kinetics and reactor simulation*. Catalysis Today, 2005. **106**(1-4): p. 41-46.

46. Ma, S., Simmons, J.M., Yuan, D., Li, J.-R., Weng, W., Liu, D.-J., and Zhou, H.-C., *A nanotubular metal–organic framework with permanent porosity: structure analysis and gas sorption studies*. *Chemical Communications*, 2009(27): p. 4049.
47. Webb, P.A., *Introduction to chemical adsorption analytical techniques and their applications to catalysis*. Micromeritics Instrument Corp. Technical Publications, 2003.
48. Yu, C.-H., *A Review of CO₂ Capture by Absorption and Adsorption*. *Aerosol and Air Quality Research*, 2012.
49. Siriwardane, R.V., Shen, M.-S., Fisher, E.P., and Poston, J.A., *Adsorption of CO₂ on Molecular Sieves and Activated Carbon*. *Energy & Fuels*, 2001. **15**(2): p. 279-284.
50. Harlick, P.J.E. and Sayari, A., *Applications of Pore-Expanded Mesoporous Silicas. 3. Triamine Silane Grafting for Enhanced CO₂ Adsorption*. *Industrial & Engineering Chemistry Research*, 2006. **45**(9): p. 3248-3255.
51. Maurin, G., Llewellyn, P.L., and Bell, R.G., *Adsorption Mechanism of Carbon Dioxide in Faujasites: Grand Canonical Monte Carlo Simulations and Microcalorimetry Measurements*. *The Journal of Physical Chemistry B*, 2005. **109**(33): p. 16084-16091.
52. Hicks, J.C., Drese, J.H., Fauth, D.J., Gray, M.L., Qi, G., and Jones, C.W., *Designing Adsorbents for CO₂ Capture from Flue Gas-Hyperbranched Aminosilicas Capable of Capturing CO₂ Reversibly*. *J. Am. Chem. Soc.*, 2008. **130**(10): p. 2902-2903.
53. Leal, O., Bolívar, C., Ovalles, C., García, J.J., and Espidel, Y., *Reversible adsorption of carbon dioxide on amine surface-bonded silica gel*. *Inorganica Chimica Acta*, 1995. **240**(1-2): p. 183-189.
54. Sirwardane, R.V., *Solid sorbents for removal of carbon dioxide from gas streams at low temperatures*. 2005, National Energy Technology Laboratory (NETL), Pittsburgh, PA, and Morgantown, WV.
55. Xu, X., Song, C., Miller, B.G., and Scaroni, A.W., *Adsorption separation of carbon dioxide from flue gas of natural gas-fired boiler by a novel nanoporous “molecular basket” adsorbent*. *Fuel Processing Technology*, 2005. **86**(14-15): p. 1457-1472.
56. Lee, S., Filburn, T.P., Gray, M., Park, J.-W., and Song, H.-J., *Screening Test of Solid Amine Sorbents for CO₂ Capture*. *Industrial & Engineering Chemistry Research*, 2008. **47**(19): p. 7419-7423.
57. Hiyoshi, N., Yogo, K., and Yashima, T., *Adsorption of Carbon Dioxide on Amine Modified SBA-15 in the Presence of Water Vapor*. *Chem. Lett.*, 2004. **33**(5): p. 510-511.
58. Mazumder, S., van Hemert, P., Busch, A., Wolf, K.H.A.A., and Tejera-Cuesta, P., *Flue gas and pure CO₂ sorption properties of coal: A comparative study*. *International Journal of Coal Geology*, 2006. **67**(4): p. 267-279.
59. Plaza, M.G., González, A.S., Pevida, C., Pis, J.J., and Rubiera, F., *Valorisation of spent coffee grounds as CO₂ adsorbents for postcombustion capture applications*. *Applied Energy*, 2012. **99**: p. 272-279.
60. Plaza, M.G., Pevida, C., Arias, B., Feroso, J., Arenillas, A., Rubiera, F., and Pis, J.J., *Application of thermogravimetric analysis to the evaluation of aminated solid sorbents for CO₂ capture*. *J Therm Anal Calorim*, 2008. **92**(2): p. 601-606.

61. Radosz, M., Hu, X., Krutkramelis, K., and Shen, Y., *Flue-Gas Carbon Capture on Carbonaceous Sorbents: Toward a Low-Cost Multifunctional Carbon Filter for "Green" Energy Producers †*. Industrial & Engineering Chemistry Research, 2008. **47**(10): p. 3783-3794.
62. Thallapally, P.K., McGrail, B.P., Atwood, J.L., Gaeta, C., Tedesco, C., and Neri, P., *Carbon Dioxide Capture in a Self-Assembled Organic Nanochannels*. Chemistry of Materials, 2007. **19**(14): p. 3355-3357.
63. Thallapally, P.K., Peter McGrail, B., Dalgarno, S.J., Schaef, H.T., Tian, J., and Atwood, J.L., *Gas-induced transformation and expansion of a non-porous organic solid*. Nature Materials, 2008. **7**(2): p. 146-150.
64. Furukawa, H. and Yaghi, O.M., *Storage of Hydrogen, Methane, and Carbon Dioxide in Highly Porous Covalent Organic Frameworks for Clean Energy Applications*. J. Am. Chem. Soc., 2009. **131**(25): p. 8875-8883.
65. Babarao, R. and Jiang, J., *Molecular Screening of Metal–Organic Frameworks for CO₂ Storage*. Langmuir, 2008. **24**(12): p. 6270-6278.
66. Babarao, R. and Jiang, J., *Unprecedentedly High Selective Adsorption of Gas Mixtures in rho Zeolite-like Metal–Organic Framework: A Molecular Simulation Study*. J. Am. Chem. Soc., 2009. **131**(32): p. 11417-11425.
67. Balsamo, M., Budinova, T., Erto, A., Lancia, A., Petrova, B., Petrov, N., and Tsyntsarski, B., *CO₂ adsorption onto synthetic activated carbon: Kinetic, thermodynamic and regeneration studies*. Separation and Purification Technology, 2013. **116**: p. 214-221.
68. Caglayan, B.S. and Aksoylu, A.E., *CO₂ adsorption on chemically modified activated carbon*. Journal of Hazardous Materials, 2013. **252-253**: p. 19-28.
69. Deng, S., Wei, H., Chen, T., Wang, B., Huang, J., and Yu, G., *Superior CO₂ adsorption on pine nut shell-derived activated carbons and the effective micropores at different temperatures*. Chemical Engineering Journal, 2014. **253**: p. 46-54.
70. Heidari, A., Younesi, H., Rashidi, A., and Ghoreyshi, A.A., *Evaluation of CO₂ adsorption with eucalyptus wood based activated carbon modified by ammonia solution through heat treatment*. Chemical Engineering Journal, 2014. **254**: p. 503-513.
71. Yin, G., Liu, Z., Liu, Q., and Wu, W., *The role of different properties of activated carbon in CO₂ adsorption*. Chemical Engineering Journal, 2013. **230**: p. 133-140.
72. Cinke, M., Li, J., Bauschlicher, C.W., Ricca, A., and Meyyappan, M., *CO₂ adsorption in single-walled carbon nanotubes*. Chemical Physics Letters, 2003. **376**(5-6): p. 761-766.
73. Hsu, S.-C., Lu, C., Su, F., Zeng, W., and Chen, W., *Thermodynamics and regeneration studies of CO₂ adsorption on multiwalled carbon nanotubes*. Chemical Engineering Science, 2010. **65**(4): p. 1354-1361.
74. Lithoxoos, G.P., Labropoulos, A., Peristeras, L.D., Kanellopoulos, N., Samios, J., and Economou, I.G., *Adsorption of N₂, CH₄, CO and CO₂ gases in single walled carbon nanotubes: A combined experimental and Monte Carlo molecular simulation study*. The Journal of Supercritical Fluids, 2010. **55**(2): p. 510-523.
75. Su, F., Lu, C., Cnen, W., Bai, H., and Hwang, J.F., *Capture of CO₂ from flue gas via multiwalled carbon nanotubes*. Science of The Total Environment, 2009. **407**(8): p. 3017-3023.

76. Zhou, X., Yi, H., Tang, X., Deng, H., and Liu, H., *Thermodynamics for the adsorption of SO₂, NO and CO₂ from flue gas on activated carbon fiber*. Chemical Engineering Journal, 2012. **200-202**: p. 399-404.
77. Moon, S.-H. and Shim, J.-W., *A novel process for CO₂/CH₄ gas separation on activated carbon fibers—electric swing adsorption*. Journal of Colloid and Interface Science, 2006. **298**(2): p. 523-528.
78. Shen, C., Grande, C.A., Li, P., Yu, J., and Rodrigues, A.E., *Adsorption equilibria and kinetics of CO₂ and N₂ on activated carbon beads*. Chemical Engineering Journal, 2010. **160**(2): p. 398-407.
79. Yang, H., Gong, M., and Chen, Y., *Preparation of activated carbons and their adsorption properties for greenhouse gases: CH₄ and CO₂*. Journal of Natural Gas Chemistry, 2011. **20**(5): p. 460-464.
80. Zhang, Z., Xu, M., Wang, H., and Li, Z., *Enhancement of CO₂ adsorption on high surface area activated carbon modified by N₂, H₂ and ammonia*. Chemical Engineering Journal, 2010. **160**(2): p. 571-577.
81. Abuilaiwi, F.A., Laoui, T., Al-Harathi, M., and Atieh, M.A., *Modification and functionalization of multiwalled carbon nanotube (MWCNT) via fischer esterification*. Arabian Journal for Science and Engineering, 2010. **35**(1C): p. 37-48.
82. Andersen, A., Divekar, S., Dasgupta, S., Cavka, J.H., Aarti, Nanoti, A., Spjelkavik, A., Goswami, A.N., Garg, M.O., and Blom, R., *On the development of Vacuum Swing adsorption (VSA) technology for post-combustion CO₂ capture*. Energy Procedia, 2013. **37**: p. 33-39.
83. Ebbesen, T.W. and Ajayan, P.M., *Large-scale synthesis of carbon nanotubes*. Nature, 1992. **358**(6383): p. 220-222.
84. Harris, P.J.F., *Carbon Nanotubes and Related Structures*. 1999: Cambridge University Press (CUP).
85. Iijima, S., *Helical microtubules of graphitic carbon*. Nature, 1991. **354**(6348): p. 56-58.
86. Journet, C. and Bernier, P., *Production of carbon nanotubes*. Applied Physics A: Materials Science & Processing, 1998. **67**(1): p. 1-9.
87. Jung, S.H., Kim, M.R., Jeong, S.H., Kim, S.U., Lee, O.J., Lee, K.H., Suh, J.H., and Park, C.K., *High-yield synthesis of multi-walled carbon nanotubes by arc discharge in liquid nitrogen*. Applied Physics A: Materials Science & Processing, 2003. **76**(2): p. 285-286.
88. Srivastava, D., Wei, C., and Cho, K., *Nanomechanics of carbon nanotubes and composites*. Applied Mechanics Reviews, 2003. **56**(2): p. 215.
89. Thess, A., Lee, R., Nikolaev, P., Dai, H., Petit, P., Robert, J., Xu, C., Lee, Y.H., Kim, S.G., Rinzler, A.G., Colbert, D.T., Scuseria, G.E., Tomanek, D., Fischer, J.E., and Smalley, R.E., *Crystalline Ropes of Metallic Carbon Nanotubes*. Science, 1996. **273**(5274): p. 483-487.
90. Al-Hakami, S.M., Khalil, A.B., Laoui, T., and Atieh, M.A., *Fast Disinfection of Escherichia coli Bacteria Using Carbon Nanotubes Interaction with Microwave Radiation*. Bioinorganic Chemistry and Applications, 2013. **2013**: p. 1-9.
91. Atieh, M.A., Bakather, O.Y., Al-Tawbini, B., Bukhari, A.A., Abuilaiwi, F.A., and Fettouhi, M.B., *Effect of Carboxylic Functional Group Functionalized on Carbon*

- Nanotubes Surface on the Removal of Lead from Water*. Bioinorganic Chemistry and Applications, 2010. **2010**: p. 1-9.
92. Atieh, M.A., Bakather, O.Y., Tawabini, B.S., Bukhari, A.A., Khaled, M., Alharthi, M., Fettouhi, M., and Abuilaiwi, F.A., *Removal of Chromium (III) from Water by Using Modified and Nonmodified Carbon Nanotubes*. Journal of Nanomaterials, 2010. **2010**: p. 1-9.
 93. Kabbashi, N.A., Atieh, M.A., Al-Mamun, A., Mirghami, M.E.S., Alam, M.D.Z., and Yahya, N., *Kinetic adsorption of application of carbon nanotubes for Pb(II) removal from aqueous solution*. Journal of Environmental Sciences, 2009. **21**(4): p. 539-544.
 94. Tawabini, B., Al-Khalidi, S., Atieh, M., and Khaled, M., *Removal of mercury from water by multi-walled carbon nanotubes*. Water Science & Technology, 2010. **61**(3): p. 591.
 95. Tawabini, B.S., Al-Khalidi, S.F., Khaled, M.M., and Atieh, M.A., *Removal of arsenic from water by iron oxide nanoparticles impregnated on carbon nanotubes*. Journal of Environmental Science and Health, Part A, 2011. **46**(3): p. 215-223.
 96. Zeino, A., Abulkibash, A., Khaled, M., and Atieh, M., *Bromate Removal from Water Using Doped Iron Nanoparticles on Multiwalled Carbon Nanotubes (CNTS)*. Journal of Nanomaterials, 2014. **2014**: p. 1-9.
 97. Fatemi, S., Vesali-Naseh, M., Cyrus, M., and Hashemi, J., *Improving CO₂/CH₄ adsorptive selectivity of carbon nanotubes by functionalization with nitrogen-containing groups*. Chemical Engineering Research and Design, 2011. **89**(9): p. 1669-1675.
 98. Gui, M.M., Yap, Y.X., Chai, S.-P., and Mohamed, A.R., *Multi-walled carbon nanotubes modified with (3-aminopropyl)triethoxysilane for effective carbon dioxide adsorption*. International Journal of Greenhouse Gas Control, 2013. **14**: p. 65-73.
 99. Liu, Q., Shi, Y., Zheng, S., Ning, L., Ye, Q., Tao, M., and He, Y., *Amine-functionalized low-cost industrial grade multi-walled carbon nanotubes for the capture of carbon dioxide*. Journal of Energy Chemistry, 2014. **23**(1): p. 111-118.
 100. Su, F., Lu, C., Chung, A.-J., and Liao, C.-H., *CO₂ capture with amine-loaded carbon nanotubes via a dual-column temperature/vacuum swing adsorption*. Applied Energy, 2014. **113**: p. 706-712.
 101. Su, F., Lu, C., and Chen, H.-S., *Adsorption, Desorption, and Thermodynamic Studies of CO₂ with High-Amine-Loaded Multiwalled Carbon Nanotubes*. Langmuir, 2011. **27**(13): p. 8090-8098.
 102. Dillon, E.P., Crouse, C.A., and Barron, A.R., *Synthesis, Characterization, and Carbon Dioxide Adsorption of Covalently Attached Polyethyleneimine-Functionalized Single-Wall Carbon Nanotubes*. ACS Nano, 2008. **2**(1): p. 156-164.
 103. Düren, T., *How does the pore morphology influence the adsorption performance of metal-organic frameworks? A molecular simulation study of methane and ethane adsorption in Zn-MOFs*, in *From Zeolites to Porous MOF Materials - The 40th Anniversary of International Zeolite Conference, Proceedings of the 15th International Zeolite Conference*. 2007, Elsevier BV. p. 2042-2047.

104. Furukawa, H., Cordova, K.E., O'Keeffe, M., and Yaghi, O.M., *The Chemistry and Applications of Metal-Organic Frameworks*. Science, 2013. **341**(6149): p. 1230444-1230444.
105. Li, G., Xiao, P., Xu, D., and Webley, P.A., *Dual mode roll-up effect in multicomponent non-isothermal adsorption processes with multilayered bed packing*. Chemical Engineering Science, 2011. **66**(9): p. 1825-1834.
106. Kuppler, R.J., Timmons, D.J., Fang, Q.-R., Li, J.-R., Makal, T.A., Young, M.D., Yuan, D., Zhao, D., Zhuang, W., and Zhou, H.-C., *Potential applications of metal-organic frameworks*. Coordination Chemistry Reviews, 2009. **253**(23-24): p. 3042-3066.
107. Lu, H., *Interfacial Synthesis of Metal-organic Frameworks*. 2012.
108. Carné-Sánchez, A., Imaz, I., Cano-Sarabia, M., and Maspocho, D., *A spray-drying strategy for synthesis of nanoscale metal-organic frameworks and their assembly into hollow superstructures*. Nature Chemistry, 2013. **5**(3): p. 203-211.
109. Campagnol, N., Van Assche, T., Boudewijns, T., Denayer, J., Binnemans, K., De Vos, D., and Fransaer, J., *High pressure, high temperature electrochemical synthesis of metal-organic frameworks: films of MIL-100 (Fe) and HKUST-1 in different morphologies*. J. Mater. Chem. A, 2013. **1**(19): p. 5827.
110. Li, M. and Dincă, M., *Reductive Electrosynthesis of Crystalline Metal-Organic Frameworks*. J. Am. Chem. Soc., 2011. **133**(33): p. 12926-12929.
111. Plabst, M., Stock, N., and Bein, T., *Hydrogen-Bonded Networks of Ammonium Bis- and Tetrakisphosphonates—Synthesis, High-Throughput Screening and Structural Trends*. Crystal Growth & Design, 2009. **9**(12): p. 5049-5060.
112. Kharissova, O.V., Kharisov, B.I., and Méndez, U.O., *Microwave-Assisted Synthesis of Coordination and Organometallic Compounds*. ChemInform, 2012. **43**(8): p. no.
113. Lu, C.-M., Liu, J., Xiao, K., and Harris, A.T., *Microwave enhanced synthesis of MOF-5 and its CO₂ capture ability at moderate temperatures across multiple capture and release cycles*. Chemical Engineering Journal, 2010. **156**(2): p. 465-470.
114. CCDC. 2014; Support Solution]. Available from: www.ccdc.cam.ac.uk.
115. Willis, R., *Carbon Dioxide Removal from Flue Gas Using Microporous Metal Organic Frameworks*. 2010.
116. Coudert, F.-X., *The osmotic framework adsorbed solution theory: predicting mixture coadsorption in flexible nanoporous materials*. Phys. Chem. Chem. Phys., 2010. **12**(36): p. 10904.
117. Xie, L.-H. and Suh, M.P., *Flexible Metal-Organic Framework with Hydrophobic Pores*. Chemistry - A European Journal, 2011. **17**(49): p. 13653-13656.
118. Yuan, D., Zhao, D., and Zhou, H.-C., *Pressure-Responsive Curvature Change of a "Rigid" Geodesic Ligand in a (3,24)-Connected Mesoporous Metal-Organic Framework*. Inorganic Chemistry, 2011. **50**(21): p. 10528-10530.
119. Zhao, Z., Li, Z., and Lin, Y.S., *Adsorption and Diffusion of Carbon Dioxide on Metal-Organic Framework (MOF-5)*. Industrial & Engineering Chemistry Research, 2009. **48**(22): p. 10015-10020.

120. Yuan, D., Getman, R.B., Wei, Z., Snurr, R.Q., and Zhou, H.-C., *Stepwise adsorption in a mesoporous metal–organic framework: experimental and computational analysis*. Chemical Communications, 2012. **48**(27): p. 3297.
121. Coudert, F.-X., Mellot-Draznieks, C., Fuchs, A.H., and Boutin, A., *Prediction of Breathing and Gate-Opening Transitions Upon Binary Mixture Adsorption in Metal–Organic Frameworks*. J. Am. Chem. Soc., 2009. **131**(32): p. 11329-11331.
122. Zhao, G., Aziz, B., and Hedin, N., *Carbon dioxide adsorption on mesoporous silica surfaces containing amine-like motifs*. Applied Energy, 2010. **87**(9): p. 2907-2913.
123. Nakhla, J., *Metal Organic Frameworks (MOFs)*. Adrich ChemFiles, Jan, 2009. **1**: p. 3.
124. Leus, K., Muylaert, I., Van Speybroeck, V., Marin, G.B., and Van Der Voort, P., *A coordinative saturated vanadium containing metal organic framework that shows a remarkable catalytic activity*, in *Scientific Bases for the Preparation of Heterogeneous Catalysts - Proceedings of the 10th International Symposium, Louvain-la-Neuve, Belgium, July 11-15, 2010*. 2010, Elsevier BV. p. 329-332.
125. González, A.S., Plaza, M.G., Pis, J.J., Rubiera, F., and Pevida, C., *Post-combustion CO₂ capture adsorbents from spent coffee grounds*. Energy Procedia, 2013. **37**: p. 134-141.
126. Marco-Lozar, J.P., Kunowsky, M., Suárez-García, F., and Linares-Solano, A., *Sorbent design for CO₂ capture under different flue gas conditions*. Carbon, 2014. **72**: p. 125-134.
127. Plaza, M.G., García, S., Rubiera, F., Pis, J.J., and Pevida, C., *Post-combustion CO₂ capture with a commercial activated carbon: Comparison of different regeneration strategies*. Chemical Engineering Journal, 2010. **163**(1-2): p. 41-47.
128. Thiruvenkatachari, R., Su, S., Yu, X.X., and Bae, J.-S., *Application of carbon fibre composites to CO₂ capture from flue gas*. International Journal of Greenhouse Gas Control, 2013. **13**: p. 191-200.
129. González, A.S., Plaza, M.G., Rubiera, F., and Pevida, C., *Sustainable biomass-based carbon adsorbents for post-combustion CO₂ capture*. Chemical Engineering Journal, 2013. **230**: p. 456-465.
130. Gil, M.V., Álvarez-Gutiérrez, N., Martínez, M., Rubiera, F., Pevida, C., and Morán, A., *Carbon adsorbents for CO₂ capture from bio-hydrogen and biogas streams: Breakthrough adsorption study*. Chemical Engineering Journal, 2015. **269**: p. 148-158.
131. Hosseini, S., Bayesti, I., Marahel, E., Eghbali Babadi, F., Chuah Abdullah, L., and Choong, T.S.Y., *Adsorption of carbon dioxide using activated carbon impregnated with Cu promoted by zinc*. Journal of the Taiwan Institute of Chemical Engineers, 2015. **52**: p. 109-117.
132. Dantas, T.L.P., Luna, F.M.T., Silva Jr, I.J., Torres, A.E.B., de Azevedo, D.C.S., Rodrigues, A.E., and Moreira, R.F.P.M., *Modeling of the fixed - bed adsorption of carbon dioxide and a carbon dioxide - nitrogen mixture on zeolite 13X*. Brazilian Journal of Chemical Engineering, 2011. **28**(3): p. 533-544.
133. Wang, L., Liu, Z., Li, P., Yu, J., and Rodrigues, A.E., *Experimental and modeling investigation on post-combustion carbon dioxide capture using zeolite 13X-APG by hybrid VTSA process*. Chemical Engineering Journal, 2012. **197**: p. 151-161.

134. Cho, Y., Lee, J.-Y., Bokare, A.D., Kwon, S.-B., Park, D.-S., Jung, W.-S., Choi, J.-S., Yang, Y.-M., Lee, J.-Y., and Choi, W., *LiOH-embedded zeolite for carbon dioxide capture under ambient conditions*. Journal of Industrial and Engineering Chemistry, 2015. **22**: p. 350-356.
135. Hefti, M., Marx, D., Joss, L., and Mazzotti, M., *Adsorption equilibrium of binary mixtures of carbon dioxide and nitrogen on zeolites ZSM-5 and 13X*. Microporous and Mesoporous Materials, 2015. **215**: p. 215-228.
136. Ye, S., Jiang, X., Ruan, L.-W., Liu, B., Wang, Y.-M., Zhu, J.-F., and Qiu, L.-G., *Post-combustion CO₂ capture with the HKUST-1 and MIL-101(Cr) metal-organic frameworks: Adsorption, separation and regeneration investigations*. Microporous and Mesoporous Materials, 2013. **179**: p. 191-197.
137. W. Xu, W., Pramanik, S., Zhang, Z., Emge, T.J., and Li, J., *Microporous metal organic framework [M₂(hfipbb)₂(ted)] (M=Zn, Co; H₂hfipbb=4,4-(hexafluoroisopropylidene)-bis(benzoic acid); ted=triethylenediamine): Synthesis, structure analysis, pore characterization, small gas adsorption and CO₂/N₂ separation properties*. Journal of Solid State Chemistry, 2013. **200**: p. 1-6.
138. Sabouni, R., Kazemian, H., and Rohani, S., *Carbon dioxide adsorption in microwave-synthesized metal organic framework CPM-5: Equilibrium and kinetics study*. Microporous and Mesoporous Materials, 2013. **175**: p. 85-91.
139. Millward, A.R. and Yaghi, O.M., *Metal-Organic Frameworks with Exceptionally High Capacity for Storage of Carbon Dioxide at Room Temperature*. J. Am. Chem. Soc., 2005. **127**(51): p. 17998-17999.
140. Li, B., Zhang, Z., Li, Y., Yao, K., Zhu, Y., Deng, Z., Yang, F., Zhou, X., Li, G., Wu, H., Nijem, N., Chabal, Y.J., Lai, Z., Han, Y., Shi, Z., Feng, S., and Li, J., *Enhanced Binding Affinity, Remarkable Selectivity, and High Capacity of CO₂ by Dual Functionalization of a rht-Type Metal-Organic Framework*. Angewandte Chemie International Edition, 2011. **51**(6): p. 1412-1415.
141. Nalaparaju, A., Khurana, M., Farooq, S., Karimi, I.A., and Jiang, J.W., *CO₂ capture in cation-exchanged metal-organic frameworks: Holistic modeling from molecular simulation to process optimization*. Chemical Engineering Science, 2015. **124**: p. 70-78.
142. Camacho, B.C.R., Ribeiro, R.P.P.L., Esteves, I.A.A.C., and Mota, J.P.B., *Adsorption equilibrium of carbon dioxide and nitrogen on the MIL-53(Al) metal organic framework*. Separation and Purification Technology, 2015. **141**: p. 150-159.
143. Xian, S., Peng, J., Zhang, Z., Xia, Q., Wang, H., and Li, Z., *Highly enhanced and weakened adsorption properties of two MOFs by water vapor for separation of CO₂/CH₄ and CO₂/N₂ binary mixtures*. Chemical Engineering Journal, 2015. **270**: p. 385-392.
144. Hedin, N., Andersson, L., Bergström, L., and Yan, J., *Adsorbents for the post-combustion capture of CO₂ using rapid temperature swing or vacuum swing adsorption*. Applied Energy, 2013. **104**: p. 418-433.
145. Sumida, K., Rogow, D.L., Mason, J.A., McDonald, T.M., Bloch, E.D., Herm, Z.R., Bae, T.-H., and Long, J.R., *Carbon Dioxide Capture in Metal-Organic Frameworks*. Chemical Reviews, 2012. **112**(2): p. 724-781.

146. Sabouni, R., *Carbon dioxide adsorption by metal organic frameworks (Synthesis, Testing and Modeling)*. 2013.
147. Yazaydin, A.Ö., Snurr, R.Q., Park, T.-H., Koh, K., Liu, J., LeVan, M.D., Benin, A.I., Jakubczak, P., Lanuza, M., Galloway, D.B., Low, J.J., and Willis, R.R., *Screening of Metal–Organic Frameworks for Carbon Dioxide Capture from Flue Gas Using a Combined Experimental and Modeling Approach*. *J. Am. Chem. Soc.*, 2009. **131**(51): p. 18198-18199.
148. Han, S., Huang, Y., Watanabe, T., Nair, S., Walton, K.S., Sholl, D.S., and Carson Meredith, J., *MOF stability and gas adsorption as a function of exposure to water, humid air, SO₂, and NO₂*. *Microporous and Mesoporous Materials*, 2013. **173**: p. 86-91.
149. Yu, J. and Balbuena, P.B., *Water Effects on Postcombustion CO₂ Capture in Mg-MOF-74*. *J. Phys. Chem. C*, 2013. **117**(7): p. 3383-3388.
150. Fracaroli, A.M., Furukawa, H., Suzuki, M., Dodd, M., Okajima, S., Gándara, F., Reimer, J.A., and Yaghi, O.M., *Metal–Organic Frameworks with Precisely Designed Interior for Carbon Dioxide Capture in the Presence of Water*. *J. Am. Chem. Soc.*, 2014. **136**(25): p. 8863-8866.
151. Dantas, T.L.P., Luna, F.M.T., Silva, I.J., Torres, A.E.B., de Azevedo, D.C.S., Rodrigues, A.E., and Moreira, R.F.P.M., *Carbon dioxide–nitrogen separation through pressure swing adsorption*. *Chemical Engineering Journal*, 2011. **172**(2-3): p. 698-704.
152. Chaffee, A.L., Knowles, G.P., Liang, Z., Zhang, J., Xiao, P., and Webley, P.A., *CO₂ capture by adsorption: Materials and process development*. *International Journal of Greenhouse Gas Control*, 2007. **1**(1): p. 11-18.
153. Li, G., Xiao, P., Webley, P., Zhang, J., Singh, R., and Marshall, M., *Capture of CO₂ from high humidity flue gas by vacuum swing adsorption with zeolite 13X*. *Adsorption*, 2008. **14**(2-3): p. 415-422.
154. Mérel, J., Clause, M., and Meunier, F., *Carbon dioxide capture by indirect thermal swing adsorption using 13X zeolite*. *Environ. Prog.*, 2006. **25**(4): p. 327-333.
155. Wang, L., Yang, Y., Shen, W., Kong, X., Li, P., Yu, J., and Rodrigues, A.E., *Experimental evaluation of adsorption technology for CO₂ capture from flue gas in an existing coal-fired power plant*. *Chemical Engineering Science*, 2013. **101**: p. 615-619.
156. Gomes, V.G. and Yee, K.W.K., *Pressure swing adsorption for carbon dioxide sequestration from exhaust gases*. *Separation and Purification Technology*, 2002. **28**(2): p. 161-171.
157. Cho, S.-H., Park, J.-H., Beum, H.-T., Han, S.-S., and Kim, J.-N., *A 2-stage PSA process for the recovery of CO₂ from flue gas and its power consumption**, in *Carbon Dioxide Utilization for Global Sustainability, Proceedings of 7th International Conference on Carbon Dioxide Utilization*. 2004, Elsevier BV. p. 405-410.
158. Zhang, J., Webley, P.A., and Xiao, P., *Effect of process parameters on power requirements of vacuum swing adsorption technology for CO₂ capture from flue gas*. *Energy Conversion and Management*, 2008. **49**(2): p. 346-356.

159. Choi, W.-K., Kwon, T.-I., Yeo, Y.-K., Lee, H., Song, H.K., and Na, B.-K., *Optimal operation of the pressure swing adsorption (PSA) process for CO₂ recovery*. Korean Journal of Chemical Engineering, 2003. **20**(4): p. 617-623.
160. Merel, J., Clause, M., and Meunier, F., *Experimental Investigation on CO₂ Post-Combustion Capture by Indirect Thermal Swing Adsorption Using 13X and 5A Zeolites*. Industrial & Engineering Chemistry Research, 2008. **47**(1): p. 209-215.
161. Clause, M., Merel, J., and Meunier, F., *Numerical parametric study on CO₂ capture by indirect thermal swing adsorption*. International Journal of Greenhouse Gas Control, 2011. **5**(5): p. 1206-1213.
162. Ribeiro, R.P.P.L., Grande, C.A., and Rodrigues, A.E., *Activated carbon honeycomb monolith – Zeolite 13X hybrid system to capture CO₂ from flue gases employing Electric Swing Adsorption*. Chemical Engineering Science, 2013. **104**: p. 304-318.
163. Cavenati, S., Grande, C.A., and Rodrigues, A.E., *Adsorption Equilibrium of Methane, Carbon Dioxide, and Nitrogen on Zeolite 13X at High Pressures*. Journal of Chemical & Engineering Data, 2004. **49**(4): p. 1095-1101.
164. Casas, N., Schell, J., Blom, R., and Mazzotti, M., *MOF and UiO-67/MCM-41 adsorbents for pre-combustion CO₂ capture by PSA: Breakthrough experiments and process design*. Separation and Purification Technology, 2013. **112**: p. 34-48.
165. Dantas, T.L.P., Luna, F.M.T., Silva, I.J., de Azevedo, D.C.S., Grande, C.A., Rodrigues, A.E., and Moreira, R.F.P.M., *Carbon dioxide-nitrogen separation through adsorption on activated carbon in a fixed bed*. Chemical Engineering Journal, 2011. **169**(1-3): p. 11-19.
166. Sipöcz, N., Tobiesen, F.A., and Assadi, M., *The use of Artificial Neural Network models for CO₂ capture plants*. Applied Energy, 2011. **88**(7): p. 2368-2376.
167. Siahpoosh, M., Fatemi, S., and Vatani, A., *Mathematical Modeling of Single and Multi-Component Adsorption Fixed Beds to Rigorously Predict the Mass Transfer Zone and Breakthrough Curve*. Iran. J. Chem. Chem. Eng. Vol, 2009. **28**(3).
168. Shafeeyan, M.S., Wan Daud, W.M.A., and Shamiri, A., *A review of mathematical modeling of fixed-bed columns for carbon dioxide adsorption*. Chemical Engineering Research and Design, 2014. **92**(5): p. 961-988.
169. Helfferich, F.G., *Principles of adsorption & adsorption processes*, by D. M. Ruthven, John Wiley & Sons, 1984, xxiv + 433 pp. AIChE Journal, 1985. **31**(3): p. 523-524.
170. Jee, J.-G., Park, H.-J., Haam, S.-J., and Lee, C.-H., *Effects of Nonisobaric and Isobaric Steps on O₂ Pressure Swing Adsorption for an Aerator †*. Industrial & Engineering Chemistry Research, 2002. **41**(17): p. 4383-4392.
171. Kim, M.-B., Bae, Y.-S., Choi, D.-K., and Lee, C.-H., *Kinetic Separation of Landfill Gas by a Two-Bed Pressure Swing Adsorption Process Packed with Carbon Molecular Sieve: Nonisothermal Operation*. Industrial & Engineering Chemistry Research, 2006. **45**(14): p. 5050-5058.
172. Rezaei, F. and Grahn, M., *Thermal Management of Structured Adsorbents in CO₂ Capture Processes*. Industrial & Engineering Chemistry Research, 2012. **51**(10): p. 4025-4034.

173. Khalighi, M., Farooq, S., and Karimi, I.A., *Nonisothermal Pore Diffusion Model for a Kinetically Controlled Pressure Swing Adsorption Process*. Industrial & Engineering Chemistry Research, 2012. **51**(32): p. 10659-10670.
174. Kumar, R., *Adsorption column blowdown: adiabatic equilibrium model for bulk binary gas mixtures*. Industrial & Engineering Chemistry Research, 1989. **28**(11): p. 1677-1683.
175. Delgado, J.A., Uguina, M.A., Sotelo, J.L., and Ruíz, B., *Fixed-bed adsorption of carbon dioxide–helium, nitrogen–helium and carbon dioxide–nitrogen mixtures onto silicalite pellets*. Separation and Purification Technology, 2006. **49**(1): p. 91-100.
176. Delgado, J.A., Uguina, M.A., Sotelo, J.L., Ruíz, B., and Rosário, M., *Separation of carbon dioxide/methane mixtures by adsorption on a basic resin*. Adsorption, 2007. **13**(3-4): p. 373-383.
177. Shendalman, L.H. and Mitchell, J.E., *A study of heatless adsorption in the model system CO₂ in He, I*. Chemical Engineering Science, 1972. **27**(7): p. 1449-1458.
178. Cen, P. and Yang, R.T., *Separation of a Five-Component Gas Mixture by Pressure Swing Adsorption*. Separation Science and Technology, 1985. **20**(9-10): p. 725-747.
179. Raghavan, N.S., Hassan, M.M., and Ruthven, D.M., *Numerical simulation of a PSA system. Part I: Isothermal trace component system with linear equilibrium and finite mass transfer resistance*. AIChE Journal, 1985. **31**(3): p. 385-392.
180. Kapoor, A. and Yang, R.T., *Kinetic separation of methane–carbon dioxide mixture by adsorption on molecular sieve carbon*. Chemical Engineering Science, 1989. **44**(8): p. 1723-1733.
181. Cavenati, S., Grande, C.A., and Rodrigues, A.E., *Upgrade of Methane from Landfill Gas by Pressure Swing Adsorption*. Energy & Fuels, 2005. **19**(6): p. 2545-2555.
182. Ahn, H. and Brandani, S., *Dynamics of Carbon Dioxide Breakthrough in a Carbon Monolith Over a Wide Concentration Range*. Adsorption, 2005. **11**(S1): p. 473-477.
183. Hwang, K.S., Jun, J.H., and Lee, W.K., *Fixed-bed adsorption for bulk component system. Non-equilibrium, non-isothermal and non-adiabatic model*. Chemical Engineering Science, 1995. **50**(5): p. 813-825.
184. Chou, C.-T. and Chen, C.-Y., *Carbon dioxide recovery by vacuum swing adsorption*. Separation and Purification Technology, 2004. **39**(1-2): p. 51-65.
185. Mulgundmath, V.P., Jones, R.A., Tezel, F.H., and Thibault, J., *Fixed bed adsorption for the removal of carbon dioxide from nitrogen: Breakthrough behaviour and modelling for heat and mass transfer*. Separation and Purification Technology, 2012. **85**: p. 17-27.
186. Doong, S.J. and Yang, R.T., *Bulk separation of multicomponent gas mixtures by pressure swing adsorption: Pore/surface diffusion and equilibrium models*. AIChE Journal, 1986. **32**(3): p. 397-410.
187. Diagne, D., Goto, M., and Hirose, T., *Numerical analysis of a dual refluxed PSA process during simultaneous removal and concentration of carbon dioxide dilute gas from air*. J. Chem. Technol. Biotechnol., 1996. **65**(1): p. 29-38.

188. Lee, C.-H., Yang, J., and Ahn, H., *Effects of carbon-to-zeolite ratio on layered bed H₂ PSA for coke oven gas*. *AIChE Journal*, 1999. **45**(3): p. 535-545.
189. Park, J.-H., Kim, J.-N., and Cho, S.-H., *Performance analysis of four-bed H₂ PSA process using layered beds*. *AIChE Journal*, 2000. **46**(4): p. 790-802.
190. Kaguei, S. and Wakao, N., *Validity of infinite bed assumption in the estimation of parameters from thermal waves measured in a non-isothermal adsorption column*. *Chemical Engineering Science*, 1985. **40**(10): p. 1851-1853.
191. Hwang, K.S. and Lee, W.K., *The Adsorption and Desorption Breakthrough Behavior of Carbon Monoxide and Carbon Dioxide on Activated Carbon. Effect of Total Pressure and Pressure-Dependent Mass Transfer Coefficients*. *Separation Science and Technology*, 1994. **29**(14): p. 1857-1891.
192. Carter, J.W. and Husain, H., *The simultaneous adsorption of carbon dioxide and water vapour by fixed beds of molecular sieves*. *Chemical Engineering Science*, 1974. **29**(1): p. 267-273.
193. Ding, Y. and Alpay, E., *Equilibria and kinetics of CO₂ adsorption on hydrotalcite adsorbent*. *Chemical Engineering Science*, 2000. **55**(17): p. 3461-3474.
194. Takamura, Y., *Evaluation of dual-bed pressure swing adsorption for CO₂ recovery from boiler exhaust gas*. *Separation and Purification Technology*, 2001. **24**(3): p. 519-528.
195. Cavenati, S., Grande, C.A., and Rodrigues, A.E., *Separation of mixtures by layered pressure swing adsorption for upgrade of natural gas*. *Chemical Engineering Science*, 2006. **61**(12): p. 3893-3906.
196. Moreira, R.F.P.M., Soares, J.L., Casarin, G.L., and Rodrigues, A.E., *Adsorption of CO₂ on Hydrotalcite-like Compounds in a Fixed Bed*. *Separation Science and Technology*, 2006. **41**(2): p. 341-357.
197. Dantas, T.L., Amorim, S.M., Luna, F.M.T., Silva Jr, I.J., de Azevedo, D.C., Rodrigues, A.E., and Moreira, R.F., *Adsorption of carbon dioxide onto activated carbon and nitrogen-enriched activated carbon: surface changes, equilibrium, and modeling of fixed-bed adsorption*. *Separation Science and Technology*, 2009. **45**(1): p. 73-84.
198. Biswas, P., Agrawal, S., and Sinha, S., *Modeling and simulation for pressure swing adsorption system for hydrogen purification*. *Chemical and Biochemical Engineering Quarterly*, 2010. **24**(4): p. 409-414.
199. Agarwal, A., *Advanced strategies for optimal design and operation of pressure swing adsorption processes*. 2010, Carnegie Mellon University Pittsburgh, PA.
200. Casas, N., Schell, J., Pini, R., and Mazzotti, M., *Fixed bed adsorption of CO₂/H₂ mixtures on activated carbon: experiments and modeling*. *Adsorption*, 2012. **18**(2): p. 143-161.
201. Krishnamurthy, S., Rao, V.R., Guntuka, S., Sharratt, P., Haghpanah, R., Rajendran, A., Amanullah, M., Karimi, I.A., and Farooq, S., *CO₂ capture from dry flue gas by vacuum swing adsorption: A pilot plant study*. *AIChE Journal*, 2014. **60**(5): p. 1830-1842.
202. ANSYS-Fluent-Inc., *manual*. 2012: USA.
203. Britt, D., Furukawa, H., Wang, B., Glover, T.G., and Yaghi, O.M., *Highly efficient separation of carbon dioxide by a metal-organic framework replete with open*

- metal sites*. Proceedings of the National Academy of Sciences, 2009. **106**(49): p. 20637-20640.
204. Seo, Y.-K., Yoon, J.W., Lee, J.S., Lee, U.H., Hwang, Y.K., Jun, C.-H., Horcajada, P., Serre, C., and Chang, J.-S., *Large scale fluorine-free synthesis of hierarchically porous iron(III) trimesate MIL-100(Fe) with a zeolite MTN topology*. Microporous and Mesoporous Materials, 2012. **157**: p. 137-145.
 205. Ferey, G., *Hybrid porous solids: past, present, future*. Chemical Society Reviews, 2008. **37**(1): p. 191-214.
 206. He, W., Lv, W., and Dickerson, J.H., *Gas Diffusion Mechanisms and Models*, in *Gas Transport in Solid Oxide Fuel Cells*. 2014, Springer International Publishing: Cham. p. 9-17.
 207. Incropera; Frank, P.D., David P. , *Fundamentals of Heat and Mass Transfer*. 2007: J. Wiley.
 208. Funazukuri, T., Kong, C., and Kagei, S., *Effective axial dispersion coefficients in packed beds under supercritical conditions*. The Journal of Supercritical Fluids, 1998. **13**(1–3): p. 169-175.
 209. Susarla, N., Haghpanah, R., Karimi, I.A., Farooq, S., Rajendran, A., Tan, L.S.C., and Lim, J.S.T., *Energy and cost estimates for capturing CO₂ from a dry flue gas using pressure/vacuum swing adsorption*. Chemical Engineering Research and Design, 2015. **102**: p. 354-367.
 210. Qasem, N.A.A. and El-Shaarawi, M.A.I., *Improving ice productivity and performance for an activated carbon/methanol solar adsorption ice-maker*. Solar Energy, 2013. **98, Part C**: p. 523-542.
 211. Qasem, N.A.A. and El-Shaarawi, M.A.I., *Thermal analysis and modeling study of an activated carbon solar adsorption icemaker: Dhahran case study*. Energy Conversion and Management, 2015. **100**: p. 310-323.
 212. Ye, F., Xiao, J., Hu, B., Benard, P., and Chahine, R., *Implementation for Model of Adsorptive Hydrogen Storage Using UDF in Fluent*. Physics Procedia, 2012. **24**: p. 793-800.
 213. Millward, A.R. and Yaghi, O.M., *Metal-organic frameworks with exceptionally high capacity for storage of carbon dioxide at room temperature*. J Am Chem Soc, 2005. **127**(51): p. 17998-9.
 214. Mason, J.A., Veenstra, M., and Long, J.R., *Evaluating metal-organic frameworks for natural gas storage*. Chemical Science, 2014. **5**(1): p. 32-51.
 215. Kloutse, F.A., Zacharia, R., Cossement, D., and Chahine, R., *Specific heat capacities of MOF-5, Cu-BTC, Fe-BTC, MOF-177 and MIL-53 (Al) over wide temperature ranges: Measurements and application of empirical group contribution method*. Microporous and Mesoporous Materials, 2015. **217**: p. 1-5.
 216. Liu, D., Purewal, J.J., Yang, J., Sudik, A., Maurer, S., Mueller, U., Ni, J., and Siegel, D.J., *MOF-5 composites exhibiting improved thermal conductivity*. International Journal of Hydrogen Energy, 2012. **37**(7): p. 6109-6117.
 217. Mu, B. and Walton, K.S., *Thermal Analysis and Heat Capacity Study of Metal–Organic Frameworks*. The Journal of Physical Chemistry C, 2011. **115**(46): p. 22748-22754.

218. Saha, D., Bao, Z., Jia, F., and Deng, S., *Adsorption of CO₂, CH₄, N₂O, and N₂ on MOF-5, MOF-177, and Zeolite 5A*. Environmental Science & Technology, 2010. **44**(5): p. 1820-1826.
219. Zheng, H., Han, L., Ma, H., Zheng, Y., Zhang, H., Liu, D., and Liang, S., *Adsorption characteristics of ammonium ion by zeolite 13X*. J Hazard Mater, 2008. **158**(2-3): p. 577-84.
220. Chan, K.C., Chao, C.Y.H., and Wu, C.L., *Measurement of properties and performance prediction of the new MWCNT-embedded zeolite 13X/CaCl₂ composite adsorbents*. International Journal of Heat and Mass Transfer, 2015. **89**: p. 308-319.
221. Chan, K.C.C., Christopher Y. H., *[Improved thermal conductivity of 13X/CaCl₂ composite adsorbent by cnt embedment*. ASME Proceedings, Heat Transfer in Energy Systems, 2013. **1**: p. HT2013-17168, pp. V001T01A040; 10 pages
222. Han, T., Xiao, Y., Tong, M., Huang, H., Liu, D., Wang, L., and Zhong, C., *Synthesis of CNT@MIL-68(Al) composites with improved adsorption capacity for phenol in aqueous solution*. Chemical Engineering Journal, 2015. **275**: p. 134-141.
223. Han, Z. and Fina, A., *Thermal conductivity of carbon nanotubes and their polymer nanocomposites: A review*. Progress in Polymer Science, 2011. **36**(7): p. 914-944.
224. Qadir, N.U., Said, S.A.M., Mansour, R.B., Mezghani, K., and Ul-Hamid, A., *Synthesis, characterization, and water adsorption properties of a novel multi-walled carbon nanotube/MIL-100(Fe) composite*. Dalton Transactions, 2016. **45**(39): p. 15621-15633.
225. Prasanth, K.P., Rallapalli, P., Raj, M.C., Bajaj, H.C., and Jasra, R.V., *Enhanced hydrogen sorption in single walled carbon nanotube incorporated MIL-101 composite metal-organic framework*. International Journal of Hydrogen Energy, 2011. **36**(13): p. 7594-7601.
226. Wang, L.J., Deng, H., Furukawa, H., Gándara, F., Cordova, K.E., Peri, D., and Yaghi, O.M., *Synthesis and Characterization of Metal-Organic Framework-74 Containing 2, 4, 6, 8, and 10 Different Metals*. Inorganic Chemistry, 2014. **53**(12): p. 5881-5883.
227. Yang, D.-A., Cho, H.-Y., Kim, J., Yang, S.-T., and Ahn, W.-S., *CO₂ capture and conversion using Mg-MOF-74 prepared by a sonochemical method*. Energy & Environmental Science, 2012. **5**(4): p. 6465-6473.
228. Ferey, G., Mellot-Draznieks, C., Serre, C., Millange, F., Dutour, J., Surble, S., and Margiolaki, I., *A chromium terephthalate-based solid with unusually large pore volumes and surface area*. Science, 2005. **309**(5743): p. 2040-2.
229. Liu, Q., Ning, L., Zheng, S., Tao, M., Shi, Y., and He, Y., *Adsorption of carbon dioxide by MIL-101(Cr): regeneration conditions and influence of flue gas contaminants*. Sci Rep, 2013. **3**: p. 2916.
230. Munusamy, K., Sethia, G., Patil, D.V., Somayajulu Rallapalli, P.B., Somani, R.S., and Bajaj, H.C., *Sorption of carbon dioxide, methane, nitrogen and carbon monoxide on MIL-101(Cr): Volumetric measurements and dynamic adsorption studies*. Chemical Engineering Journal, 2012. **195-196**: p. 359-368.
231. Shen, C., Liu, Z., Li, P., and Yu, J., *Two-Stage VPSA Process for CO₂ Capture from Flue Gas Using Activated Carbon Beads*. Industrial & Engineering Chemistry Research, 2012. **51**(13): p. 5011-5021.

232. Cho, S.H., Park, J.H., Beum, H.T., Han, S.S., and Kim, J.N., *A 2-stage PSA process for the recovery of CO₂ from flue gas and its power consumption*, in *Studies in Surface Science and Catalysis*. 2004. p. 405-410.
233. Merel, J., Clause, M., and Meunier, F., *Experimental Investigation on CO₂ Post-Combustion Capture by Indirect Thermal Swing Adsorption Using 13X and 5A Zeolites*. *Industrial & Engineering Chemistry Research*, 2008. **47**(1): p. 209-215.

Vitae

Name :Naef A. A. Qasem

Nationality :Yemen

Date of Birth :8/29/1983

Email :naefqasem@kfupm.edu.sa; naefqasem@gmail.com

Address :KFUPM Campus

Academic Background

2003-2008

B.Sc. (graduated in February, 2008) in Mechanical Engineering, King Khalid University (KKU), KSA (with GPA: **4.82** out of **5** and excellent category with "**First Class Honor**", **first top student** in the College of Mechanical Engineering).

2010-2013

M.Sc. (graduated in May, 2013) in Mechanical Engineering, King Fahd University of Petroleum and Minerals (KFUPM), KSA (with GPA: **3.906** out of **4**).
Thesis title: *Thermodynamic Analysis and Modeling Study of an Intermittent Solar Adsorption Refrigeration System.*

2014-2017

Ph.D. (dissertation defense on May 17, 2017) in Mechanical Engineering, King Fahd University of Petroleum and Minerals (KFUPM), KSA (with GPA: **3.722** out of **4**).
Dissertation title: *Physical Adsorption of Carbon Dioxide Capture by Novel Materials.*

Research Publications from the Dissertation

- 1- Ben-Mansour, R., Habib, M.A., Bamidele, O.E., Basha, M., **Qasem, N.A.A.**, Peedikakkal, A., Laoui, T., and Ali, M., *Carbon capture by physical adsorption: Materials, experimental investigations and numerical modeling and simulations – A review*. Applied Energy, 2016. 161: p. 225-255.
- 2- R. Ben-Mansour, M. Basha, and **N.A.A. Qasem**, *Multicomponent and multi-dimensional modeling and simulation of adsorption-based carbon dioxide separation*. Computers & Chemical Engineering, 2017. 99: p. 255-270.
- 3- **Qasem, Naef A.A.**, Ben-Mansour, Rached, and Habib, Mohamed A., *Enhancement of adsorption carbon capture capacity of 13X with optimal incorporation of CNT*. International Journal of Energy and Environmental Engineering, 2017.
- 4- **Qasem, Naef A.A.**, Qadir, Najam U., Ben-Mansour, Rached, and Said, Syed A.M., *Synthesis, Characterization, and CO₂ Breakthrough Adsorption of a Novel MWCNT/MIL-101(Cr) Composite*, Journal of CO₂ Utilization. (**Submitted**)
- 5- Ben-Mansour, Rached, **Qasem, Naef A. A.**, and Habib, Mohamed A., *Adsorption Characterization and CO₂ Breakthrough of MWCNT/Mg-MOF-74 and MWCNT/MIL-100(Fe) Composites*. (**Submitted**)
- 6- Effect of regeneration process on CO₂ uptake using MWCNT/MOF-74 and MWCNT/13X. (**In progress**)
- 7- Carbon dioxide breakthrough separation from dry and humid CO₂/N₂ mixture using Mg-MOF-74: CFD modeling. (**Submitted**)
- 8- An efficient vapor pressure swing adsorption process to separate CO₂ from CO₂/N₂ mixture. (**Submitted**)
- 9- Optimizing temperature swing adsorption process for carbon dioxide separation from CO₂/N₂ mixture. (**Submitted**)
- 10- An efficient carbon dioxide adsorptive storage using MOF-5 and MOF-177. (**Submitted**)